이학박사학위논문

Engineering Carbon Nanomaterials for Stem cell and Tissue regeneration
탄소 나노 재료를 이용한 줄기세포 조절 및 조직 재생에 관한 연구

2015 년 2 월

서울대학교 대학원

화학부 물리화학 전공

박 수 범

Engineering Carbon Nanomaterials for Stem cell and Tissue regeneration

탄소 나노 재료를 이용한 줄기세포 조절 및 조직 재생에 관한 연구

지도교수: 홍 병 희

이 논문을 이학박사 학위논문으로 제출함

2015년 10월

서울대학교 대학원

화학부 물리화학전공

박수범

박수범의 이학박사 학위논문을 인준함

2015년 1월

위 원 장 장 두 전 ㊞

부위원장 홍 병 희 ㊞

위 원 이 연 ㊞

위 원 조 성 표 ㊞

위 원 윤 명 한 ㊞

Ph. D. Thesis

Engineering Carbon Nanomaterials for Stem cell and Tissue regeneration

Supervisor: Professor Byung Hee Hong

Major: Physical Chemistry

By Subeom Park

Department of Chemistry

Graduate School of Seoul National University

2015

Abstract

With the recent advances in stem cell engineering and tissue regeneration, stem cell-based regenerative medicine provides a promising strategy for the treatment of heart failure, neuronal disorders or neurodegenerative diseases, which are still one of the leading causes of human death and disability in the world. Nevertheless, the current clinical treatments for heart failure, neuronal disorders or neurodegenerative disease are quite limited, and the number of people affected by these diseases consistently increases every year. As a direct result, there is a great need to discover alternative therapies for these disorders or diseases. Recently, graphene has been recognized as a biomimetic nanomaterial and has been proposed for a number of biomedical applications because of their fascinating properties different from those of the carbon-based graphitic materials. This dissertation is the result of an effort to develop 2D and 3D platforms for controlling cell microenvironment for various cell and tissue engineering applications. The specific objectives of my thesis are as follow: (1) the development of an efficient 2D platform for the growth and differentiation of stem cells, which is crucial for autologous cell therapy and tissue engineering to treat various disorders and diseases, and the investigation of the effects of graphene on the enhanced differentiation process through analyzing the expressions of extracellular matrix (ECM) proteins and cell signaling molecules, (2) the improvement of nanoengineering approaches for controlling 3D cell microenvironment and the use of these facile techniques to regulate cell fate decisions. The main results of my dissertation research can be summarized as follows.

First, we found that the 3D spheroid structure could be formed from aggregated hMSCs grown on monolayer of graphene without the use of any external factors. Second, we have provided the first demonstration that graphene can be used as a stem cell culture substrate to promote the cardiomyogenic differentiation process of MSCs without the use of any exogenous chemical inducers. Finally, the culture of hESCs on graphene promotes the stepwise differentiation of these cells into mesodermal cells and endodermal cells and their subsequent cardiomyogenic differentiation compared with their culture on glass. However, for the success of clinical regenerative application, a three-dimensional (3D) scaffold is a demanding field in terms of development of microenvironments and appropriate synergistic cell guidance cues. Thus, the following part II of the thesis presents the development and applications of carbon nanomaterial-based 3D scaffolds. Recently, graphene has been proposed as a tool for pioneering approach in the progress of designing nano-engineered cell culture platforms or scaffolds. Development of transplantable 3D hybrid graphene scaffold *in vivo* that can be applied in practical use for regenerative therapy is urgently needed. Especially, it is important to verify the superiority of graphenes as regenerative nanocomposites by applying to real disease animal model. Here, we developed a novel method for fabricating a hybrid bioscaffold composed of CNTs and BC for bone regeneration. Lastly, we developed a strategy to hybridize graphene with the 3D layer by layer scaffold and investigate its impact on the fundamental neuron study. This dissertation provides the details of my work on all projects related to designing scaffolds for tissue engineering and regenerative

Keywords: Graphene, Carbon nanotubes, Stem cells, Biomimetic, Biomaterials, Tissue engineering

Student Number: 2011-30906

Contents

1. General introduction

Part I 2D Graphene based stem cell engineering

2. Graphene-directed spheroid formation of mesenchymal stem cells for enhanced neuronal differentiation

3. Graphene enhances the cardiomyogenic differentiation of human embryonic stem cells

4. Graphene-regulated cardiomyogenic differentiation process of mesenchymal stem cells by enhancing the expression of extracellular matrix proteins and cell signaling molecules

Part II Engineering nature-driven three-dimensional bioscaffolds with carbon nanomaterials

5. Binding behavior of hybrid system for the APCLP coated-carbon nanotube and graphene with bacterial cellulose

6. *In Situ* hybridization of carbon nanotubes with bacterial cellulose for three-dimensional bioscaffolds

7. *In vivo*-like three-dimensional neuronal networks engineered by Graphene bioscaffolds

Abstract (Korean)

Acknowledgement

List of Figures

Chapter 1

Figure 3. Schematic diagram depicting the possible ability of carbon nanomaterials to induce stem cells differentiation into specific cell lineages.

Chapter 2

Figure 1. Fabrication and characterization of highly uniform graphene for the growth and neuronal differentiation of stem cells. a, Schematic of the spheroid formation and neuronal differentiation of hMSCs using high-quality graphene. b, Raman spectroscopy of the transferred graphene. c, TEM image of a graphene sheet on a TEM grid. d, The SAED pattern. e, Intensity profile of the diffraction spots along a line connecting points p and q in the single-layer graphene diffraction pattern. The uniform intensity profile between the inner and outer spots proves that the graphene sheet consists of a single layer. f, High-resolution STEM image of at low-magnification. g, High-resolution STEM image of at high-magnification.

Figure 2. Growth of hMSCs on highly uniform graphene. a, Representative immunofluorescent images of hMSCs cultured on a graphene-uncoated glass substrate and high-quality graphene. b, Quantification of the cell body and the nucleus, indexed by the axial ratio of the cell body and the width and length of the nucleus. c, Quantification of the amount of focal adhesion. One-hundred cells were used in the quantification process. d, Western blot analysis and quantification of the levels of Cx43 expression in the hMSCs cultured. e, Proliferation of cells on the substrates for 7 days. Three independent experiments were conducted. f, Representative immunofluorescent images of STRO-1 and a western blot analysis of

the hMSCs cultured on the substrates for 10 days. The error bars represent the standard deviation.

Figure 3. Neuronal differentiation of hMSCs on highly uniform graphene. a, Representative phase-contrast images of the hMSCs cultured on the substrates in the growth medium or the neuronal differentiation medium. b, Representative immunostaining images of TUJ1, NeuN, GFAP, and DAPI of the hMSCs cultured in the neuronal differentiation medium for 5 days. c, Representative Nissl staining images of hMSCs cultured in the neuronal differentiation medium for 5 days. d, the neuritie lengths e. One-hundred cells were used in the quantification process. f, qRT–PCR analysis of hMSCs cultured in the neuronal differentiation medium for 5 days. Three independent experiments were conducted, and the error bars represent the standard deviation.

Figure 4. Response of neuronal differentiated cells from hMSCs grown on highly uniform graphene to high K^+ stimulation on high-quality graphene. The cells were pre-incubated with Fluo-4 AM dye and imaged before and after the stimulations. Representative fluorescence images on the fluorescence intensity change on the cells were obtained before and after high K^+ stimulations. Representative plot of the relative fluorescence intensity change $\Delta F/F$ of the cell indicated by the red arrow.

Figure 5. A case study for autologous stem cell based therapy. a, An *in vitro* protocol to highlight the potential of the differentiated neurons from hMSCs grown on graphene as a source for cell therapy to treat neuronal diseases. It was hypothesized that the differentiated neurons from hMSCs grown on graphene could be transferred into the body to treat neuronal diseases. b, Representative Nissl staining images of

the cells cultured on the glass substrates in the growth media for 2 days (total 10 day culture) after re-seeding the detached differentiated hMSCs onto graphene or a glass substrate using the trypsin treatment.

Figure S1. Schematic of fabrication of the high quality graphene on glass substrate for growth and neuronal differentiation of stem cells.

Figure S2. a, AFM image of graphene growth on copper foil. b, Atmosphere STM image of graphene grown on Cu foil. c, Typical optical microscope image of graphene transferred onto 300 nm SiO2/Si substrate. d, UV–vis spectra of transferred graphene on the glass substrate. e, Contact angle of graphene and coverslip f, Sheet resistance mapping of the graphene.

Figure S3. AFM topography images of the graphene and glass substrate. The values indicate the roughness of the surfaces.

Figure S4. a, Low magnification images of hMSCs cultured on the graphene and glass substrate for 1 day. The cells were stained by crystal violet to show the formation of 3D spheroids on the graphene. b, Representative phase-contrast images of hMSCs cultured on the graphene for 1 day and 7 days, respectively. The white arrows indicate the spheroids of hMSCs.

Figure S5. Representative immunostaining images of actin, nucleus, and fibronectin on the graphene and glass substrate after culturing hMSCs for 7 days.

<u>Chapter 3</u>

Figure 1. Preparation and characterization of large-area graphene substrates. a, Schematic of the preparation process used to produce the graphene coating on a glass

coverslip. b, A typical optical microscopic image of graphene transferred onto 300-nm-thick SiO_2/Si substrate. c, Photograph d, contact angle of a glass coverslip and graphene on a glass coverslip. e, Raman spectroscopy of the transferred graphene. f, UV-visible spectra of transferred graphene on a glass coverslip and a glass coverslip substratum, showing the transparency of the graphene on the coverslip. g, TEM image of graphene on a TEM grid. h, SAED pattern. i, Sheet resistance of monolayer graphene on a glass coverslip.

Figure 2. The coating of graphene with VN is required to achieve a high viability of hESCs cultured on the graphene. hESCs were cultured on graphene for two days. a, Light microscopic images of hESCs cultured on the graphene. b, Fluorescence microscopic images of hESCs stained with FDA and EB. The green and orange-red colors indicate viable and dead cells, respectively. c, SEM image of hESCs cultured on graphene. The scale bars indicate (a) 200 μm, (b) 100 μm, and (c) 20 μm.

Figure 3. Culture on graphene enhances the mesodermal and endodermal lineage differentiation of hESCs. a, A schematic diagram for the cardiomyogenic differentiation of hESCs in a two-dimensional, stepwise differentiation system. b, The mesodermal c, cardiac mesodermal d, endodermal, and e, ectodermal gene expression profiles of hESCs cultured for 21 days on Matrigel-coated glass (Matrigel), VN-coated glass (glass), or VN-coated graphene (graphene), as determined by qRT-PCR assay. The values were normalized to the levels obtained for the Matrigel group (n=4 per group, *$p<0.05$ versus Matrigel, #$p<0.05$ versus glass).

Figure 4. Culture on graphene enhances the cardiomyogenic differentiation of hESCs. a, A schematic diagram of the gene expression profile during the cardiomyogenic differentiation process of hESCs. b, Cardiomyogenic gene expression profiles of hESCs cultured for 21 days on Matrigel-coated glass (Matrigel), VN-coated glass (glass), or VN-coated graphene (graphene), as determined by qRT-PCR assay. The values were normalized to the levels obtained for the Matrigel group (n=4 per group, *$p<0.05$ versus Matrigel, #$p<0.05$ versus glass).

Figure 5. Culture on graphene enhances cardiac-specific ECM expression in hESCs. Gene expression profiles of extracellular matrix proteins in hESCs cultured for 21 days on Matrigel-coated glass (Matrigel), VN-coated glass (glass), or VN-coated graphene (graphene), as determined by qRT-PCR assay. The values were normalized to the levels obtained for the Matrigel group (n=4 per group, *$p<0.05$ versus Matrigel, #$p<0.05$ versus glass).

Figure 6. Mechanisms underlying the graphene-enhanced cardiomyogenic differentiation Nanoroughness of graphene, FAK, and ERK signaling. a, AFM images and surface nanoroughness of VN-coated glass (glass group) and VN-coated graphene (graphene group). b, a schematic diagram of the signal transduction pathways associated with the cardiomyogenic differentiation of hESCs cultured on graphene. The enhanced hESC adhesion and the subsequent upregulation of ERK signaling of hESCs cultured on graphene were likely attributed to the nanoroughness of the graphene. ECM: extracellular matrix, α, β: integrin α and β subunits, PAX: paxillin, VIN: vinculin. c, Western blot analyses of hESCs cultured on Matrigel-

coated glass (Matrigel), VN-coated glass (glass), or VN-coated graphene (graphene) to analyze the molecules involved in the signal transduction pathways, and quantification of the relative protein expression levels of the cell signaling molecules. The values were normalized to the levels obtained for the Matrigel group (n=3 per group, *p<0.05 versus Matrigel, #p<0.05 versus glass).

Chapter 4

Figure 1. Characterization of graphene substrates. a, AFM topography images, b, photographs, and c, contact angle images of (i) coverslip and (ii) graphene on coverslip. d, Raman spectroscopy of graphene. e, Transparency of graphene films transferred on coverslip. TEM image of graphene sheet on a TEM grid at f, low and g, high magnifications. h, The SAED pattern. i, Intensity profile of the diffraction spots along a line connecting points E and F in the single-layer graphene diffraction pattern. The uniform intensity profile between the inner and outer spots proves that the graphene sheet consists of a single layer.

Figure 2. *In vitro* biocompatibility of graphene. a, Live/dead assay of MSCs cultured on graphene and coverslips for 3 days and 1 week. The live cells were stained with calcein-AM (green), and the dead cells were stained with ethidium homodimer (red). The scale bar represents 200 μm. b, The number of live cells is expressed relative to the number of live cells on a coverslip on day 1. The number of live cells was counted using CCK-8. c, Upregulation of Bcl-2, an anti-apoptotic marker, and downregulation of caspase-3, a pro-apoptotic marker, in MSCs cultured on graphene for 3 weeks relative to MSCs cultured on coverslips, as evaluated by qRT-PCR. *p

< 0.05 compared to MSCs cultured on coverslips. d, Proliferation of MSCs cultured on coverslips and graphene. The proliferation was evaluated by PCNA staining. The proliferating cells were stained with PCNA (red), and the nuclei were stained with DAPI (blue). The scale bar represents 200 μm. e, Growth of MSCs cultured on graphene and coverslips. The growth was evaluated by counting the number of cells at various time points using hemocytometer.

Figure 3. Enhanced expression of cardiomyogenic genes in MSCs cultured on graphene without using chemical induction materials. Two and three weeks after cell seeding, the MSCs cultured on graphene exhibited an upregulation of the mRNA expression of an early cardiomyogenic transcriptional factor (GATA4), cardiomyogenic contractile proteins (cardiac actin, β-MHC, cTnT, MLC2a, and MLC2), and gap junction protein (Cx43) compared with MSCs cultured on coverslips. The mRNA expression levels were evaluated by qRT-PCR. $^*p < 0.05$ compared to MSCs cultured on coverslips.

Figure 4. Enhanced gene expression of ECM proteins in MSCs cultured on graphene. The MSCs cultured on graphene for 2 weeks exhibited an upregulation of the mRNA expression of Col I, Col III, Col IV, fibronectin, and laminin, which are known to promote the cardiomyogenic differentiation of stem cells compared with those on coverslips. The mRNA expression levels were evaluated by qRT-PCR. $^*p < 0.05$ compared to MSCs cultured on coverslips.

Figure 5. Activation of molecules involved in cardiomyogenic differentiation and survival-related signal transduction pathways in MSCs cultured on graphene. a, Western blot analyses of MSCs cultured on graphene or coverslips for 3 weeks to

analyze the molecules involved in the signal transduction pathways. Quantification of the relative protein expressions of the cell signaling molecules (n = 3). $^*p < 0.05$ compared to MSCs cultured on coverslips. b, A schematic diagram of the signal transduction pathways associated with cardiomyogenic differentiation and survival. Arrows indicate expression upregulations.

Figure S1. Schematic of fabrication of the high quality graphene on glass substrate for growth and neuronal differentiation of stem cells.

Chapter 5

Figure 1. Dispersion behavior of CNT

Figure 2. Optimized geometries

Figure 3. Front and side views of a, the geometry optimized by DFT calculations and b, that obtained from molecular dynamics simulations for the cellulose-polymer (HPOEM)/CNT system

Figure 4. Front and side views of geometries obtained from the molecular dynamics simulations for a, cellulose-cellulose, b, polymer(HPOEM)-CNT hybrid, and c, cellulose-CNT systems

Figure 5. Front and side views of geometries obtained from the molecular dynamics simulations for a, cellulose-CNT, b, polymer(HPOEM)-CNT, and **c,** cellulose-polymer(HPOEM)/CNT systems for the time scale (0.0 ps - 4.0 ps - 12.5 ps)

Figure 6. Molecular dynamic simulations for a, rGO-BC and b, GO-BC

Figure 7. Molecular dynamic simulations for a, rGO-APCLP and b, GO-APCLP

Figure 8. Molecular dynamic simulations for APCLP-coated a, rGO-BC and b, GO-

BC

Chapter 6

Figure 1. APCLP-mediated dispersion of CNTs. a, MD simulation of APCLP-coated CNT. b, SEM and TEM images of CNTs before and after APCLP coating. c, Fourier transform infrared spectroscopy spectrum of CNT, APCLP and APCLP-coated CNT. d, Colloidal stability of CNT and APCLP-coated CNT after centrifugation and after 3 months. e, Colloidal stability of APCLP-coated CNT in various pH conditions of culture medium.

Figure 2. APCLP-induced hybridization of CNTs and BC. a, Schematic representation of APCLP-coated CNT-BC hybridization. b, Binding energies measured by ab initio calculations. c, MD simulations for CNT-BC and APCLP-coated CNT-BC. d, Schematic illustration for the fabrication processes of BC, CNT-BC-Imm and CNT-BC-Syn.

Figure 3. TEM analyses of CNT-BC hybrid. a, TEM images of BC, CNT-BC-Imm and CNT-BC-Syn. b, Thickness distribution of BC on CNTs, showing the partial exposure of bare CNTs. c, EELS spectra of BC and CNT-BC-Syn showing the core-shell hybridization structure of CNT-BC-Syn.

Figure 4. Analyses showing the homogenous distribution of CNTs in CNT-BC-Syn. a, Cross-sectional optical images of BC, CNT-BC-Imm and CNT-BC-Syn. Scale bars, 20 µm. b, SEM images of BC, CNT-BC-Imm and CNT-BC-Syn with top and cross-sectional views. Scale bar, 5 µm. c, Raman mapping of CNT-BC-Imm and CNT-BC-

Syn. d, Force mapping of BC, CNT-BC-Imm and CNT-BC-Syn on the surface measured by contact-mode AFM. Scale bars, 2 μm.

Figure 5. Bone regeneration efficacy of the scaffolds. a, Bone regeneration evaluated by micro-CT analyses. Quantification of the bone formation area of defects. b, Goldner's trichrome staining of mouse calvarial defect areas. Quantification of bone formation area and bone density of defects. **c,** Immunohistochemistry of mouse calvarial defect areas. DAPI staining indicates osteoconductivity of the scaffolds. Osteocalcin staining indicates osteoinductivity of the scaffolds. Scale bars, 2 mm. *$p < 0.05$ compared to any other group. #$p < 0.05$ compared to no treatment, BC and CNT-BC.

Figure S1. BC preparation and optimization processes and parameters. a, Images of *G. xylinus* and BC. b, Effect of pH, temperature, culture time, APCLP concentration and ethanol concentration on BC yield. Cells were cultivated for 7 days in a mannitol medium.

Chapter 7

Figure 1. Fabrication and characterization of bare/graphene composited BC. a, Schematic explanation of Acetobacter Xylinum producing cellulose nanofiber and in situ composition of graphene. b, Top view and lateral view of bacterial cellulose exhibit nanofibrillar cellulose and stacked layered structure, respectively. c, Top view of GO (left) and rGO (right) composited BC. d, High resolution TEM image of bare bacterial cellulose and their crystallinity. e, Raman spectroscopic measurement confirms the presence of GO and rGO with corresponding vibration peaks. f. Liquid

AFM measurement of elastic modulus along normal direction.

Figure 2. Detailed neuronal morphology and controlled z-directional neuronal outgrowth. a, scanning electron microscope images represent interfacial region between 3-div neuron and BC. b z-directional neuronal outgrowth of bare and graphene composited BC. MAP2 and Tau labels neuronal dendrites and axons, respectively. c, statistical representation of z-directional neuronal outgrowth depending presence of graphene composition d, BET measurements exhibit modulation of bacterial cellulose porosity by means of graphene composition. e, schematic figure of outgrowing neuron toward to counter BC surfaces. f, Fluorescence y-stacked image of widely culture (3.5 mm × 3.5 mm × 1 mm) 20-div neuron. g, Fluorescence light intensity decay of fluorescence beads depending on depth of BC.

Figure 3. Neuronal kinetics in BC a, comparison of neuronal development on glass and BC substrate b, statistical analysis of neuronal polarity. c, time evolutional trajectory of 3-div outgrowing axon on BC and glass substrate. (n = 20 for BC and glass, 5 sec for time interval) d, extracted quantitative information of outgrowing axon reveal total traveling length and final length of axon which composed or substrate by forward and backward motion. e, traced 20-div neuronal morphology on BC exhibits delicate and distinct neuronal sub-cell type. f, synchronization of axon branching at the certain depth (700 μm) of BC.

Figure 4. Comparison of calcium signalling of cultured neuron on BC and glass substrates. a,b, calcium signalling of 14-div cultured neurons show difference calcium spike frequency and duration. Cell density is 20-30/mm^2. c, collection of

calcium spike peakes with respect to time for 14-div neuron on glass and BC substrate.

List of Tables and Schemes

Chapter 1

Table 1. 2D graphene based cell modulation

Table 2. 3D graphene based cell modulation

Chapter 3

Table 1. Human-specific primers for each gene analyzed through the qRT-PCR assay.

Chapter 5

Table 1. Binding energies E_b and interatomic distance between GO(rGO) and adsorbates.

Chapter 6

Table 1. Properties of BC, CNT-BC-Imm and CNT-BC-Syn

Scope and Format of Dissertation

The dissertation is divided into two parts comprised of six research chapters. Chapter 1 describe the current advances made with carbon nanomaterials based platforms in the stem cell engineering field and the challenges facing these exciting new tools both in terms of biological activity and toxicological profiling *in vitro* and *in vivo*. The next three chapter provide the contents for Part I. Part I developed a series of graphene as an efficient platform for stem cell based therapy. In Chapter 2 shows that monolayer graphene-directed growth and neuronal differentiation of mesenchymal stem cells. In Chapter 3 describes that graphene-regulated cardiomyogenic differentiation process of mesenchymal stem cells by enhancing the expression of extracellular matrix proteins and cell signaling molecules. In Chapter 4 shows that graphene promotes the stepwise differentiation of embryonic stem cells into mesodermal cells and endodermal cells and their subsequent cardiomyogenic differentiation. The hybridization of functional nanomaterials with three-dimensional (3D) scaffolds for biomedical applications has been extensively studied, but further advancements have been hampered by unstable integration and inhomogeneous distribution of the nanomaterials. Part II is comprised of the next three chapters and develop a series of nature driven architecture for tissue engineering with controlled properties. In Chapter 5 provides a simple and nontoxic method for dispersal of carbon nanomaterials was investigated using amphiphilic comb-like polymer (APCLP) and its mechanism was elucidated by simulation. In Chapter 6 demonstrates that a new method for *in situ* hybridization of CNTs with bacterial cellulose (BC) by utilizing APCLP. In Chapter 7 demonstrates that *in vivo*-like three-dimensional neuronal networks engineered by graphene bioscaffolds.

Chapter 1

General introduction

Introduction

1.1 Summary

Stem cells represent a promising tool for tissue engineering and regenerative medicine. Nevertheless, they require a particular niche to grow and regenerate. Carbon nanomaterials have attracted much attention as promising materials for biomedical applications due to their extraordinary physicochemical properties, such as their extracellular matrix-like structure, nanotopographic surface, elasticity, high mechanical strength, high electrical conductivity, and good molecule absorption. Recently, the physicochemical properties of graphene and its biocompatibility have inspired scientists to utilize this material for regulating the growth and differentiation of stem cells engineering. Even though studies on carbon-based nanomaterials are still very much at the ‘nascent’ stage, graphene has been attracting great interest in stem cell engineering and tissue regeneration. In this chapter, we introduce some of the interesting properties of graphene that could impose profound effects on stem cell behavior. After introduction of the properties of graphene, we summarize the advances in graphene-based stem cell engineering applications; how it affects cell behavior and differentiation.

1.2 Histological background

The existence of graphene was predicted over 40 years ago but it was not until 2004 when Geim and Novoselov of Manchester University successfully isolated single layer of graphite for the first time using scotch tapes. In 2005, Geim group discovered particles that follow Fermi Dirac statistics and Philip Kim group of Columbia University found the Half-Integer Quantum Hall Effect in graphene, bringing light to some of the toughest conundrums in physics. Previously the general belief was that graphene cannot maintain its 2D structure in the natural environment and it is thermodynamically unstable with low melting point. However the discovered graphene was very stable and had high crystallinity.

Graphene can be seen as carbon atoms with different electronic characteristics coming together to form two triangular sub-lattice and then form hexagonal lattices as they overlap. The electrons of carbon atoms move around by jumping between atoms of same characteristics. The speed of the electron mobility is 20,000-50,000cm^2/Vs, which is hundred times faster than that of Si semiconductors. Graphene also has low electrical resistivity and therefore have low heat generation. Recently, graphene has been recognized as a biomimetic nanomaterial and has been proposed for a number of biomedical applications because of their fascinating properties different from those of the carbon-based graphitic materials. (e.g., high elasticity, extremely high charge carrier mobility, large surface area, thermal/electrical conductivity, mechanical strength and chemical/mechanical stability). The carbon atoms forming graphene provide the basis for its enhancement with both positive and negative functional groups. In biomedical and nanoengineering, graphene and its derivatives have been used for a variety of applications such as nano carriers for drug/gene delivery, photodynamic therapy of cancer, biosensors, conductive scaffolds, cell imaging and to name a few. It also has the potential to be used as a reinforcement material in hydrogels, biodegradable films, electrospun fibers and other tissue engineering scaffolds. (Fig. 1.)

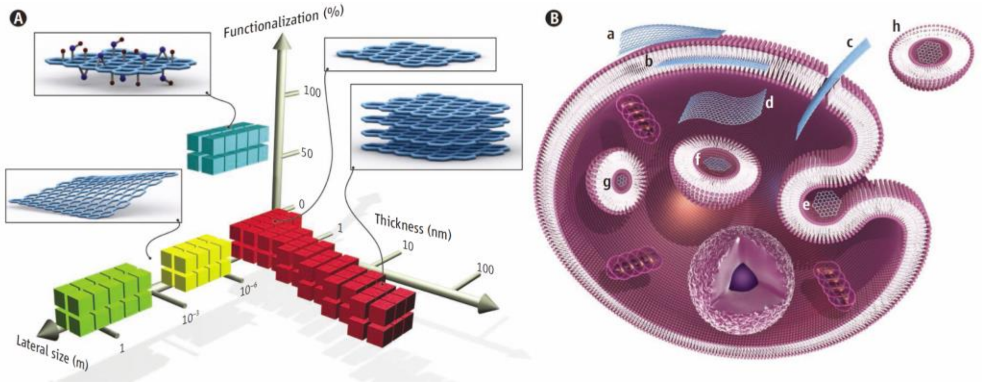

Figure 1 | Graphene materials and their biological interactions. (A) A parameter space for the most widely used graphene materials can be described by the dimensions and surface functionalization of the material, the latter defined as the percentage of the carbon atoms in sp3 hybridization. Green squares represent epitaxially grown graphene; yellow, mechanically exfoliated graphene; red, chemically exfoliated graphene; blue, graphene oxide. Note that a number of other graphene-related materials (such as graphene quantum dots and graphene nanoribbons) are also being used in experiments. (B) Possible interactions between graphene-related materials with cells (the graphene flakes are not to scale). (a) Adhesion onto the outer surface of the cell membrane. (b) Incorporation in between the monolayers of the plasma membrane lipid bilayer. (c) Translocation of membrane. (d) Cytoplasmic internalization. (e) Clathrin-mediated endocytosis. (f) Endosomal or phagosomal internalization. (g) Lysosomal or other perinuclear compartment localization. (h) Exosomal localization. The biological outcomes from such interactions can be considered to be either adverse or beneficial, depending on the context of the particular biomedical application. Different graphene-related materials will have different preferential mechanisms of interaction with cells and tissues that largely await discovery.[1]

1.3 Plausible mechanism of carbon nanomateirals’s positive effects on the stem cell and tissue regeneration

It has been well known that surface morphology, physical properties, and chemistry of carbon nanomateirals are critical parameters for regulating cell fates. With recent years, the several possible mechanisms have been reported to explain the interactive effects and further develop carbon nanomateirals as a scaffold for tissue engineering applications. (Fig. 2).

The ability of graphene sheets and carbon nanotubes to enhance the adhesion and differentiation of cells, including neurons[2], osteoblasts[3], cardiomyocytes[4,5], and stem cells has been demonstrated (Fig. 3).

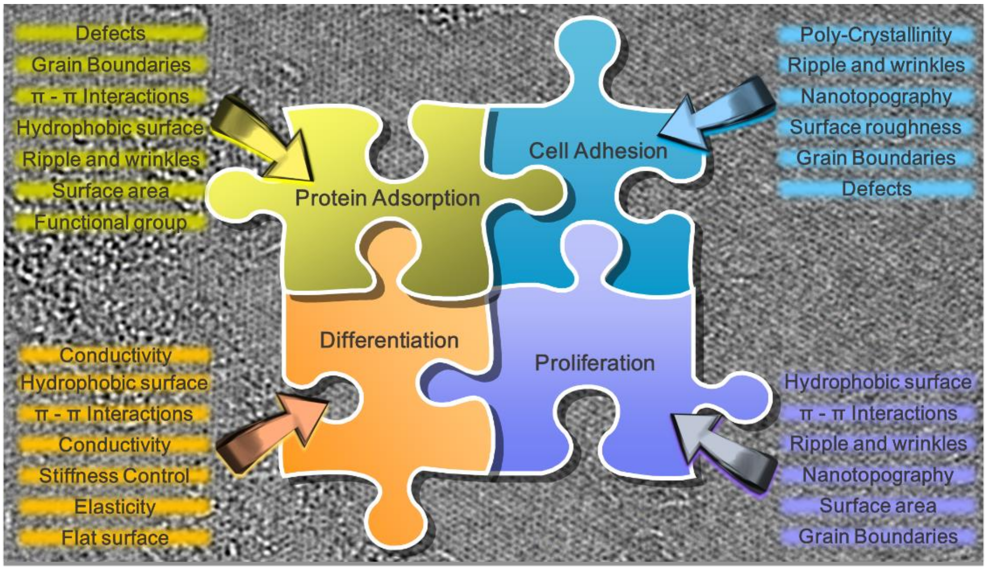

Figure **2 |** Schematic diagram depicting the possible interaction between carbon nanomaterials with stem cells fates

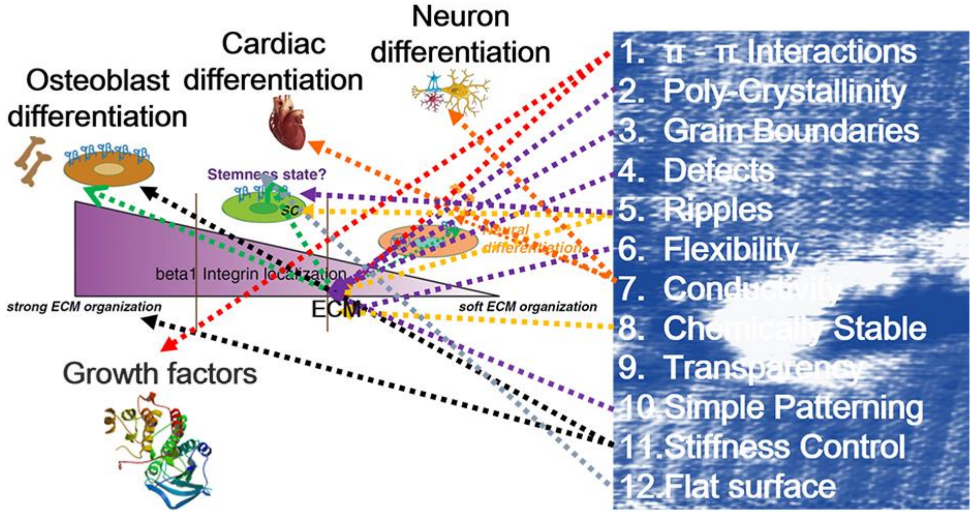

Figure 3 | Schematic diagram depicting the possible ability of carbon nanomaterials to induce stem cells differentiation into specific cell lineages.

Protein adhesion mechanism

Another important aspect of the protein and small molecular chemicals adsorption capacity is the effect on the stem cell niche. In order to or communicate with neighboring cells many of the stem cells secrete signaling molecules that affect both their differentiation status and the influence of their local microenvironments. Graphene show quite high adsorption performance. Solution based reduced graphene oxide (rGO) and Graphene oxide (GO), the oxidized counterpart of graphene, contains functional groups such as oxygen, hydrogen, epoxide, carboxyl and hydroxyl groups in variable ratios which can undergo electrostatic, covalent or hydrogen bonding with protein. CVD graphene, the two dimensional sheet of sp^2-conjugated atomic carbon basal plane, contains defects, nano topographical repetitious structure, numerous nano-sized grain boundary, and recurrent ripples which provide delocalized surface π electrons with protein and small molecular chemicals. Presence of delocalized surface π electrons and functional groups of graphene allows for high density protein adhesion via both covalent and non-covalent bonding. Such substances such as TGF-β, insulin, albumin, fibrinogen, interferons and etc, are adsorbed onto graphene surface via hydrophobic or π–π stacking interactions which affect cell proliferation and differentiation. Moreover, large theoretical specific surface area ($2630\ m^2g^{-1}$) of graphene allows for high density protein loading capacity. For instance, protein loading capacity was ~2-fold, ~9-fold, and ~10-fold higher than that of BSA of single-walled carbon nanotubes

(SWNTs), multiwalled carbon nanotubes (MWNTs), and graphene, respectively, which are well known carbon materials with high protein adsorption ability.

Furthermore, the attractive π-π stacking forces are created by the sp^2-conjugated atomic carbon basal plane allow some amino acids contain benzene rings to absorb on graphene via hydrophobic-hydrophobic interactions. For example, bone morphogenetic proteins (BMPs), a well are a group of multi-functional growth factors, was found that graphene tends to bind well with proteins. It appears that graphene tends to bind or interaction well with a range of proteins such as trypsin, heparin, lysozyme, and peptides. The π electron cloud carried on graphene is speculated to interact with hydrophobic part of protein, resulting in the initial stage of addition involving the physicochemical linkages between cells and graphene through strong covalent bonding or indirectly bonding through an alteration in the adsorption of conditioning molecules. Findings on the effect of benzene rings of graphene surface is affected not only by surface chemistry but also by topographical parameters such as roughness and texture. Graphene on osteogenic and adipogenic differentiation inferred to be caused by the adsorption of small molecule dexamethasone and beta-glycerolphosphate protein on graphene. Moreover, insulin, which is known to enhance adipogenic differentiation gets denatured on graphene surface which in turn results in inhibition of adipogenic differentiation. Hence as protein and low molecular weight chemical gets adsorbed and deformed by graphene. Graphene can impose a great influence on cells depending on their hydrophobicity.

The protein and small molecular chemicals adsorption capacity is affected not only by surface functionality but by nano topographical parameters such as roughness and texture. The protein and small molecular chemicals adsorption capacity would make the graphene to serve as a promising platform for stem cell engineering

Conductivity

Owing to their conductivity properties, Carbon nanotube and graphene have been intensively studied for electro-active tissue. In particular, graphene has emerged as a powerful platform for enhancing the differentiation of stem cells into neurons due to its excellent properties, including nanotopographic surface and electrical conductivity. On this account, the graphene based materials would be an ideal breakthrough for biomedical applications of nervous system model. Firstly, excellent electrical conductivity of graphene make them suitable for nervous system model. In the presence of an electrical stimulation, excellent electrical conductivity graphene can modulate cell adhesion, migration, propagation, differentiation, protein secretion and DNA synthesis of electrically active cells, such as muscle, bone, cardiac and nerve cells. For example, Park et al. reported that graphene as a substrate improved cell adhesion and differentiation of human neural stem cell into neurons.[2] This study demonstrated that graphene-coated glass can enhance the promotion of neuronal differentiation of neural stem cells, especially favoring neurons versus glia cells, compared to the use of a substrate not coated with graphene (pure glass). In another study, Li et al. indicated graphene substrates enhanced expression of growth-associate protein-43(GAP43), resulting in the boost of neurite sprouting and outgrowth to the maximal extent. There are mainly two causes for such phenomena. First, the surrounding matrix of neurons may have mimicked the topography of wrinkled and rippled chemical vapor deposition (CVD)-grown graphene substrate, which may assist neuron growth. Second, the high electrical conductivity of graphene could also account for better neurite outgrowth, as in previous study it has been shown that the electrical conductivity of carbon nanotube (CNT) does promote neuron growth. In another study, Heo et al. used graphene/ polyethylene terephthalate substrate for modulating neural cell-to-cell interactions.[6] The results show that graphene-coated glass can increase cell-to-cell interaction and further strengthened. Not only that the graphene/PET film substrata was improved cell adhesion and differentiation compared to the conventional polystyrene tissue culture substrata which indicated that the graphene substrata was biocompatible and suitable for neuronal biomedical applications. In addition, not only can the electronic properties of graphene can be tailored to match the charge transport required for electrical cellular interfacing, but also the chemically stable properties of graphene can facilitate integration with neural tissues. These unique properties offer great advantages for neuronal or other purposes.

Surface morphology

Surface wrinkling in 2D materials is a well-known and common phenomenon.[7] It has been evident from TEM images and Monte Carlo simulations that graphene is not perfectly flat but contoured with intrinsic ripples with deformations up to 1 nm normal to the plane. Specially, CVD graphene consists of high densities of wrinkles on the nanometer- scale. The main driving force for wrinkling in 2D materials is difference between the thermal expansion coefficient mismatch of graphene and copper generated during growth and cooling process. Surface wrinkling is an important factor to be considered to account for the stem cell adhesion, growth and differentiation.

The Cell and molecular biology have shown that cell interaction with adhesive substrates. Furthermore, it is clear that interaction exists between cells and nano- and micro-scale topological features. However, there are not good enough to prove that the mechanism of these effects.

Nayak et al. shows that graphene provides a promising biocompatible scaffold that does not hamper the proliferation of human mesenchymal stem cells (hMSCs) and accelerates their specific differentiation into bone cells.[8] Nayak et al. also found that Wrippled and wrinkled topography of CVD graphene mimics the disordered nanopit array.[9] Such large-scale disorder in CVD graphene could play a role in protein adsorption, cell adhesion, proliferation, and differentiation. Nayak et al. believe that the surface wrinkling and ripples provide local curvature and, hence, could further enhance the reactivity of such graphene sheets. Ripples in graphene suggest that the resultant local curvatures affect reactivity such as protein anchoring, cell adhesion, and cell align which can change many aspects of the cell function. The study by Tang a et al. studies show that increasing roughness of the cross-linked GO film facilitates the adhesion of stem cells, which in turns increases the rate of proliferation.[10] Furthermore, the rougher surface topology of cross-linked GO film provides more anchoring points for the stem cell adhesion, growth and differentiation of hMSCs. In another study, Kim et al. hypothesized that the unique characteristics of the asymmetrical nanotopology cue of graphene and its secondary effects such as stiffness and roughness within substrata might play a crucial role in the enhancement of hMSC differentiation.[11] This study demonstrated that that RGO–chitosan substrata with asymmetrical nanotopology provided a suitable environment for the adhesion and proliferation of hMSCs as well as enhanced cell–substrate interaction and cell–cell contacts.

1.4 2D graphene based stem cell engineering

Stem cells represent a promising tool for tissue engineering and regenerative medicine. However, they require appropriate environments to grow and regenerate. Recently, 2D graphene based platforms have attracted much attention as promising materials for cell modulation applications due to the physicochemical properties of graphene and its biocompatibility have inspired scientists to utilize this material for regulating the growth and differentiation of stem cells engineering. Although 2D graphene based stem cell engineering, it is in a relatively nascent stage. Graphene has been attracting great interest in the field of biomedical engineering. Many systematic studies have been carried out on various topics of interest that range from cell regulation to tissue regeneration. Many results that are rigorously proved and accepted for future 2D graphene based platforms and will no doubt greatly benefit tissue engineering and regenerative medicine. In this context, we introduce some of the interesting advances in 2D graphene-based stem cell engineering applications; how it affects cell behavior and differentiation. Some of the most interesting examples that have reported use of 2D graphene based platforms for cell engineering purposes.

For bone tissue engineering, there are a large number of studies which report the promise of biomimetic 2-D graphene platform which promote the adhesion, proliferation, and osteogenic differentiation of MSCs or osteoblasts. Graphene provides a new kind of solutions to integrate several elements (active and passive) on the 2D graphene scaffolds. The variety of favourable properties for bone tissue engineering that graphene provides include also efficient modulation of stem cell, due to the intrinsic properties. The physiochemical and mechanical property implies that graphene has unique properties for the differentiation of stem cell. This was well described by Lee et al.[3] This study represents an interesting example where MSC osteogenic differentiation can be achieved even in the absence of chemical inducer in the culture medium. The protein adsorption ability of graphene is of particular importance because the chemical interactions between the substrates and soluble factors is able to stimulate cell growth and differentiation.

For neural tissue engineering, there are several studies have been reported about the interactions of nervous systems with 2D graphene platform. Recent studies strongly appealed that the potential of graphene to stimulate neurite sprouting. For example, Solanki et al. found that the engineered microenvironment consisting of nanotopographical features modified with GO provides instructive physical cues that lead to enhanced and then. They also demonstrated that the engineered microenvironment consisting of nanotopographical features modified with GO provides instructive physical cues that lead to enhanced neuronal differentiation of hNSCs along with significant axonal alignment.[12] The same positive results have been observed by Li et al. that utilized graphene as a substrate for the promotion of neurite sprouting and the outgrowth of mouse hippocampal cells. Furthermore, graphene was recently applied as an electrode in the electrical stimulation of NSCs, because stimulation can control the physiological activities of stem cells, such as cell viability, division, differentiation and migration, applicable in spinal cord and tumor therapies.[13] In this regard, Park et al. reported that CVD graphene as a substrate improved cell adhesion and differentiation of human neural stem cell into neurons. This study demonstrated that graphene-coated glass can enhance the promotion of neuronal differentiation of neural stem cells rather than glia, which differentiate further in the absence of biochemical motifs or co-culturing.[2] In fact, the increased differentiation of hNSCs towards neurons than glia is essential in neural regeneration and brain repair.

For cardiac tissue engineering, as well reported above, it is reported that MSC differentiation could be modulated through cellular interactions with culture substrates *in vitro*. However, only a few studies have studied the effect of cell culture substrates on cardiomyogenic differentiation of MSCs. Recently, Park et al. demonstrated that graphene can be used as a stem cell culture substrate to promote the cardiomyogenic differentiation process of MSCs without the use of any exogenous chemical inducers.[5] Graphene exhibited no sign of cytotoxicity for stem cell culture, and provided a suitable environment for MSC proliferation. The MSC commitment towards cardiomyogenic lineage was stimulated by simply culturing the MSCs on graphene, even in the absence of exogenous inducers for cardiomyogenic differentiation. They suggest that graphene may promote the cardiomyogenic differentiation and diverse behaviors of MSCs through specific cell–ECM interactions and regulation of cell signaling pathway. Lee et al. demonstrated that graphene enhances the cardiomyogenic differentiation of human ESCs (hESCs).[4] The coating of the graphene with vitronectin (VN) was required to ensure high viability of the hESCs cultured on the graphene. hESCs were cultured on either VN-coated glass (glass group) or VN-coated graphene (graphene group) for 21 days. The spontaneous cardiomyogenic differentiation of hESCs was investigated by culturing hESCs on either glass (control) or graphene without the addition of exogenous chemicals for differentiation induction and by evaluating the expression of cardiac-specific genes. The differentiation of these cells was also compared with that of cells cultured on Matrigelcoated glass, which is a substrate used in the conventional, directed two-dimensional culture differentiation systems for the cardiomyogenic differentiation of hESCs without forming embryoid bodies. This culture system showed an efficient differentiation into cardiomyocyte phenotype. The mesodermal and endodermal differentiations were compared among the experimental groups because these differentiations are known to be intermediate stages of the cardiomyogenic differentiation of hESCs. The mechanisms underlying the enhanced cardiomyogenic differentiation were also investigated. Moreover, the analysis of the cardiomyogenic differentiation of hESCs cultured on graphene or Matrigel revealed that graphene was superior to Matrigel, which is a substrate used in conventional cardiomyogenic differentiation systems. The enhanced cardiomyogenic differentiation may be, at least in part, due to nanoroughness of graphene, which enhanced hESC adhesion and the upregulation of extracellular signal-regulated kinase signaling. We further highlight how 2D graphene based platforms are being exploited for cell modulation in tissue engineering, comprehensively surveying recent experimental works are summarized in Table 1.

Table 1. 2D graphene based cell modulation

2D graphene based platform	Cell type	Main results	References
CVD graphene on SiO_2	SAOS-2, MSCs	The graphene probably has a potential to induce MSC differentiation into the osteoblast lineage	Kalbacova et al, *Carbon*, 48, 4323 (2010)
Graphene/chitosan composite film	L929	The graphene/chitosan composites were biocompatible to L929 cells	Fan et al, *Biomacromolecules*, 11, 2345 (2010)
CVD graphene on glass	hNSCs	Graphene substrate enhanced the differentiation of hNSCs to neurons compared with glass substrates	Park et al, *Adv Mater*, 23, 263 (2011)
Graphene and GO	iPSCs	The different surface properties of G and GO governed the iPSCs behavior	Chen et al. *Biomaterials*, 33, 418 (2012)
Graphene and fluorinated graphene	hMSCs	Fluorinated graphene can be used to enhance cell adhesion and proliferation of MSCs	Wang et al, *Adv Mater*, 24, 4285 (2012)
CVD graphene on glass	hMSCs	MSC commitment towards cardiomyogenic lineage was stimulated by simply culturing the MSCs on graphene, even in the absence of chemical inducers	Park et al, *Adv. Healthcare Mater*. 3, 176 (2013)
Graphene-incorporated chitosan composite film	hMSCs	Graphene enhance cell–cell and cell–material interactions for promoting functions of hMSCs	Kim et al, *J. Mater. Chem*. B, 1, 933 (2013)
CVD graphene on glass	hESCs	Graphene enhanced the gene expression of cardiac-specific extracellular matrices	Lee et al, *Biochem Biophys Res Commun*, 12, 174 (2014)
CVD graphene on glass	hMSCs	Graphene is advantageous for the differentiation of hMSCs into neurons	Kim et al, *J. Biomed. Nanotech*, (2014)

1.5 3D graphene based stem cell engineering

Two-dimensional (2D) surface represent a simple model system for isolating the control factors for stem cell in fundamental research. Much of our understanding of the biological mechanisms that underlie cellular functions, such as migration, differentiation and force sensing has been garnered from studying cells cultured on two-dimensional (2D) glass or plastic surfaces. However, the natural niche for cell is not two-dimensional (2D) surface. Cells are not static and can “feel” the presence of cellular microenvironments in which cells relies on *in vivo* comprise soluble chemical factors, biomechanic factors, structural environment, neighbor cells, and ECM, and cell–biomaterial interactions which can eventually be converted into biological signals to regulate the function of cells. A 3D porous structure is an indispensable component of tissue engineering scaffolds for the provision of sufficient surface and space for cell adhesion, migration, growth and tissue formation. Therefore, this has spurred substantial efforts towards the development of in vitro 3D biomimetic environments and has encouraged much cross-disciplinary work among biologists, material scientists and tissue engineers. In this context, we introduce some of the interesting advances in 3D graphene-based stem cell engineering applications; how it affects cell behavior and differentiation. Recently, multi-dimensional carbon-nanomaterial (zero-dimensional, one-dimensional, two-dimensional, and three dimensional) has been shown to promote cell adhesion, proliferation, and differentiation *in vitro* and repair tissue *in vivo*. Among these materials, graphene could be combined with commonly used bio-scaffolds for stem cell engineering to modulate their biological functionality. 3D graphene based platforms have attracted much attention as promising new platform for cell modulation applications due to the physicochemical properties of graphene and its biocompatibility have inspired scientists to utilize this material for engineering a range of biomaterial and tissue-engineering applications. To date, several fabrication technologies, such as chemical vapor deposition method using template, a polymeric sponge impregnation process, foaming, sol–gel methods, extrusion forming, gel-casting, thermally induced phase separation, carbonization with thermal decomposition, and etc have been developed for the fabrication of 3D graphene based platforms. Some of the most interesting examples that have reported use of 3D graphene based platforms for cell engineering purposes are summarized in Table 2.

Table 2. 3D graphene based cell modulation

3D graphene based platform	Cell type	Main results	References
Graphene LbL Deposition on 3D Scaffolds.	E14 Primary Cortical Neurons.	Electroactive scaffold modification assist in neuronal regeneration,	Zhou et al, *ACS Appl. Mater. Interfaces*, 4, 4524 (2012)
rGO/ZnO/Anti-EpCAM Foam	MCF7 cell	It can successfully capture cancer cells from blood spiked with MCF-7 cells due to the enhanced local topographic interactions.	Yin et al, *Adv. Mater. Interfaces*, 1, 13 (2014)
Three-dimensional graphene foams (3D-GFs)	Human mesenchymal stem cells (hMSCs)	3D GFs support the attachment and viability of hMSCs, and induce spontaneous osteogenic differentiation.	W. Crowder et al, *Nanoscale*, 5, 4171 (2013)
Three-dimensional graphene foams (3D-GFs)	Neural stem cell (NSC)	3D-GFs keep cells at a more active proliferation state with upregulation of Ki67 expression than that of 2D graphene films.	Li et al, *Scientific Reports*, 3, 1604 (2013)
Porous and flexible 3D GOx-based scaffolds	Embryonic neural progenitor cells	Highly viable and interconnected neural networks were formed on these 3D scaffolds	Serrano et al, *J. Mater. Chem. B*, 2, 5698 (2014)

1.7 References

[1]. Kostarelos, Kostas, and Kostya S. Novoselov. Exploring the Interface of Graphene and Biology. *Science*. **2014**, 344. 261-263.

[2]. Park, S. Y., Park, J., Sim, S. H., Sung, M. G., Kim, K. S., Hong, B. H., & Hong, S. Enhanced differentiation of human neural stem cells into neurons on graphene. *Adv Mater.* **2011**, 23(36), H263-H267.

[3]. Lee, W. C., Lim, C. H. Y., Shi, H., Tang, L. A., Wang, Y., Lim, C. T., & Loh, K. P. Origin of enhanced stem cell growth and differentiation on graphene and graphene oxide. *ACS nano*, **2011**, 5(9), 7334-7341.

[4]. Lee, T. J., Park, S., Bhang, S. H., Yoon, J. K., Jo, I., Jeong, G. J., & Kim, B. S. Graphene enhances the cardiomyogenic differentiation of human embryonic stem cells. *Biochem. Biophys. Res. Commun.* **2014**, 452.1, 174-180.

[5]. Park, J., Park, S., Ryu, S., Bhang, S. H., Kim, J., Yoon, J. K & Kim, B. S. Graphene–Regulated Cardiomyogenic Differentiation Process of Mesenchymal Stem Cells by Enhancing the Expression of Extracellular Matrix Proteins and Cell Signaling Molecules. *Adv Healthcare Mater*. **2014**, 3(2), 176-181.

[6]. Heo, Chaejeong, et al. The control of neural cell-to-cell interactions through non-contact electrical field stimulation using graphene electrodes. *Biomaterials*, **2011**, 32.1, 19-27.

[7]. Sutter, Peter, Jerzy T. Sadowski, and Eli Sutter. Graphene on Pt (111): Growth and substrate interaction. *Phys Rev B,* **2009**, 80.24, 245411.

[8]. Nayak, Tapas R., et al. Graphene for controlled and accelerated osteogenic differentiation of human mesenchymal stem cells. *ACS nano*, **2011**, 5.6, 4670-4678.

[9]. Dalby, Matthew J., et al. The control of human mesenchymal cell differentiation using nanoscale symmetry and disorder. *Nat Mater*, **2007**, 6.12, 997-1003.

[10]. Tang, Lena AL, et al. Highly Wrinkled Cross-Linked Graphene Oxide Membranes for Biological and Charge-Storage Applications. *Small*, **2012**, 8.3, 423-431.

[11]. Kim, Jangho, et al. "Graphene-incorporated chitosan substrata for adhesion and differentiation of human mesenchymal stem cells." *J Mater Chem B*, **2013**, 1, 933-938.

[12]. Solanki, Aniruddh, et al. Axonal Alignment and Enhanced Neuronal Differentiation of Neural Stem Cells on Graphene-Nanoparticle Hybrid Structures. *Adv Mater.* **2013**, 25, 5477-5482

[13]. Li, Ning, et al. The promotion of neurite sprouting and outgrowth of mouse hippocampal cells in culture by graphene substrates. *Biomaterials*. **2011**, 32.35, 9374-9382

Part I

2D Graphene based stem cell engineering

Chapter 2

Graphene-directed spheroid formation of mesenchymal stem cells for enhanced neuronal differentiation

Introduction

Neuronal disorders or neurodegenerative diseases are still one of the leading causes of human death and disability in the world. For example, stroke causes approximately 150,000 American die every year, and Parkinson's disease affects over 1 million people in the European Union.[1-4] Nevertheless, the current clinical treatments for neuronal disorders or neurodegenerative disease are quite limited, and the number of people affected by these diseases consistently increases every year.[1] As a direct result, there is a great need to discover alternative therapies for these disorders or diseases. Autologous stem cell based therapy and tissue engineering are currently considered as promising strategies that could allow the functional replacement of missing or damaged neurons by transplanting undifferentiated or/and differentiated stem cells alone or in combination with appropriate scaffolds for the treatment of neuronal disorders or diseases.[1-5] In this regard, it is crucial to develop a highly efficient platform for the growth and neuronal differentiation of stem cells.

Carbon-based nanomaterials have exhibited great potential for regulating the growth and differentiation of stem cells due to their biocompatibility and their unique physicochemical properties, which are comparable to a natural extracellular matrix (ECM) and can promote essential cellular processes for enhancing the growth and function of stem cells.[6-14] Guided by these considerations, here, we propose the use of highly uniform graphene as an efficient platform for stem cell based therapy for the treatment of neuronal disorders or diseases. It is hypothesized that the use of high quality graphene would provide a unique environment for the growth and neuronal differentiation of stem cells (Fig. 1A). To address this challenge, we fabricated highly uniform monolayers of graphene and investigated how this platform could influence the adhesion, proliferation, and differentiation of human mesenchymal stem cells (hMSCs) into functional neurons, which may have considerable potential for use in autologous stem cell-based therapy to treat neuronal disorders or diseases.

Experimental

Fabrication and characteristics of highly uniform graphene

Highly uniform graphene was synthesized by the CVD process (Supplementary Fig. S1).[14,15] The graphene film grown on the copper foil was covered by poly(methyl methacrylate) (PMMA) and floated on the surface of an aqueous solution of 0.1 M ammonium persulphate [$(NH_2)_4S_2O_8$]. After all of the copper layers were etched away, the floating PMMA/graphene film was collected using a clean PET film and transferred to deionized water. The cleaning process was repeated five times. The graphene film with the PMMA support was transferred to coverslips. The samples were dried with nitrogen gas immediately after the transfer and baked for 8 h on a hot plate at 60℃. The samples were then cleaned using acetone at room temperature for 30 min to remove the PMMA support layer. The samples were then dried and baked for 8 h on a hot plate at 60℃.

The graphene fabricated in this study were characterized by atomic force microscopy (AFM), Raman spectroscopy, ultraviolet–visible spectrometer, TEM, and SAED. The surface morphology examination of the samples was conducted through non-contact mode AFM (XE-100 system, Park Systems, Korea). The structural properties of the graphene on the coverslip were further investigated through Raman spectroscopy (RM 1000-Invia, Renishaw, UK). The Raman spectra were recorded by using an argon ion laser (514 nm) as the excitation source with a notch filter of 50 cm^{-1}. The typical scan range was from 1000 to 3000 cm^{-1} and the instrumental resolution was 10 cm^{-1}. The optical transmittance of the graphene on the coverslip was measured using an ultraviolet–visible spectrometer (UV-3600, Shimadzu, Japan). The TEM and SAED analyses were conducted on a transmission electron microscopy (TEM) (JEOL 2100, JEOL, Japan) operated at 200 kV. The rotation between the TEM images and the corresponding SAED patterns was calibrated using molybdenum trioxide crystals. The sheet resistances of the graphene on the glass were measured through the van der Pauw four-probe method using a Hall measurement system.

hMSC culture on highly uniform graphene

Adipose tissues were isolated from the patients undergoing ear surgeries under sufficient informed consent at the Ajou University School of Medicine (Suwon, Korea).[12,21,28] The experimental protocol was approved by the Institutional Review Board at the same university. Tissues were washed with PBS and digested with 100 Unit/mL collagenase type I (Sigma-Aldrich, St. Louis, MO, USA) with low glucose Dulbecco's modified Eagle's medium (DMEM; Gibco-BRL, Grand Island, NY, USA) and incubated for 8 h to lyse the adipose tissues. The stromal fraction was collected by centrifugation and then passed through a cell strainer (100 μm size) to remove any large cell clumps and particles. For cell culture and expansion of adipose-derived hMSCs, cells were grown in low glucose DMEM with 10% fetal bovine serum (FBS) and 1% penicillin-streptomycin (Gibco, Milan, Italy) at 37℃ in a 5% CO2 atmosphere. All cells used in this study were at passage 3 or 4.

For the adhesion and proliferation of hMSCs, cells (4×10^4 cells/sample) were seeded onto samples and cultured in DMEM (Sigma-Aldrich, Milwaukee, WI, USA) with 10% FBS (Sigma-Aldrich, Milwaukee, WI, USA) and 1% antibiotics (Sigma-Aldrich, Milwaukee, WI, USA) at 37℃ in a humidified atmosphere containing 5% CO_2. The quantitative analysis of the cell proliferation on the nanogrooved matrices was performed using WST-1 assay (EZ-Cytox Cell Viability Assay Kit, Daeillab Service Co., LTD). For the neuronal differentiation of hMSCs, early-passage hMSCs and commercially available neuronal differentiation media (Promocell, Heidelerg, Germany) were used.

Immunofluorescence staining

Adhered cells on samples were fixed with a 4% paraformaldehyde solution (Sigma-Aldrich, Milwaukee, WI, USA) for 20 min, permeabilized with 0.2% Triton X-100 (Sigma-Aldrich, WI, Milwaukee, USA) for 15 min, and stained with TRITC-conjugated phalloidin (Millipore, Billerica, MA, USA) and 4, 6-diamidino-2-phenylindole (DAPI; Millipore, Billerica, MA, USA) for 1 h. FAs were also stained with a monoclonal anti-vinculin antibody (1:100; Millipore, Billerica, MA, USA) and a FITC-conjugated goat anti-mouse secondary antibody (1:500; Millipore, Billerica, MA, USA). To check neurogenesis of hMSCs, analysis of the immunostaining of TUJ1 (Cell Signaling Technology, Beverly, MA, USA), NeuN (Millipore, Billerica, MA, USA), and GFAP (Millipore, Billerica, MA, USA) were used. Images of the stained cells were taken using a fluorescence microscope (Zeiss, Germany). Mouse anti-STRO-1 (R&D systems, USA) and secondary anti-rabbit IgG (FITC) (Jackson ImmunoResearch Laboratories) were used for the investigation of hMSCs phenotype. For the quantitative analysis of the images, the custom written

MATLAB script was used.

Western blot

Cells were lysed in RIPA buffer, supplemented with Xpert Protease Inhibitor Cocktail Solution (100X) GenDepot, Barker, TX, USA). An equal amount of protein was loaded in each lane of a sodium dodecyl sulfate polyacrylamide gel electrophoresis (SDS-PAGE). Proteins were separated by electrophoresis and transferred to a (Polyvinylidene difluoride) PVDF membrane. Following transfer, membranes were blocked for 1 h with 5% skim milk in PBS + 0.05% Tween 20. Primary antibodies against Connexin 43 (Cell Signaling Technology, Danvers, MA, USA), STRO-1 (R&D systems, USA) and β-actin (Cell Signaling Technology, Danvers, MA, USA) were used. The immunoblots were washed and incubated with secondary antibodies conjugated with horseradish peroxidase (Santa Cruz Biotechnology, CA). Immunoblot bands were visualized by enhanced chemiluminescence (ECL; GenDEPOT, TX, USA).

Nissle staining

The Nissle staining was performed to evaluate the differentiated cells from hMSCs in the neuronal differentiation. The cells were fixed with a 4% paraformaldehyde solution (Sigma-Aldrich, Milwaukee, WI, USA) for 20 min after PBS washing three times. The cells were washed by PBS three times and then stained by 1% Cresyl violet solution.

Quantitative real-time polymerase chain reaction (qRT-PCR)

To evaluate Nestin, TUJ1, and MAP2 mRNA expression levels, quantitative real time PCR (qRT-PCR) was performed. Total RNA was extracted from cells according to the manufacturer's instructions using an Easy-BLUE RNA extraction kit (iNtRON Biotech, Sungnam, Korea). First-strand cDNA synthesis was carried out in a 20 μl reverse transcription (RT) reaction with oligo dT, dNTPs and reverse transcriptase (GenDEPOT, Barker, TX, USA). Fuorescence based real-time PCR was carried out using SYBR Green Premix Ex Taq (TaKaRa, Dalian, China) and an applied Biosystems 7500 Real-Time PCR system (Applied Biosystems; Foster City, CA, USA). The following primers were used for qRT-PCR: human Nestin (Fw) 5'- GAA ACA GCC ATA GAG GGC AAA-3'; (Rv) 5'- TGG TTT TCC AGA GTC TTC AGT GA-3', beta III tubulin (Fw) 5'- CGA AGC CAG CAG TGT CTA AA-3'; (Rv) 5'- GGA GGA CGA GGC CAT AAA TA -3', beta III tubulin (Fw) 5'- CCA ATG GAT TCC CAT ACA GG -3'; (Rv) 5'- TCC TTG CAG ACA CCT CCT CT--3', GAPDH (Fw) 5'- GCA AAT TCC ATG GCA CCG TC -3'; (Rv) 5'- TCG CCC CAC TTG ATT TTG G--3'. For quantification, GAPDH was used as the reference for normalization of each sample.

Calcium imaging

For high K^+ stimulation experiment, culture media were exchanged to Normal Tyrode's (NT) solution (pH 7.3, 148 mmol NaCl, 5 mmol KCl, 2 mmol $CaCl_2$, 2 mmol $MgCl_2$, 10 mmol HEPES, 10 mmol Glucose). After washing the cells by NT solution, the cells were loaded with Fluo-4 AM dye (2 μmol, Invitrogen, CA, USA) for 30 min at 37℃ followed by washing for 30 min at room temperature. The fluorescence was monitored using Nikon TE-2000U (Nikon, Japan) equipped with CV-S3200 CCD camera (JAI, Japan). All fluorescent images were analyzed by NIS-Elements software version 2.4 (Nikon, Japan) and ImageJ.

Statistical analysis

Student’s t-test or one-way ANOVA followed by Duncan's multiple range test was used for statistical analysis. All quantitative results were presented as mean ± standard deviation (SD).

Results and Discussion

We synthesized highly uniform graphene by using the chemical vapor deposition (CVD) method.[14,15] The detailed procedure to prepare a high quality graphene-coated glass substrate is described in Supplementary Fig. S1. As shown in Fig. 1 and Supplementary Figs. S2-S5, we qualified the presence of the high-quality monolayer graphene used in this study. In particular, a selected-area electron diffraction (SAED) pattern (Figs. 1D and E) and high-resolution scanning transmission electron microscopy (STEM) images (Figs. 1F and G) clearly demonstrated that high-quality graphene was successfully synthesized. We also determined that the sheet resistance and surface roughness (root-mean-square deviation, Rq) of graphene-coated glass were 552 ± 22 Ω/□ (Supplementary Fig. S4) and 2.90 nm (Supplementary Fig. S5) with a high uniformity, respectively. Note that the surface roughness of graphene-uncoated glass was 5.03 nm (Supplementary Fig. S5). We first explored the effects of stem cell growth on highly uniform graphene (Fig. 2). To investigate the adhesion of stem cells, we cultured hMSCs on the graphene-coated substrates and the uncoated substrates using normal growth medium. After culturing the cells onto the substrates for 14 h, we carefully removed the unattached cells from the substrates by washing with phosphate buffered saline. As shown in Fig. 2A, the typically spread shapes and focal adhesions (FAs) of hMSCs were observed on the glass substrate in the immunofluorescence staining analysis. In contrast, we found that the hMSCs on graphene exhibited distinctly different properties of adhesion compared to those on the glass substrate. Interestingly, three dimensional (3D) spheroids of hMSCs were

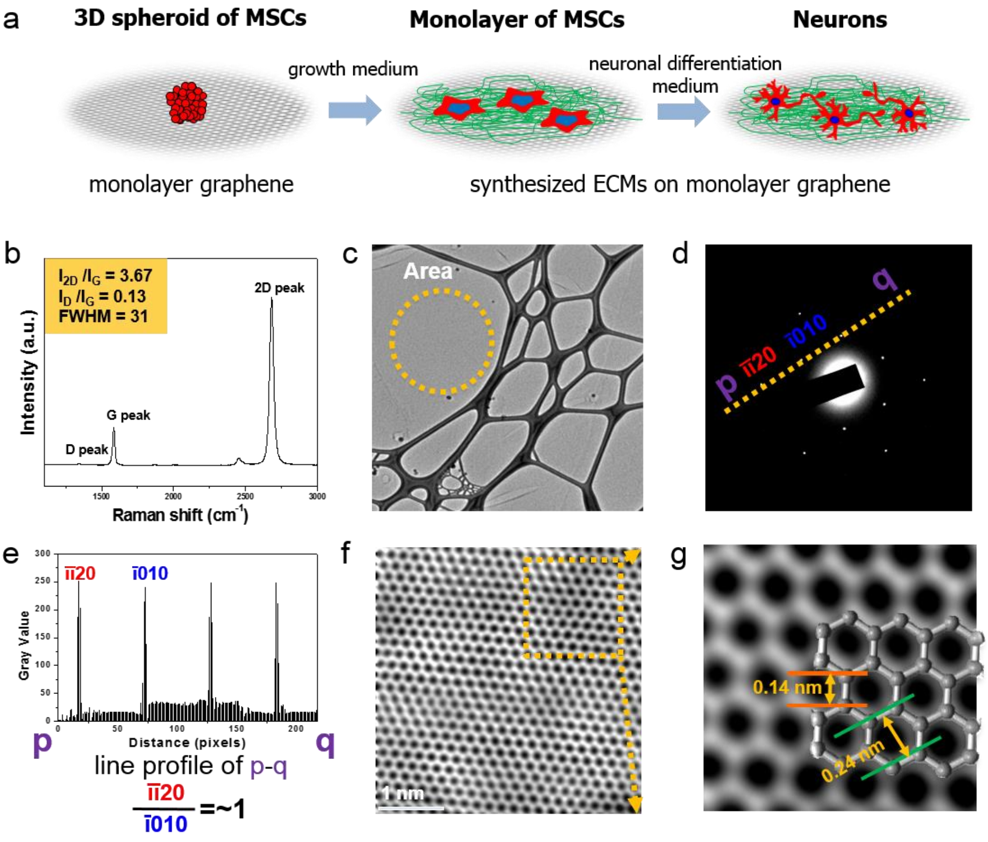

Figure 1 | Fabrication and characterization of highly uniform graphene for the growth and neuronal differentiation of stem cells. a, Schematic of the spheroid formation and neuronal differentiation of hMSCs using high-quality graphene. b, Raman spectroscopy of the transferred graphene. c, TEM image of a graphene sheet on a TEM grid. d, The SAED pattern. e, Intensity profile of the diffraction spots along a line connecting points p and q in the single-layer graphene diffraction pattern. The uniform intensity profile between the inner and outer spots proves that the graphene sheet consists of a single layer. f, High-resolution STEM image of at (F) low-magnification. g, High-resolution STEM image of at high-magnification.

formed on the graphene (Fig. 1A and Supplementary Fig. S6A). The size of cell spheroids for hMSCs ranged from 50 µm to 150 µm.

To our knowledge, this is the first report demonstrating that graphene can induce spheroid formation of aggregated cells in the absence of any external factors.[16-21] A possible explanation for the spheroid formation is the surface properties of the highly uniform graphene, which might not provide sufficient cell adhesion motifs for the cells at the initial stage of the cell culture. Namely, the limited cell adhesion motifs on the surface of high-quality graphene might restrict the full adhesion of cells to the substrates, which could eventually promote high cell-cell adhesion instead of cell-substrate adhesion. It is widely accepted that the initially stable cell-cell interactions, such as those in 3D tissues or organs, play an important role in regulating cellular behavior.[22] In particular, the phenomenon of spheroid formation of stem cells is highly related to the direct functions of the stem cells, such as stemness and differentiation,[13,24] suggesting that that the use of high quality graphene alone to generate 3D spheroid of stem cells would an interesting method for use in stem cell biology or engineering.

We observed the spheroids formed of aggregated hMSCs on the graphene up to ~ 7 days during the cell culture period, after which the spheroids usually disappeared (Supplementary Fig. S6B). The produced extracellular matrix (ECM) from the aggregated cells and the adsorbed adhesive-related molecules from the growth medium on the graphene during the process time of the cell culture could promote the full adhesion of the cells onto the substrates (Fig. 2A, Supplementary Figs. S4 and S5). The single cells that migrated from the spheroids on the graphene exhibited

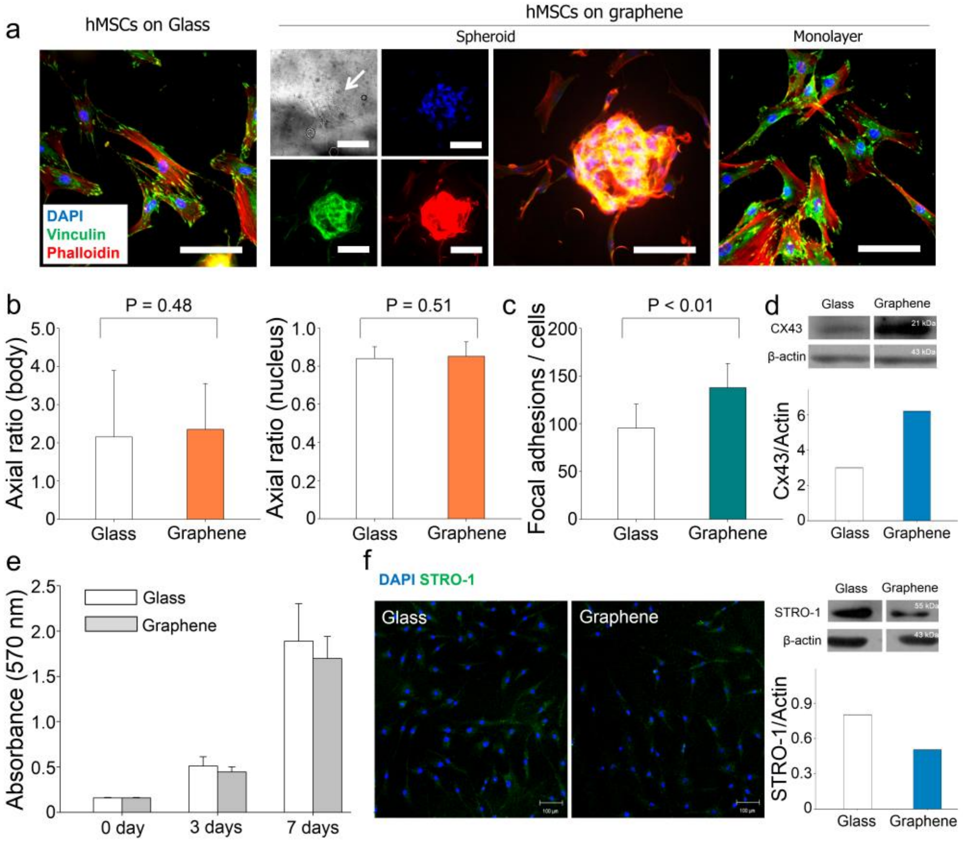

Figure 2 | Growth of hMSCs on highly uniform graphene. a, Representative immunofluorescent images of hMSCs cultured on a graphene-uncoated glass substrate and high-quality graphene. b, Quantification of the cell body and the nucleus, indexed by the axial ratio of the cell body and the width and length of the nucleus. c, Quantification of the amount of focal adhesion. One-hundred cells were used in the quantification process. d, Western blot analysis and quantification of the levels of Cx43 expression in the hMSCs cultured. e, Proliferation of cells on the substrates for 7 days. Three independent experiments were conducted. f, Representative immunofluorescent images of STRO-1 and a western blot analysis of the hMSCs cultured on the substrates for 10 days. The error bars represent the standard deviation.

the typical hMSC morphology (Fig. 1A).

To determine whether the high quality graphene is capable of altering the interactions at the cell-substrate and the cell-cell interfaces, we cultured hMSCs on the substrates for 7 days before the complete confluence of hMSCs. We analyzed the body and nucleus elongation of cells at the single cell level because it is known that the architecture and organization of the body and the nucleus may influence the cell function.[25-28]

To determine whether the high quality graphene is capable of altering the interactions at the cell-substrate and the cell-cell interfaces, we cultured hMSCs on the substrates for 7 days before the complete confluence of hMSCs. We analyzed the body and nucleus elongation of cells at the single cell level because it is known that the architecture and organization of the body and the nucleus may influence the cell function.[25-28]
Our results indicated that there was no significant difference between using the graphene-coated and the glass (graphene uncoated) substrates, suggesting that the presence of a uniform monolayer of graphene does not strongly influence the structural changes of hMSC (Fig. 2B). However, we found that the use of graphene enhanced the formation of FAs, as determined by vinculin immunostaining, compared to the use of glass substrates (Fig. 2C). In addition, a western blot analysis clearly indicated the greatly enhanced expression of the connexin 43 (Cx43), a major cell junction protein, in cultured hMSCs on the graphene compared to that on the glass substrates (Fig. 2C). Taken together, these findings indicate that the high quality graphene provides specific environmental cues to hMSCs, resulting in the enhanced cell-substrate and cell-cell interactions.

The proliferation of hMSCs cells on the high quality graphene was continually monitored during the experiment. We cultured hMSCs on the graphene-coated and the uncoated substrates using a normal growth medium for 7 days. Our quantified data at 1, 3, and 7 days indicate that the proliferation of cells on the graphene was slightly lower than on the glass substrates although the graphene exhibited time-dependent proliferation of the hMSCs (Fig. 2E). We hypothesized that a uniform monolayer of graphene alone might induce the differentiation of hMSCs into other lineages. Note that the initial formation of spheroids from aggregated MSCs, even in a short time, could affect their differentiation.[22] To verify this hypothesis, we cultured for 10 days hMSCs on the graphene-coated and the uncoated substrates using a normal growth medium that did not induce the differentiation of hMSCs. To identify the phenotypes of the stem cells, the expression of STRO-1 protein from cells cultured on the substrates was determined. Interestingly, our immunostaining analysis and western blot analysis clearly indicated the down-regulation of STRO-1 protein expression on the graphene compared to that on the glass substrate, suggesting that the high-quality graphene might promotes the differentiation of hMSCs.

In this study, we aimed to promote the neuronal differentiation of hMSCs as a step towards the neurogenesis of stem cells by using a highly uniform monolayer graphene with unique nanosurface properties and electrical conductivity (Fig. 1 and Supplementary Figs. S2-S5) as well as enhanced cellular interactions on the graphene (i.e., the initial 3D spheroid formation, the enhanced formation of FAs, and the gap junction expression of hMSCs) (Fig. 2). After culturing the hMSCs on the

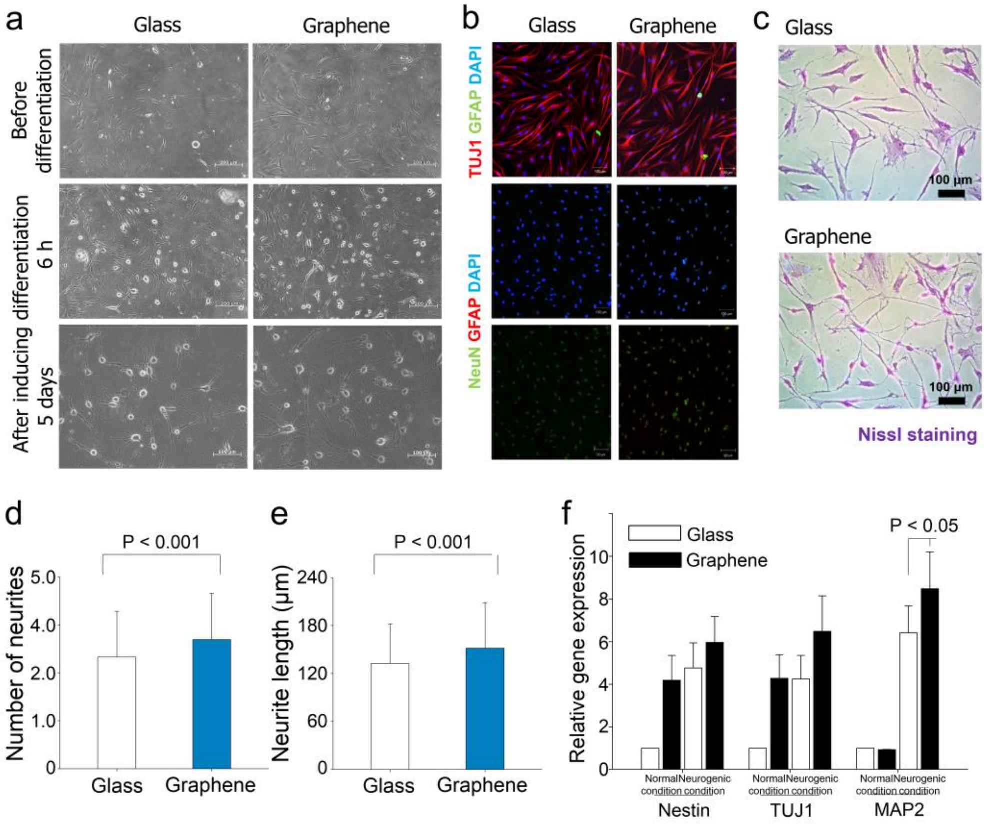

Figure 3 | Neuronal differentiation of hMSCs on highly uniform graphene a, Representative phase-contrast images of the hMSCs cultured on the substrates in the growth medium or the neuronal differentiation medium. b, Representative immunostaining images of TUJ1, NeuN, GFAP, and DAPI of the hMSCs cultured in the neuronal differentiation medium for 5 days. c, Representative Nissl staining images of hMSCs cultured in the neuronal differentiation medium for 5 days. d, Quantification of the number of neurities and the neuritie lengths. One-hundred cells were used in the quantification process. f, qRT–PCR analysis of hMSCs cultured in the neuronal differentiation medium for 5 days.

substrates for 3 days in the normal growth media, we then replaced the media withthe neurogenic media to induce neuronal differentiation of the hMSCs. After inducing neuronal differentiation of the hMSCs on the substrates for 6 h, we observed that the hMSCs exhibited higher activation for neuronal differentiation on graphene.

Three independent experiments were conducted, and the error bars represent the standard deviation.the graphene compared to the differentiation exhibited on the glass substrate (Fig. 3A). After 5 days of neuronal differentiation, the cells on both of the substrates exhibited neuron-like cell morphology and neurite outgrowths. Compared to the cells differentiated on the glass substrates, the cells on the graphene exhibited a more elongated neuritis, which lead to network formations (Fig. 3A).

To confirm the differentiated cells, we first analyzed the immunostaining of TUJ1 (early neuron marker), Neun (later neuron marker), and GFAP (glia cell marker). We observed that the cells expressed TUJ1 and Neun, whereas they did not express GFAP on both of the substrate types, indicating that we successfully induced the differentiation of hMSCs into only neurons and not into glia cells (Fig. 3B). Interestingly, the higher expression of TUJ1 and Neun as well as the enhanced neurite outgrowths were observed on the monolayer graphene than on the glass substrate. We also verified the presence of the differentiated cells using Nissl staining, which indicated that most of the cells were stained on the graphene, whereas the cells were only slightly stained on the glass substrata; which again confirmed that the graphene could enhance the neurite outgrowths (Figs. 3D and E).

To quantify the degree of enhanced neuronal differentiation of hMSCs by high-quality graphene in further detail, we performed the quantitative real-time reverse transcription-polymerase chain reaction (qRT-PCR) analysis. We cultured hMSCs on the graphene-coated substrates and the uncoated substrates with normal or neurogenic medium for 5 days after cell seeding. Strikingly, the expressions of neurogenesis-related genes (i.e., Nestin (early marker), TUJ1 (early marker), and MAP2 (later marker)) were promoted on the high-quality graphene relative to the expressions on the glass substrate (Fig. 3D). An interesting finding was derived from this experiment: the expressions of the early neurogenic transcriptional factors (Nestin and TUJ1) were upregulated in the hMSCs cultured on graphene, even in the normal growth medium, compared to those on the uncoated substrates. Surprisingly, the upregulation degree of the early neurogenesis-related genes in the hMSCs cultured on graphene with the normal growth medium was similar to that in the hMSCs cultured on the glass substrate with the neurogenic medium. Taken together, our findings demonstrated that highly uniform graphene could promote the neurogenesis of hMSCs as well as the neurite outgrowths, which can be used as a platform for autologous stem cell-based therapy to treat neuronal disorders or diseases.

We evaluated the response of differentiated neurons from hMSCs on the highly uniform graphene by external cues. It is known that the $Ca2^+$ uptake plays a major role in controlling the excitability for regulating a range of processes in neurons.[29] To investigate whether the differentiated neurons respond to external signals, high K^+ stimulation was applied to the cells using Fluo-4 AM dye to analyze the intracellular $Ca2^+$ uptake after hMSC differentiation for 5 days.[29] As shown in Fig. 4, the fluorescence level of the cells on graphene was greatly increased during the

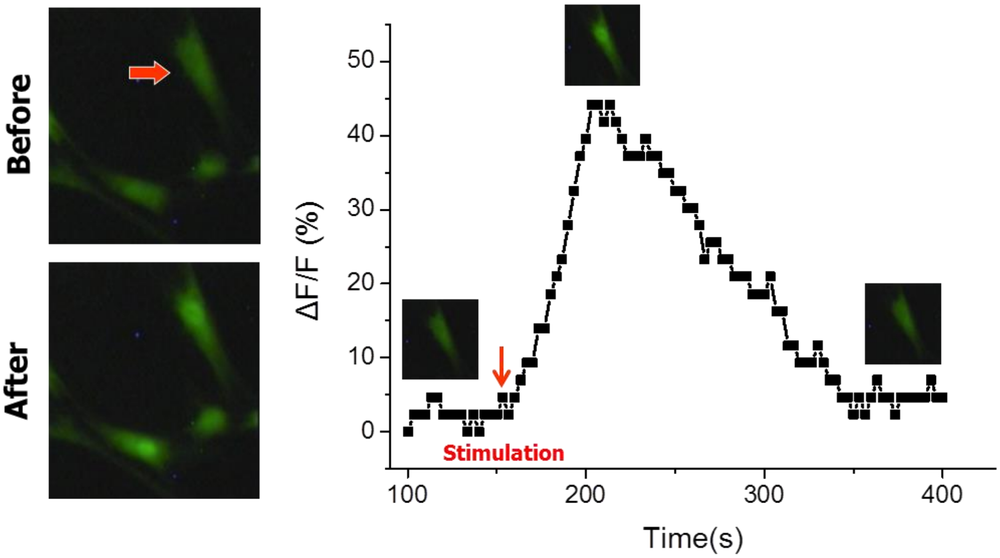

Figure 4 | Response of neuronal differentiated cells from hMSCs grown on highly uniform graphene to high K$^+$ stimulation on high-quality graphene. The cells were pre-incubated with Fluo-4 AM dye and imaged before and after the stimulations. Representative fluorescence images on the fluorescence intensity change on the cells were obtained before and after high K$^+$ stimulations. Representative plot of the relative fluorescence intensity change ΔF/F of the cell indicated by the red arrow.

stimulation. Approximately 40-100% fluorescence intensity, defined by the fluorescence intensity ΔF/F, was increased by K^+ treatment, indicating that the activated voltage-operated calcium channels of cells allowed the extracellular $Ca2^+$ influx. Our data demonstrated that the differentiated neurons from hMSCs on the graphene could be sensitive to external stimulation, thereby exhibiting potential as activated functional neurons in the neural networks.

One possible autologous stem cell based therapy for the treatment of neuronal diseases is to transplant differentiated functional neurons from stem cells in the in vitro culture into the target locations for the replacement of missing or damaged neurons. Here, we explore a possible therapeutic application for autologous stem cell based therapy by using the differentiated neurons of hMSCs on graphene. To this end, we prepared an *in vitro* protocol to indicate the potential of the differentiated neurons from hMSCs on highly uniform graphene for use as a source of cells for stem cell therapy to treat neuronal diseases (Fig. 5A): (i) culturing hMSCs on graphene in a growth medium → (ii) inducing neuronal differentiation of hMSCs using differentiation medium → (iii) detaching the differentiated hMSCs (neurons) on the graphene and re-seeding them onto a glass substrate → (iv) growing the differentiated cell culture on the glass substrate in the growth medium. We hypothesized that the differentiated cells detached from the graphene could maintain the functional neuronal property, in contrast to those from the graphene-uncoated glass substrate; this experiment simulated the transplanting of neurons into the body as a cell therapy to treat neuronal diseases.

We cultured the cells under study (i.e., the detached differentiated hMSCs from highly uniform graphene or the glass substrate with the trypsin treatment) on glass substrates. After the cells grew for 2 days in the growth media, we evaluated whether the cells could maintain their differentiated properties. Interestingly, using the Nissl staining, we found that the differentiated cells detached from the graphene were still expressed and had more elongated neuritis and network formations compared to the differentiated cells from the glass (Figs. 5 B and C). Our case study suggests that the differentiated neurons from hMSCs on the graphene could maintain their functional property even after re-seeding the cells detached from the graphene into the normal cell culture substrate in the growth medium, which can be an efficient source for autologous stem cell based therapy to treat neuronal disorders or diseases, although a more in-depth study, including molecular signaling and an *in vivo* study, must be performed to further verify the clinical applicability.

Nanoengineering systems have attracted considerable attention from scientific communities for stem cell engineering platforms, which can create biomimetic cellular environments to control or improve the function of stem cells.[30-34] Recently, the use of carbon-based nanomaterials, such as carbon nanotubes and graphene, has been proposed as a pioneering approach in the progress of designing nanoengineered stem cell culture platforms or scaffolds. [6-13,20,21] Two distinct strategies in using carbon-based nanomaterials have been typically used for stem cell engineering, with specific emphasis on differentiating the cells into various tissue lineages, including neuronal differentiation[12]: (i) stem cell culture with nanomaterials as the suspended conditions and (ii) stem cell culture on nanomaterials-coated or -incorporated substrates. Among them, the second approach has been widely proposed to

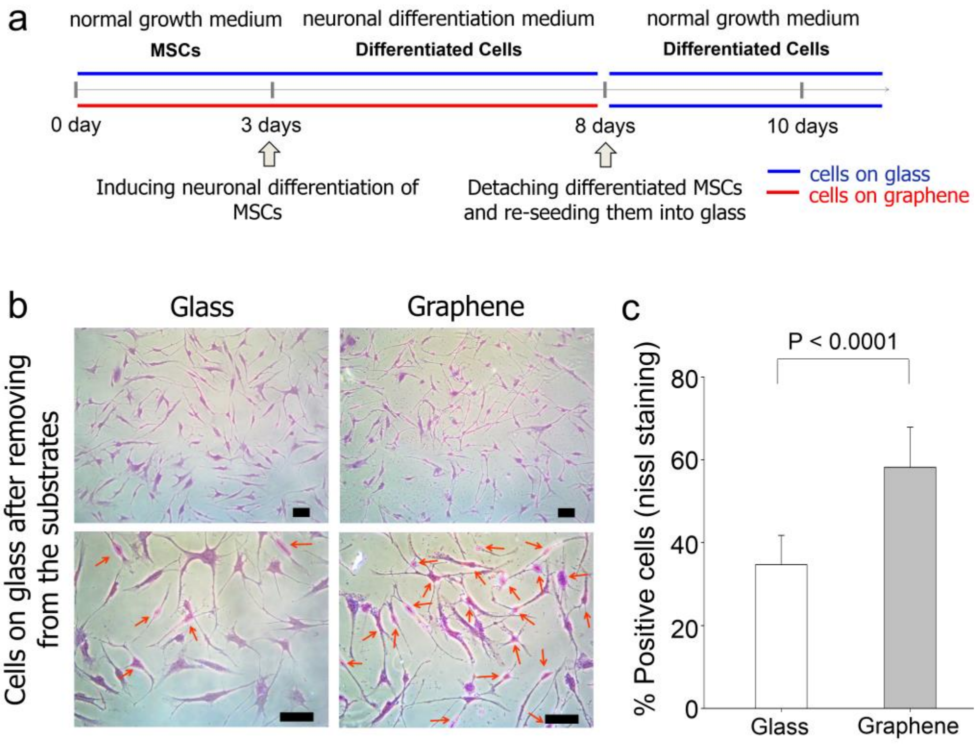

Figure 5 | A case study for autologous stem cell based therapy. a, An *in vitro* protocol to highlight the potential of the differentiated neurons from hMSCs grown on graphene as a source for cell therapy to treat neuronal diseases. It was hypothesized that the differentiated neurons from hMSCs grown on graphene could be transferred into the body to treat neuronal diseases. b, Representative Nissl staining images of the cells cultured on the glass substrates in the growth media for 2 days (total 10 day culture) after re-seeding the detached differentiated hMSCs onto graphene or a glass substrate using the trypsin treatment. c, Quantification of the number of cells stained by Nissl staining. Two-hundred cells were used in the quantification process regulate the growth and differentiation of stem cells because nanomaterials-coated substrates could provide ECM-like topographical cues as well as chemical cues. In conjunction with the context, our current study proposes that the highly uniform graphene may provide a unique cellular environment in promoting the growth and neuronal differentiation of stem cells, which can be used as efficient stem cell culture platforms or scaffolds.

Based on our experimental observations in this study, we found two notable findings: the highly uniform graphene (Fig. 1) can (1) create the unique cellular environments for 3D spheroid formation from aggregated hMSCs (Fig. 2) and (2) promote the neurogenesis of hMSCs, even in absence of any external neurogenic factors (Figs. 3-5).

(1) hMSCs have emerged as a primary candidate for cell therapy and tissue engineering, especially in clinical trials for a wide range of diseases.[4,35] Recently, it has been reported that self-assembly of hMSCs into tightly packed clusters to form 3D cellular aggregates can create an "*in vivo*-like" microenvironment that can enhance the regenerative capacity of hMSCs by promoting the secretion of cytokines and chemotaxic factors, even during short-term post expansion[35-37]; along these lines, we demonstrated that the short 3D spheroid formation of hMSCs (~ 7 days) could enhance the neuronal differentiation of hMSCs (Figs. 2 and 3). Thus, we believe that our finding that the highly uniform graphene alone can result in 3D spheroid formation of stem cells would be a valuable and easy protocol for various stem-cell applications, including cell therapy and tissue engineering. For example, our protocol can be used for the assembly of neural stem cells into 3D neurospheres,

which has been found to cause progenitor cells to revert to an early phenotype, thereby promoting the growth and differentiation of neural stem cells.[35]

(2) Neural differentiation of adult stem cells has been a promising strategy for the treatment of neuronal disorders or neurodegenerative diseases1. In particular, hMSCs hold great potential in clinical trials for autologous cell therapy because they can be easily obtained from patients and can potentially provide neuronal protection and repair.[4,35] Interestingly, we found that the high-quality graphene alone enhances the neural differentiation process of hMSCs without the use of any neurogenic chemical factors (Fig. 3). Leong's group reported that anisotropically nanopatterned substrates could induce the differentiation of hMSCs into the neuronal lineage without use of the neuronal induction medium.[38] They speculated that the significantly aligned and elongated cytoskeleton as well as the nuclei of the hMSCs by the nanotopographical cues might upregulate the neuronal markers.[38] In contrast, we found that the body and nuclei shapes of hMSCs on the graphene was not significantly different compared to those on the graphene-uncoated glass substrate (Fig. 2B), suggesting that other graphene-induced factors, such as the small 3D spheroid structure formation (Figs. 2A and Supplementary Fig. S4), enhanced FA formation (Fig. 2C) and cell-cell communication (Fig. 2D) of hMSCs as well as the natural properties of graphene (Supplementary Figs. S2 and S3), such as nanoscale structure, strong stiffness, roughness, electrical conductivity, and absorption of biomolecules, can collectively influence the enhanced neural differentiation of hMSCs.

In this study, although we have focused on the enhancement of differentiation of hMSCs into the functional neurons, we believe that the use of high-quality graphene is equally applicable to other systems, such as osteogenesis, adipogenesis, epithelial genesis, cardiomyogenic differentiation, or differentiation into the glia cells by various types of stem cells and appropriate chemical agents. We also expect to find further enhanced stem cell functions, including differentiation into specific lineages, by using high-quality graphene-based platforms (e.g., graphene-incorporated scaffolds and graphene-coated biomimetic tissue-like structure) for stem-based regenerative medicine.

Conclusions

In summary, our study supports the notion that highly uniform graphene can be used as an efficient platform for the growth and neural differentiation of hMSCs. We found that the 3D spheroid structure could be formed from aggregated hMSCs grown on highly uniform monolayer of graphene without the use of any external factors. We also found that the produced ECM molecules from hMSCs on graphene might guide the full adhesion of the cells onto the substrates, thereby enhancing the formation of FAs and the expression of the connexin 43 of the hMSCs. These graphene-induced interactions at the cell-substrate and cell-cell interfaces might collectively promote the neurogenesis of hMSCs as well as the neurite outgrowths. In particular, we found that the early neurogenesis-related genes in the hMSCs were highly upregulated on grapheme, even in the absence of any external neurogenic factors. The responses of differenced neurons from hMSCs on graphene were quite sensitive to external stimulation. The cells could maintain their neuronal properties, even after re-seeding the detached differenced neurons removed from graphene onto the normal cell culture substrate in the growth medium. Although in-depth studies must be performed to accurately understand the underlying molecular mechanisms, our current work has revealed that the highly uniform graphene may be able to regulate the growth and the neural differentiation of hMSCs, which would enable an efficient strategy for autologous stem cell based therapy to treat neuronal disorders or diseases, as well as for designing scaffolds for tissue engineering and regenerative medicine.

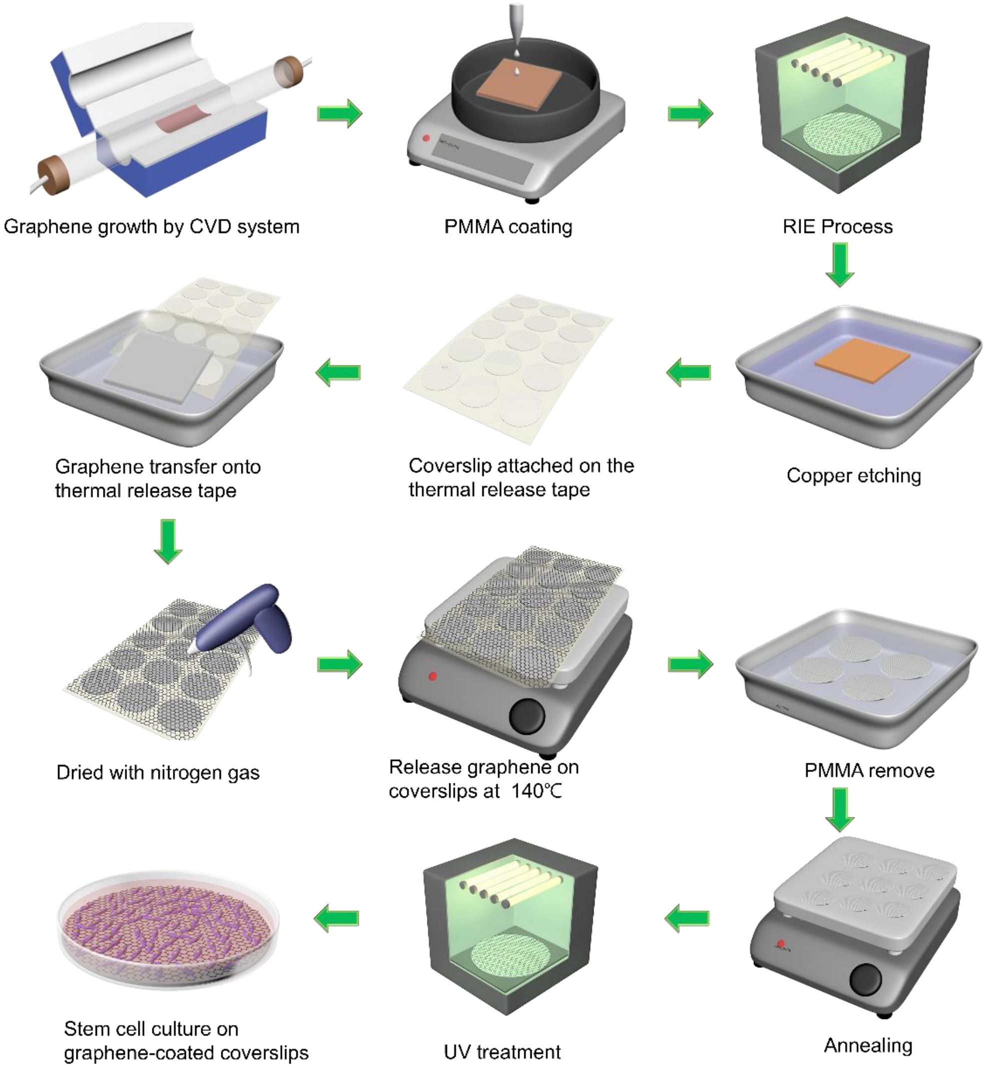

Figure S1 | Schematic of fabrication of the high quality graphene on glass substrate for growth and neuronal differentiation of stem cells

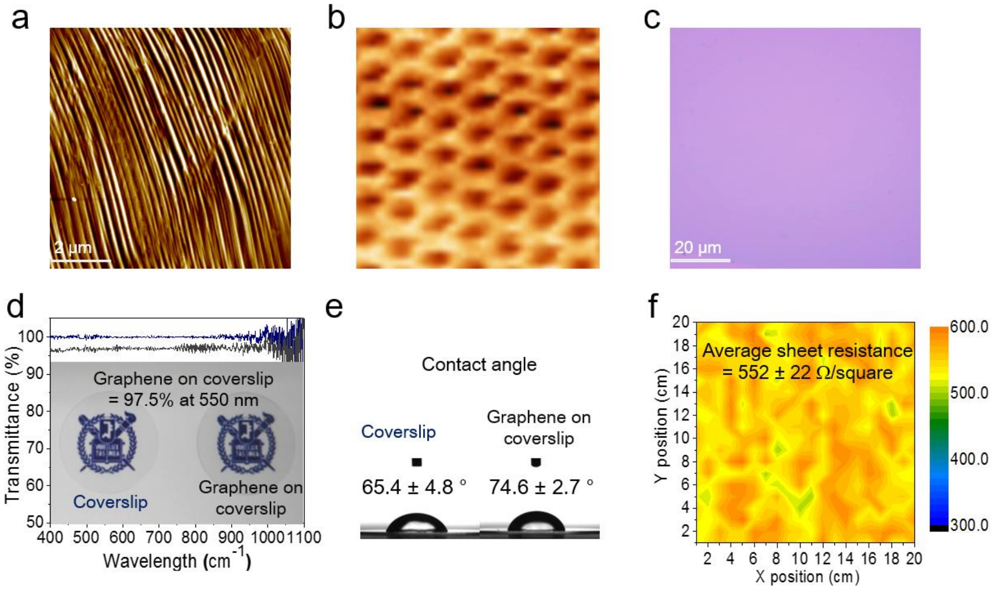

Figure S2 | a, AFM image of graphene growth on copper foil. b, Atmosphere STM image of graphene grown on Cu foil. c, Typical optical microscope image of graphene transferred onto 300 nm SiO$_2$/Si substrate. d, UV–vis spectra of transferred graphene on the glass substrate. e, Contact angle of graphene and coverslip f, Sheet resistance mapping of the graphene.

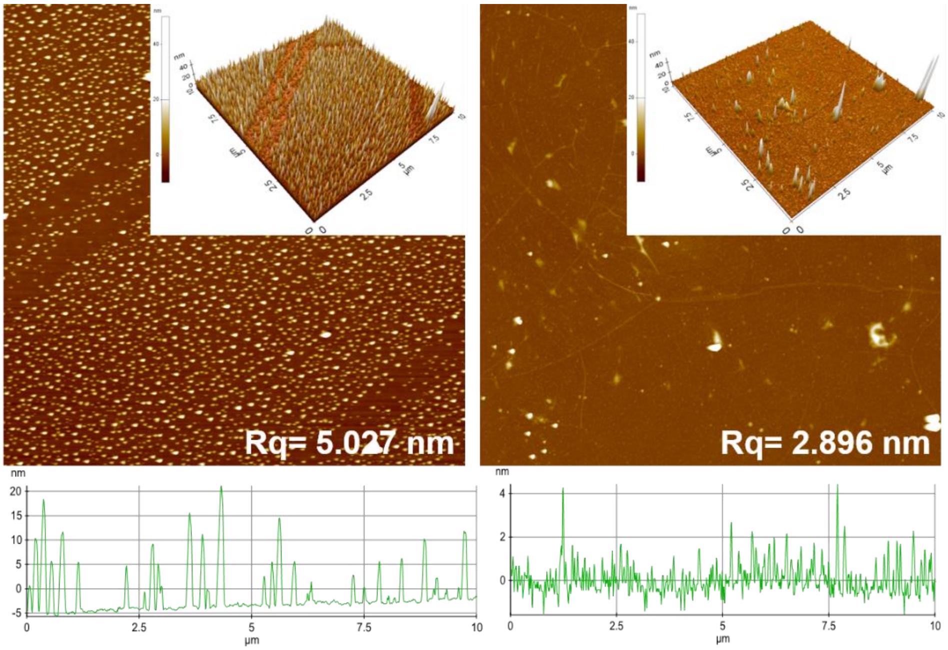

Figure S3 | AFM topography images of the graphene and glass substrate. The values indicate the roughness of the surfaces.

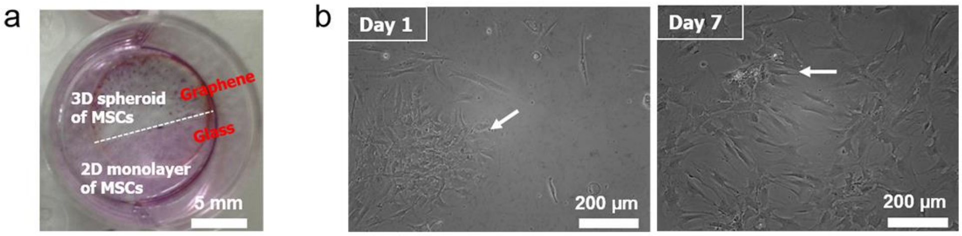

Figure S4 | a, Low magnification images of hMSCs cultured on the graphene and glass substrate for 1 day. The cells were stained by crystal violet to show the formation of 3D spheroids on the graphene. b, Representative phase-contrast images of hMSCs cultured on the graphene for 1 day and 7 days, respectively. The white arrows indicate the spheroids of hMSCs.

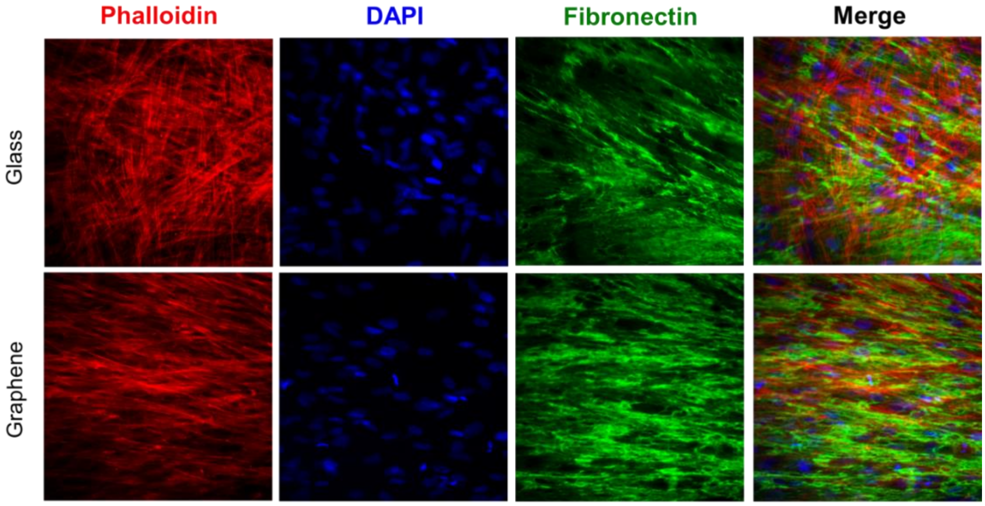

Figure S5 | Representative immunostaining images of actin, nucleus, and fibronectin on the graphene and glass substrate after culturing hMSCs for 7 days.

References

[1]. Delcroix, G. J., Schiller, P. C., Benoit, J. P. & Montero-Menei, C. N. Adult cell therapy for brain neuronal damages and the role of tissue engineering. *Biomaterials.* **2010**, 31, 2105-2120.

[2]. Prabhakaran, M. P., Venugopal, J. R. & Ramakrishna, S. Mesenchymal stem cell differentiation to neuronal cells on electrospun nanofibrous substrates for nerve tissue engineering. *Biomaterials*, **2009**, 30, 4996-5003.

[3]. David J., T. et al. Traumatic brain injury-related hospital discharges. results from a 14-state surveillance system, 1997. MMWR: Surveillance Summaries, **2003**, 52, 1-20.

[4]. Kim, S. U. & de Vellis, J. Stem cell-based cell therapy in neurological diseases: a review. *Journal of neuroscience research*, **2009**, 87, 2183-2200.

[5]. Deng, J., Petersen, B. E., Steindler, D. A., Jorgensen, M. L. & Laywell, E. D. Mesenchymal stem cells spontaneously express neural proteins in culture and are neurogenic after transplantation. *Stem cells*, **2006**, 24, 1054-1064.

[6]. Park, S. Y. et al. Enhanced differentiation of human neural stem cells into neurons on graphene. *Adv Mater.* **2011**, 23, 263-267.

[7]. Li, N. et al. Three-dimensional graphene foam as a biocompatible and conductive scaffold for neural stem cells. *Scientific reports*, **2013**, 3, 1604.

[8]. Wang, Y. et al. Fluorinated graphene for promoting neuro-induction of stem cells. *Adv Mater.* **2012**, 24, 4285-4290.

[9]. Solanki, A. et al. Axonal alignment and enhanced neuronal differentiation of neural stem cells on graphene-nanoparticle hybrid structures. *Adv Mater.* **2013**, 25, 5477-5482.

[10]. Nayak, T. R. et al. Graphene for Controlled and Accelerated Osteogenic Differentiation of Human Mesenchymal Stem Cells. *ACS Nano.* **2012**, 5, 4670-4678.

[11]. Lee, W. C. et al. Origin of Enhanced Stem Cell Growth and Differentiation on Graphene and Graphene Oxide. *ACS Nano.* **2012**, 5, 7334-7341.

[12]. Kim, J. et al. Bioactive effects of graphene oxide cell culture substratum on structure and function of human adipose-derived stem cells. *Journal of biomedical materials research. Part A.* **2013**, 101, 3520-3530.

[13]. Kalbacova, M., Broz, A., Kong, J. & Kalbac, M. Graphene substrates promote adherence of human osteoblasts and mesenchymal stromal cells. *Carbon,* **2010**, 48, 4323-4329.

[14]. Bae, S. et al. Roll-to-roll production of 30-inch graphene films for transparent electrodes. *Nat. Nanotechnol.***2010**, 574-578.

[15].Kim, K. S. et al. Large-scale pattern growth of graphene films for stretchable transparent electrodes. *Nature*. **2009**, 457, 706-710.

[16]. Li, N. et al. The promotion of neurite sprouting and outgrowth of mouse hippocampal cells in culture by graphene substrates. *Biomaterials.* **2011**, 32, 9374-9382.

[17]. Shi, X. et al. Regulating Cellular Behavior on Few-Layer Reduced Graphene Oxide Films with Well-Controlled Reduction States. *Adv Funct Mater*. **2012**, 22, 751-759.

[18]. Bendali, A. et al. Purified neurons can survive on peptide-free graphene layers. *Adv Healthcare Mater*. **2013**, 2, 929-933.

[19]. Ku, S. H. & Park, C. B. Myoblast differentiation on graphene oxide. *Biomaterials*. **2013**, 34, 2017-2023.

[20]. Park, J. et al. Graphene-Regulated Cardiomyogenic Differentiation Process of Mesenchymal Stem Cells by Enhancing the Expression of Extracellular Matrix Proteins and Cell Signaling Molecules. *Adv Healthcare Mater*. **2013**, 1-6.

[21]. Kim, J. et al. Graphene-incorporated chitosan substrata for adhesion and differentiation of human mesenchymal stem cells. *J. Mater. Chem. B*. 2013, 1, 933.

[22]. Kim, J. A. et al. High-throughput generation of spheroids using magnetic nanoparticles for three-dimensional cell culture. *Biomaterials*. **2013**, 34, 8555-8563.

[23]. Huang, G. S., Dai, L. G., Yen, B. L. & Hsu, S. H. Spheroid formation of mesenchymal stem cells on chitosan and chitosan-hyaluronan membranes. *Biomaterials*. **2011**, 32, 6929-6945.

[24]. Hsu, S. H. et al. Enhanced chondrogenic differentiation potential of human gingival fibroblasts by spheroid formation on chitosan membranes. *Tissue Eng Part A*. **2012**, 18, 67-79.

[25]. Chalut, K. J., Kulangara, K., Giacomelli, M. G., Wax, A. & Leong, K. W. Deformation of stem cell nuclei by nanotopographical cues. *Soft matter*. **2010**, 6, 1675-1681.

[26]. Cha, C., Liechty, W. B., Khademhosseini, A. & Peppas, N. A. Designing Biomaterials To Direct Stem Cell Fate. *ACS Nano*. **2012**, 6, 9353-9358.

[27]. Kim, J. et al. Charged nanomatrices as efficient platforms for modulating cell adhesion and shape. *Tissue Eng Part C Methods*, **2012**, 18, 913-923.

[28]. Kim, J. et al. Synergistic effects of nanotopography and co-culture with endothelial cells on osteogenesis of mesenchymal stem cells. *Biomaterials*. **2013**, 34, 7257-7268.

[29]. Tang, M. et al. Enhancement of electrical signaling in neural networks on graphene films. *Biomaterials*. **2013**, 34, 6402-6411.

[30]. Ferreira, L., Karp, J. M., Nobre, L. & Langer, R. New Opportunities: The Use of Nanotechnologies to Manipulate and Track Stem Cells. *Cell Stem Cell*. **2008**, 3, 136-146.

[31]. Kim, H. N. et al. Nanotopography-guided tissue engineering and regenerative medicine. *Adv. Drug Deliv. Rev*. **2013**, 65, 536-558.

[32]. Kim, J. et al. Designing nanotopographical density of extracellular matrix for controlled morphology and function of human mesenchymal stem cells. *Sci Rep*. **2013**, 3, 3552.

[33]. Guilak, F. et al. Control of Stem Cell Fate by Physical Interactions with the Extracellular Matrix. *Cell Stem Cell*. **2009**, 5, 17-26.

[34]. Kim, D. H., Provenzano, P. P., Smith, C. L. & Levchenko, A. Matrix nanotopography as a regulator of cell function. *J. Cell Biol*. **2012**,197, 351-360.

[35]. Sart S Fau - Tsai, A.-C., Tsai Ac Fau - Li, Y., Li Y Fau - Ma, T. & Ma, T. Three-dimensional Aggregates of Mesenchymal Stem Cells: Cellular Mechanisms, Biological Properties, and Applications.

[36]. Bartosh, T. J. et al. Aggregation of human mesenchymal stromal cells (MSCs) into 3D spheroids enhances their antiinflammatory properties. *Proc. Natl. Acad. Sci. U.S.A.* **2010**, 107, 13724-13729.

[37]. Cheng, N.-C., Chen, S.-Y., Li, J.-R. & Young, T.-H. Short-Term Spheroid Formation Enhances the Regenerative Capacity of Adipose-Derived Stem Cells by Promoting Stemness, Angiogenesis, and Chemotaxis. *Stem Cells Transl Med*. 2013, 2, 584-594.

[38]. Yim, E. K. F., Pang, S. W. & Leong, K. W. Synthetic nanostructures inducing differentiation of human mesenchymal stem cells into neuronal lineage. *Exp Cell Res*. **2007**, 313, 1820-1829.

Chapter 3

Graphene enhances the cardiomyogenic differentiation of human embryonic stem cells

Introduction

Due to the unique physical and chemical properties of graphene, this material has been reported to act as a culture substrate that promotes the lineage specification of adult mesenchymal stem cells (MSCs) and neural stem cells, both of which are multipotent stem cells. The culture of human neural stem cells (hNSCs) on graphene promotes their differentiation toward neurons through electrical stimulation facilitated by graphene. [1,2] Graphene can also promote the adhesion of MSCs,[3] and the culture of MSCs on graphene enhances their osteogenic differentiation through strong cell adhesion to graphene.[4] Graphene has also been used for the culture of pluripotent stem cells. Graphene maintains the pluripotency of mouse induced pluripotent stem cells.[5] Human embryonic stem cells (hESCs) adhered to Geltrex®-coated graphene remained viable and pluripotent and proliferated.[6] However, the effect of graphene on the differentiation of pluripotent ESCs has not yet been reported.

Cardiomyocytes generated from stem cells would be a useful cell source for cell-based therapies for ischemic heart diseases. A variety of adult stem cells, such as bone marrow-derived stem cells,[7] adipose-derived stem cells,[8] resident cardiac stem cells,[9] and umbilical cord blood stem cells,[10] have been used to treat ischemic heart diseases. However, these adult stem cells are known to have limited ability to differentiate into cardiomyocytes.[11] In contrast, ESCs are known to differentiate spontaneously into cardiomyocytes.[12] When these cells are transplanted into a damaged heart, ESCs integrate into the recipient heart and improve the heart functions.[13] Therefore, hESCs would be a useful cell-source for stem cell-based therapy for ischemic heart diseases.

Although graphene exerts stimulatory effects on the lineage specification of multipotent adult stem cells, its effects on the differentiation of pluripotent ESCs have not yet been reported. In the present study, we investigated whether culture on graphene enhances the cardiomyogenic differentiation of hESCs. Large-area graphene on glass coverslips was prepared through the chemical vapor deposition method. The spontaneous cardiomyogenic differentiation of hESCs was investigated by culturing hESCs on either glass (control) or graphene without the addition of exogenous chemicals for differentiation induction and by evaluating the expression of cardiac-specific genes. The differentiation of these cells was also compared with that of cells cultured on Matrigel-coated glass, which is a substrate used in the conventional, directed two-dimensional culture differentiation systems for the cardiomyogenic differentiation of hESCs without forming embryoid bodies.[14] The direct two-dimensional culture differentiation system is an efficient method for cardiomyogenic differentiation of hESCs, since it was reported that 70% of hESC clusters were contracting and 90% of cells had a cardiomyocyte phenotype after culture through.[14] The mesodermal and endodermal differentiations were compared among the experimental groups because these differentiations are known to be intermediate stages of the cardiomyogenic differentiation of hESCs.[14] The mechanisms underlying the enhanced cardiomyogenic differentiation were also investigated.

Experimental

Graphene Preparation and Characterization

Monolayer graphene was synthesized through the CVD process. The graphene film grown on the copper foil was covered by poly(methyl methacrylate) (PMMA) and floated on the surface of an aqueous solution of 0.1 M ammonium persulphate [$(NH_2)_4S_2O_8$]. After all of the copper layers were etched away, the floating PMMA/graphene film was collected using a clean PET film and transferred to deionized water. The cleaning process was repeated five times. The graphene film with the PMMA support was transferred to glass coverslips. The samples were dried with nitrogen gas immediately after the transfer and baked for 8 h on a hot plate at 60 ℃. The samples were then cleaned using acetone at room temperature for 30 min to remove the PMMA support layer. The samples were then dried and baked for 8 h on a hot plate at 60 ℃. The graphene was sterilized by UV treatment for 30 min prior to cell culture. The samples were characterized by Raman spectroscopy, ultraviolet-visible spectrometry, transmission electron microscopy (TEM), and selected area electron diffraction (SAED). The structural properties of the graphene on the glass coverslip were further investigated through Raman spectroscopy (RM 1000-Invia, Renishaw, UK). The Raman spectra were recorded using an argon ion laser (514 nm) as the excitation source with a notch filter of 50 cm^{-1}. The typical scan range was from 1000 to 3000 cm^{-1}, and the instrumental resolution was 10 cm^{-1}. The optical transmittance of the graphene on the coverslip was measured using an ultraviolet-visible spectrometer (UV-3600, Shimadzu, Japan). The TEM and SAED analyses were conducted on a TEM (JEOL 2100, JEOL, Japan) operated at 200 kV. The rotation between the TEM images and the corresponding SAED patterns was calibrated using molybdenum trioxide crystals. The sheet resistances of the graphene on the coverslip were measured through the van der Pauw four-probe method using a Hall measurement system. The surface morphology of graphene and glass was examined with non-contact mode AFM (XE-100 system, Park Systems, Suwon, Korea).

hESC culture

SNUhES31 (Institute of Reproductive Medicine and Population, Medical Research Center, Seoul National University, Seoul, Korea), which is a hESC line, was maintained in their undifferentiated state by feeder-free culturing on human recombinant VN (Life Technologies, Carlsbad, CA, USA)-coated (0.5 μg/cm^2) culture dishes with Essential 8™ medium (Life Technologies) as previously described.[40] The culture medium was changed daily, and the hESCs were passaged every week.

Differentiation of hESCs into cardiomyocytes using a two-dimensional system

For the cardiomyogenic differentiation of cultured hESCs using a two-dimensional system, cultured hESC colonies were fragmented into small clumps with uniform sizes using the STEMPRO® EZPassage tool (Life Technologies). Prior to cell plating, glass coverslips were coated with Matrigel (BD Bioscience, San Jose, CA, USA)[41] or VN[42] as previously described for hESCs culture. Graphene on glass coverslips was also coated with VN. The Matrigel- or VN-coated glass and VN-coated graphene were placed onto six-well plates. Small clumps of hESCs were plated on each of the Matrigel- or VN-coated glass and VN-coated graphene in the six-well plates (150 clumps per well). The cardiomyogenic differentiation of the culture was performed as previously described.[14] Briefly, the attached hESCs were expanded in hESC media composed of Dulbecco's Modified Eagle's Medium (DMEM)/F12 (Gibco BRL, Gaithersburg, MD, USA) supplemented with 20% (v/v) knockout serum replacement (Life Technologies), 4 ng/ml FGF2 (R&D Systems, Minneapolis, MN, USA), 1% nonessential amino acid (Life Technologies), 0.1 mM β-mercaptoethanol (Sigma), and 0.2% primocin (InvivoGen, San Diego, CA, USA) for four days and then cultured in hESC media without FGF2 for three days. The cells were cultured in DMEM (Gibco BRL) containing 10% (v/v) fetal bovine serum (FBS, Gibco BRL) for seven days. Finally, the cells were cultured in DMEM containing 20% (v/v) FBS for seven days. The culture media were changed every 24 h.

Viability of hESCs cultured on graphene

The viability of hESCs cultured on graphene was examined by live and dead assay at day 2. The live and dead cells on non-coated graphene or VN-coated graphene were detected with fluorescein diacetate (FDA, Sigma-Aldrich, St. Louis, MO, USA) and ethidium bromide (EB, Sigma). The hESCs were incubated in FDA/EB (5 μg/ml or 10 μg/ml) solution for 5 min at 37 °C and then washed twice in PBS. The dead cells were stained orange due to the nuclear permeability of EB. The viable cells, which are capable of converting the non-fluorescent FDA into fluorescein, were stained green. After staining, the samples were examined using a fluorescence microscope (Model IX71 Olympus, Tokyo, Japan). Adhesion morphology of hESCs on graphene was examined by scanning electron microscopy (SEM; JSM-6701F, JEOL, Tokyo, Japan).

Quantitative real-time reverse transcription-polymerase chain reaction (qRT-PCR) of EBs

The mRNA expression levels of differentiated hESCs were analyzed through qRT-PCR. The total RNA was extracted from the differentiated hESCs on days 4, 7, 14, and 21 and reverse-transcribed into cDNA. The qRT-PCR was performed using the StepOnePlus real-time PCR system (Applied Biosystems, Foster City, CA, USA) with a FAST SYBR Green PCR master mix (Applied Biosystems). Each of the 45 cycles performed consisted of the following temperature program: 94 ℃ for 3 sec and 60 ℃ for 30 sec. The primer sequences are shown in Table 1.

Western blot assay

hESCs cultured for 21 days on Matrigel- or VN-coated glass and VN-coated graphene were lysed with sodium dodecyl-sulfate (SDS) sample buffer [62.5 mM Tris–HCl (pH 6.8), 2% (w/v) SDS, 10% (v/v) glycerol, 50 mM dithiothreitol, and 0.1% (w/v) bromophenol blue]. The total protein concentration was determined through a bicinchoninic acid protein assay (Pierce Biotechnology, USA). Western blot analysis was performed through 10% (w/v) SDS-polyacrylamide gel electrophoresis. The proteins were first transferred to an Immobilon-P membrane

(Millipore Corp., USA) and then probed with antibodies against human vinculin (Abcam, Cambridge, UK), paxillin (Abcam), FAK (Abcam), pFAK (Abcam), ERK 1/2 (Abcam), and pERK 1/2 (Abcam). The proteins were then incubated with a horseradish peroxidase-conjugated secondary antibody (Santa Cruz Biotechnology, USA) for 1 h at room temperature. The blots were developed using an enhanced chemiluminescence detection system (Amersham Bioscience, USA). The data were quantified through densitometric scanning (Image-Pro Plus software, Media Cybernetics, Marlow, UK).

Statistical analysis

The quantitative data are expressed as the means ± standard deviation. The statistical analysis was performed by analysis of variance (ANOVA) using a Bonferroni test. A p value < 0.05 was considered statistically significant.

Results and Discussion

The large-area, monolayer graphene used in this study was synthesized on copper foils through the chemical vapor deposition (CVD) method (Figure 1a). To confirm the presence of graphene, the graphene was transferred onto a SiO_2/Si substrate according to a previously reported method.[15] Figure 1b shows an optical micrograph of a graphene film transferred onto a SiO_2/Si substrate. The uniform color contrast of the optical micrograph indicates that the graphene film has excellent thickness uniformity. Although the graphene film was only one-atom thick on SiO_2/Si substrates with a well-defined oxide thickness (300 nm), it was easily observed with a simple conventional optical microscope. Optical images of the glass coverslip and the graphene-coated glass coverslip showed that both were transparent (Figure 1c). The contact angle measurements showed that the graphene-coated glass coverslip was slightly hydrophobic (74.4 ± 3.5°), whereas the contact angle of the coverslip was 64.2 ± 3.7° (Figure 1d). To determine the quality of the graphene, the transferred graphene film was characterized through Raman spectroscopy (Figure 1e). The Raman spectrum of graphene is characterized by three main characteristic peaks. The G peak is commonly found in carbon-based materials with a hexagonal pattern. The G peak near 1580 cm^{-1} arises from the emission of zone-center optical phonons, the D band near 1350 cm^{-1} arises from the doubly resonant disorder-induced mode, and the 2D peak is the second order of the D peak that moves from the K to the K' point and the symmetry-allowed 2D over-tune mode near 2700 cm^{-1}. The shift and

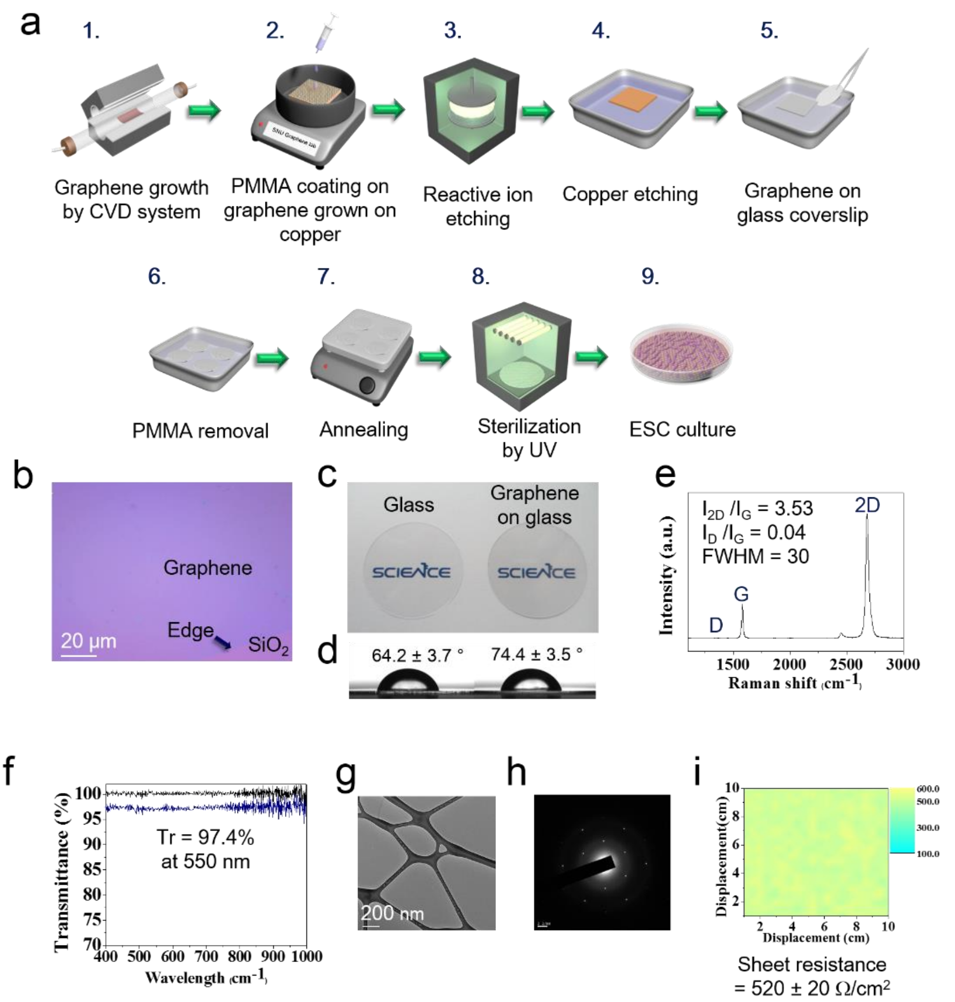

Figure 1 | Preparation and characterization of large-area graphene substrates. a, Schematic of the preparation process used to produce the graphene coating on a glass coverslip. b, A typical optical microscopic image of graphene transferred onto 300-nm-thick SiO_2/Si substrate. c, Photograph d, contact angle of a glass coverslip and graphene on a glass coverslip. e, Raman spectroscopy of the transferred graphene. f, UV-visible spectra of transferred graphene on a glass coverslip and a glass coverslip substratum, showing the transparency of the graphene on the coverslip. g, TEM image of graphene on a TEM grid. h, SAED pattern. i, Sheet resistance of monolayer graphene on a glass coverslip.

line shape associated with these modes have been used to determine the quality of graphene and the number of graphene layers. The peak located at ~2700 cm^{-1} (G′ band) exhibits a full width at half-maximum (fwhm) of 26~33 cm^{-1}. The intensity of the I_{2D}/I_G ratio is more than three-fold higher than that of the peak located at ~1600 cm^{-1} (the G band), and there is no measurable peak observed at ~1350 cm^{-1} (the D band), which indicates the synthesis of high-quality monolayer graphene. In addition, the graphene-coated glass coverslip exhibited high transparency with a transmittance that exceeded 97.4% at a wavelength of 550 nm (Figure 1f), which confirms the presence of uniform and monolayer graphene. Figure 1g shows a representative low-magnification TEM image of graphene sheet on a TEM grid. The typical SAED pattern for well-synthesized graphene was observed for the graphene used in this study (Figure 1h). The transferred graphene on the coverslip showed a sheet resistance of 520 ± 20 Ω/cm^2 with a high uniformity (Figure 1i).

Prior to culture for cardiomyogenic differentiation, we tested whether hESCs could adhere to graphene and survive. hESC clumps were plated on non-coated graphene and vitronectin (VN)-coated graphene. Two days later, the hESCs on VN-coated graphene showed good cell-attachment and colony formation (Figure 2a). In contrast, the hESCs did not adhere to non-coated graphene. The viability of hESCs cultured on non-coated graphene and VN-coated graphene was evaluated by live and dead assays with FDA/EB staining (Figure 2b). The hESCs on non-coated graphene were dead (orange-red color), whereas the hESCs cultured on VN-coated graphene were viable (green color, Figure 2b). A SEM image showed that hESCs are well-adherent to VN-coated graphene (Figure 2c), whereas all hESCs were detached from non-coated graphene. These results indicate that coating of graphene with VN is required for a high viability of hESCs cultured on the graphene. Thus, VN-coated graphene was used for the hESC culture in the present study.

hESCs first differentiate into mesodermal cells and endodermal cells, and the mesodermal cells further differentiate into cardiogenic lineages in two-dimensional, directed differentiation systems (Figure 3a).[14] Endodermal cells appear to interact with mesodermal cells to induce the differentiation of the mesodermal cells toward cardiogenic lineages.[14] hESCs were cultured on Matrigel-coated glass (Matrigel group), VN-coated glass (glass group), or VN-coated graphene (graphene group) for 21 days, and the mesodermal, cardiac mesodermal, endodermal, and ectodermal gene expression profiles were determined by qRT-PCR assay. On day 14, the graphene group showed a significantly enhanced expression of mesodermal genes (T and M-CAD) and a cardiac mesodermal gene (MESP1) compared with both the Matrigel and the glass groups (Figure 3b, c). On day 21, only a cardiac mesodermal gene (MESP1) was enhanced in the graphene group compared with both the Matrigel and the glass groups. T expression is known to induce the expression of MESP1,[16] which is a master regulator of cardiac progenitor specification and is needed to enter the cardiac mesodermal stage.[17-19] The graphene group showed higher expression of SOX17 on day 14 and FOXA2 on days 14 and 21, both of which are endodermal genes, compared with the Matrigel and the glass groups (Figure 3d). In contrast, the ectodermal gene (TUBB3) expression, which may not be involved in the cardiomyogenic differentiation process of hESCs, was not increased in the graphene

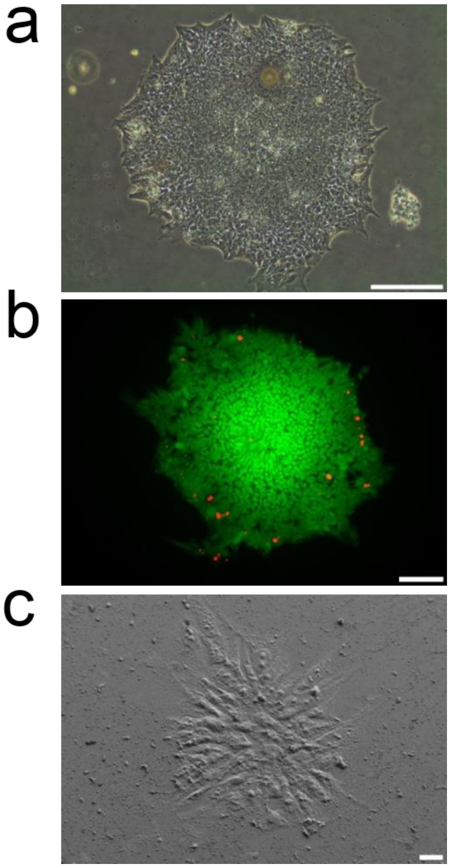

Figure 2 | The coating of graphene with VN is required to achieve a high viability of hESCs cultured on the graphene. hESCs were cultured on graphene for two days. a, Light microscopic images of hESCs cultured on the graphene. b, Fluorescence microscopic images of hESCs stained with FDA and EB. The green and orange-red colors indicate viable and dead cells, respectively. c, SEM image of hESCs cultured on graphene. The scale bars indicate (a) 200 μm, (b) 100 μm, and (c) 20 μm.

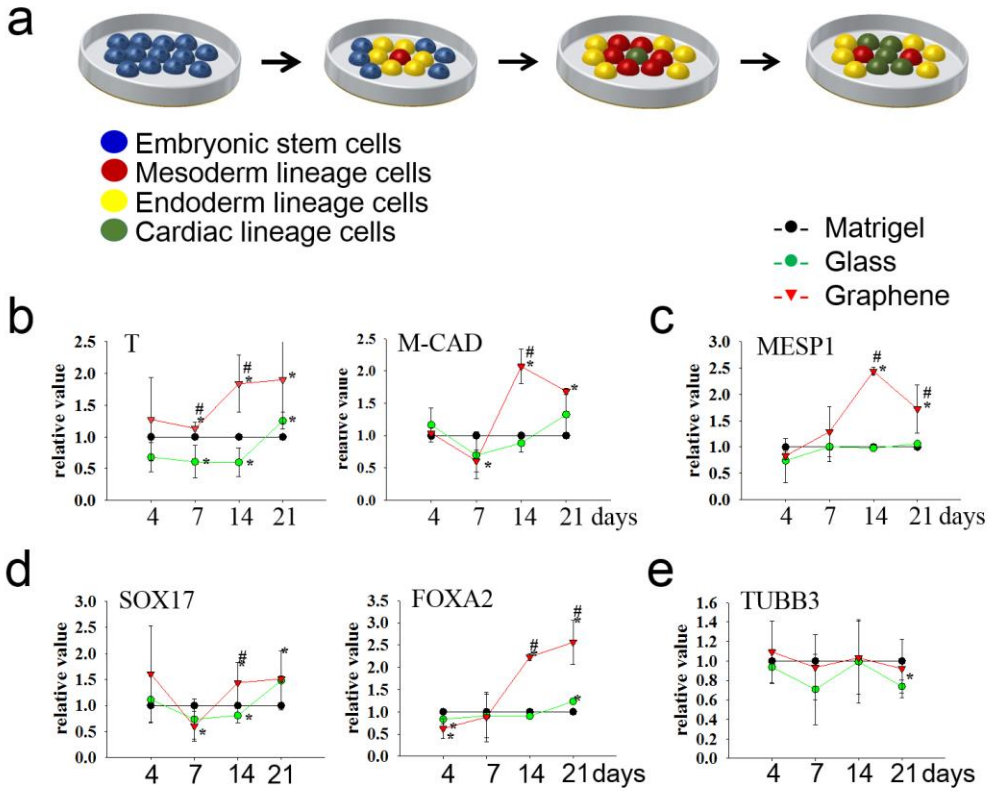

Figure 3 | Culture on graphene enhances the mesodermal and endodermal lineage differentiation of hESCs. a, A schematic diagram for the cardiomyogenic differentiation of hESCs in a two-dimensional, stepwise differentiation system. b, The mesodermal c, cardiac mesodermal d, endodermal, and e, ectodermal gene expression profiles of hESCs cultured for 21 days on Matrigel-coated glass (Matrigel), VN-coated glass (glass), or VN-coated graphene (graphene), as determined by qRT-PCR assay. The values were normalized to the levels obtained for the Matrigel group (n=4 per group, *p<0.05 versus Matrigel, #p<0.05 versus glass).

group compared with the Matrigel and the glass group throughout the culture period (Figure 3e). These results suggest that graphene promotes mesodermal lineage differentiation at the middle-stage time point and differentiation into the cardiac mesodermal lineage, which is a more cardiogenic lineage than the mesodermal lineage, at the end-stage time point.

The endodermal lineage induction by graphene may promote the cardiomyogenic differentiation of hESCs. Signals from the endoderm, such as bone morphogenetic protein (BMP) and fibroblast growth factor (FGF), are important for cardiac development.[20] It is known that factors secreted by endodermal lineage cells, such as BMP-2, FGF4, and transforming growth factor-β, are needed to induce the cardiac differentiation of murine ESCs and heart development.[21, 22] It has also been reported that co-culture with a endodermal cell line induces the cardiac differentiation of hESCs.[23] In two-dimensional culture systems, the presence of endodermal cells around the mesodermal cells appear to induce the cardiomyogenic differentiation of hESCs.[14] Therefore, the enhanced endodermal lineage differentiation by graphene (Figure 3d) may induce an enhancement in the cardiomyogenic differentiation of hESCs.

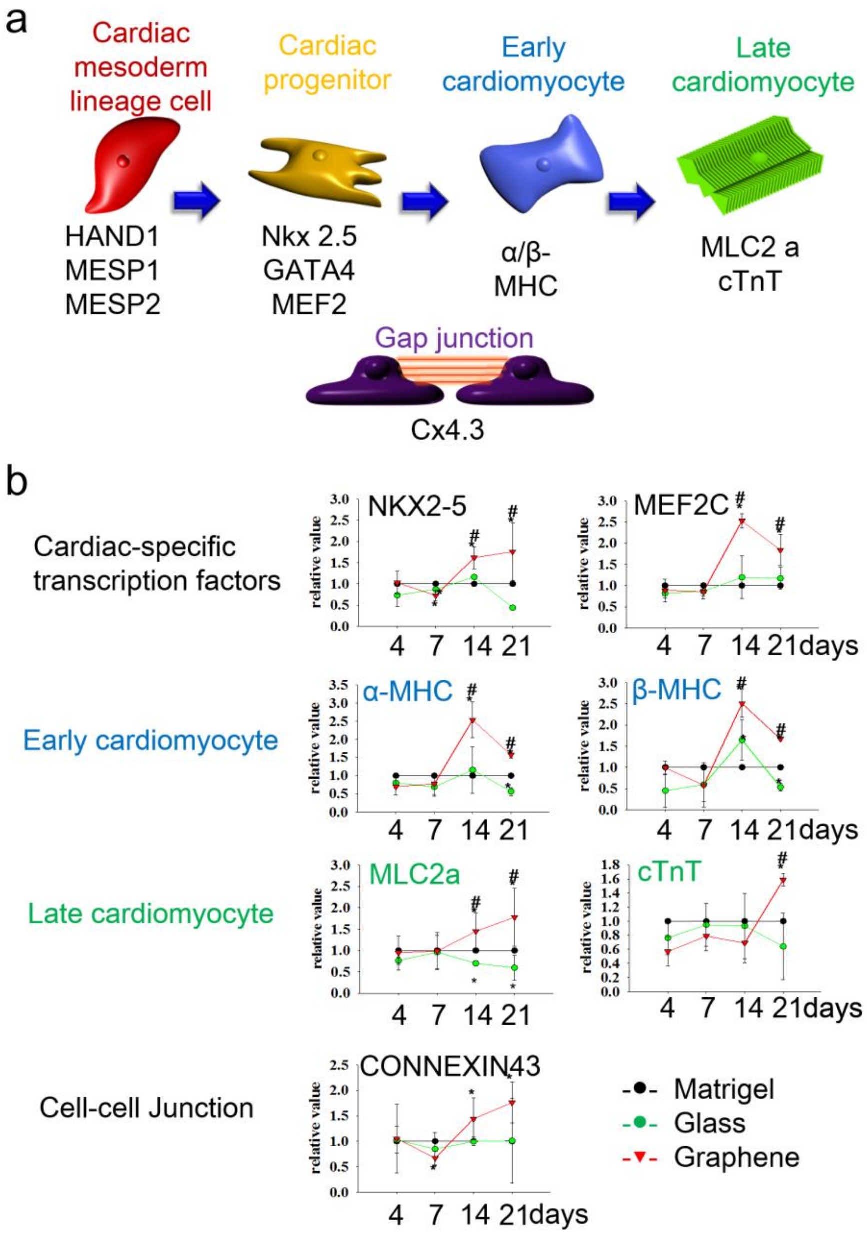

Figure 4 | Culture on graphene enhances the cardiomyogenic differentiation of hESCs. a, A schematic diagram of the gene expression profile during the cardiomyogenic differentiation process of hESCs. b, Cardiomyogenic gene expression profiles of hESCs cultured for 21 days on Matrigel-coated glass (Matrigel), VN-coated glass (glass), or VN-coated graphene (graphene), as determined by qRT-PCR assay. The values were normalized to the levels obtained for the Matrigel group (n=4 per group, *$p<0.05$ versus Matrigel, #$p<0.05$ versus glass).

We investigated whether the culture of hESCs on graphene promotes their cardiomyogenic differentiation by evaluating the cardiomyogenic gene expression through a qRT-PCR assay. Cardiac mesodermal lineage cells differentiate into cardiac progenitor cells, which further differentiate into cardiomyocytes (Figure 4a). Strikingly, the expression of many cardiomyogenic markers, as shown in Figure 4a, was enhanced in the graphene group compared with both the Matrigel and the glass groups, even in the absence of cardiomyogenic inducers in the culture medium (Figure 4b).

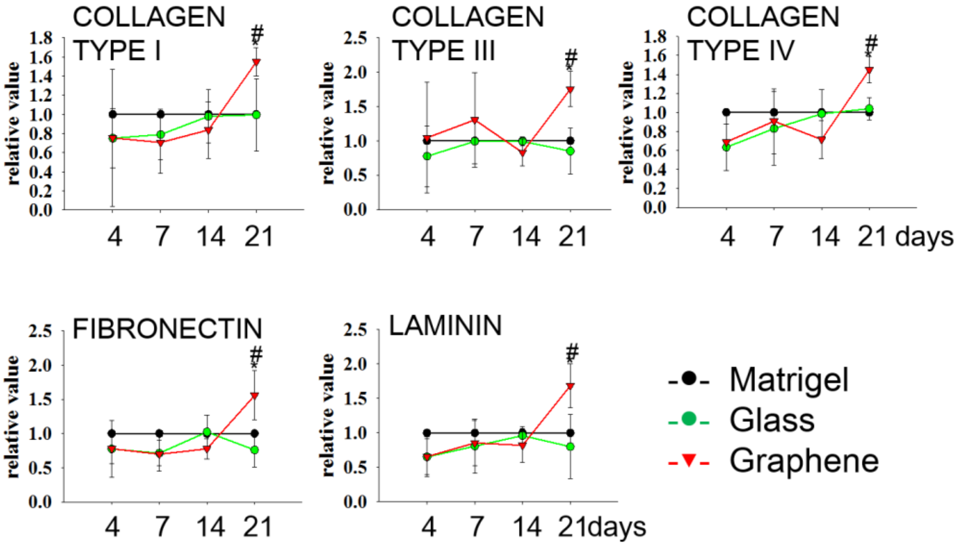

Figure 5 | Culture on graphene enhances cardiac-specific ECM expression in hESCs. Gene expression profiles of extracellular matrix proteins in hESCs cultured for 21 days on Matrigel-coated glass (Matrigel), VN-coated glass (glass), or VN-coated graphene (graphene), as determined by qRT-PCR assay. The values were normalized to the levels obtained for the Matrigel group (n=4 per group, *$p<0.05$ versus Matrigel, #$p<0.05$ versus glass).

The gene expression of cardiomyogenic transcriptional factors (NKX2-5, GATA4, and MEF2C), cardiomyogenic contractile proteins (α-MHC, β-MHC, MLC2a, and cTnT), and gap junction proteins (CONNEXIN43) was significantly higher in the graphene group compared with both the Matrigel and the glass groups on days 14 and/or 21. Early cardiomyocyte marker (α-MHC and β-MHC) expression was maximal on day 14 and decreased on day 21 in the graphene group, whereas late cardiomyocyte marker (MLC2a, and cTnT) expression increased with the culture time from day 14 to day 21. To further investigate the effects of graphene on the cardiomyogenic differentiation of hESCs, the gene expression of cardiac-specific ECMs was evaluated through a qRT-PCR assay. The gene expression of cardiac-specific ECMs, such as COLLAGEN TYPE I, COLLAGEN TYPE III, COLLAGEN TYPE IV, FIBRONECTIN, and LAMININ, was enhanced on day 21 in the graphene group compared with both the Matrigel and the glass groups (Figure 5).

The mechanisms underlying the graphene-enhanced cardiomyogenic differentiation were investigated. The enhanced cardiomyogenic differentiation may be, at least in part, due to nanotopography of graphene, which enhanced hESC adhesion and the upregulation of extracellular signal-regulated kinase (ERK) signaling. Graphene showed more nanotopographical features than glass (Figure 6a).

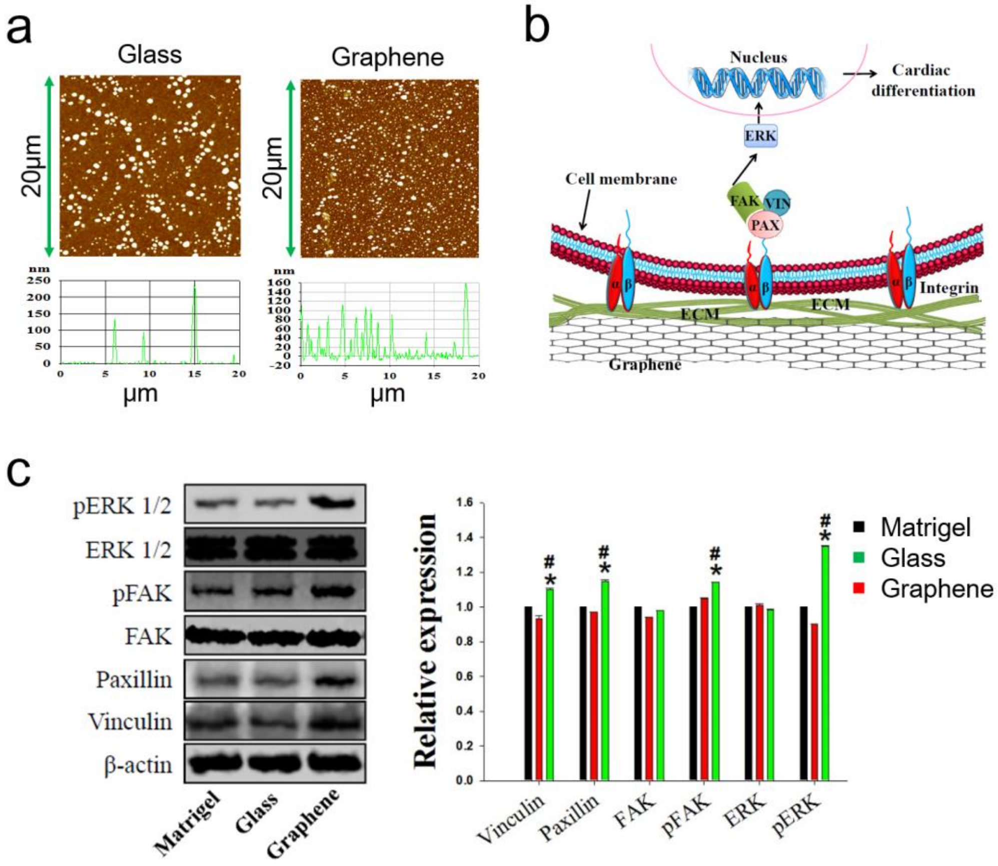

Figure 6 | Mechanisms underlying the graphene-enhanced cardiomyogenic differentiation Nanoroughness of graphene, FAK, and ERK signaling. a, AFM images and surface nanoroughness of VN-coated glass (glass group) and VN-coated graphene (graphene group). b, a schematic diagram of the signal transduction pathways associated with the cardiomyogenic differentiation of hESCs cultured on graphene. The enhanced hESC adhesion and the subsequent upregulation of ERK signaling of hESCs cultured on graphene were likely attributed to the nanoroughness of the graphene. ECM: extracellular matrix, α, β: integrin α and β subunits, PAX: paxillin, VIN: vinculin. c, Western blot analyses of hESCs cultured on Matrigel-coated glass (Matrigel), VN-coated glass (glass), or VN-coated graphene (graphene) to analyze the molecules involved in the signal transduction pathways, and quantification of the relative protein expression levels of the cell signaling molecules. The values were normalized to the levels obtained for the Matrigel group (n=3 per group, *p<0.05 versus Matrigel, #p<0.05 versus glass).

Graphene enhanced hESC adhesion, as the expression of phosphorylated focal adhesion kinase (pFAK), vinculin, and paxillin, which are related to the focal adhesion of cells (Figure 6b),[24,25] was enhanced in the graphene group compared with the other groups (Figure 6c). The enhanced hESC adhesion on graphene with nanotopographical features is consistent with the results of previous studies in which cell adhesion was enhanced on substrates with nanoscale protrusions (15-45 nm [26] and 250-300 nm [27]). First, strong hESC adhesion to graphene may be responsible for the enhanced cardiomyogenic differentiation. It has been shown that stem cell differentiation is enhanced on nanotopographical substrates through FAK.[28] Also, a previous study showed that the enhanced neuronal differentiation of hNSCs cultured on laminin-coated graphene compared to laminin-coated glass was likely due to the enhanced cell adhesion to laminin-coated graphene.[2] Second, the enhancement of hESC adhesion in the graphene group may promote the cardiomyogenic differentiation of hESCs through ERK signaling (Figure 6b). Graphene enhanced the expression of phosphorylated ERK (pERK) compared with both the Matrigel and the glass groups (Figure 6c). It has been reported that the activation of ERK enhances the cardiomyogenic differentiation of hESCs.[29]

Conclusions

The culture of hESCs on graphene promotes the stepwise differentiation of these cells into mesodermal cells and endodermal cells and their subsequent cardiomyogenic differentiation compared with their culture on glass. Moreover, the analysis of the cardiomyogenic differentiation of hESCs cultured on graphene or Matrigel revealed that graphene was superior to Matrigel, which is a substrate used in conventional cardiomyogenic differentiation systems. The graphene-enhanced cardiomyogenic differentiation may be, at least in part, due to nanotopography of graphene, which enhanced hESC adhesion and the upregulation of ERK signaling. The data suggest that graphene is a novel culture substrate for the enhancement of the differentiation of hESCs into cardiomyogenic lineage cells, which would be useful for the development of stem cell-based therapies for ischemic heart diseases.

Table 1. Human-specific primers for each gene analyzed through the qRT-PCR assay.

Gene	Primer
GAPDH	sense 5′- GTC GGA GTC AAC GGA TTT GG -3′ antisense 5′- GGG TGG AAT CAA TTG GAA CAT -3′
BRACHYURY (T)	sense 5′- CAG TGA CTT TTT GTC GTG GCA -3′ antisense 5′- CCA ACT GCA TCA TCT CCA CA -3′
MESP1	sense 5′- TGT GAG CAC CGA GGC TTT TT-3′ antisense 5′- TCC TGC TTG CCT CAA AGT GT-3′
SOX17	sense : 5′- AAC TGG TTG GCT TGT CAT GAG-3′ antisense 5′- TAC TTC CAA GGA ACT GCA TGG-3′
FOXA2	sense 5′- CCA TTG CTG TTG TTG CAG GGA AGT-3′ antisense 5′- CAC CGT GTC AAG ATT GGG AAT GCT -3′
TUBB3	sense 5′- TTC CTG CAC TGG TAC ACG G-3′ antisense 5′- TGC GAG CAG CTT CAC TTG-3′
NKX2-5	sense 5′-GCA GAG ACC TCC CGT TTT GTT -3′ antisense 5′- GCC ACC GAC ACG TCT CAC T -3′
MEF2C	sense 5′-CCT GCA AAT ATG GCC CTA GAA -3′ antisense 5′- CGG GAT TGT TCA ACA GTC CTA-3′
α-MHC	sense 5′-GCC CCG CCC CAC AT -3′ antisense 5′- CCG GAT TCT CCC GTG ATG-3′
β-MHC	sense 5′- CCA CCC AAG TTC GAC AAA ATC -3′ antisense 5′- CGT AGC GAT CCT TGA GGT TGT A -3′
MLC2a	sense 5′- CCC CAG CGG CAA AGG -3′ antisense 5′- CCA CCT CAG CTG GAG AGA ACT T -3′
cTnT	sense 5′- CAG GAT CAA CGA TAA CCA GAA AGT C -3′ antisense 5′- GTG AAG GAG GCC AGG CTC TA -3′
CONNEXIN43	sense 5′- ACT GGC GAC AGA AAC AAT TCT TC -3′ antisense 5′- TTC TGC ACT GTA ATT AGC CCA GTT -3′
COLLAGEN TYPE I	sense 5′- CAG CCG CTT CAC CTA CAG C -3′ antisense 5′- TTT TGT ATT CAA TCA CTG TCT T -3′
COLLAGEN TYPE III	sense 5′- GGG AAT GGA GCA AAA CAG TCT T -3′ antisense 5′- CCA ACG TCC ACA CCA AAT TCT -3′
COLLAGEN TYPE IV	sense 5′- TGT CCA ATA TGA AAA CCG TAA AGT G -3′ antisense 5′- CAC TAT TGA AAG CTT ATC GCT GTC TT -3′
FIBRONECTIN	sense 5′- TCC ACG GGA GCC TCG AA -3′ antisense 5′- ACA ACC GGG CTT GCT TTG -3′
LAMININ	sense 5′- CAC AAC AAC ATT GAC ACG ACA GA -3′ antisense 5′- GCT GGA GGG CAT CAC CAT AGT -3′

References

[1]. Heo, C.; Yoo, J.; Lee, S.; Jo, A.; Jung, S.; Yoo, H.; Lee, Y.H.; Suh, M. The control of neural cell-to-cell interactions through non-contact electrical field stimulation using graphene electrodes. *Biomaterials*. **2011**, 32, 19-27.

[2]. Park, S.Y.; Park, J.; Sim, S.H.; Sung, M.G.; Kim, K.S.; Hong, B.H.; Hong, S. Enhanced differentiation of human neural stem cells into neurons on graphene. *Adv. Mater.* **2011,** 23, H263-267.

[3]. Kalbacova, M.; Broz, A.; Kong, J.; Kalbac, M. Graphene substrates promote adherence of human osteoblasts and mesenchymal stromal cells. *Carbon*. **2010,** 48, 4323-4329.

[4]. Nayak, TR.; Andersen, H.; Makam, V.S.; Khaw, C.; Bae, S.; Xu, X.; Ee, P.L.; Ahn, J.H.; Hong, B.H.; Pastorin, G.; *et al*. Graphene for controlled and accelerated osteogenic differentiation of human mesenchymal stem cells. *ACS Nano*. **2011,** 5, 4670-4678.

[5]. Chen, G.Y.; Pang, D.W.; Hwang, S.M.; Tuan, H.Y.; Hu,Y.C. A graphene-based platform for induced pluripotent stem cells culture and differentiation. *Biomaterials*. **2012,** 33, 418-427.

[6]. Sebaa, M.; Nguyen, T. Y.; Paul, R. K.; Mulchandani, A.; Liu, H. Graphene and carbon nanotube–graphene hybrid nanomaterials for human embryonic stem cell culture. *Materials Letters*. **2013,** 92, 122–125.

[7]. Tang, X.L.; Rokosh, D.G.; Guo, Y.; Bolli, R. Cardiac progenitor cells and bone marrow-derived very small embryonic-like stem cells for cardiac repair after myocardial infarction. *Circ. J.* **2010,** 74, 390-404.

[8]. Planat-Bénard, V.; Menard, C.; André, M.; Puceat, M.; Perez, A.; Garcia-Verdugo, J.M.; Pénicaud, L.; Casteilla, L. Spontaneous cardiomyocyte differentiation from adipose tissue stroma cells. *Circ. Res.* **2004,** 94, 223-229.

[9]. Unno, K.; Jain, M.; Liao, R. Cardiac side population cells: moving toward the center stage in cardiac regeneration. *Circ. Res.* **2012,** 110, 1355-1363.

[10]. Schlechta, B.; Wiedemann, D.; Kittinger, C.; Jandrositz, A.; Bonaros, N.E.; Huber, J.C.; Preisegger, K.H.; Kocher, A.A. Ex-vivo expanded umbilical cord blood stem cells retain capacity for myocardial regeneration. *Circ. J.* **2010,** 74, 188-194.

[11]. Mignone, J.L.; Kreutziger, K.L.; Paige, S.L.; Murry, C.E. Cardiogenesis from human embryonic stem cells. *Circ. J.* **2010,** 74, 2517-2526.

[12]. Kehat, I.; Kenyagin-Karsenti, D.; Snir, M.; Segev, H.; Amit, M.; Gepstein, A.; Livne, E.; Binah, O.; Itskovitz-Eldor, J.; Gepstein, L. Human embryonic stem cells can differentiate into myocytes with structural and functional properties of cardiomyocytes. *J. Clin. Invest.* **2001,** 108, 407-414.

[13]. Shiba, Y.; Fernandes, S.; Zhu, W.Z.; Filice, D.; Muskheli, V.; Kim, J.; Palpant, N.J.; Gantz, J.; Moyes, K.W.; Reinecke, H.; *et al*. Human ES-cell-derived cardiomyocytes electrically couple and suppress arrhythmias in injured hearts. *Nature*. **2012,** 489, 322-325.

[14]. Moon, S.H.; Ban, K.; Kim, C.; Kim, S.S.; Byun, J.; Song, M.K.; Park, I.H.; Yu, S.P.; Yoon, Y.S. Development of a novel two-dimensional directed differentiation

system for generation of cardiomyocytes from human pluripotent stem cells. *Int. J. Cardiol.* **2013,** 168, 41-52.

[15]. Kim, K.S.; Zhao, Y.; Jang, H.; Lee, S.Y.; Kim, J.M.; Kim, K.S.; Ahn, J.H.; Kim, P.; Choi, J.Y.; Hong, B.H. Large-scale pattern growth of graphene films for stretchable transparent electrodes. *Nature.* **2009,** 457, 706-710.

[16]. David, R.; Jarsch, V.B.; Schwarz, F.; Nathan, P.; Gegg, M.; Lickert, H.; Franz, W.M. Induction of MesP1 by Brachyury(T) generates the common multipotent cardiovascular stem cell. *Cardiovasc. Res*. **2011,** 92, 115-122.

[17]. Bondue, A.; Lapouge, G.; Paulissen, C.; Semeraro, C.; Iacovino, M.; Kyba, M.; Blanpain, C. Mesp1 acts as a master regulator of multipotent cardiovascular progenitor specification. *Cell Stem Cell*. **2008,** 3, 69-84.

[18]. Wu, S.M. Mesp1 at the heart of mesoderm lineage specification. *Cell Stem Cell*. **2008,** 3, 1-2.

[19]. Bondue, A.; Tännler, S.; Chiapparo, G.; Chabab, S.; Ramialison, M.; Paulissen, C.; Beck, B.; Harvey, R.; Blanpain, C. Defining the earliest step of cardiovascular progenitor specification during embryonic stem cell differentiation. *J. Cell. Biol.* **2011,** 192, 751-765.

[20]. Olson, E.N. Development. The path to the heart and the road not taken. *Science.* **2001,** 291, 2327-2328.

[21]. Rudy-Reil, D.; Lough, J. Avian precardiac endoderm/mesoderm induces cardiac myocyte differentiation in murine embryonic stem cells. *Circ. Res*. **2004,** 94, e107-116.

[22]. Lough, J.; Sugi, Y. Endoderm and heart development. *Dev. Dyn.* **2000,** 217, 327-342.

[23]. Mummery, C.; Ward-van Oostwaard, D.; Doevendans, P.; Spijker, R.; van den Brink, S.; Hassink, R.; van der Heyden, M.; Opthof, T.; Pera, M.; de la Riviere, A.B.; Differentiation of human embryonic stem cells to cardiomyocytes: role of coculture with visceral endoderm-like cells. *Circulation*. **2003,** 107, 2733-2740.

[24]. Rodina, A.; Schramm, K.; Musatkina, E.; Kreuser, E.D.; Tavitian, A.; Tatosyan, A. Phosphorylation of p125FAK and paxillin focal adhesion proteins in src-transformed cells with different metastatic capacity. *FEBS Lett.* **1999,** 455, 145-148.

[25]. Raz, A.; Geiger, B. Altered organization of cell-substrate contacts and membrane-associated cytoskeleton in tumor cell variants exhibiting different metastatic capabilities. *Cancer Res.* **1982,** 42, 5183-5190.

[26]. Lim, J.Y.; Hansen, J.C.; Siedlecki, C.A.; Hengstebeck, R.W.; Cheng, J.; Winograd, N.; Donahue, H.J. Osteoblast adhesion on poly(L-lactic acid)/polystyrene demixed thin film blends: effect of nanotopography, surface chemistry, and wettability. *Biomacromolecules.* **2005,** 6, 3319-3327.

[27]. Milner, K.R.; Siedlecki, C.A. J. Submicron poly(L-lactic acid) pillars affect fibroblast adhesion and proliferation. *Biomed. Mater. Res. A.* **2007,** 82, 80-91.

[28]. Teo, B.K.; Wong, S.T.; Lim, C.K.; Kung, T.Y.; Yap, C.H.; Ramagopal, Y.; Romer, L.H.; Yim, E.K. Nanotopography modulates mechanotransduction of stem cells and induces differentiation through focal adhesion kinase. *ACS Nano*. **2013,** 7, 4785-4798.

[29]. Gao, M.; Yang, J.; Wei, R.; Liu, G.; Zhang, L.; Wang, H.; Wang, G.; Gao, H.; Chen, G.; Hong, T. Ghrelin induces cardiac lineage differentiation of human embryonic stem cells through ERK1/2 pathway. *Int. J. Cardiol.* **2013,** 167, 2724-2733.

[30]. Chen, G.; Gulbranson, D.R.; Hou, Z.; Bolin, J.M.; Ruotti, V.; Probasco, M.D.; Smuga-Otto, K.; Howden, S.E.; Diol, N.R.; Propson, N.E.; *et al*. Chemically defined conditions for human iPSC derivation and culture. *Nat. Methods*. **2011,** 8, 424-429.

[31]. Braam, S.R.; Denning, C.; Matsa, E.; Young, L.E.; Passier, R.; Mummery, C.L. Feeder-free culture of human embryonic stem cells in conditioned medium for efficient genetic modification. *Nat. Protoc.* **2008,** 3,1435-1443.

[32]. Braam, S.R.; Zeinstra, L.; Litjens, S.; Ward-van Oostwaard, D.; van den Brink, S.; van Laake, L.; Lebrin, F.; Kats, P.; Hochstenbach, R.; Passier, R. et al. Recombinant vitronectin is a functionally defined substrate that supports human embryonic stem cell self-renewal via alphavbeta5 integrin. *Stem Cells.* **2008,** 26, 2257-2265.

Chapter 4

Graphene-regulated cardiomyogenic differentiation process of mesenchymal stem cells by enhancing the expression of extracellular matrix proteins and cell signaling molecules

Introduction

Stem cell-based regenerative medicine provides a promising strategy for the treatment of heart failure, which is one of the common causes of mortality in the world.[1] Specifically, mesenchymal stem cells (MSCs) have been shown to have great potential to repair heart diseases. However, the therapeutic efficacy of the treatment is quite limited as MSCs hardly differentiate into cardiomyocytes *in vivo*.[2] For example, it has been known that the transplantation of cardiomyogenically differentiated MSCs greatly improved myocardial contractility.[3] Therefore, many researchers have attempted to develop methods for the promotion of *in vitro* cardiomyogenic differentiation of MSCs. Specifically, 5-azacytidine has been utilized to commit MSCs toward the cardiomyogenic lineage.[4] However, 5-azacytidine-treated MSCs are not clinically suitable because it has been anticipated to interfere with normal cell activity by inhibiting deoxyribonucleic acid methylation, [5] suggesting that other methods for MSC commitment toward the cardiomyogenic lineage without using exogenous chemical inducers that may interfere with normal cell activity should be developed for clinical stem cell therapies for myocardial infarction.

It is reported that MSC differentiation could be modulated through cellular interactions with culture substrates *in vitro*.[6] However, only a few studies have studied the effect of cell culture substrates on cardiomyogenic differentiation of MSCs. Recently, graphene has drawn attention as a platform for cell culture due to its unique physical, chemical, and mechanical properties and its effects on stem cell lineage specifications.[7-9] Guided by these considerations, here we propose for the first time that graphene can promote the expression of cardiomyogenic genes of MSCs. We also investigated a potential mechanism of the effects of graphene on the enhanced cardiomyogenic differentiation process through analyzing the expressions of extracellular matrix (ECM) proteins and cell signaling molecules that are known to promote the cardiomyogenic differentiation of stem cells.

Experimental

Graphene Preparation

The entire fabrication process to produce graphene on coverslips is shown in the schematic illustration. In the first step, high-quality, large-scale monolayer graphene was synthesized by chemical vapor deposition (CVD) process, which is described in the literature.[46] Secondly, 300nm thin poly(methyl methacrylate) (PMMA), which we call the ‘supporting layer’, was coated onto as graphene films and annealed at 140 ℃ for 1min to cure it. Thirdly, the back side growth graphene is then removed by reactive ion etching (RIE) with a power of 100 W and O_2 etching gas of 20 sccm. the PMMA coated graphene growth copper foil is subsequently etched away and floated on the surface of an aqueous solution of 0.1 M ammonium persulphate $[(NH_2)_4S_2O_8]$. After all of the copper layers were etched away, the floating PMMA/graphene film was collected using a clean PET film and transferred to deionized water. The cleaning process was repeated five times. After that, the graphene film with the PMMA support was transferred to the coverslips. The samples were dried with nitrogen gas immediately after the transfer and baked for 8 h on a hot plate at 60 ℃. The samples were then cleaned using acetone at room temperature for 30 min to remove the PMMA support layer. The samples were dried with nitrogen gas immediately after the transfer and baked for 8 h on a hot plate at 60 ℃. The samples were then dried and baked for 8 h on a hot plate at 60 ℃. Finally, the graphene on coverslips sample was obtained. (Figure S1).

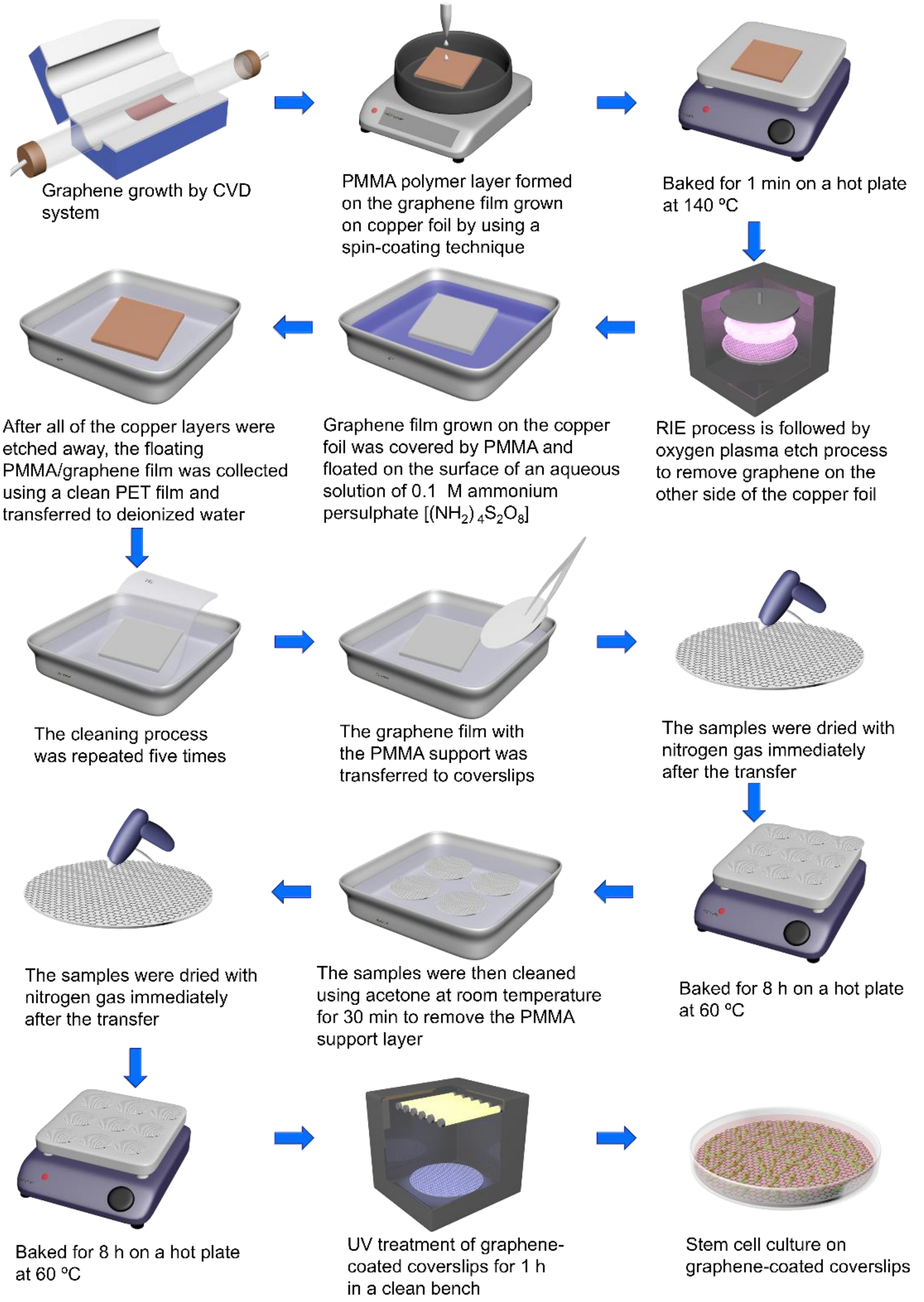

Figure S1 | Schematic flows of various key steps during the fabrication of showing preparation process to produce graphene on coverslips

Characterization

The samples were characterized by AFM, Raman spectroscopy, ultraviolet–visible spectrometer, TEM, and SAED. The surface morphology examination of the samples was conducted through non-contact mode AFM (XE-100 system, Park Systems, Korea). The structural properties of the graphene on the coverslip were further investigated through Raman spectroscopy (RM 1000-Invia, Renishaw, UK). The Raman spectra were recorded by using an argon ion laser (514 nm) as the excitation source with a notch filter of 50 cm^{-1}. The typical scan range was from 1000 to 3000 cm^{-1} and the instrumental resolution was 10 cm^{-1}. The optical transmittance of the graphene on the coverslip was measured using an ultraviolet–visible spectrometer (UV-3600, Shimadzu, Japan). The TEM and SAED analyses were conducted on a TEM (JEOL 2100, JEOL, Japan) operated at 200 kV. The rotation between the TEM images and the corresponding SAED patterns was calibrated using molybdenum trioxide crystals. The sheet resistances of the graphene on the coverslip were measured through the van der Pauw four-probe method using a Hall measurement system.

Cell Culture

Human bone marrow-derived MSCs were purchased from a commercial source (Lonza, USA) and cultured in Dulbecco's modified Eagle's medium (DMEM, Gibco BRL, USA) containing 10% (v/v) fetal bovine serum (FBS; Gibco-BRL) and 1% (v/v) penicillin–streptomycin (PS; Gibco-BRL). At passage 4, the MSCs were plated at a cell density of 1×10^3 cells/cm^2 for the experiments. The medium was changed every 2 days.

Cell Viability and Proliferation

The live and dead cells were assessed by calcein-AM and ethidium homodimer, relatively, using a two-color fluorescence live/dead assay kit (Molecular Probes, USA). The gene expression levels of Bcl-2 and caspase-3 were evaluated by qRT-PCR to assess the expression of anti-apoptotic and apoptotic genes, respectively, in MSCs. The proliferating cells were analyzed by immunofluorescence staining using antibodies against PCNA (Abcam, UK). The samples were mounted in 4,6-diamidino-2-phenylindole (DAPI, Vector Laboratories, USA) for nuclear staining. The cell proliferation was quantitatively measured by counting the number of cells using CCK-8 (Sigma, USA) and a hemocytometer (Paul Marienfeld GmbH and Co., Germany).

Cardiomyogenic Gene Expression

The hMSCs were cultured for 2 and 3 weeks on a coverslip or graphene in DMEM containing 10% FBS and 1% PS and analyzed through qRT-PCR.

Gene Expression of Extracellular Matrix Proteins: The hMSCs were cultured for 2 and 3 weeks on a coverslip or graphene in DMEM containing 10% FBS and 1% PS and analyzed through qRT-PCR.

qRT-PCR

Ribonucleic acid (RNA) samples were extracted using Qiagen RNeasy mini kit according to the manufacturer's instructions (Qiagen, Germany). The total RNA concentration was determined using a NanoDrop spectrometer (ND-2000, NanoDrop Technologies, USA). The RNA (500 ng) from each sample was reverse-transcribed to obtain cDNA using GoScript Reverse Transcriptase (Promega, USA). SYBR green-based qRT-PCR was performed using a StepOnePlus Real-Time PCR System (Applied Biosystems, USA) instrument with the TOPreal qPCR Premix (Enzynomics, Korea). After a 10-min pre-incubation, 40 amplification cycles were performed and each cycle consists of three steps; 30 s at 94℃, 45 s at 55℃, and 45 s at 72℃. The primer sequences for the qRT-PCR analyses are listed in Table 1. All of the data were analyzed using the $2^{-\Delta\Delta Ct}$ method.

Analysis of the Signal Transduction Molecules

The MSCs cultured for 3 weeks on a coverslip or graphene were lysed with sodium dodecyl-sulfate (SDS) sample buffer (62.5 mM Tris–HCl (pH 6.8), 2% (w/v) SDS, 10% (v/v) glycerol, 50 mM dithiothreitol, and 0.1% (w/v) bromophenol blue). The total protein concentration was determined through a bicinchoninic acid protein assay (Pierce Biotechnology, USA). Western blot analysis was performed through 10% (w/v) SDS-polyacrylamide gel electrophoresis. The proteins were first transferred to an Immobilon-P membrane (Millipore Corp., USA) and then probed with antibodies against human FAK (Abcam, USA), paxillin (Abcam), vinculin (Abcam), Src (Abcam), ERK (Abcam), JNK (Abcam), PI3K (Abcam), Cdc42 (Abcam), Rac1 (Abcam), Wnt7a (Abcam), and Akt (Abcam). The proteins were then incubated with a horseradish peroxidase-conjugated secondary antibody (Santa Cruz

Biotechnology, USA) for 1 h at room temperature. The blots were developed using an enhanced chemiluminescence detection system (Amersham Bioscience, USA). The data were quantified through densitometric scanning (Image-Pro Plus software, Media Cybernetics, Marlow, UK).

Results and Discussion

High quality and large-scale graphene used in this study was synthesized by the chemical vapor deposition (CVD) method on copper foils. After synthesis, copper foil was etched and the same batch of graphene was transferred to coverslip, following a previously reported method.[36] Atomic force microscopy (AFM) was used to analyze the surface roughness (the root-mean-square deviation (Rq)) of the coverslip with and without graphene. AFM images of graphene on coverslip and coverslip distinctly show difference in their morphological property (figure 2a). AFM image of graphene on coverslip revealed the typical flat but wrinkled graphene morphology compared to graphene on coverslip. The surface roughness (Rq) was 4.87 nm and 4.93 nm for coverslip and graphene-coated coverslip, respectively, and there was no significant difference. Optical image of coverslip and graphene transferred to coverslip, showing that both coverslip and graphene-coated coverslip are nearly transparent (Figure 1b). Contact angle measurement showed that graphene transferred coverslip is slightly hydrophobic (73.9 ± 1.2°), while the contact angle of coverslip is 64.7 ± 2.8° (Figure 1c).

To confirm monolayer graphene, the transferred graphene film was characterized by Raman spectroscopy. Raman spectra result of as-grown graphene transferred on SiO_2 (300 nm)/Si substrate (Figure 1d). The Raman spectrum of graphene is characterized by three main characteristic peaks. G peak is shown commonly in carbon-based materials that have hexagonal pattern. The G peak near 1580 cm^{-1} arising from emission of zone-center optical phonons, the D band near

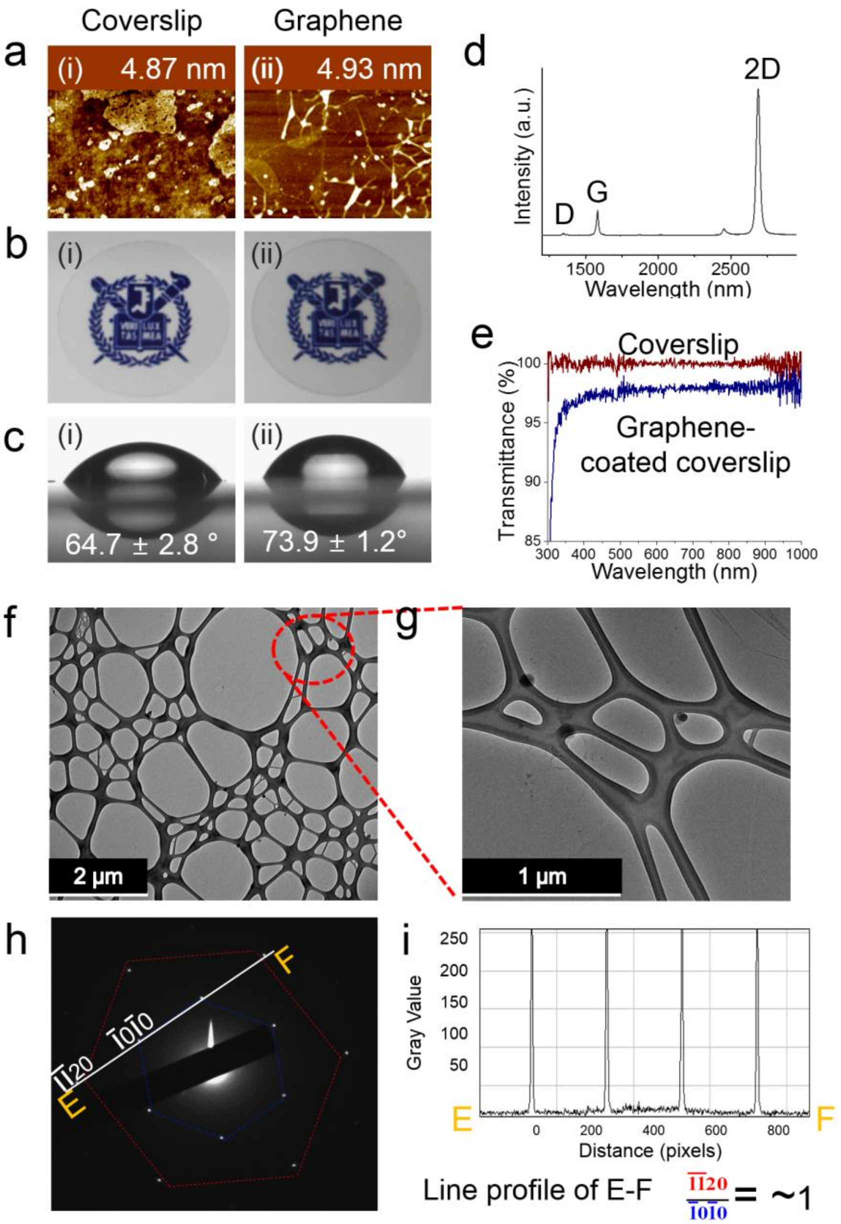

Figure 1| Characterization of graphene substrates. a, AFM topography images, b, photographs, and c, contact angle images of (i) coverslip and (ii) graphene on coverslip. d, Raman spectroscopy of graphene. e, Transparency of graphene films transferred on coverslip. TEM image of graphene sheet on a TEM grid at f, low and g, high magnifications. h, The SAED pattern. i, Intensity profile of the diffraction spots along a line connecting points E and F in the single-layer graphene diffraction pattern. The uniform intensity profile between the inner and outer spots proves that the graphene sheet consists of a single layer.

1350 cm^{-1} arising from the doubly resonant disorder-induced mode and 2D peak is the second order of D peak moves from K to K' point and the symmetry-allowed 2D over tune mode near 2700 cm^{-1}. The shift and line shape associated with these modes have been used to determine the quality of grapheme and the number of graphene layers. The peak located at ~2700 cm^{-1} (G′ band) with a full width at half-maximum (FWHM) is 26~33 cm^{-1}, the ration of I_{2D}/I_G ratio is more than three times as intense as the peak located at ~1600 cm^{-1} (the G band) and there is no measurable peak observed at ~1350 cm^{-1} (the D band), indicating the successful growth of high-quality monolayer graphene. In addition, graphene-coated coverslip exhibited high transparency with transmittance exceeding 97.4% at 550 nm wavelength (Figure 1e). This is evidence of uniform and monolayer graphene. Raman spectrum and the transmittance are consistent with previously reported paper[13] and we confirmed that graphene film used in this study was monolayer. Figure 1f shows the representative low-magnification transmission electron microscopy (TEM) image of graphene sheet on a TEM grid, and Figure 1g shows TEM image of the circled region in Figure 1f.

We have included a selected area electron diffraction (SAED) patterns image in order to show the good crystallinity of the graphene used in our experiments (see Figure 1h). A typical SAED pattern obtained from graphene sheet shows the six-fold symmetry that is expected for graphene. Intensity profile of equivalent Bragg reflections taken along the line denoted showed that the intensities of the $\bar{1}0\bar{1}0$(inner hexagon) and $\bar{1}\bar{1}20$(outer hexagon) spots were equivalent, indicating that the set of diffraction spots originated from a single-layer graphene sheet (Figure 1i).[14] We

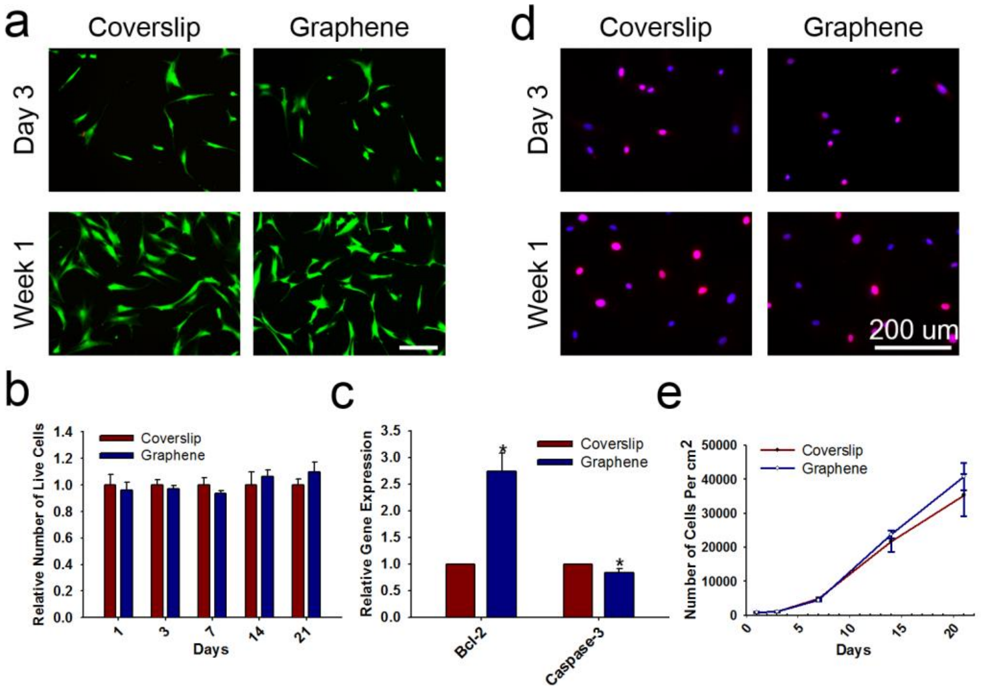

Figure 2 | *In vitro* biocompatibility of graphene. a, Live/dead assay of MSCs cultured on graphene and coverslips for 3 days and 1 week. The live cells were stained with calcein-AM (green), and the dead cells were stained with ethidium homodimer (red). The scale bar represents 200 μm. b, The number of live cells is expressed relative to the number of live cells on a coverslip on day 1. The number of live cells was counted using CCK-8. c, Upregulation of Bcl-2, an anti-apoptotic marker, and downregulation of caspase-3, a pro-apoptotic marker, in MSCs cultured on graphene for 3 weeks relative to MSCs cultured on coverslips, as evaluated by qRT-PCR. $*p < 0.05$ compared to MSCs cultured on coverslips. d, Proliferation of MSCs cultured on coverslips and graphene. The proliferation was evaluated by PCNA staining. The proliferating cells were stained with PCNA (red), and the nuclei were stained with DAPI (blue). The scale bar represents 200 μm. e, Growth of MSCs cultured on graphene and coverslips. The growth was evaluated by counting the number of cells at various time points using hemocytometer.

continually investigated the sheet resistance of the graphene on coverslip by a four-point probe method. The transferred graphene on coverslip show 500 Ω/□ sheet resistance with high uniformity.

We first evaluated the biocompatibility of graphene by comparing viability and proliferation of MSCs cultured on graphene and coverslips. MSCs were cultured in Dulbecco’s modified Eagle’s medium (DMEM) containing 10% (v/v) fetal bovine serum (FBS) and 1% (v/v) penicillin/streptomycin (PS). The viabilities of MSCs after culturing on graphene and coverslips were evaluated using live/dead staining with calcein-AM and ethidium homodimer. It stains live cells with green and dead cells with red, respectively. Fluorescence microscopy revealed that most of the cells were alive regardless of the substrate (Figure 2a). Figure 2b shows that there were no significant difference in the relative numbers of live cells at various time points when analyzed using cell counting kit-8 (CCK-8). CCK-8 was used instead of methylthiazolyldiphenyl-tetrazolium bromide (MTT) assay because MTT is spontaneously reduced by graphene, and therefore results in false positive signal.[15] However, it is very interesting to note that when we analyzed the gene expression at 3 weeks after cell seeding, Bcl-2, an anti-apoptotic gene, was upregulated on MSCs cultured on graphene compared MSCs cultured on coverslips, while caspase-3, a cysteine protease that is activated during programmed cell death, was decreased when cells were cultured on graphene as compared to cells cultured on coverslips (Figure 2c). Next, the proliferation of MSCs cultured on graphene was assessed by proliferating cell nuclear antigen (PCNA) staining and counting of the cells using hemocytometer. PCNA staining that stains proliferating cells demonstrated cell

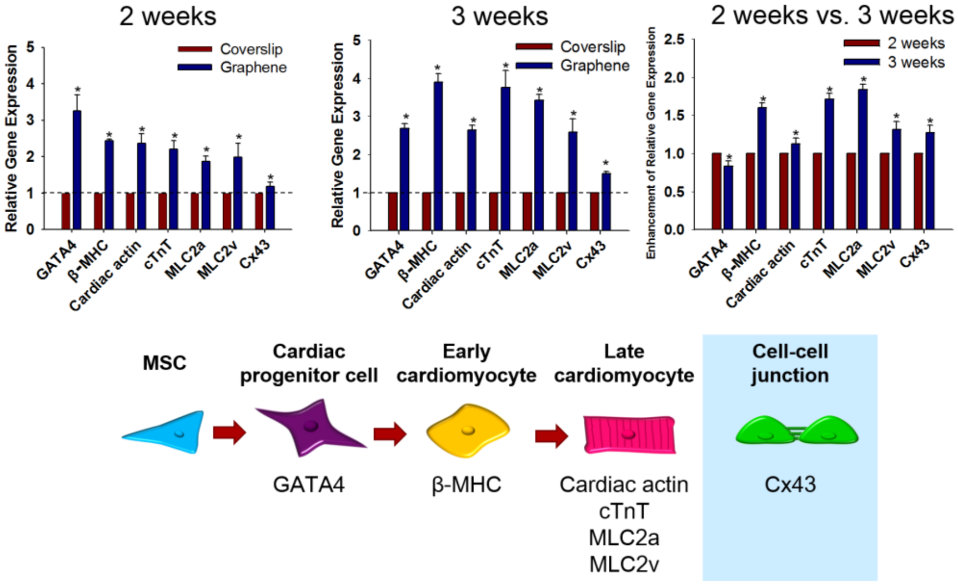

Figure 3 | Enhanced expression of cardiomyogenic genes in MSCs cultured on graphene without using chemical induction materials. Two and three weeks after cell seeding, the MSCs cultured on graphene exhibited an upregulation of the mRNA expression of an early cardiomyogenic transcriptional factor (GATA4), cardiomyogenic contractile proteins (cardiac actin, β-MHC, cTnT, MLC2a, and MLC2), and gap junction protein (Cx43) compared with MSCs cultured on coverslips. The mRNA expression levels were evaluated by qRT-PCR. *$p < 0.05$ compared to MSCs cultured on coverslips.

proliferation is similar regardless of the substrate (Figure 2d). Cell counting also showed that there was no significant difference in the number of cells cultured on graphene and coverslip at all time points (Figure 2e). The cell viability and proliferation assay indicated that graphene is biocompatible when single-layer is coated on coverslips for cell culture.

In a second set of experiments, we have examined cardiomyogenic specific markers at transcript level to determine the cardiomyogenic commitment of MSCs cultured on graphene in DMEM (10% FBS and 1% PS) at 2 and 3 week time points after cell seeding. Interestingly, all cardiomyogenesis-related markers have been enhanced in MSCs cultured on graphene compared to MSCs cultured on coverslip even in the absence of the induction media. Early cardiomyogenic transcriptional factor GATA4 was enhanced on MSCs cultured on graphene compared to the MSCs cultured on coverslip, indicating the enhanced early stage cardiomyogenesis by using graphene as cell culture substrate. Although the fold increase of GATA4 of MSCs cultured on graphene compared to the cells on coverslip has decreased slightly at week 3 compared to week 2, the presence of graphene was able to maintain more than 2-fold increase in GATA4 expression in MSCs compared to MSCs cultured on coverslips (Figure 3). In addition, the gene expressions of all cardiomyogenic contractile proteins, including cardiac actin, beta-type myosin heavy chain (β-MHC), cardiac troponin T (cTnT), ventricular myosin light chain-2 (MLC2v), and atrial myosin light chain 2 (MLC2a), were enhanced on graphene compared to coverslips at 2 weeks after cell seeding (Figure 3a). These genes have been further upregulated at week 3 in MSCs cultured on graphene compared to MSCs cultured on normal coverslips. Gene expression of gap junction protein, connexin 43 (Cx43), has also been enhanced by culturing MSCs on graphene, which may have been attributed to conductivity of graphene (Figure 3).[16] However, MSCs did not show functional and electrophysiological properties of mature cardiomyocytes regardless of the substrate.

Stem cell-ECM interactions may play key roles in cardiomyogenic differentiation of the stem cells. Thus, we next investigated whether MSC culture on graphene as compared to culture on coverslips affected on the expressions of cardiomyogenic differentiation-related ECM genes in the MSCs. Among various ECM proteins, we chose type I collagen (Col I), type III collagen (Col III), type IV collagen (Col IV), fibronectin, and laminin for analysis. Collagen, fibronectin, and laminin are the major components of cardiac ECM.[17] Embryonic stem cell-derived beating cardiomyocytes were reported to be surrounded in a network of fibronectin,

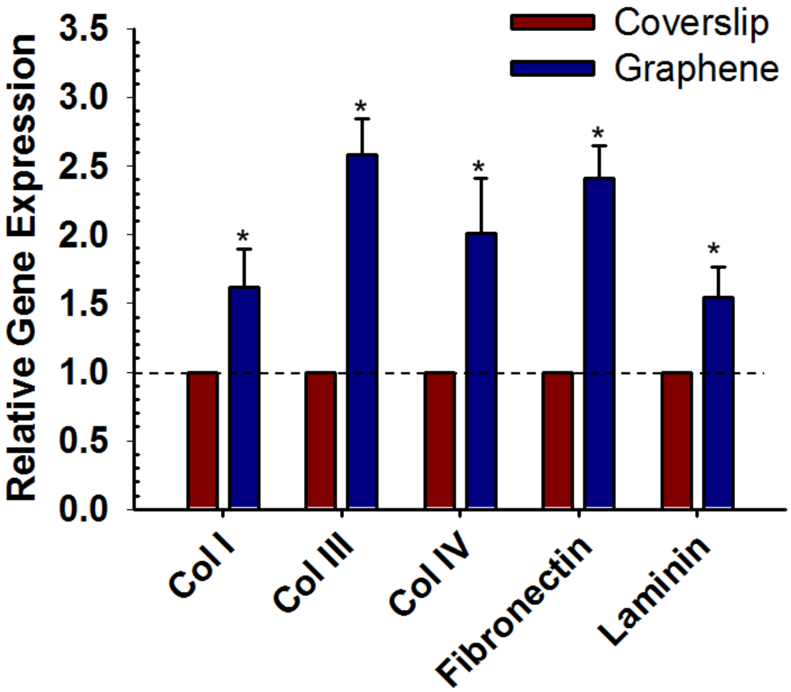

Figure 4 | Enhanced gene expression of ECM proteins in MSCs cultured on graphene. The MSCs cultured on graphene for 2 weeks exhibited an upregulation of the mRNA expression of Col I, Col III, Col IV, fibronectin, and laminin, which are known to promote the cardiomyogenic differentiation of stem cells compared with those on coverslips. The mRNA expression levels were evaluated by qRT-PCR. $^*p < 0.05$ compared to MSCs cultured on coverslips.

laminin, Col I and Col IV.[18] Col I and Col III, both of which are produced by cardiac stem cells and cardiac fibroblasts,[19] represent approximately 80% and 11% of total collagen in myocardium, respectively.[20] Collagen was essential for cardiomyogenic differentiation of mouse embryonic stem cells, as the use of collagen synthesis inhibitors inhibited cardiac differentiation.[25] A recent study also demonstrated that culture of embryonic stem cell-derived embryonic bodies on Col IV-coated surfaces enhanced cardiomyogenic differentiation synergistically with hypoxia, while culture on fibronectin-coated surfaces enhanced cardiomyogenic differentiation under normoxia.[21] Laminin was essential for development to cardiomyocytes capable of propagating electrical signals between neighboring cardiomyocytes.[27] As compared to MSC culture on coverslips, that on graphene upregulated the gene expressions of cardiomyogenic differentiation-related ECMs (i.e., Col I, Col III, Col IV, fibronectin, and laminin), as evaluated by quantitative reverse transcriptase polymerase chain reaction (qRT-PCR, Figure 4). The upregulation of the ECM gene expression may, at least in part, be responsible for the enhanced cardiomyogenic differentiation of MSCs cultured on graphene (Figure 3).

Cardiomyogenic differentiation of stem cells could be regulated through modulation of signal transduction. Therefore, we investigated how signal transduction of MSCs cultured on graphene is affected as compared to MSCs cultured on coverslips (Figure 5a). Among various cell signaling molecules, we first examined the effect of graphene on Focal adhesion kinase (FAK) expression (Figure 5b). FAK was upregulated in MSCs cultured on graphene. Next, we examined the expression of focal adhesion components, such as vinculin and paxillin, which are

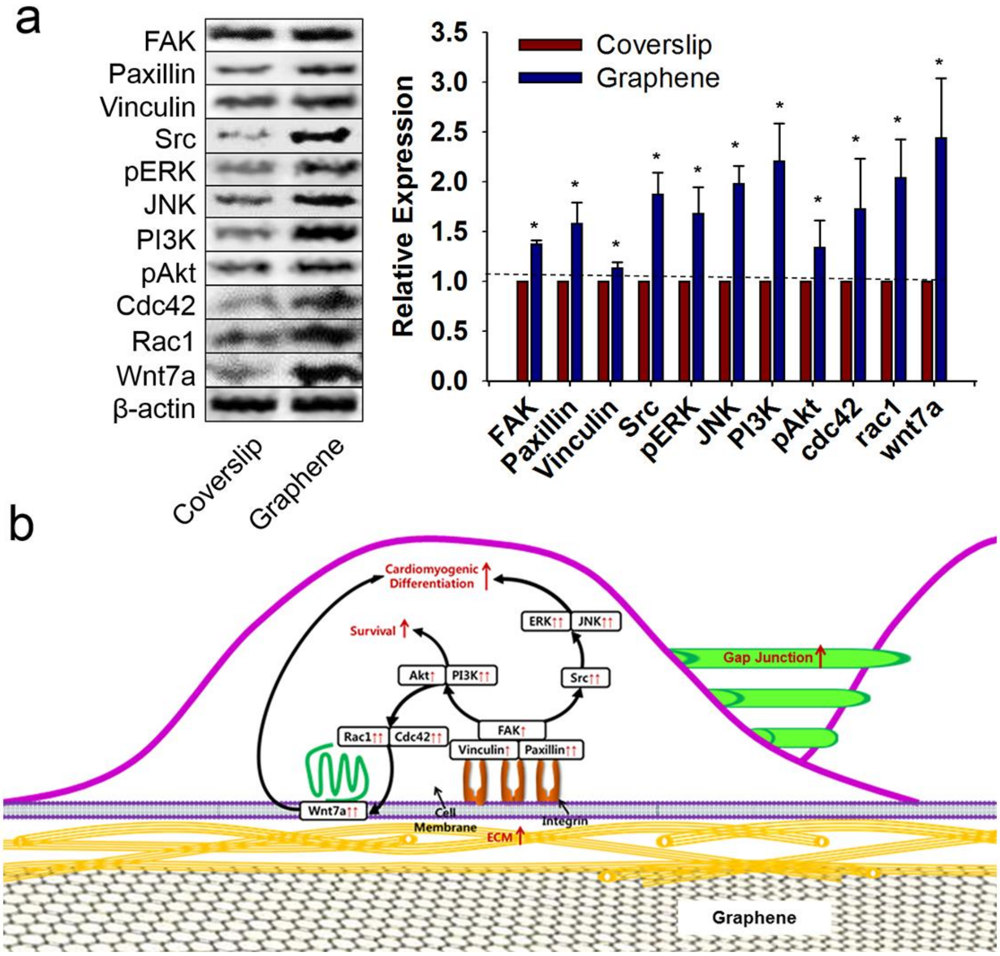

Figure 5 | Activation of molecules involved in cardiomyogenic differentiation and survival-related signal transduction pathways in MSCs cultured on graphene. a, Western blot analyses of MSCs cultured on graphene or coverslips for 3 weeks to analyze the molecules involved in the signal transduction pathways. Quantification of the relative protein expressions of the cell signaling molecules (n = 3). $*p < 0.05$ compared to MSCs cultured on coverslips. b, A schematic diagram of the signal transduction pathways associated with cardiomyogenic differentiation and survival. Arrows indicate expression upregulations.

recruited for the clustering of activated integrins, and the remodeling of actin cytoskeletons. Graphene enhanced the expression of both paxillin and vinculin (Figure 5b), which may occur due to the cell-substrate adhesiveness of graphene.[22,23]

FAK is activated by binding of integrins to ECM ligands when cell adhesion to the substrate occurs, and in turn, mediate a series of signaling events in cells. Integrins are transmembrane receptors that are engaged in the attachment between cells and surrounding cells and ECM. Activation of FAK mediates variety of adhesion-dependent biological processes including cell proliferation, migration, differentiation, and apoptosis.[24] Autophosphorylation of tyrosine 397 of FAK and allows FAK to bind Src[25] and phosphatidylinositol 3-kinase (PI3K),[26] which in turn mediates multiple signaling events that regulate stem cell survival and differentiation (Figure 5a).

Extracellular signal-regulated kinases (ERK) and c-Jun N-terminal kinases (JNK) were analyzed to examine whether cardiomyogenic gene expressions of MSCs could be affected by using graphene as the culture substrate. JNK and ERK are activated during cardiomyogenic differentiation.[27] Graphene has upregulated both ERK and JNK (Figure 5b). Both PI3K and Akt were upregulated in MSCs cultured on graphene compared to MSCs cultured on coverslips (Figure 5b). Upregulation of PI3K/Akt promotes cell survival, at least in part by regulating the downstream effectors, such as Bcl-2 family proteins.[28] The enhanced Bcl-2 gene expression of MSCs cultured on graphene compared to group cultured on coverslip (Figure 2b) may be, at least in part, due to the upregulation of PI3K/Akt (Figure 5b). In addition, activation of PI3K/Akt may have attributed to enhanced cardiomyogenic gene expressions of MSCs cultured on graphene as compared to coverslips, as it has been demonstrated in previous studies that the inhibition of PI3K suppresses cardiomyocyte differentiation[29], while upregulation of PI3K/Akt signaling pathway enhances cardiomyogenesis.[30,31]

In this study, Wnt7a, which have been demonstrated to be required for the myogenic differentiation of stem cells,[32] the development of cardiac conduction system,[33] and the modulation of cardiomyogenic versus chondrogenic cell fate decision,[34] was also highly expressed in MSCs cultured on graphene (Figure 5b). Wnt 7a has been shown to be upregulated when Cdc42 and Rac1 expressions are enhanced.[34] Cdc42 and Rac1 are proteins that are upregulated by the activation of PI3K/Akt, and promote the formation of actin polymerization.[35] Cdc42 and Rac1 are both upregulated in MSCs cultured on graphene (Figure 5b). Therefore, graphene may have upregulated cardiomyogenic gene expressions of MSCs through regulation of cell-substrate adhesion, but soluble signals may be needed to promote MSC differentiations to mature cardiomyocytes.

Conclusions

To summarize, we have demonstrated that for the first time the cardiomyogenic gene expression of MSCs can be upregulated by culturing MSCs on graphene. The viability and proliferation analyses of MSCs cultured on graphene compared to MSCs cultured on coverslips show that graphene is highly biocompatible and supportive when single-layer graphene is coated on coverslips. In addition, we confirmed that the ECM gene expressions of MSCs have been enhanced on graphene, resulting in the activation of cell signaling molecules in signal transduction pathways. The activated cell signaling transduction pathways and the ECM gene expressions possibly enhances cardiomyogenic gene expressions by culturing MSCs on graphene. Therefore, graphene has significant effects on the cell viability, proliferation, and cardiomyogenic gene expressions as well as extracellular matrix gene expressions of MSCs. Our results suggest that graphene is a promising scaffold for MSC adhesion and differentiation to be utilized for various therapeutic applications including cardiomyogenic regeneration.

References

[1]. Pittenger, M. F.; Mackay, A. M.; Beck, S. C.; Jaiswal, R. K.; Douglas, R.; Mosca, J. D.; Moorman, M. A.; Simonetti, D. W.; Craig, S.; Marshak, D. R. Multilineage Potential of Adult Human Mesenchymal Stem Cells. *Science* **1999,** *284*, 143-147.

[2]. Minguell, J. J.; Erices, A.; Conget, P. Mesenchymal Stem Cells. *Exp. Biol. Med.* **2001,** *226*, 507-520.

[3]. Devine, S. M. Mesenchymal Stem Cells: Will They Have a Role in the Clinic? *J. Cell. Biochem.* **2002**, 73-79.

[4]. Engler, A. J.; Sen, S.; Sweeney, H. L.; Discher, D. E. Matrix Elasticity Directs Stem Cell Lineage Specification. *Cell* **2006,** *126*, 677-689.

[5]. Dalby, M. J.; Gadegaard, N.; Tare, R.; Andar, A.; Riehle, M. O.; Herzyk, P.; Wilkinson, C. D. W.; Oreffo, R. O. C. The Control of Human Mesenchymal Cell Differentiation Using Nanoscale Symmetry and Disorder. *Nat. Mater.* **2007,** *6*, 997-1003.

[6]. Orza, A.; Soritau, O.; Olenic, L.; Diudea, M.; Florea, A.; Ciuca, D. R.; Mihu, C.; Casciano, D.; Biris, A. S. Electrically Conductive Gold-Coated Collagen Nanofibers for Placental-Derived Mesenchymal Stem Cells Enhanced Differentiation and Proliferation. *ACS Nano* **2011,** *5*, 4490-4503.

[7]. Curran, J. M.; Chen, R.; Hunt, J. A. The Guidance of Human Mesenchymal Stem Cell Differentiation in Vitro by Controlled Modifications to the Cell Substrate. *Biomaterials* **2006,** *27*, 4783-4793.

[8]. Park, S. Y.; Park, J.; Sim, S. H.; Sung, M. G.; Kim, K. S.; Hong, B. H.; Hong, S.

Enhanced Differentiation of Human Neural Stem Cells into Neurons on Graphene. *Adv. Mater.* **2011,** *23*, H263-+.

[9]. Wang, Y.; Lee, W. C.; Manga, K. K.; Ang, P. K.; Lu, J.; Liu, Y. P.; Lim, C. T.; Loh, K. P. Fluorinated Graphene for Promoting Neuro-Induction of Stem Cells. *Adv. Mater.* **2012,** *24*, 4285-+.

[10]. Kalbacova, M.; Broz, A.; Kong, J.; Kalbac, M. Graphene Substrates Promote Adherence of Human Osteoblasts and Mesenchymal Stromal Cells. *Carbon* **2010,** *48*, 4323-4329.

[11]. Nayak, T. R.; Andersen, H.; Makam, V. S.; Khaw, C.; Bae, S.; Xu, X. F.; Ee, P. L. R.; Ahn, J. H.; Hong, B. H.; Pastorin, G.*, et al.* Graphene for Controlled and Accelerated Osteogenic Differentiation of Human Mesenchymal Stem Cells. *ACS Nano* **2011,** *5,* 4670-4678.

[12]. Lee, W. C.; Lim, C. H.; Shi, H.; Tang, L. A.; Wang, Y.; Lim, C. T.; Loh, K. P. Origin of Enhanced Stem Cell Growth and Differentiation on Graphene and Graphene Oxide. *ACS Nano* **2011,** *5*, 7334-7341.

[13]. Kim, K. S.; Zhao, Y.; Jang, H.; Lee, S. Y.; Kim, J. M.; Ahn, J. H.; Kim, P.; Choi, J. Y.; Hong, B. H. Large-Scale Pattern Growth of Graphene Films for Stretchable Transparent Electrodes. *Nature* **2009,** *457*, 706-710.

[14]. Datta, S. S.; Strachan, D. R.; Khamis, S. M.; Johnson, A. T. C. Crystallographic Etching of Few-Layer Graphene. *Nano Lett.* **2008,** *8*, 1912-1915.

[15]. Liao, K. H.; Lin, Y. S.; Macosko, C. W.; Haynes, C. L. Cytotoxicity of Graphene Oxide and Graphene in Human Erythrocytes and Skin Fibroblasts. *ACS Appl. Mater. Interfaces* **2011,** *3,* 2607-2615.

[16]. You, J.-O.; Rafat, M.; Ye, G. J. C.; Auguste, D. T. Nanoengineering the Heart: Conductive Scaffolds Enhance Connexin 43 Expression. *Nano Lett.* **2011,** *11*, 3643-3648.

[17]. Moore, L.; Fan, D.; Basu, R.; Kandalam, V.; Kassiri, Z. Tissue Inhibitor of Metalloproteinases (Timps) in Heart Failure. *Heart Fail. Rev.* **2012,** *17*, 693-706.

[18]. van Laake, L. W.; van Donselaar, E. G.; Monshouwer-Kloots, J.; Schreurs, C.; Passier, R.; Humbel, B. M.; Doevendans, P. A.; Sonnenberg, A.; Verkleij, A. J.; Mummery, C. L. Extracellular Matrix Formation after Transplantation of Human Embryonic Stem Cell-Derived Cardiomyocytes. *Cellular and molecular life sciences : CMLS* **2010,** *67*, 277-90.

[19]. Kurazumi, H.; Kubo, M.; Ohshima, M.; Yamamoto, Y.; Takemoto, Y.; Suzuki, R.; Ikenaga, S.; Mikamo, A.; Udo, K.; Hamano, K., *et al.* The Effects of Mechanical Stress on the Growth, Differentiation, and Paracrine Factor Production of Cardiac Stem Cells. *PLoS One* **2011,** *6*, e28890.

[20]. Eghbali, M.; Weber, K. T. Collagen and the Myocardium: Fibrillar Structure, Biosynthesis and Degradation in Relation to Hypertrophy and Its Regression. *Mol. Cell. Biochem.* **1990,** *96*, 1-14.

[21]. Horton, R. E.; Auguste, D. T. Synergistic Effects of Hypoxia and Extracellular Matrix Cues in Cardiomyogenesis. *Biomaterials* **2012,** *33*, 6313-6319.

[22]. Bendori, R.; Salomon, D.; Geiger, B. Contact-Dependent Regulation of Vinculin Expression in Cultured Fibroblasts - a Study with Vinculin-Specific Cdna Probes. *EMBO J.* **1987,** *6*, 2897-2905.

[23]. Ungar, F.; Geiger, B.; Benzeev, A. Cell Contact-Dependent and Shape-

Dependent Regulation of Vinculin Synthesis in Cultured Fibroblasts. *Nature* **1986,** *319*, 787-791.

[24]. Hynes, R. O. Integrins - Versatility, Modulation, and Signaling in Cell-Adhesion. *Cell* **1992,** *69*, 11-25.

[25]. Schaller, M. D.; Hildebrand, J. D.; Shannon, J. D.; Fox, J. W.; Vines, R. R.; Parsons, J. T. Autophosphorylation of the Focal Adhesion Kinase, Pp125fak, Directs Sh2-Dependent Binding of Pp60src. *Mol. Cell. Biol.* **1994,** *14*, 1680-1688.

[26]. Chen, H. C.; Appeddu, P. A.; Isoda, H.; Guan, J. L. Phosphorylation of Tyrosine 397 in Focal Adhesion Kinase Is Required for Binding Phosphatidylinositol 3-Kinase. *J. Biol. Chem.* **1996,** *271*, 26329-26334.

[27]. Eriksson, M.; Leppa, S. Mitogen-Activated Protein Kinases and Activator Protein 1 Are Required for Proliferation and Cardiomyocyte Differentiation of P19 Embryonal Carcinoma Cells. *J. Biol. Chem.* **2002,** *277*, 15992-16001.

[28]. Cantley, L. C. The Phosphoinositide 3-Kinase Pathway. *Science* **2002,** *296*, 1655-1657.

[29]. Naito, A. T.; Tominaga, A.; Oyamada, M.; Oyamada, Y.; Shiraishi, I.; Monzen, K.; Komuro, I.; Takamatsu, T. Early Stage-Specific Inhibitions of Cardiomyocyte Differentiation and Expression of Csx/Nkx-2.5 and Gata-4 by Phosphatidylinositol 3-Kinase Inhibitor Ly294002. *Exp. Cell Res.* **2003,** *291*, 56-69.

[30]. Naito, A. T.; Akazawa, H.; Takano, H.; Minamino, T.; Nagai, T.; Aburatani, H.; Komuro, I. Phosphatidylinositol 3-Kinase–Akt Pathway Plays a Critical Role in Early Cardiomyogenesis by Regulating Canonical Wnt Signaling. *Circ. Res.* **2005,** *97*, 144-151.

[31]. Heo, J. S.; Lee, J. C. Beta-Catenin Mediates Cyclic Strain-Stimulated Cardiomyogenesis in Mouse Embryonic Stem Cells through Ros-Dependent and Integrin-Mediated Pi3k/Akt Pathways. *J. Cell. Biochem.* **2011,** *112*, 1880-1889.

[32]. Polesskaya, A.; Seale, P.; Rudnicki, M. A. Wnt Signaling Induces the Myogenic Specification of Resident Cd45+ Adult Stem Cells During Muscle Regeneration. *Cell* **2003,** *113*, 841-852.

[33]. Bond, J.; Sedmera, D.; Jourdan, J.; Zhang, Y. H.; Eisenberg, C. A.; Eisenberg, L. M.; Gourdie, R. G. Wnt11 and Wnt7a Are up-Regulated in Association with Differentiation of Cardiac Conduction Cells in Vitro and in Vivo. *Dev. Dyn.* **2003,** *227*, 536-543.

[34]. Kim, M.-H.; Kino-oka, M.; Maruyama, N.; Saito, A.; Sawa, Y.; Taya, M. Cardiomyogenic Induction of Human Mesenchymal Stem Cells by Altered Rho Family Gtpase Expression on Dendrimer-Immobilized Surface with D-Glucose Display. *Biomaterials* **2010,** *31*, 7666-7677.

[35]. Auer, M.; Hausott, B.; Klimaschewski, L. Rho Gtpases as Regulators of Morphological Neuroplasticity. *Ann. Anat.* **2011,** *193*, 259-266.

[36]. Bae, S.; Kim, H.; Lee, Y.; Xu, X. F.; Park, J. S.; Zheng, Y.; Balakrishnan, J.; Lei, T.; Kim, H. R.; Song, Y. I., *et al.* Roll-to-Roll Production of 30-Inch Graphene Films for Transparent Electrodes. *Nat. Nanotechnol.* **2010,** *5*, 574-578.

Part I I

Engineering nature-driven three-dimensional bioscaffolds with functional nanomaterials

Chapter 5

Binding behavior of hybrid system for the APCLP coated-carbon nanotube and graphene with bacterial cellulose

Introduction

Natural materials can be extremely complex, the key structural motifs that lead to their extraordinary properties typically span multiple length scales, and it is often not clear which of them are critical to achieve certain properties. Bacterial cellulose, for example, are remarkably robust because a specific combination of 2 dimensional network and 3 dimensional layer by layer structure results in the excellent properties, but at present it is challenging to fabricate new materials with such key structural advantages across so many length scales.

Today it is possible to routinely synthesize nanoscale building blocks with many excellent material properties, such as carbon nanotubes or graphene sheets which have unique electrical conductivity, chemical structure, and mechanical resilience. However, support structure is required to utilize carbon nanomaterials for various applications. It seems natural therefore; the two building blocks in the new nanocomposite are both exciting materials in their own properties.

In previous methods, carbon nanomaterials are simply mixed with polymer solution or coated on polymer matrices. However, disordered carbon nanomaterials arrays, and inhomogeneous structure were generated by these methods. In addition, high dispersity and strong attachment of carbon nanomaterials on polymer matrices are still unsolved problems that still need to be solved. For the first time, we propose a method to utilize a living organism for the production of uniform and stable integration carbon nanomaterials into three-dimensional highly porous matrices composed of nano-fibrils. In order for stable CNT colloidal suspension, we have modified CNTs with water soluble amphiphilic comb-like polymer. APCLP is composed of a long hydrophobic (methyl methacrylate, MMA) backbone, short hydrophilic (hydroxyl-poly (oxyethylene) methacrylate (HPOEM)), and (poly (ethylene glycol) methacrylate (POEM)) side chains. APCLP-modified carbon nanomaterials were able to maintain stable colloidal solution. We hypothesize that the hydrophobic backbone of APCLP would be adsorbed on hydrophobic carbon nanomaterials surface by hydrophobic interaction, whereas the hydrophilic side chains that face outwards would provide an environment where hydrophilic BC nano-fibrils can adhere and grow, thereby acting as a glue between carbon nanomaterials and BC nano-fibrils (Fig. 1b). This was also demonstrated by the simulation.

Experimental

Computational methods for CNT-BC-Syn

To explain binding mechanism among CNT, polymer and cellulose, we have performed the density functional theory (DFT) calculation within generalized gradient approximation (GGA) using the Vienna ab initio simulation package (VASP). [1-3] The projector augmented wave (PAW) potentials, as implemented in the VASP, were employed to describe the potentials from atom centers. The energy cutoff for the plane-wave basis was set to 400 eV in GGA. Geometries were optimized until the Hellman-Feynman forces acting on the atoms became smaller than 0.03 eV/Å. For investigation of binding mechanism, amphiphilic comb-like polymers (MMA and HPOEM) is considered between cellulose and CNT. To include weak van der Waals (vdW) interactions among them, we adopt the Grimme's DFT-D2 vdW correction based on a semi-empirical GGA-type theory.[4] For the Brillouin-zone interaction we used a 5×1×1 grid in Monkhorst-Pack special k-point scheme. In order to explain the behaviors of GO hybrids for large-scale dynamic system, we also have performed molecular dynamics (MD) simulation for GO hybrids structures at room temperature (300 K). We performed NVT-MD simulations using the Large-scale Atomic/Molecular Massively Parallel Simulator (LAMMPS) with a reactive force field (ReaxFF) potential[5] for 12.5 ps.

Computational methods for GO-Syn-BC-Syn

Our density functional theory (DFT) calculations use generalized gradient approximation (GGA) in the Vienna ab initio simulation package (VASP). [1-3] The kinetic energy cut-off is set to 400 eV. For the van der Waals (vdW) correction, we employ Grimme's DFT-D2 method, based on a semi-empirical GGA-type theory.[4] All atomic coordinates are fully relaxed until the Hellmann-Feynman forces are less than 0.025 eV/Å . For the Brillouin-zone integration, we use 3x3x1 and 3x1x1 for GO hybrids with BC and APCLP, respectively. In order to explain the binding behaviors of (r)GO hybrids for large-scale dynamic system, we also have performed molecular dynamics (MD) simulation for (r)GO hybrid structures at room temperature (300 K). For NVT-MD simulations, we use the Large-scale Atomic/Molecular Massively Parallel Simulator (LAMMPS) with a reactive force field (ReaxFF) potential[5]

Results and discussion

Before explaining about the binding mechanism for these hybrid systems, we have focused the dispersion of CNTs. The dispersion of CNTs have been given a considerable attention in producing CNT and polymer composites for CNT applications. However, it is difficult to disperse the CNTs in solution due to the entanglement of CNT bundles. Now, we have considered the CNT dispersion using APCLP. Figure 1 shows the dispersion behavior of CNT with APCLP. Three different configurations of CNTs are selected for the dispersion behavior in MD calculations. After doing ultra-sonication for the CNT in solutions, the CNTs are separated small size of bundles or each other as shown in figure 2. The inter-CNT distance is about (a) 3.3, (b) 10.0, and (c) 30.0 Å, respectively. The short distance between CNTs such as small size bundles do not have enough space to insert the APCLPs to them. Thus, the APCLPs are wrapping the small size CNT bundle as shown in figure 2 (a). On the other hand, the APCLPs infiltrate into the large separation of CNTs then the CNTs are well dispersed as shown in figure 2 (b) and (c). The dispersion ability of CNTs with APCLPs are good for the biomedical applications.

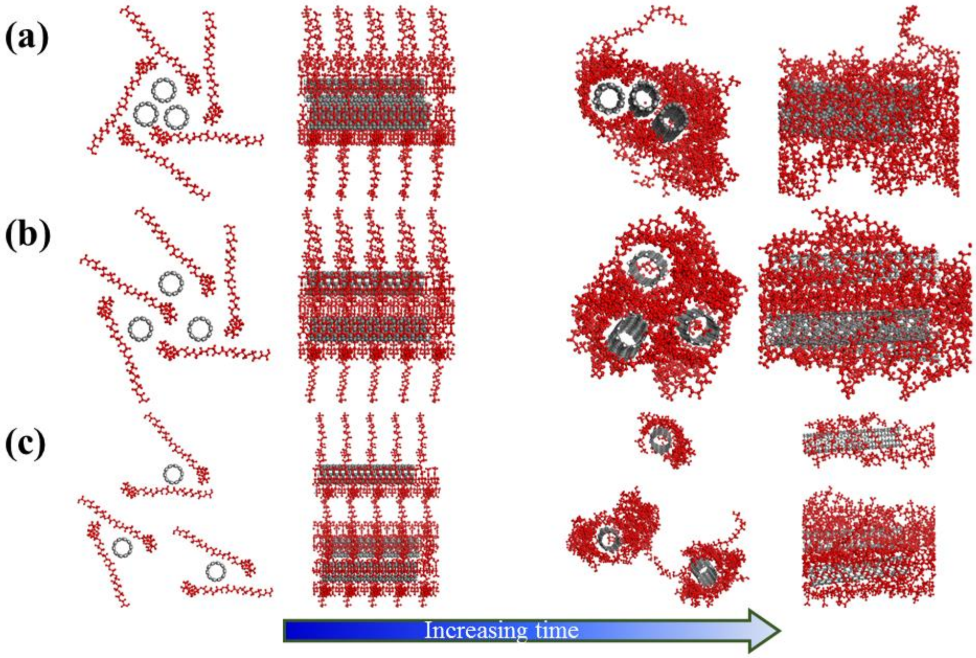

Figure 1 | Dispersion behavior of CNT

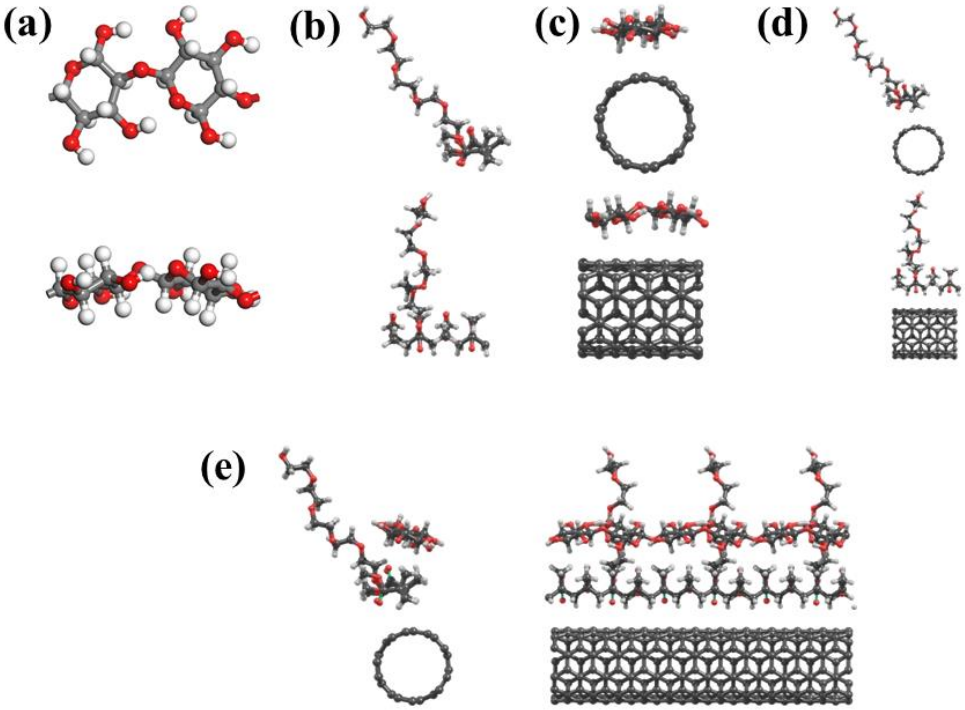

Figure 2 | Optimized geometries

First, we have performed the density functional theory calculations to find the geometries optimized for the bacterial cellulose and amphiphilic comb-like polymer. Figure 2 (a) and (b) show the optimized geometries of BC and APCLP, respectively. The component ratio of MMA (backbone), HPOEM (chain), and POEM (chain) is 6:2:2, respectively, in the hydrophobic backbone of APCLP. For our calculations, APCLP is approximated to only HPOEM connected to MMA because the structure of POEM is very similar to that of HPOEM except for the terminal part. We investigate the binding strength of hybridized cellulose-cellulose, cellulose-polymer, cellulose-CNT, polymer-CNT, and cellulose-polymer/CNT configurations. Here, the binding energies are defined as $E_b = -[E_{total}-E_{constituent1}-E_{constituent2}]$, where E_{total}, $E_{constituent1}$, and $E_{constituent2}$ are total energies of total combined system (e.g., cellulose-CNT), constituent 1 (cellulose), and constituent 2 (CNT), respectively. It is found that the binding energies are 0.68, 0.68, -0.05, and 0.03 eV (per given unit) for cellulose-cellulose, cellulose-polymer, cellulose-CNT, and polymer-CNT systems, respectively, which means that CNT does not interact with cellulose or polymer.

Figure 2(e) shows the optimized geometries of hybrid cellulose-polymer/CNT structure obtained by DFT calculations. The nearest interatomic distances between cellulose and HPOEM (or HPOEM and CNT) are 2.22 (or 2.78 Å) and the binding energy between cellulose and polymer/CNT is 0.71 eV. The polymer and cellulose are weakly combined with CNTs. From these results, the interfacial interaction between polymer (APCLP) and CNT and between cellulose and polymer/CNT is found to be a weak one. Overall, our ab initio calculations show that APCLP does not combine well with CNT contrary to our expectation.

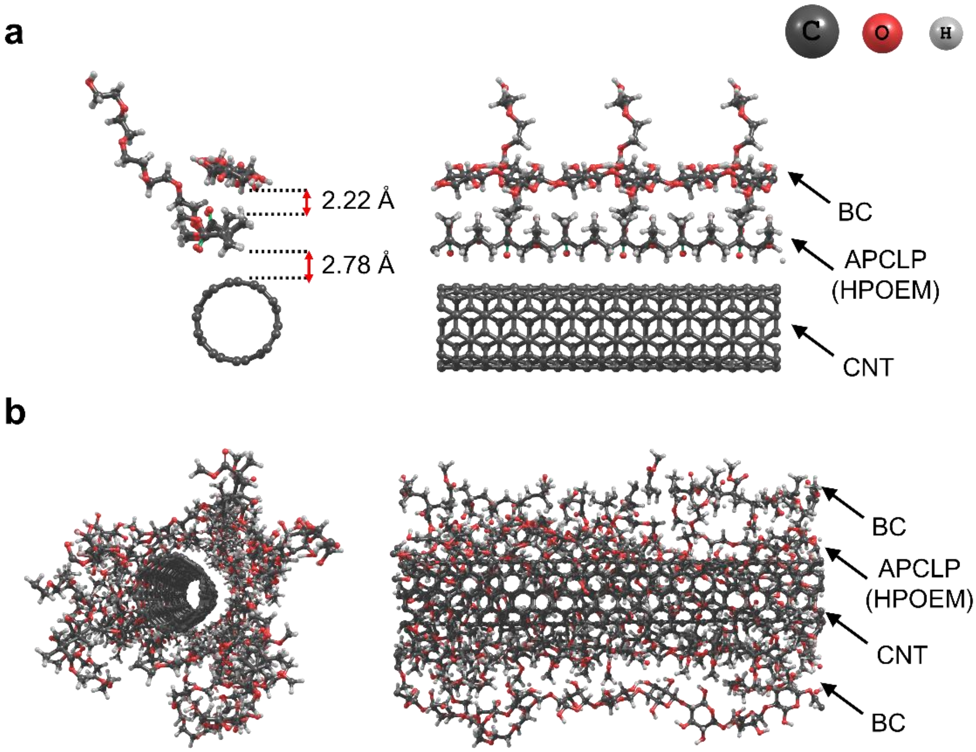

Figure 3 | Front and side views of (a) the geometry optimized by DFT calculations and (b) that obtained from molecular dynamics simulations for the cellulose-polymer (HPOEM)/CNT system

To clearly understand binding behaviors between BC and CNTs mediated by APCLPs, we have performed density functional theory (DFT) calculations and molecular dynamics (MD) simulations..

First, we investigate the binding strength of hybridized cellulose-cellulose, cellulose-polymer, cellulose-CNT, polymer-CNT, and cellulose-polymer/CNT configurations. Here, the binding energies are defined as $E_b = -[E_{total}-E_{constituent1}-E_{constituent2}]$, where E_{total}, $E_{constituent1}$, and $E_{constituent2}$ are total energies of total combined system (e.g., cellulose-CNT), constituent 1 (cellulose), and constituent 2 (CNT), respectively. It is found that the binding energies are 0.68, 0.68, -0.05, and 0.03 eV (per given unit) for cellulose-cellulose, cellulose-polymer, cellulose-CNT, and polymer-CNT systems, respectively, which means that CNT does not interact with cellulose or polymer. Figure 3(a) shows the optimized geometries of hybrid cellulose-polymer/CNT structure obtained by DFT calculations. The nearest interatomic distances between cellulose and HPOEM (or HPOEM and CNT) are 2.22 (or 2.78 Å) and the binding energy between cellulose and polymer/CNT is 0.71 eV. The polymer and cellulose are weakly combined with CNTs. From these results, the interfacial interaction between polymer (APCLP) and CNT and between cellulose and polymer/CNT is found to be a weak one. Overall, our ab initio calculations show that APCLP does not combine well with CNT contrary to our expectation.

In this regard, we have performed the molecular dynamics (MD) calculations to investigate binding mechanism of cellulose with cellulose itself, CNT, or polymer/CNT and further to understand their dynamical combining processes. Since

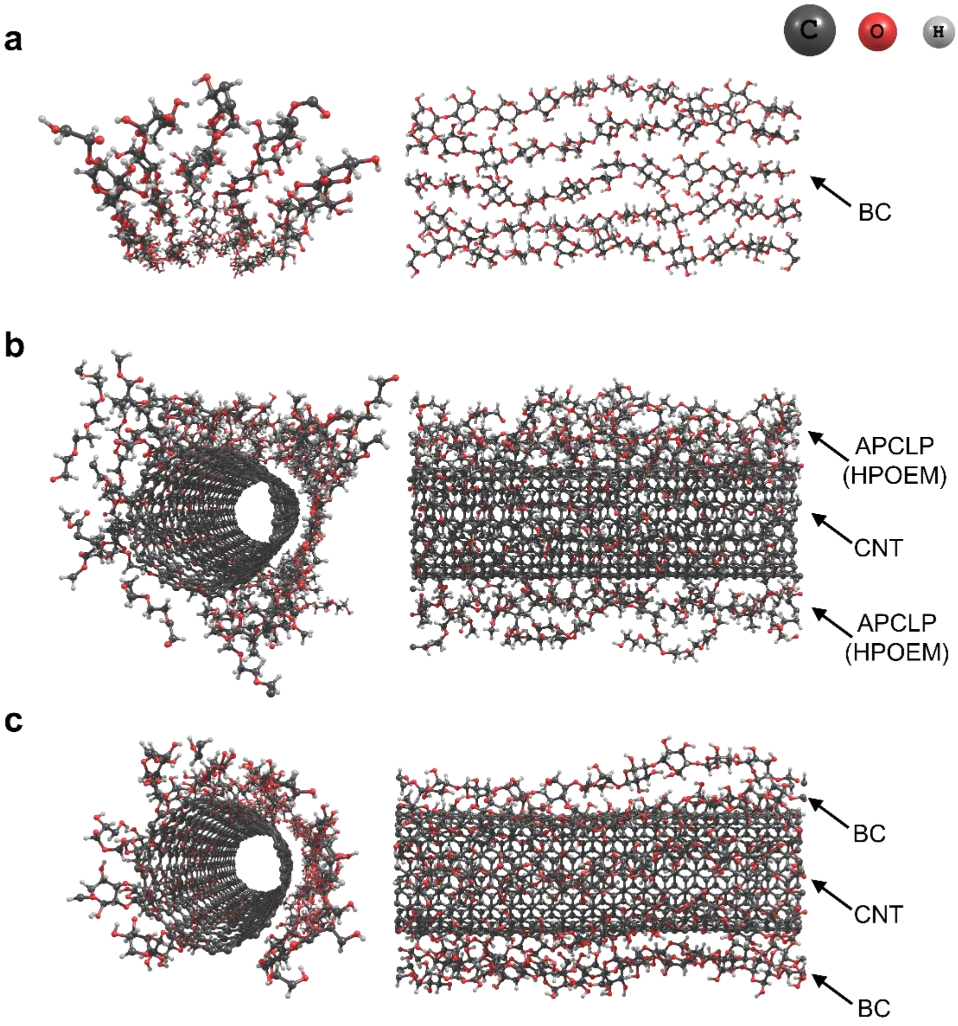

Figure 4 | Front and side views of geometries obtained from the molecular dynamics simulations for (a) cellulose-cellulose, (b) polymer(HPOEM)-CNT hybrid, and (c) cellulose-CNT systems cellulose is found to be formed into a comb-like structure when spurted out from G. xylinus bacteria, the binding behavior between cellulose is first considered. Cellulose looks like being self-assembled in our calculations, forming comb-like structures, as shown in Figure 4 (a). Note that the HPOEM or POEM is a chain-like structure as shown in Figure 3 (a). Thus, the CNTs are wrapped by the HPOEM of APCLP during the dispersion of CNTs, as shown in Figure 4(b) in calculations. It seems that the CNTs are structurally covered up with the HPOEM of APCLPs as a hook; that is, they are expected to mechanically bind each other. We simulate the CNTs surrounded by the HPOEM with cellulose. As a result, the celluloses are combined with the APCLP-covered CNT surface, as shown in Figure 3 (b). We finally consider the cellulose-CNT hybrids without APCLP to investigate the effect of APCLP on binding between cellulose and CNT. After the cellulose is assembled each other, the assembled cellulose is placed on the CNT as shown in Figure 3 (c), in comparison with the hybrid cellulose-polymer/CNT system. Figure 5 shows the obtained geometries for the time scale by 0.0 ps – 4.0 ps – 12.5 ps, for left, middle, and right panel, respectively. Our MD simulation results well explain the hybrid structures consisting of cellulose, APCLP and CNT, observed in experiment. Based on our results, we suggest that APCLP is a good medium to help binding between cellulose and CNT.

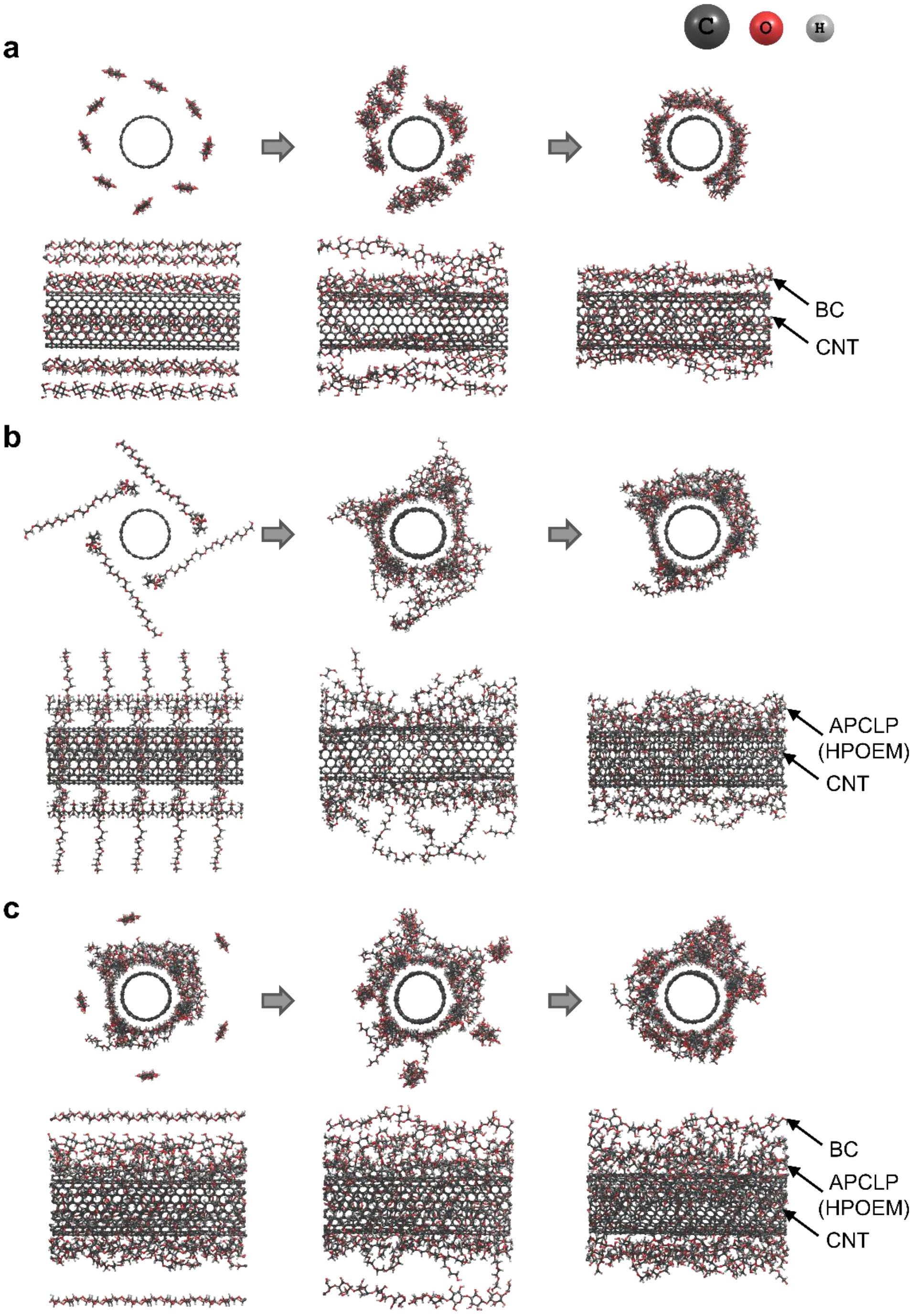

Figure 5 | Front and side views of geometries obtained from the molecular dynamics simulations for (a) cellulose-CNT, (b) polymer(HPOEM)-CNT, and (c) cellulose-polymer(HPOEM)/CNT systems for the time scale (0.0 ps - 4.0 ps - 12.5 ps)

We have performed DFT calculations for graphene oxide (GO) and reduced graphene oxide (rGO) hybrids with bacterial cellulose (BC) and amphiphilic comb-like polymer (APCLP). Table 1 shows the binding energies Eb and interatomic distance d between (r)GO and several adsorbates (APCLP, BC, or APCLP+BC). Binding energies are defined by following equation for each (r)GO hybrid.

$$E_b = -[\,E_{total} - \,E_{(r)GO} - E_{adsorbate}\,]$$

Here, E_{total}, $E_{(r)GO}$, and $E_{adsorbate}$ are total energies of the (r)GO hybrid system, (r)GO, adsorbate, respectively. Our calculation results represent weak interaction between (r)GO and adsorbates with small binding energies. However, GO interact more strongly with all adsorbates than rGO, representing the small interatomic distance as shown in Table 1.

We have performed DFT calculations for graphene oxide (GO) and reduced graphene oxide (rGO) hybrids with bacterial cellulose (BC) and amphiphilic comb-like polymer (APCLP). Table 1 shows the binding energies E_b and interatomic distance d between (r)GO and several adsorbates (APCLP, BC, or APCLP+BC). Binding energies are defined by following equation for each (r)GO hybrid.

$$E_b = -[\,E_{total} - \,E_{(r)GO} - E_{adsorbate}\,]$$

Here, E_{total}, $E_{(r)GO}$, and $E_{adsorbate}$ are total energies of the (r)GO hybrid system, (r)GO, adsorbate, respectively. Our calculation results represent weak interaction between (r)GO and adsorbates with small binding energies. However, GO interact more strongly with all adsorbates than rGO, representing the small interatomic distance as shown in Table 1.

Table 1. Binding energies E_b and interatomic distance d between GO(rGO) and adsorbates

	GO(rGO)-BC	GO(rGO)-APCLP	APCLP-coated GO(rGO)-BC
E_b (eV)	0.69 (0.83)	0.77 (0.93)	1.61 (1.64)
d (Å)	2.09 (2.42)	2.10 (2.60)	2.05 (2.60)

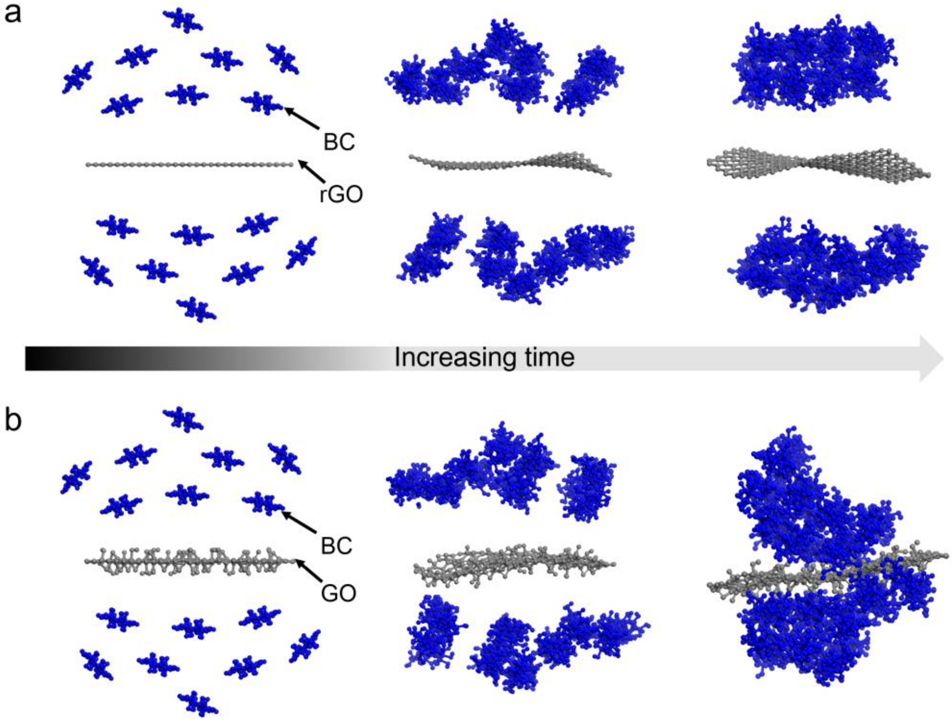

Figure 6 | Molecular dynamic simulations for (a) rGO-BC and (b) GO-BC

First, we have performed the MD simulations for the (r)GO hybrids with BC as shown in Figure 6(a) and (b). Our simulations show that BCs prefer to move toward the GO than rGO in the same time. These behaviors explain that functional groups of GO such as O or –OH play an essential role in interaction between GO and BC, implying a weaker interaction between BC and rGO than GO due to elimination of some functional groups in GO.

Second, MD simulation is done for the (r)GO hybrids with APCLP, as shown in Figure 8. Our results show that both GO and rGO are covered up with APCLP layers, representing the different behaviors to each other. APCLPs prefer to move towards another APCLP than rGO due to more strong interaction with APCLP than rGO. As a result, APCLP are evenly well adsorbed on rGO as shown in Figure 7(a). However, APCLP moves directly toward GO than another APCLP. This binding behavior implies that the functional groups of GO interacts more strongly with APCLP. Therefore, it seems that APCLP are randomly adsorbed on GO than rGO as shown in Figure 7(b).

Finally, we perform MD simulation for the (r)GO hybrid with APCLP+BC by considering adsorption of BC on the (r)GO hybrid structure shown in Figure 8(a) and (b). Our calculations show that BCs move towards APCLP and become seated on APCLP covering (r)GO as shown in Figure 8(a) and (b). (r)GO hybrid with APCLP interacts well with BC due to the presence of APCLP which mediates binding between (r)GO and BC. As shown in Figure 8(a), BC is evenly well adsorbed on APCLP-coated rGO, because APCLP is already evenly well dispersed on rGO in Figure 7(a). However, BCs seem that randomly adsorbed on APCLP-coated GO in

Figure 8(b), because they are adsorbed on APCLPs which are already randomly adsorbed on GO in Figure 7(b). These behaviors are well matched with experimental results, representing adsorption of BC on the (r)GO hybrid with APCLP.

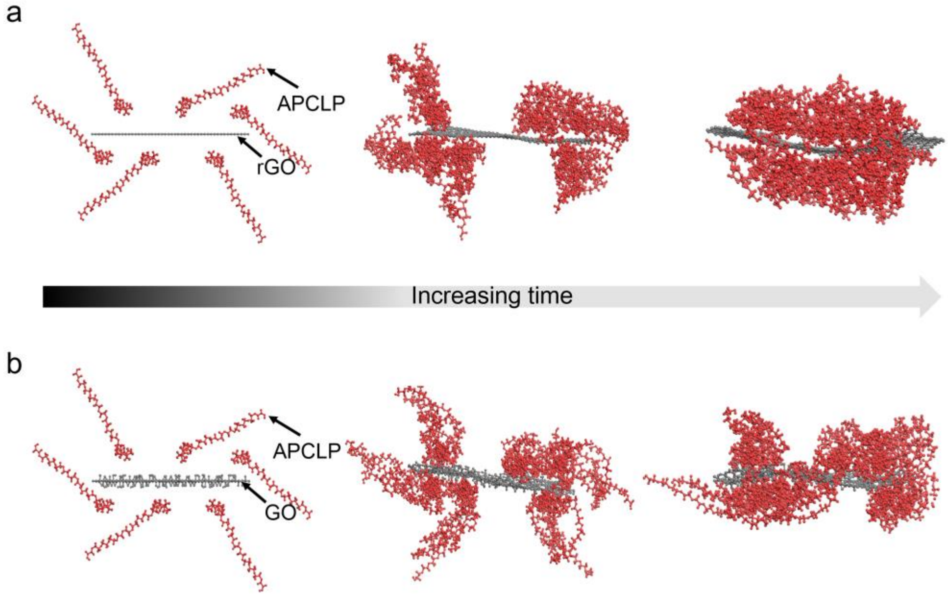

Figure 7 | Molecular dynamic simulations for a, rGO-APCLP and b, GO-APCLP

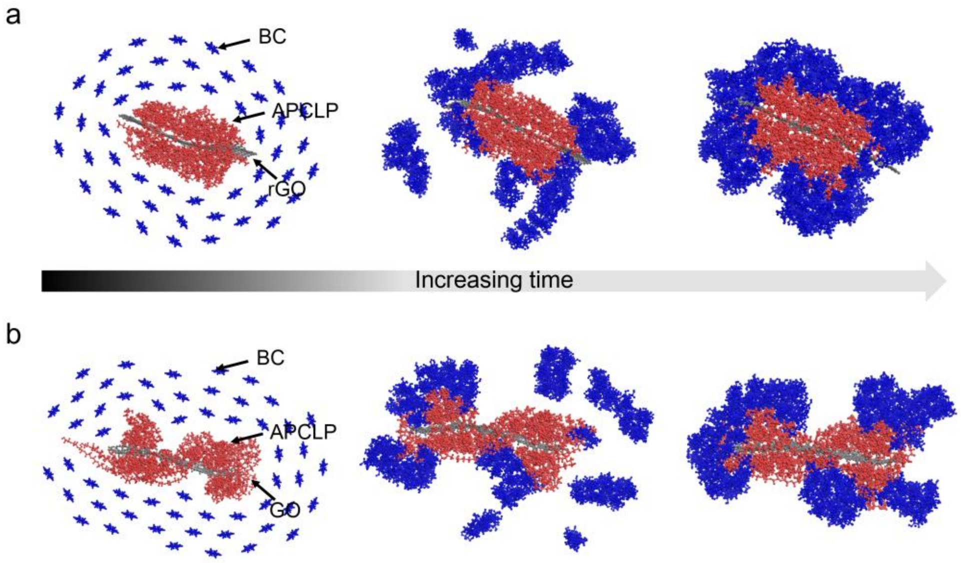

Figure 8 | Molecular dynamic simulations for APCLP-coated a, rGO-BC and b, GO-BC

Conclusions

In this study, an important method was introduced for the development 3D biofunctional scaffolds through hybridization with carbon nanomaterials for biomedical applications. BC was chosen as the 3D scaffold material for the hybridization of carbon nanomaterials due to its ideal structure for tissue engineering scaffolds. APCLP was utilized to promote colloidal stability of carbon nanomaterials and induce the hybridization between carbon nanomaterials and BC, which enabled homogeneous and effective.

References

[1]. Kresse, G.; Furthmuller, Efficient iterative schemes for ab initio total-energy calculations using a plane-wave basis set. *J. Phys. Rev. B* **1996**, 54 (16), 11169–11186.

[2]. Kresse, G.; Furthmuller, Efficient iterative schemes for ab initio total-energy calculations using a plane-wave basis set. *J. Comput. Mater. Sci*. **1996**, 6 (1), 15–50.

[3]. Perdew J P, Burke K and Ernzerhof M, Generalized Gradient Approximation Made Simple. Phys. Rev. Lett., **1996,** 77, 3865.

[4]. Grimme, S. Semiempirical GGA-type density functional constructed with a long-range dispersion correction. *J. Comput. Chem.* **2006**, *27*, 1787-1799.

[5] A. Strachan, A. C. T. van Duin, D. Chakraborty, S. Dasgupta, and W. A. Goddard III, Shock waves in high-energy materials: the initial chemical events in nitramine RDX, *Phys. Rev. Lett.* **2003**, 91, 098301.

Chapter 6

In situ hybridization of carbon nanotubes with bacterial cellulose for three-dimensional bioscaffods

Introduction

Microorganisms in nature are capable of forming remarkable structures with unique characteristics that are difficult to mimic artificially. *Gluconacetobacter xylinus* (*G. xylinus*), for example, can easily synthesize a large amount of bacterial cellulose (BC) composed of nanofiber networks stacked into layer-by-layer hierarchical structures. BC consists of many structural aspects favourable for bone grafting, including large pores, and nano-scale fibers in three-dimensional (3D) structure.[1-3] These requirements were difficult to achieve simultaneously using polymers or hydrogels because of the current technical limitations.[4]

Carbon nanotubes (CNTs) have gained great popularity for the use in bone regeneration. It is known that CNTs can promote osteogenesis of mesenchymal stem cells,[5] as well as osteoblast functioning,[6] and bone calcification.[7] However, despite the enormous efforts made in utilizing CNTs for *in vivo* bone regeneration, further advancements have been hampered by the technical limitations for the fabrication of 3D porous scaffolds using CNT framework. A 3D porous structure is an indispensable component of tissue engineering scaffolds for the provision of sufficient surface and space for cell adhesion, migration, growth, and tissue formation.[8,9] Although the method for fabricating 3D CNT-based scaffolds by soaking bioscaffolds in a CNT-containing solution has been reported, the resulting scaffolds showed an inhomogeneous distribution of CNTs.[10]

In this study, we developed a new method to fabricate CNT-based 3D scaffold that is composed of nanoscale fiber framework and large pores. Amphiphilic comb-like polymer (APCLP) was used to facilitate colloidal stability of CNTs in medium and to induce the hybridization of CNTs and BC. When *G. xylinus* was cultured in a culture medium containing APCLP-coated CNTs, the BC nanofibrils synthesized by *G. xylinus* wrap around APCLP-coated CNTs, resulting in a stable hybridization between CNTs and BC. As collodally stable CNTs are hybridized *in situ* into the newly forming BC nanofibers, which form the framework of the final scaffold, CNTs are homogeneously distributed throughout the scaffold.

The resulting scaffold showed a combination of the advantages of BC and CNTs for bone regeneration. The structure of the CNT-BC hybrid scaffold resembles the architecture of BC with larger pores. 3D architecture that is composed of nanofibers and large pores resulted in high osteoconductivity of the scaffold. In addition, the CNT-based framework caused high osteoinductivity, which is not achievable solely by BC. Therefore, with high osteoconductivity and osteoinductivity, the CNT-BC hybrid showed high bone regeneration efficacy *in vivo*

Experimental

Preparation of amphiphilic comb-like polymer (APCLP)

APCLP was synthesized by free radical polymerization of MMA (Aldrich), poly(ethylene glycol) methacrylate (Aldrich, Mn 360 g/mol, corresponding to n = 6) and poly(ethylene glycol) methyl ether methacrylate (Aldrich, Mn 475 g/mol, corresponding to n = 9), in tetrahydrofuran for 18 h. The CNTs (purity >95%, lljin Nanotech Co., Korea) produced by the chemical vapor deposition method were used without further purification or treatment. The CNTs were determined to have an outer diameter of about 10–20 nm and a length of 150–200 μm. A total of 1 mg of CNT was added to 10 mL of APCLP solution (30% ethanol, 0.001% APCLP), after which the samples were sonicated using a horn-type ultrasonic generator (Fisher Scientific Co., USA) with a frequency of 23 kHz and a power of 30 W for 20 min at room temperature**.**

G.xylinus culture

G. xylinus (KCCM 40216) was obtained from the Korean Culture Center of Microorganisms. The bacterium was cultured on medium composed of 2.5% (w/w) mannitol, 0.5% (w/w) yeast extract and 0.3% (w/w) bacto-peptone. The culture media were sterilized in an autoclave at 120 ◦C for 20 min and then poured into 500 mL flasks. The pre-inoculum for all experiments was prepared by transferring a single G. xylinus colony grown on agar culture medium into a 100 mL Erlenmeyer flask filled with mannitol culture medium. The optimal culture conditions were determined empirically (Figure S1).

Computational methods

To explain binding mechanism among CNT, polymer and cellulose, we have performed the density functional theory (DFT) calculation within generalized gradient approximation (GGA) using the Vienna ab initio simulation package (VASP).[1-3] The projector augmented wave (PAW) potentials, as implemented in the VASP, were employed to describe the potentials from atom centers. The energy cutoff for the plane-wave basis was set to 400 eV in GGA. Geometries were optimized until the Hellman-Feynman forces acting on the atoms became smaller than 0.03 eV/Å. For investigation of binding mechanism, amphiphilic comb-like polymers (MMA and HPOEM) is considered between cellulose and CNT. To include weak van der Waals (vdW) interactions among them, we adopt the Grimme's DFT-D2 vdW correction based on a semi-empirical GGA-type theory.[4] For the Brillouin-zone interaction we used a 3×1×1 grid in Monkhorst-Pack special k-point scheme. In order to explain the behaviors of CNT-BC hybrids for large-scale dynamic system, we also have performed molecular dynamics (MD) simulation for CNT hybrids structures at room temperature (300 K). We performed NVT-MD simulations using the Large-scale Atomic/Molecular Massively Parallel Simulator (LAMMPS) with a reactive force field (ReaxFF) potential for 12.5 ps.[5]

Preparation of CNT-BC

The pre-cultured culture cell suspension was introduced into 1 × 10^{-3} % (w/v) multi-walled CNT-dispersed culture medium (pH 6.0) at a ratio of 1:10 and incubated at 28 ◦C for 2 weeks. The CNT-incorporated BC (CNT–BC) membrane biosynthesized in the medium was simply harvested and purified by boiling in 1 wt% sodium hydroxide for 2 h at 90 ◦C. Subsequently, the membrane was thoroughly washed with running distilled water, after which it was soaked in 1 wt% aqueous sodium hydroxide solution for 24 h at room temperature to eliminate the cell debris and components of the culture liquid. The pH was then reduced to 7.0 by repetitive washing with distilled water. Next, the membrane was bleached by immersion in 1 wt% aqueous sodium hypochlorite for 2 h, after which it was washed with running distilled water until pH 7 was attained. Finally, the membrane was vacuum-dried at 60 ◦C for 12 h. The normal BC membrane was prepared by harvesting a single *G. xylinus* colony in mannitol culture medium without CNTs, purifying and bleaching as described above. The membrane stored in distilled water was immersed in 1×10^{-3}% (w/v) CNT-dispersed culture medium (pH 6.0) at 28 ◦C for 2 weeks. The BC membranes were washed with running distilled water and vacuum-dried at 60 ◦C for 12 h.

In vivo implatation

Six-week-old, female ICR mice (Koatech, Pyeongtaek, Korea) were anesthetized with xylazine (10 mg kg-1) and ketamine (100 mg kg-1) intraperitoneally. After shaving the scalp hair, a longitudinal incision was made in the midline of the cranium from the nasal bone to the posterior nuchal line and the periosteum was elevated to expose the surface of the parietal bones. Using a surgical trephine bur (Ace Surgical Supply Co., Brockton, MA, USA) and a low speed micromotor, two transosseous defects (4 mm diameter, circular) were produced in the skull. The defect size corresponded to the critical defect size for the mouse calvarial defect model. The drilling site was irrigated with saline, and bleeding points were electrocauterized. The periosteum was removed and never restored. The defect was filled with nothing, BC, CNT-BC-imm, CNT-BC-syn, or Col-BMP-2 ($n = 6$ implants per group). The periosteum and skin were then closed in layers with resorbable 6-0 Vicryl® sutures (Ethicon, Edinburgh, UK). The mice were housed singly after surgery. The study was approved by the Institutional Animal Care and Use Committee of Seoul National University (SNU-110121-3). The implants were retrieved for analysis at 8 weeks after the surgery.

Statistical analysis

Quantitative data were expressed as mean ± standard deviation. Statistical analyses were performed using analysis of variance (ANOVA). A p value of less than 0.05 was considered statistically significant.

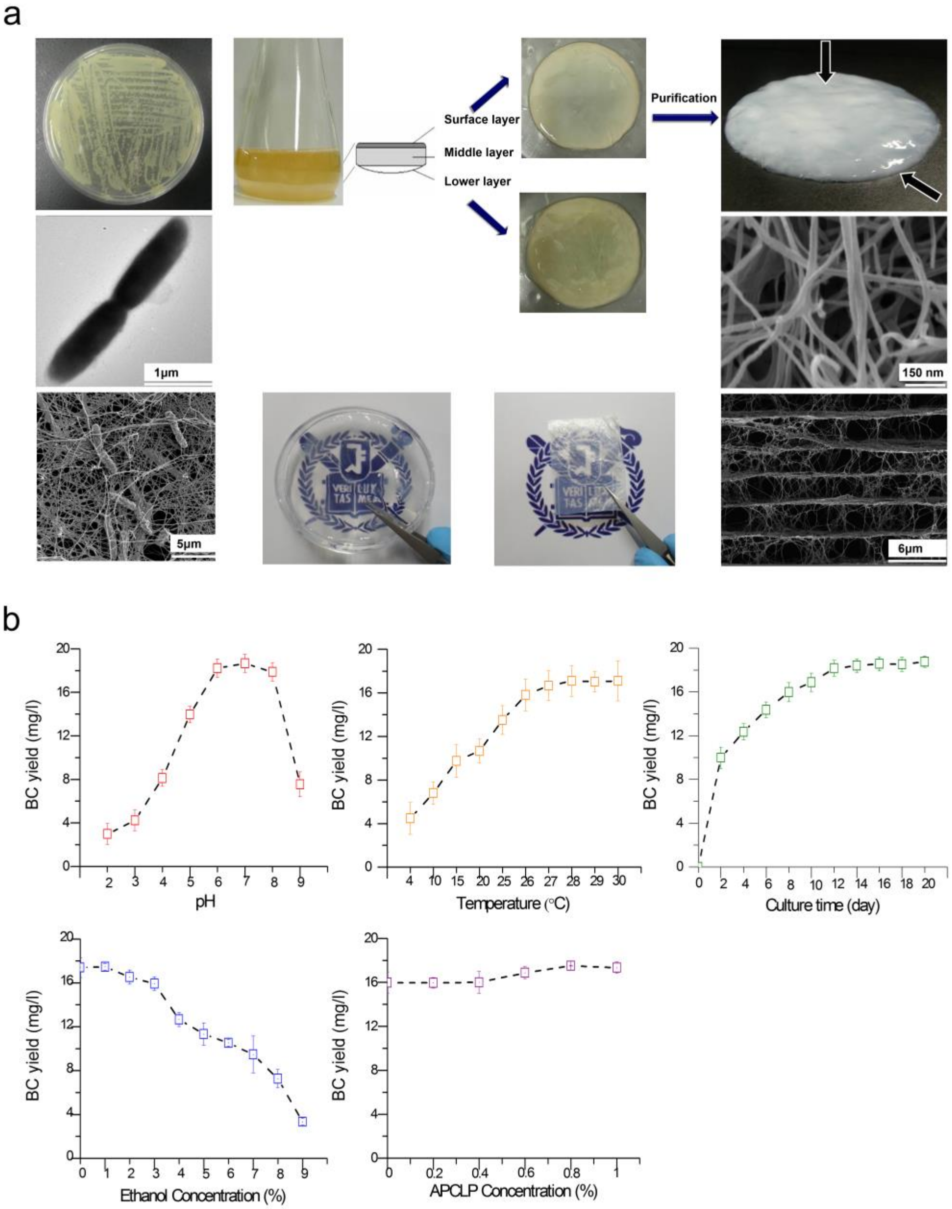

Figure S1 | BC preparation and optimization processes and parameters. a, Images of *G. xylinus* and BC. b, Effect of pH, temperature, culture time, APCLP concentration and ethanol concentration on BC yield. Cells were cultivated for 7 days in a mannitol medium.

Results and Discussion

APCLP plays a critical role in the fabrication of CNT-BC-Syn as it facilitates the dispersion of CNTs and meanwhile induces the hybridization of CNTs with BC. APCLP is composed of long a hydrophobic methyl methacrylate (MMA) backbone and short hydrophilic side chains that consist of hydroxyl polyoxyethylene methacrylate (HPOEM) and polyethylene glycol methacrylate (POEM) (Figure 1a). Molecular dynamics (MD) simulation suggested that APCLP modified the CNT surface through its unique comb-like molecular structure. The simulation showed that the hydrophobic backbone was attached to CNTs via hydrophobic-hydrophobic interactions, and the hydrophilic side chains wrapped around CNTs to form an amphiphilic surface (Figure 1a).

The amphiphilic surface facilitates the dispersion of APCLP-coated CNTs in the culture medium (Figure 1). Images obtained by scanning electron microscopy (SEM) and transmission electron microscopy (TEM) indicated that CNTs were uniformly dispersed after being treated with APCLP (Figure 1b). We further confirmed the APCLP coating on CNTs by means of fourier transform infrared spectroscopy (Figure 1c), and the results showed that APCLP-coated CNTs were well dispersed in culture medium for more than 3 months after APCLP coating (Figure 1d). In addition, the colloidal stability of APCLP-coated CNTs was not influenced by pH change (Figure 1e).

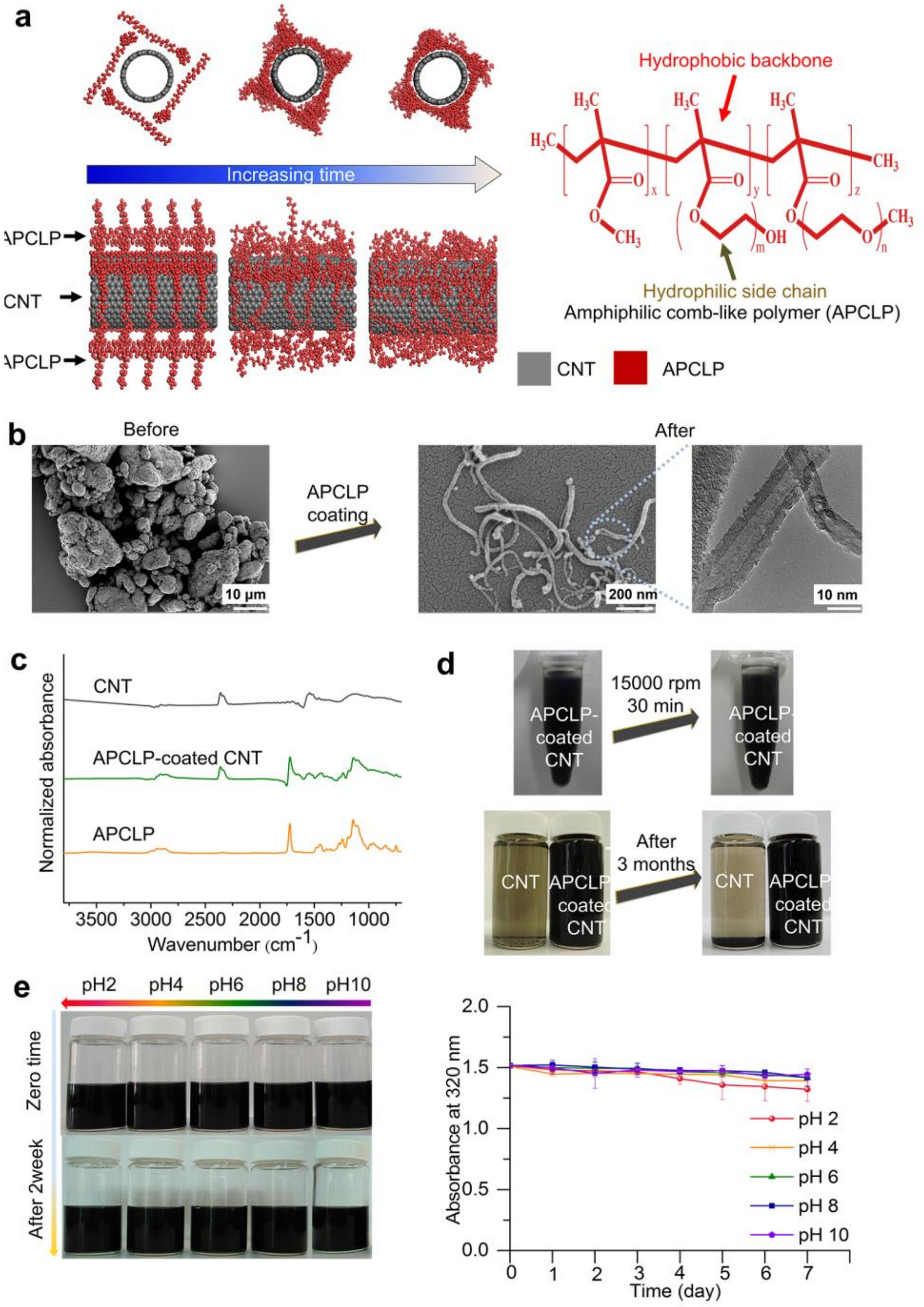

Figure 1 | APCLP-mediated dispersion of CNTs. a, MD simulation of APCLP-coated CNT. b, SEM and TEM images of CNTs before and after APCLP coating. c, Fourier transform infrared spectroscopy spectrum of CNT, APCLP and APCLP-coated CNT. d, Colloidal stability of CNT and APCLP-coated CNT after centrifugation and after 3 months. e, Colloidal stability of APCLP-coated CNT in various pH conditions of culture medium.

We prepared a CNT-based scaffold by utilizing *G. xylinus* for synthesizing BC nanofibrils that wrapped around CNTs. To achieve this, *G. xylinus* was simply cultured in a culture medium containing APCLP-coated multi-walled CNTs. The hybrid scaffold was purified after fabrication to eliminate *G. xylinus* and other contaminations.

As stated earlier, APCLP can induce the hybridization of CNTs with BC (Figure 2a). To clearly understand the APCLP-mediated binding of CNTs to BC, we performed *ab initio* calculations and MD simulations. First, the binding energies of CNT-BC and APCLP-coated CNT-BC were compared (Figure 2b). The binding energy, E_b, is defined as $E_b = -[E_{total} - E_{constituent1} - E_{constituent2}]$, where E_{total}, $E_{constituent1}$ and $E_{constituent2}$ are the energies of the total system (i.e., CNT-BC), constituent 1 (BC), and constituent 2 (CNT), respectively. The binding energy of CNTs and BC nanofibrils was -0.05 eV (per given unit), while the binding energy between BC nanofibrils was 0.68 eV (Figure 2b). Therefore, BC nanofibrils entangle around each other without having interactions with CNTs. On the other hand, the binding energy of APCLP-coated CNTs and BC nanofibrils was 0.71 eV (Figure 2b), causing BC nanofibrils to bind to and wrap around APCLP-coated CNTs. In this regard, MD simulation was performed to investigate the mechanism of CNT-BC and APCLP-coated CNT-BC formation (Figure 2c). In the case of CNT-BC, BC assembled with each other without being hybridized with CNTs. On the contrary, in the case of APCLP-coated CNT-BC, BC nanofibrils wrapped around APCLP-coated CNTs to form a hybrid, indicating the essential role of APCLP in the hybridization of CNTs

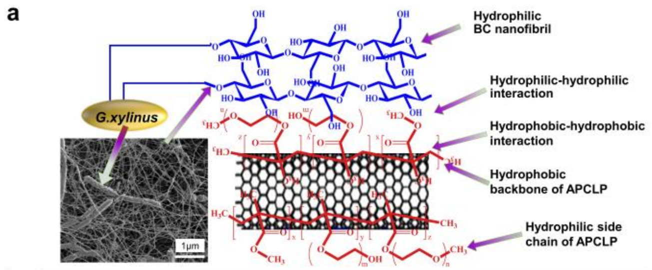

b

	BC nanofibril-BC nanofibril	CNT-BC	APCLP-coated CNT-BC
E_b	+0.68 eV	-0.05 eV	+0.71 eV

$E_b = -1/n \times [E_{tot} - n \times E_{BC}]$, n being the number of BC nanofibrils, for BC nanofibril-BC nanofibril
where $E_b = [E_{tot} - E_{CNT} - E_{BC}]$ for CNT-BC, and
$E_b = [E_{tot} - E_{APCLP/CNT} - E_{BC}]$ for APCLP-coated CNT-BC

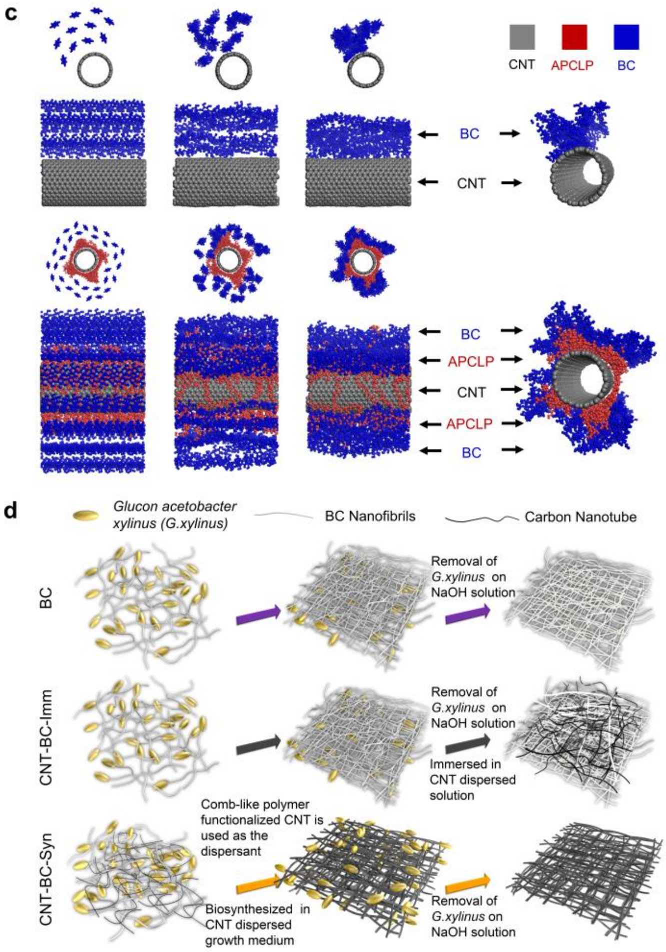

Figure 2 | APCLP-induced hybridization of CNTs and BC. a, Schematic representation of APCLP-coated CNT-BC hybridization. b, Binding energies measured by ab initio calculations. c, MD simulations for CNT-BC and APCLP-coated CNT-BC. d, Schematic illustration for the fabrication processes of BC, CNT-BC-Imm and CNT-BC-Syn.

with BC. All CNTs used in the following experiments were present in the form of APCLP-coated CNTs, as pure CNTs agglomerate and would be unsuitable for use in this study. Therefore, the word "CNTs" in all instances in the following paper indicate APCLP-coated CNTs. Due to the impracticality of using CNTs (without APCLP-coating) for the experiments, we compared the characteristics of the CNT-BC hybrid (i.e., CNT-BC-Syn) with those of CNT-coated BC formed by immersion (i.e., CNT-BC-Imm). The fabrication processes of both are shown in Figure 2d.

TEM was performed to characterize the hybridization between CNTs and BC. TEM analysis showed that CNT-BC-Syn exhibited a core-shell structure, where CNTs were packed by BC nanofibril entanglements (Figure 3a). In contrast, CNTs and BC nanofibrils in CNT-BC-Imm were separate from each other (Figure 3a). It is noteworthy that the BC nanofibrils in CNT-BC-Syn did not cover the entire surface of CNTs, resulting in a partial exposure of the CNTs to the surrounding environment (Figure 3b). The average thickness of the BC nanofibril entanglements was 4.3 nm, and about 3.9% of the CNT surface was uncovered (Figure 3b). The exposure of CNTs and thin BC coating would enable the interaction of cells with CNTs. The electron energy loss spectroscopy (EELS) spectrum collected from BC showed a broad peaks at 291 eV assigned to the 1s to 2σ* transition of carbon (Figure 3c). On the other hand, EELS spectrum of CNT-BC-Syn showed a sharp peak at 291 eV due to the 1s to p-orbital anti-bonding 2σ* band transition (Figure 3c), which was a characteristic of CNTs. This difference in EELS spectrum indicated that CNTs were embedded in the thin layer of BC in CNT-BC-Syn.

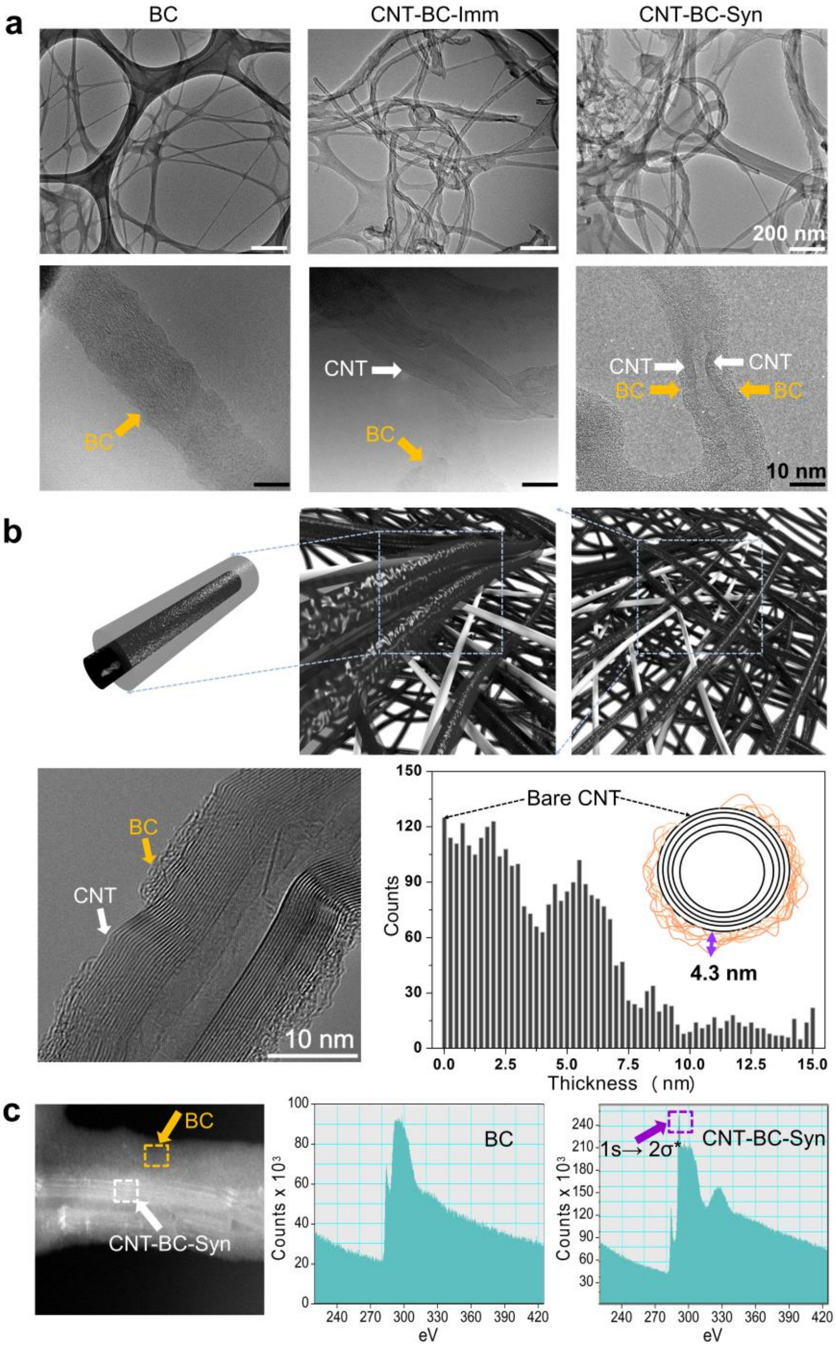

Figure 3 | TEM analyses of CNT-BC hybrid. a, TEM images of BC, CNT-BC-Imm and CNT-BC-Syn. b, Thickness distribution of BC on CNTs, showing the partial exposure of bare CNTs. c, EELS spectra of BC and CNT-BC-Syn showing the core-shell hybridization structure of CNT-BC-Syn.

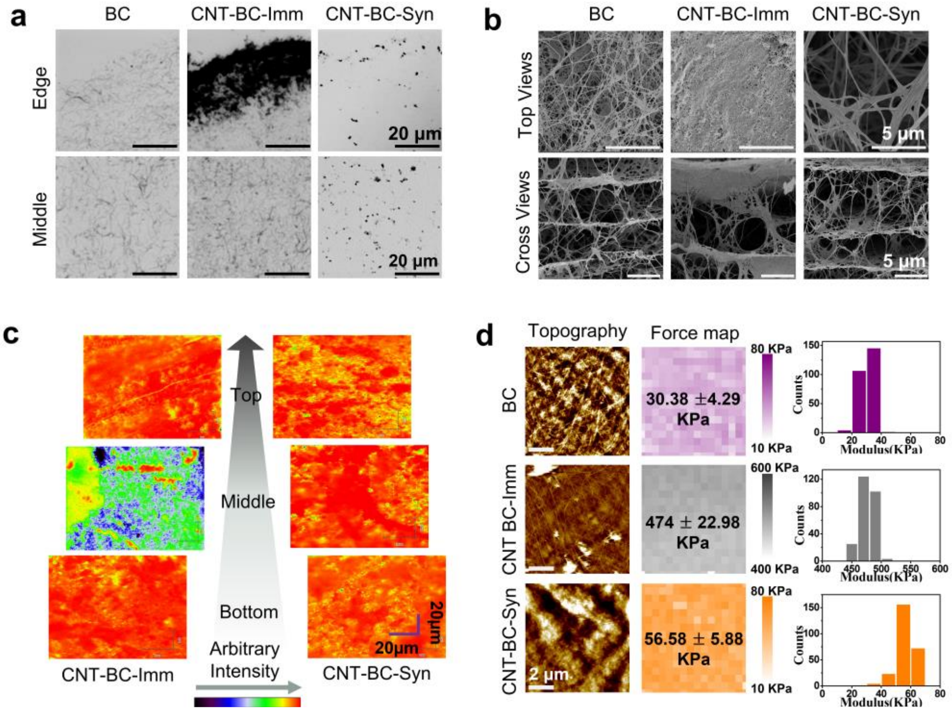

Figure 4 | Analyses showing the homogenous distribution of CNTs in CNT-BC-Syn. a, Cross-sectional optical images of BC, CNT-BC-Imm and CNT-BC-Syn. Scale bars, 20 μm. b, SEM images of BC, CNT-BC-Imm and CNT-BC-Syn with top and cross-sectional views. Scale bar, 5 μm. c, Raman mapping of CNT-BC-Imm and CNT-BC-Syn. d, Force mapping of BC, CNT-BC-Imm and CNT-BC-Syn on the surface measured by contact-mode AFM. Scale bars, 2 μm.

Intensive accumulations of black dots (i.e., CNTs) were observed on the edge of CNT-BC-Imm (Figure 4a). In contrast, CNTs in CNT-BC-Syn were homogeneously distributed throughout the scaffold. The SEM images showed that the accumulation of CNTs caused pore clogging at the CNT-BC-Imm surface (Figure 4b); on the other hand, no CNT accumulation, thus no clogged pores were observed in CNT-BC-Syn (Figure 4a and b). It is interesting to note that the porosity and pore size of CNT-BC-Syn were larger than that of pure BC (Figure 4b and Table 1). This might be because *G. xylinus* regarded CNTs as foreign substances, and therefore, formed a less compact BC.[11] In addition, all scaffolds maintained the original layer-by-layer structure of BC (Figure 4b). G-peak intensity mapping by means of Raman spectroscopy was performed to clearly depict the distribution of CNTs (Figure 4c). Although the top and bottom surfaces of CNT-BC-Imm were fully covered with CNTs, CNTs were rarely observed inside the scaffolds. This result indicated that CNTs were predominantly present on the surface and absent from the interior of the scaffold in CNT-BC-Imm (Figure 4c). On the other hand, CNTs were homogeneously distributed over the entire scaffold in CNT-BC-Syn (Figure 4c). The high Young's modulus of the CNT-BC-Imm surface measured by atomic force microscopy (AFM) indicated that the surface of the scaffold was fully covered by CNT agglomerates (Figure 4d). In addition, the homogenous distribution of CNTs in CNT-BC-Syn resulted in a reduced specific resistance and enhanced electrical conductivity, as compared with that of BC and CNT-BC-Imm (Table 1).

Overall, these results suggest that CNT-BC-Syn can be used as an ideal bone graft material due to its unique architecture. We were able to fabricate CNT-BC-Syn composed of large pores and nano-scale fibers by utilizing *G. xylinus*. The pore size of CNT-BC-Syn was suitable for cell migration and osteogenesis.[12] The nano-scale fibers constituting CNT-BC-Syn are favourable for cell attachment, proliferation, alkaline phosphatase synthesis and extracellular calcium deposition, which are all essential aspects of bone regeneration.[13,14] The resulting CNT-BC-Syn showed mechanical strength appropriate for osteogenic differentiation.[15] In addition, the hydrogel-like BC layers surrounding CNTs may act as a reservoir for accommodating various growth factors,[16,17] which in turn can enhance the cell differentiation to facilitate bone regeneration.

Previous studies have demonstrated that although CNTs and BC are not biodegradable, both have shown a high level of biocompatibility.[18,19] CNTs showed minimized local inflammatory reactions and were well integrated into the newly formed bone after *in vivo* implantation for bone regeneration.[18] Similarly, BC was well integrated into the host tissue without inducing any inflammation when implanted *in vivo*.[19] BC is composed of only cellulose without any unwanted biogenic compounds, and it is less immune-stimulatory as compared with collagen, a commonly used scaffold material.[20] To evaluate the *in vivo* performance of CNT-BC-Syn, it was applied as a bone graft for bone regeneration application, and the results were compared with those obtained by using BC, CNT-BC-Imm, and collagen sponge loaded with bone morphogenetic protein-2 (Col-BMP-2), a clinically used bone graft.[21]

The microscopic computed tomographic (micro-CT) analyses performed 8 weeks after the implantation of the scaffolds into the critical-sized defect in mouse

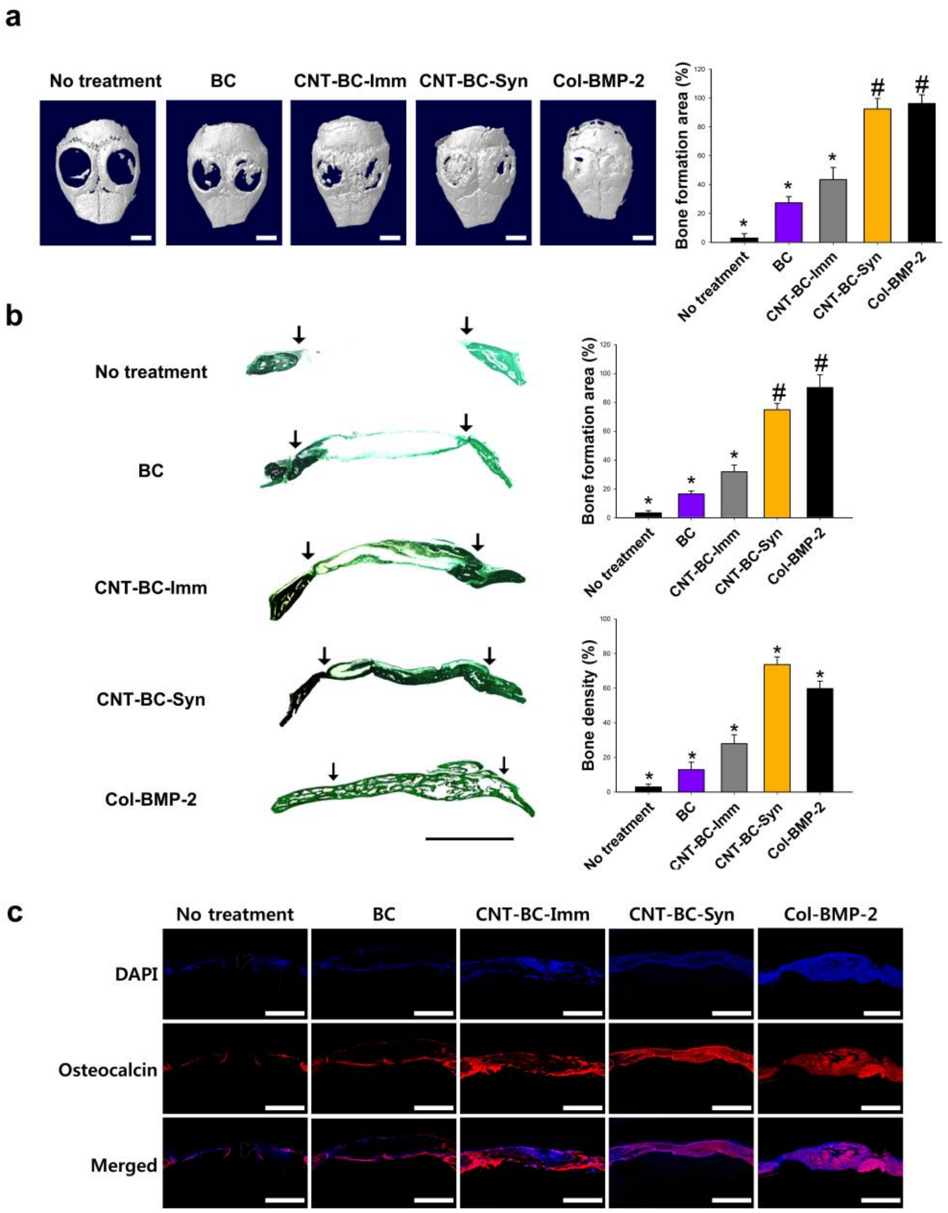

Figure 5 | Bone regeneration efficacy of the scaffolds. a, Bone regeneration evaluated by micro-CT analyses. Quantification of the bone formation area of defects. b, Goldner's trichrome staining of mouse calvarial defect areas. Quantification of bone formation area and bone density of defects. c, Immunohistochemistry of mouse calvarial defect areas. DAPI staining indicates osteoconductivity of the scaffolds. Osteocalcin staining indicates osteoinductivity of the scaffolds. Scale bars, 2 mm. $*p < 0.05$ compared to any other group. $\#p < 0.05$ compared to no treatment, BC and CNT-BC.

calvaria showed a similar bone regeneration efficacy of CNT-BC-Syn, and Col-BMP-2, which was much higher than that of BC or CNT-BC-Imm (Figure 5a). The analytical results of Goldner's trichrome staining of the histological sections revealed insufficient bone regeneration by BC and CNT-BC-Imm; in contrast, the use of CNT-BC-Syn resulted in extensive bone regeneration similar to that caused by Col-BMP-2 (Figure 5b). It is noteworthy that although Col-BMP-2 is capable of forming new bone with the area similar to that formed by CNT-BC-Syn, the density of the regenerated bone was lower than that formed by CNT-BC-Syn (Figure 5b). This indicates that CNT-BC-Syn is suitable for use as a bone graft material due to its capability in forming new bone with high density.

A good bone graft should facilitate migration of the cells from the surrounding environment to the defect area (i.e., high osteoconductivity) and promote their osteogenic differentiation (i.e., high osteoinductvity). In this study, we demonstrated that the fabricated CNT-BC-Syn exhibited excellent osteoconductivity and osteoinductivity, both of which are desirable properties for bone regeneration (Figure 5c). The 4',6-diamidino-2-phenylindole (DAPI, blue) staining of cell nuclei confirmed the cell migration into the scaffolds. The fluorescence of DAPI was visible throughout the defect area, demonstrating that CNT-BC-Syn exhibited excellent osteoconductivity for promoting cell migration (Figure 5c). In addition, the osteocalcin staining (red) revealed that the cells underwent pronounced osteogenic differentiation in CNT-BC-Syn. Most of the cells in CNT-BC-Syn were successfully labelled with red fluorescence (Figure 5c), suggesting that CNT-BC-Syn showed a high osteoinductivity. As regards to CNT-BC-Imm, the cells were found to only differentiate on the periphery of the defect area (Figure 5c).

The possible explanation for the enhanced osteoconductivity and osteoinductivity of CNT-BC-Syn, as compared with BC and CNT-BC-Imm, may be the structure of the scaffold and the distribution of CNTs. CNT-BC-Syn showed a larger average pore size than that of BC and CNT-BC-Imm (Table 1). This, at least partially, contributed to the enhanced cell migration into CNT-BC-Syn.[12] The migrated cells would interact with CNTs that were homogeneously distributed throughout CNT-BC-Syn. This, in turn, would enable the promotion of osteogenic differentiation of the migrated cells.[22] In contrast, the absence of CNTs from the core of CNT-BC-Imm resulted in the osteoinduction occurring only on the surface of the scaffold (Figure 5c)

Table 1| Properties of BC, CNT-BC-Imm and CNT-BC-Syn

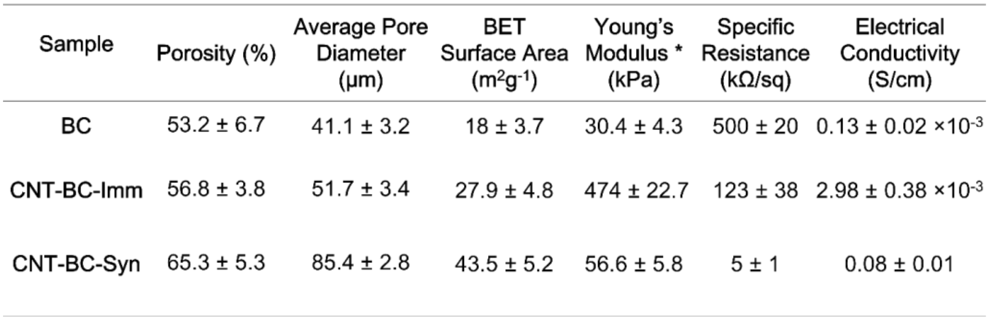

Sample	Porosity (%)	Average Pore Diameter (μm)	BET Surface Area (m^2g^{-1})	Young's Modulus * (kPa)	Specific Resistance (kΩ/sq)	Electrical Conductivity (S/cm)
BC	53.2 ± 6.7	41.1 ± 3.2	18 ± 3.7	30.4 ± 4.3	500 ± 20	$0.13 \pm 0.02 \times 10^{-3}$
CNT-BC-Imm	56.8 ± 3.8	51.7 ± 3.4	27.9 ± 4.8	474 ± 22.7	123 ± 38	$2.98 \pm 0.38 \times 10^{-3}$
CNT-BC-Syn	65.3 ± 5.3	85.4 ± 2.8	43.5 ± 5.2	56.6 ± 5.8	5 ± 1	0.08 ± 0.01

* The Young's modulus was the compressive modulus measured via AFM

Conclusions

In this study, an important method was introduced for the development 3D biofunctional scaffolds through hybridization with biofunctional nanomaterials for biomedical applications. BC was chosen as the 3D scaffold material for the hybridization of CNTs due to its ideal structure for tissue engineering scaffolds. APCLP was utilized to promote colloidal stability of CNTs and induce the hybridization between CNTs and BC, which enabled homogeneous and effective hybridization of CNTs with BC. Unlike conventional CNT-composite scaffolds fabricated through immersion of 3D BC scaffolds in CNT solution, CNT-BC-Syn scaffolds showed homogeneously distributed CNTs throughout the 3D microporous structure of BC. This resulted in excellent osteoinductivity and osteoconductivity of CNT-BC-Syn hybrid scaffolds, and in turn, high bone regeneration efficacy when implanted in vivo. This strategy for hybridizing 3D scaffolds with functional nanomaterials may present a new perspective for regenerative medicine.

References

[1]. Vandamme, E. J.; De Baets, S.; Vanbaelen, A.; Joris, K.; De Wulf, P. Improved Production of Bacterial Cellulose and Its Application Potential. *Polym. Degrad. Stab.* **1998,** *59*, 93-99.

[2]. Yeo, M.; Lee, H.; Kim, G. Three-Dimensional Hierarchical Composite Scaffolds Consisting of Polycaprolactone, Beta-Tricalcium Phosphate, and Collagen Nanofibers: Fabrication, Physical Properties, and in Vitro Cell Activity for Bone Tissue Regeneration. *Biomacromolecules* **2011,** *12*, 502-510.

[3]. Venugopal, J.; Low, S.; Choon, A. T.; Ramakrishna, S. Interaction of Cells and Nanofiber Scaffolds in Tissue Engineering. *J Biomed Mater Res B Appl Biomater* **2008,** *84*, 34-48.

[4]. Tuzlakoglu, K.; Bolgen, N.; Salgado, A. J.; Gomes, M. E.; Piskin, E.; Reis, R. L. Nano- and Micro-Fiber Combined Scaffolds: A New Architecture for Bone Tissue Engineering. *J Mater Sci Mater Med* **2005,** *16*, 1099-1104.

[5]. Li, X. M.; Liu, H. F.; Niu, X. F.; Yu, B.; Fan, Y. B.; Feng, Q. L.; Cui, F. Z.; Watari, F. The Use of Carbon Nanotubes to Induce Osteogenic Differentiation of Human Adipose-Derived Mscs in Vitro and Ectopic Bone Formation in Vivo. *Biomaterials* **2012,** *33*, 4818-4827.

[6]. Shao, S.; Zhou, S.; Li, L.; Li, J.; Luo, C.; Wang, J.; Li, X.; Weng, J. Osteoblast Function on Electrically Conductive Electrospun Pla/Mwcnts Nanofibers. *Biomaterials* **2011,** *32*, 2821-2833.

[7]. Shimizu, M.; Kobayashi, Y.; Mizoguchi, T.; Nakamura, H.; Kawahara, I.; Narita,

N.; Usui, Y.; Aoki, K.; Hara, K.; Haniu, H*., et al.* Carbon Nanotubes Induce Bone Calcification by Bidirectional Interaction with Osteoblasts. *Adv. Mater.* **2012,** *24*, 2176-2185.

[8]. Correa-Duarte, M. A.; Wagner, N.; Rojas-Chapana, J.; Morsczeck, C.; Thie, M.; Giersig, M. Fabrication and Biocompatibility of Carbon Nanotube-Based 3d Networks as Scaffolds for Cell Seeding and Growth. *Nano Lett.* **2004,** *4*, 2233-2236.

[9]. Murphy, C. M.; Haugh, M. G.; O'Brien, F. J. The Effect of Mean Pore Size on Cell Attachment, Proliferation and Migration in Collagen-Glycosaminoglycan Scaffolds for Bone Tissue Engineering. *Biomaterials* **2010,** *31*, 461-466.

[10]. Hirata, E.; Uo, M.; Takita, H.; Akasaka, T.; Watari, F.; Yokoyama, A. Multiwalled Carbon Nanotube-Coating of 3d Collagen Scaffolds for Bone Tissue Engineering. *Carbon* **2011,** *49*, 3284-3291.

[11]. Heßler, N.; Klemm, D. Alteration of Bacterial Nanocellulose Structure by in Situ Modification Using Polyethylene Glycol and Carbohydrate Additives. *Cellulose* **2009,** *16*, 899-910.

[12]. Karageorgiou, V.; Kaplan, D. Porosity of 3d Biomaterial Scaffolds and Osteogenesis. *Biomaterials* **2005,** *26*, 5474-5491.

[13]. Ma, P. X. Biomimetic Materials for Tissue Engineering. *Adv. Drug Delivery Rev.* **2008,** *60*, 184-198.

[14]. Elias, K. L.; Price, R. L.; Webster, T. J. Enhanced Functions of Osteoblasts on Nanometer Diameter Carbon Fibers. *Biomaterials* **2002,** *23*, 3279-3287.

[15]. Engler, A. J.; Sen, S.; Sweeney, H. L.; Discher, D. E. Matrix Elasticity Directs Stem Cell Lineage Specification. *Cell* **2006,** *126*, 677-689.

[16]. Silva, A. K.; Richard, C.; Bessodes, M.; Scherman, D.; Merten, O. W. Growth Factor Delivery Approaches in Hydrogels. *Biomacromolecules* **2009,** *10*, 9-18.

[17]. Shi, Q.; Li, Y.; Sun, J.; Zhang, H.; Chen, L.; Chen, B.; Yang, H.; Wang, Z. The Osteogenesis of Bacterial Cellulose Scaffold Loaded with Bone Morphogenetic Protein-2. *Biomaterials* **2012,** *33*, 6644-6649.

[18]. Usui, Y.; Aoki, K.; Narita, N.; Murakami, N.; Nakamura, I.; Nakamura, K.; Ishigaki, N.; Yamazaki, H.; Horiuchi, H.; Kato, H.*, et al.* Carbon Nanotubes with High Bone-Tissue Compatibility and Bone-Formation Acceleration Effects. *Small* **2008,** *4*, 240-246.

[19]. Helenius, G.; Backdahl, H.; Bodin, A.; Nannmark, U.; Gatenholm, P.; Risberg, B. In Vivo Biocompatibility of Bacterial Cellulose. *J. Biomed. Mater. Res. A* **2006,** *76*, 431-438.

[20]. Petersen, N.; Gatenholm, P. Bacterial Cellulose-Based Materials and Medical Devices: Current State and Perspectives. *Appl. Microbiol. Biotechnol.* **2011,** *91*, 1277-1286.

[21]. Yang, H. S.; La, W. G.; Cho, Y. M.; Shin, W.; Yeo, G. D.; Kim, B. S. Comparison between Heparin-Conjugated Fibrin and Collagen Sponge as Bone Morphogenetic Protein-2 Carriers for Bone Regeneration. *Exp. Mol. Med.* **2012,** *44*, 350-355.

[22]. Baik, K. Y.; Park, S. Y.; Heo, K.; Lee, K. B.; Hong, S. Carbon Nanotube Monolayer Cues for Osteogenesis of Mesenchymal Stem Cells. *Small* **2011,** *7*, 741-745.

[23]. Kresse, G.; Furthmuller, J. Efficient Iterative Schemes for Ab Initio Total-

Energy Calculations Using a Plane-Wave Basis Set. *Phys Rev B* **1996,** *54*, 11169-11186.

[24]. Kresse, G.; Furthmuller, J. Efficiency of Ab-Initio Total Energy Calculations for Metals and Semiconductors Using a Plane-Wave Basis Set. *Comp Mater Sci* **1996,** *6*, 15-50.

[25]. Perdew, J. P.; Burke, K.; Ernzerhof, M. Generalized Gradient Approximation Made Simple. *Phys. Rev. Lett.* **1996,** *77*, 3865-3868.

[26]. Grimme, S. Semiempirical Gga-Type Density Functional Constructed with a Long-Range Dispersion Correction. *J. Comput. Chem.* **2006,** *27*, 1787-1799.

[27]. Strachan, A.; van Duin, A. C. T.; Chakraborty, D.; Dasgupta, S.; Goddard, W. A. Shock Waves in High-Energy Materials: The Initial Chemical Events in Nitramine Rdx. *Phys. Rev. Lett.* **2003,** *91*.

Chapter 7

Nature-induced bioengineered nano-scaffolds for constructing three-dimensional mini-brain

Introduction

Over the last decade there has been remarkable progress in neurobiology and neural engineering mainly encouraged by development of innovative scientific methodologies[1]. One of the most dominant efforts is controlling neuronal functions at *in vivo* condition with targeted genetic engineering such as optogenetics[2]. An *in vitro* model system which is intended to emulate the physiological conditions at the well-defined state, shows a great advantage in terms of simplicity and thereby controllability compared to the *in vivo* model systems.

Constructing three-dimensional neuronal networks has been a challenging issue due to its difficulty in inducing physiologically-critical neuronal characteristics such as long term culture viability, appropriate protein expression, layered network formation, and synaptic connectivity evolution over time. Hydrogel is typically an attractive platform for hosting a general three-dimensional (3D) *in vitro* culture, however, several practical issues, i.e., neuronal toxicity caused by unreacted scaffold-forming monomers and complexity in anchoring cell adhesive ligands[3–5] need to be resolved. In parallel, the entangled electrospun microfiber networks or closely-packed microbead arrays were attempted as a synthetic scaffold for the 3D neuronal culture[6–13]. Such a micro-engineered material platform chemically modified with polylysine exhibit the structural modularity for scaffold fabrication and the improved viability in neuronal culture compared to the hydrogel platform, however, the microscale topographic environment allows only for the confined surface to neuronal cells, therefore, the 3D network formation is severely limited.

Moreover, the incident light is either scattered by the microscale objects or distorted at the interfacial region between water and scaffold material due to the refractive index mismatch. Such an optical hindrance prevents the microscopic interrogation of the resultant 3D neuronal network using optical tomography tools. Above all, the neuronal cells cultivated in a given neuronal scaffold have requirements to behave as if they reside at the physiological condition so that this artificial culture platform is viable as an *in vitro* model system for neuronal network study.

Bacterio-cellulose (BC) is historically known as Nata-de-coco, a tropical dietary jelly-like substance commonly used for adding flavor of appetizer in fruit salad and, recently, have found many interesting applications in biotechnonology, microbiology, and materials science due to its interesting material properties. This cellulose-based nanostructured natural material which is formed by straight sugar chain repetition and strong hydrogen bonding interactions among neighboring monosaccharides exhibit intriguing properties such as decent wettability via enriched hydroxyl functionality, nanoscopically well-organized architecture with high crystallinity, mechanical modulus as high as steel, and optical transparency above 80% in the visible light range[14–17]. The most striking aspect of this material is that this nanostructured cellulose is synthesized by bacteria even though its function is still under investigation[18–20] and this natural machinery driven by bacteria can be utilized for preparing artificial composite materials, too. Herein, the natural synthetic machinery of a bacterial strain (*Acetobacter Xylinum*) is successfully demonstrated for synthesizing the nanoengineered bacteriocellulose homogeneously hybridized with nanocarbon materials with an aim to combine the benefits from the natural nanostructured cellulose and artificial GO or rGO sheets. The resultant GO and rGO-incorporated BC carries many interesting characteristics for a novel neuronal culture platform for 3D artificial neuronal network study. Particularly, the optical transparency was remained allowing for the phase-contrast and fluorescence imaging with depth up to several mm without two-photon microscope and the nanofibillar structure of bacterial cellulose was greatly mimics the mechanical property of the brain. The growing kinetics, neuronal phenotypes, and long-range interneuronal connectivity were closely emulated with this novel material platform.

Experimental

Preparation of amphiphilic comb-like Polymer (APCLP)

APCLP was synthesized by free radical polymerization of MMA (Aldrich), poly(ethylene glycol) methacrylate (Aldrich, Mn 360 g/mol, corresponding to n = 6) and poly(ethylene glycol) methyl ether methacrylate (Aldrich, Mn 475 g/mol, corresponding to n = 9), in tetrahydrofuran for 18 h as previously described.47 The CNTs (purity >95%, lljin Nanotech Co., Korea) produced by the chemical vapor deposition method were used without further purification or treatment. The CNTs were determined to have an outer diameter of about 10–20 nm and a length of 150–200 μm. A total of 1 mg of CNT was added to 10 mL of APCLP solution (30% ethanol, 0.001% APCLP), after which the samples were sonicated using a horn-type ultrasonic generator (Fisher Scientific Co., USA) with a frequency of 23 kHz and a power of 30 W for 20 min at room temperature.

G. xylinus culture

G. xylinus (KCCM 40216) was obtained from the Korean Culture Center of Microorganisms. The bacterium was cultured on mannitol medium composed of 2.5% (w/w) mannitol, 0.5% (w/w) yeast extract and 0.3% (w/w) bacto-peptone. The culture media were sterilized in an autoclave at 120 ◦C for 20 min and then poured into 500 mL flasks. The pre-inoculum for all experiments was prepared by transferring a single *G. xylinus* colony grown on agar culture medium into a 100 mL Erlenmeyer flask filled with mannitol culture medium.

Preparation of GO and rGO-BC

The pre-cultured culture cell suspension was introduced into 1×10^{-3} % (w/v) GO and rGO-dispersed culture medium (pH 6.0) at a ratio of 1:10 and incubated at 28 °C for 2 weeks. The GO and rGO -incorporated BC (GO BC and rGO–BC) membrane biosynthesized in the medium was simply harvested and purified by boiling in 1 wt% sodium hydroxide for 2 h at 90 °C. Subsequently, the membrane was thoroughly washed with running distilled water, after which it was soaked in 1 wt% aqueous sodium hydroxide solution for 24 h at room temperature to eliminate the cell debris and components of the culture liquid. The pH was then reduced to 7.0 by repetitive washing with distilled water. Next, the membrane was bleached by immersion in 1 wt% aqueous sodium hypochlorite for 2 h, after which it was washed with running distilled water until pH 7 was attained. Finally, the membrane was vacuum-dried at 60 °C for 12 h. The normal BC membrane was prepared by harvesting a single *G. xylinus* colony in mannitol culture medium, purifying and bleaching as described above.

Analyses of GO and rGO distribution in scaffolds

To analyse the distribution of GO and rGO in BC scaffolds, BC, GO-BC-Syn, and rGO-BC-Syn were embedded in an optimal cutting temperature compound (TISSUE-TEK® 4583, Sakura Finetek USA Inc., Torrance, CA, USA), followed by freezing and slicing into 10 µm thick sections at -22 ℃. Cross-sections of the samples were analysed using an image analysis system (Axio Observer Z1, Zeiss, Göttingen, Germany) coupled to a light microscope at a magnification of ×400 and ×1000. For scanning electron microscopy (SEM) analysis, BC, GO-BC-Syn, and rGO-BC-Syn were frozen at -70 ℃, followed by freeze-drying for 1 day. The surface morphology of the samples was observed at an acceleration voltage of 5 kV using SEM (JSM-6330F, JEOL). Raman spectra were taken from top, middle and bottom layer. Raman maps are of the G peak (1560 to 1620 $cm^{-1)}$ bands. Raman spectra were recorded using a Renishaw inVia micro-Raman spectrometer (λ laser = 514 nm, ~500 nm spot size, 100× objector). The AFM observations and measurements were carried out by means of a Park systems XE-100 scanning probe microscope at ambient conditions. Silicon cantilever NSC-36 C (Mikromasch Inc) having pyramidal tips with 10 nm nominal radii of curvature(R_c). Cantilever spring constant of 0.60 N m-1 were used. Topological data was employed a compressive load of 10 nN during scanning. After getting topography images, z-scanner displacement versus force curves were recorded. Forward and backward rate was 0.3 µm/sec and a maximum compressive load of 40 nN was applied to the surface during data acquisition. The Young's modulus (E) of the samples were calculated using the Hertzian model, equation. Poisson's ratio(ν) is set to 0.5 and parabolic geometry of the indenter is set.

Analyses of scaffold properties

The porosity and the pore sizes of fabricated scaffolds were measured using mercury intrusion porosimetry (AutoporeIV9500, Micromeritics Instrument Corporation, Norcross, GA). Nitrogen physisorption measurements at 77 K were performed by a Quantachrome NOVA 4000 (U.S.A.), and Brunauer-Emmett-Teller (BET) and Barrett-Joyner-Halenda (BJH) analyses were done by Autosorb software (Quantachrome). The BET analysis was done for relative vapor pressure of 0.05 to 0.3. The BJH analysis was done from the desorption branch of the isotherm. The sheet resistance and electrical conductivity of GO-BC-Syn, and rGO-BC-Syn were measured by the van der Pauw four-probe technique with using a Hall measurement system (2400 Source Meter, Keithley).

Analyses of GO-BC-Syn, and rGO-BC-Syn integration

Transmission electron microscopy (TEM, JEOL 2100, JEOL, Japan) analyses were operated at 200 kV.

Results and Discussion

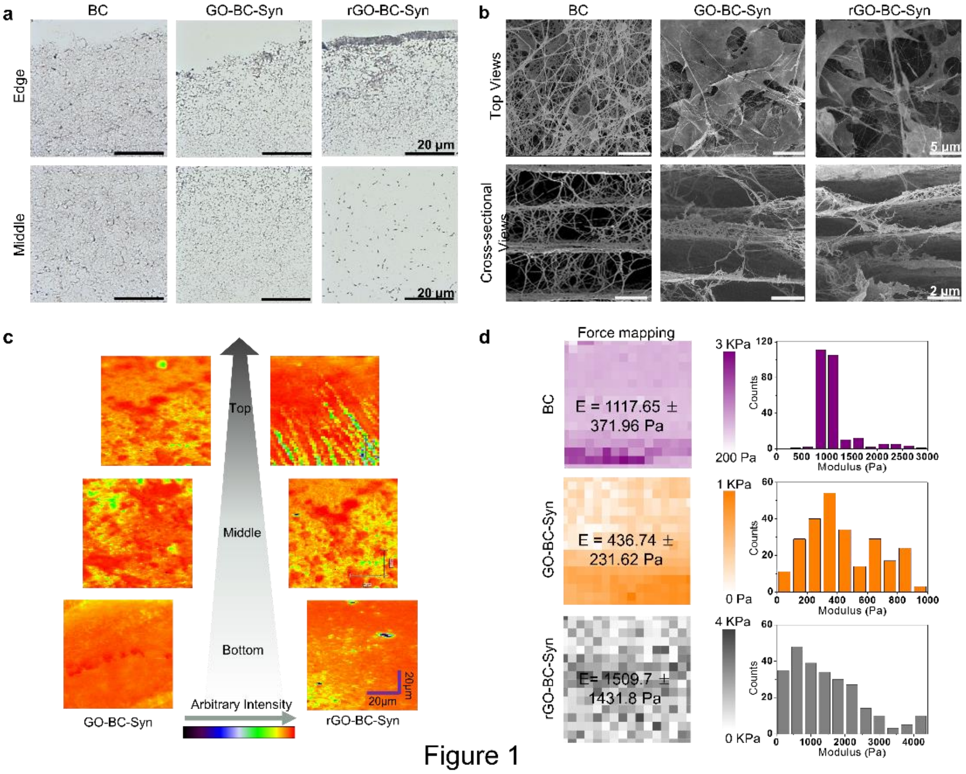

Figure 1

Figure 1 | Fabrication and characterization of bare/graphene composited BC. a, Schematic explanation of Acetobacter Xylinum producing cellulose nanofiber and in situ composition of graphene. b, Top view and lateral view of bacterial cellulose exhibit nanofibrillar cellulose and stacked layered structure, respectively. c, Top view of GO (left) and rGO (right) composited BC. d, High resolution TEM image of bare bacterial cellulose and their crystallinity. e, Raman spectroscopic measurement confirms the presence of GO and rGO with corresponding vibration peaks. f. Liquid AFM measurement of elastic modulus along normal direction.

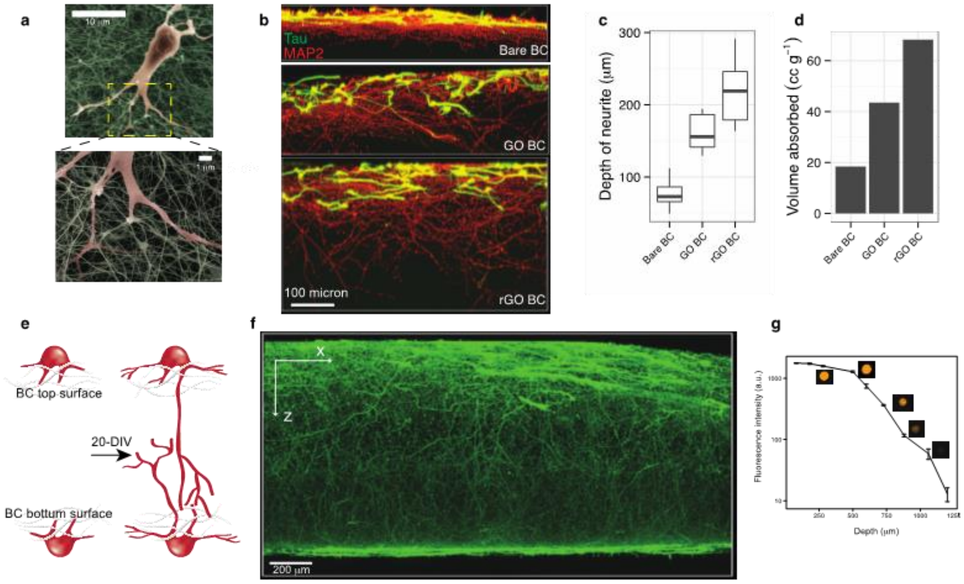

Figure 2 | Detailed neuronal morphology and controlled z-directional neuronal outgrowth. a, scanning electron microscope images represent interfacial region between 3-div neuron and BC. b z-directional neuronal outgrowth of bare and graphene composited BC. MAP2 and Tau labels neuronal dendrites and axons, respectively. c, statistical representation of z-directional neuronal outgrowth depending presence of graphene composition d, BET measurements exhibit modulation of bacterial cellulose porosity by means of graphene composition. e, schematic figure of outgrowing neuron toward to counter BC surfaces. f, Fluorescence y-stacked image of widely culture (3.5 mm × 3.5 mm × 1 mm) 20-div neuron. g, Fluorescence light intensity decay of fluorescence beads depending on depth of BC.

Since the pristine BC is a complex fibrillar network with large internal porosity and hydrophilic surface, each cellulose nanofiber is surrounded by a large number of water molecules leading to hydrogel in an aqueous condition. The hydrophilic nature of BC networks allows for an approximate swelling ratio of 25[21] . Such a high content of water in the water-absorbed BC matrix in combination with very fine morphology of nanofibrillar structures (~30 nm in diameter) and minimal visible light absorption in cellulose moiety enables marginal light scattering and autofluorescence resulting in an ideal culture platform for optical microscopy[22]. Indeed, the actin filmaments and microtubules in outgrowing neurites and growth cones of cultured neurons are clearly visible inside a milimeter-thick BC scaffold by optical fluorescence microscopy while the nanofibrillar structure of bacterial cellulose is dimly imaged by the reflection mode. The resultant 3D-organized cellular architecture could be easily reconstituted by 3D stacking method using confocal microscopy. As confirmed by the depth profile of fluorescence intensity (Figure 2b), the entangled structure of nanofibrous network does not severely interrupt light passage up to one milimeter thickness.

Figure 2c shows the false-colored SEM images of the fixed neuronal cell which is deposited on top of the pristine BC, GO-BC, and rGO-BC. Unlike the cell cultured on the flat rigid substrate, the neuronal cell on nanotextured scaffold exhibits a spherical shape of cell body reminiscent of the shape of the cell culture on very soft substrate. The neurites initially follow the BC nanofiber morphologies on the top surface and eventually penetrate into the scaffolds growing downward. The vertical movement of neurties after penetration is more prominent in the neuronal culture on the GO-BC than on the pristine BC and most prominent on rGO-BC (Figure 2d). To correlate the extent of z-directional neurite outgrowth and the porosity of culture scaffold, the surface area of each nanoengineered BC was experimentally extracted by the BET theory as the ratio between matrix surface area and its own mass so that higher surface area per volume represents higher porosity. As displayed in Figure 2f, the GO- or rGO-hybridized BCs exhibit much higher porosity than the unmodified bare BC. With the addition of nanostructured carbon materials, the cellulose chains are expected to be easily adsorbed and homogeneously hybridized on the surface of nanoscale carbon platelet during bacterial synthesis as shown in the high resolution TEM images (Figure 1). In fact, the suspended nano-membrane-like structures are more easily found in GO or rGO-incorporated BC resulting in the increased surface area (Supporting information). Furthermore, the smaller particle size of rGO may explain the larger porosity of rGO-hybridized BC than GO-BC. Therefore, the vertical outgrowth of neurites is deliberately manipulated and, possibly, inter-neuronal connectivity along the vertical direction is effectively fine-tuned by incorporation of nanostructured carbon materials.

The cellular phenotype is not only affected by genetically-encoded information but also by the external cellular environment[23–25]. It is very important to maintain the appropriate physiological condition particularly at the embryonic neuronal development stage since the minute change in the cellular environment may lead to the defect in cellular function and subsequent dysfunction of the resultant neuronal network. In this regard, the emulation of physiological condition is assumed to be

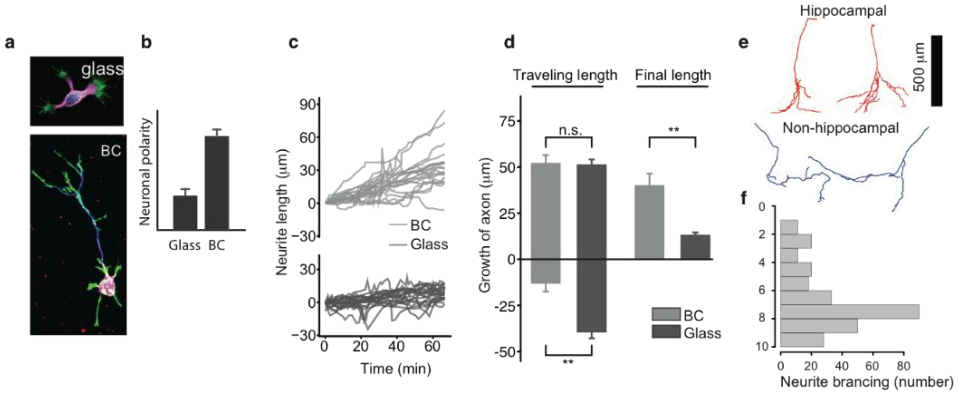

Figure 3 | Neuronal kinetics in BC a, comparison of neuronal development on glass and BC substrate b, statistical analysis of neuronal polarity. c, time evolutional trajectory of 3-div outgrowing axon on BC and glass substrate. (n = 20 for BC and glass, 5 sec for time interval) d, extracted quantitative information of outgrowing axon reveal total traveling length and final length of axon which composed or substrate by forward and backward motion. e, traced 20-div neuronal morphology on BC exhibits delicate and distinct neuronal sub-cell type. f, synchronization of axon branching at the certain depth (700 μm) of BC.

critical to generate a reliable neuronal culture condition for establishing an *in vitro* neuronal network model. From the mechanical point of view, it is well known that a brain tissue typically exhibits very low elastic modulus (<1 kPa) and the phenotypes of the constituent cells (e.g., neurons and glia) are very sensitive to the mechanical properties of culture scaffold. In the case of the 2-D neuronal culture on the flat rigid glass having high elastic modulus, the cultured cells show the typical cone-like morphology of actin filaments at the tip of growth cone and the decent expression level of focal adhesion complex proteins (i.e., paxillin, vinculin) which are matured through the extensive tug war between the stiffened integrin-ECM junction point and the retrograding myosin motor protein [28–31]. In contrast, the cells deposited on the BC-based 3-D scaffold exhibit the distinct morphology of highly-branched growth cone with fine tips and overall large surface area. Furthermore, the promoted neurite outgrowth and its accelerated polarization to axon and dendrite are clearly observed. More strikingly, the expression level of the focal adhesion protein complex is remarkably low on the 3D scaffold.[26,27] These results imply that the neurons on the BC-based scaffolds are under significantly lower tension than those in the control 2-D glass culture[32,33], which are also reasonably supported by the experimentally-measured elastic moduli of the present 3D culture scaffolds as already shown in Figure 1f (< 1kPa). Note also that the growth cone on BC not only navigate through the 3D nanostructured fibers but also move in the forward direction only while that on the control 2D culture ruffles and rambles in the random direction (Figure 1c and d and supporting movie clip). The apparent directionality of neurite outgrowth and viability of neuronal culture even without chemical modification might be related to

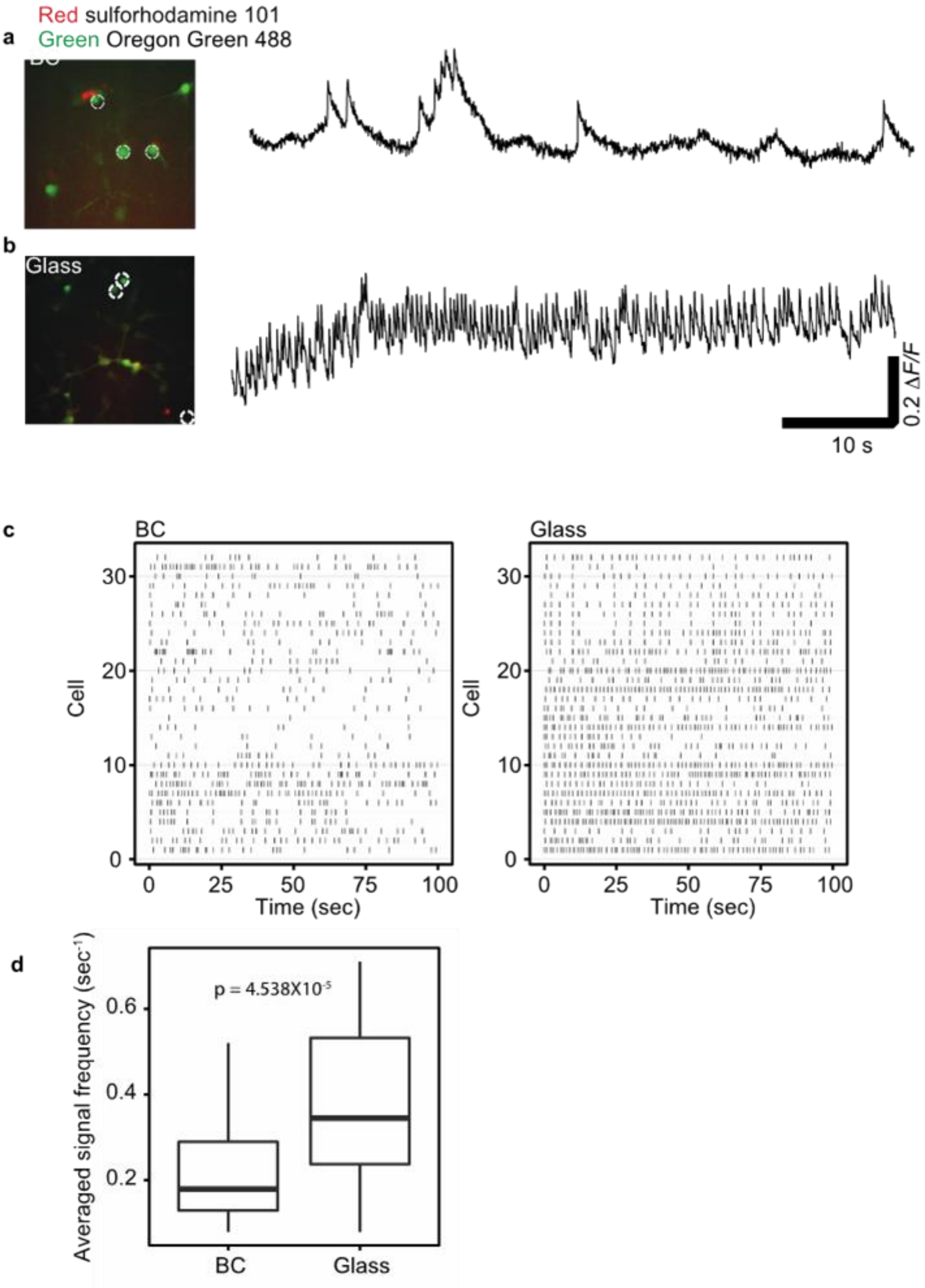

Figure 4 | Comparison of calcium signalling of cultured neuron on BC and glass substrates. a,b, calcium signalling of 14-div cultured neurons show difference calcium spike frequency and duration. Cell density is 20-30/mm^2. c, d, collection of calcium spike peakes with respect to time for 14-div neuron on glass and BC

the topographic stimulation of growth cone via nanoscale fiber morphology, however, there need to be more experimental evidences to prove this hypothesis.

One of the obvious advantages of 3D neuronal culture for a model neuronal network study is the addition of spatial degree of freedom to the network structure. Especially, the extant central nervous system has a highly-organized layered structure where the neuronal circuit in each layer is capable of information processing in a parallel manner[34,35]. This type of structural integrity is intrinsically hard to be realized in a conventional 2D network system. To mimic the stacked layers of 2D neuronal circuits, the dissociated neuron cells were seeded on to both sides of GO and rGO-composited BC scaffolds successively and cultured in 20 days *in vitro* (Figure 4a). The resultant 3D network was fixed and stained with dendrite (MAP2) and axonal (Tau) markers for interrogating neurite outgrowth behaviour and topographic connectivity between layers. In contrast to axons moving vertically, the majority of dendrites on both top and bottom BC surfaces are confined on the same surface. The interlayer connectivity and synapse formation were confirmed by tracing single dendrites and axons and staining the synaptic proteins, respectively (Figure 4c). Approximately 15% of the neurons plated on the top layer have reached the opposite layer and their 90% exhibit pyramidal neuron-type morphologies with branching at a certain depth. Interestingly, there exists a strong correlation between the frequency and the depth of axonal branching. The most of branching points are concentrated at the depth of ~800 um which is very close the metric reported in the in vivo system revealing that the neuronal cells on the present culture platform mimic well those in the physiological condition. Furthermore, the calcium imaging of the 3D cultured neurons on BC show much more random pattern of neuronal activity which is characteristic of stochastic activity of the in vivo neuronal network than that of the 2D model system on glass.

Conclusions

Considering all the above mentioned results including the soma and axonal morphologies, neurite outgrowth pattern, focal adhesion protein expression, and intracellular calcium activity of the neuronal cells cultured on top as well as their optical transparency and appropriate mechanical property, the present nanoengineered BC-based composite materials are well suited for the 3D neuronal culture platform and will serve as a valuable tool for accessing the mini-brain-like 3D neuronal network to interrogate many critical questions in neurobiology and neural engineering fields.

References

[1]. Focus on neurotechniques. *Nat. Neurosci.* **16,** 771–771 (2013).

[2]. Boguski, M. S. & Jones, A. R. Neurogenomics: at the intersection of neurobiology and genome sciences. *Nat. Neurosci.* **7,** 429–433 (2004).

[3]. Xie, J. *et al.* Nanofiber Membranes with Controllable Microwells and Structural Cues and Their Use in Forming Cell Microarrays and Neuronal Networks. *Small* **7,** 293–297 (2011).

[4]. Pautot, S., Wyart, C. & Isacoff, E. Y. Colloid-guided assembly of oriented 3D neuronal networks. *Nat. Methods* **5,** 735–740 (2008).

[5]. Yu, M. *et al.* Semiconductor Nanomembrane Tubes: Three-Dimensional Confinement for Controlled Neurite Outgrowth. *ACS Nano* **5,** 2447–2457 (2011).

[6]. Dubois-Dauphin, M. L. *et al.* The long-term survival of in vitro engineered nervous tissue derived from the specific neural differentiation of mouse embryonic stem cells. *Biomaterials* **31,** 7032–7042 (2010).

[7]. Lampe, K. J., Antaris, A. L. & Heilshorn, S. C. Design of three-dimensional engineered protein hydrogels for tailored control of neurite growth. *Acta Biomater.* **9,** 5590–5599 (2013).

[8]. Mahoney, M. J. & Anseth, K. S. Three-dimensional growth and function of neural tissue in degradable polyethylene glycol hydrogels. *Biomaterials* **27,** 2265–2274 (2006).

[9]. Luo, Y. & Shoichet, M. S. A photolabile hydrogel for guided three-dimensional cell growth and migration. *Nat. Mater.* **3,** 249–253 (2004).

[10]. Melissinaki, V. *et al.* Direct laser writing of 3D scaffolds for neural tissue engineering applications. *Biofabrication* **3,** 045005 (2011).

[11]. Annabi, N. *et al.* 25th Anniversary Article: Rational Design and Applications of Hydrogels in Regenerative Medicine. *Adv. Mater.* **26,** 85–124 (2014).

[12]. Thiele, J., Ma, Y., Bruekers, S. M. C., Ma, S. & Huck, W. T. S. 25th Anniversary Article: Designer Hydrogels for Cell Cultures: A Materials Selection Guide. *Adv. Mater.* **26,** 125–148 (2014).

[13]. Burdick, J. A. & Murphy, W. L. Moving from static to dynamic complexity in hydrogel design. *Nat. Commun.* **3,** 1269 (2012).

[14]. Iwamoto, S., Kai, W., Isogai, A. & Iwata, T. Elastic Modulus of Single Cellulose Microfibrils from Tunicate Measured by Atomic Force Microscopy. *Biomacromolecules* **10,** 2571–2576 (2009).

[15]. Iguchi, M., Yamanaka, S. & Budhiono, A. Bacterial cellulose—a masterpiece of nature's arts. *J. Mater. Sci.* **35,** 261–270 (2000).

[16]. Nogi, M., Handa, K., Nakagaito, A. N. & Yano, H. Optically transparent bionanofiber composites with low sensitivity to refractive index of the polymer matrix. *Appl. Phys. Lett.* **87,** 243110 (2005).

[17]. Nogi, M. & Yano, H. Transparent Nanocomposites Based on Cellulose Produced by Bacteria Offer Potential Innovation in the Electronics Device Industry. *Adv. Mater.* **20,** 1849–1852 (2008).

[18]. Williams, W. S. & Cannon, R. E. Alternative Environmental Roles for Cellulose Produced by Acetobacter xylinum. *Appl. Environ. Microbiol.* **55,** 2448–2452 (1989).

[19]. Valla, S. & Kjosbakken, J. Cellulose-negative Mutants of Acetobacter xylinum. *J. Gen. Microbiol.* **128,** 1401–1408 (1982).

[20]. Schramm, M. & Hestrin, S. Factors affecting Production of Cellulose at the Air/ Liquid Interface of a Culture of Acetobacter xylinum. *J. Gen. Microbiol.* **11,** 123–129 (1954).

[21]. Wei, B., Yang, G. & Hong, F. Preparation and evaluation of a kind of bacterial cellulose dry films with antibacterial properties. *Carbohydr. Polym.* **84,** 533–538 (2011).

[22]. Heller, W. Remarks on Refractive Index Mixture Rules. *J. Phys. Chem.* **69,** 1123–1129 (1965).

[23]. Trappmann, B. *et al.* Extracellular-matrix tethering regulates stem-cell fate. *Nat. Mater.* **11,** 642–649 (2012).

[24]. Discher, D. E., Mooney, D. J. & Zandstra, P. W. Growth Factors, Matrices, and Forces Combine and Control Stem Cells. *Science* **324,** 1673–1677 (2009).

[25]. Vogel, V. & Sheetz, M. Local force and geometry sensing regulate cell functions. *Nat. Rev. Mol. Cell Biol.* **7,** 265–275 (2006).

[26]. Fraley, S. I. *et al.* A distinctive role for focal adhesion proteins in three-dimensional cell motility. *Nat. Cell Biol.* **12,** 598–604 (2010).

[27]. Petroll, W. M., Ma, L. & Jester, J. V. Direct correlation of collagen matrix deformation with focal adhesion dynamics in living corneal fibroblasts. *J. Cell Sci.* **116,** 1481–1491 (2003).

[28]. Geiger, B., Spatz, J. P. & Bershadsky, A. D. Environmental sensing through focal adhesions. *Nat. Rev. Mol. Cell Biol.* **10,** 21–33 (2009).

[29]. Discher, D. E., Janmey, P. & Wang, Y. Tissue Cells Feel and Respond to the Stiffness of Their Substrate. *Science* **310,** 1139–1143 (2005).

[30]. Stricker, J., Beckham, Y., Davidson, M. W. & Gardel, M. L. Myosin II-Mediated Focal Adhesion Maturation Is Tension Insensitive. *PLoS ONE* **8,** e70652 (2013).

[31]. Kuo, J.-C., Han, X., Hsiao, C.-T., Yates Iii, J. R. & Waterman, C. M. Analysis of the myosin-II-responsive focal adhesion proteome reveals a role for β-Pix in negative regulation of focal adhesion maturation. *Nat. Cell Biol.* **13,** 383–393 (2011).

[32]. Kim, D.-H. *et al.* Actin cap associated focal adhesions and their distinct role in cellular mechanosensing. *Sci. Rep.* **2,** (2012).

[33]. Prager-Khoutorsky, M. *et al.* Fibroblast polarization is a matrix-rigidity-dependent process controlled by focal adhesion mechanosensing. *Nat. Cell Biol.* **13,** 1457–1465 (2011).

[34]. Kandel, E., Schwartz, J., Jessell, T., Siegelbaum, S. & Hudspeth, A. J. *Principles of Neural Science, Fifth Edition*. (McGraw Hill Professional, 2013).

[35]. Andersen, P. *The Hippocampus Book*. (Oxford University Press, 2007).

국문초록

최근 줄기세포와 조직공학의 발전과 더불어 줄기세포 기반의 재생의학은 심장 질환과 뇌 질환과 같은 다양한 난치병 치료에 희망적인 전략을 제공하고 있다. 그럼에도 불구하고 이러한 난치병의 치료에는 한계가 많을 뿐만 아니라 해가 지나면서 이병으로 사망하는 환자는 매년 증가 추세에 놓여있다. 이에 이러한 난치병을 효과적으로 치료할 대체치료방법의 개발은 중요하다. 최근 들어 그래핀의 표면적, 뛰어난 전자전달 능력, 높은 전기전도성과 같은 우수한 성질은 그래핀 기반의 새로운 바이오 의학 시대를 여는데 크게 이바질 할 것으로 인식되고 있다.

본 학위논문은 세포조절 및 조직공학 응용에 최적화된 이차원 혹은 삼차원 형태의 플랫폼 개발에 대한 것이다. 이에 따른 본 논문의 구체적인 목표는 다음과 같다. (1) 줄기세포의 성장 및 분화를 위한 2차원 그래핀 플랫폼 개발과 이의 세포 분화 효과를 조사하기 위하여 세포 신호 분자와 세포 외기 질 단백질의 분화도 등의 분석을 통한 메커니즘을 규명하는 것이다. (2) 나노 공학적 접근을 통한 세포 미세환경과 유사한 3차원 플랫폼을 개발하여 세포의 거동 및 분화 조절을 위한 새로운 방안제시이다.

본 논문의 주요 결과는 다음과 같다. 첫째, 처음으로 그래핀 위에서 줄기세포가 3차원 구 형태로 줄기세포가 뭉쳐지는 현상을 발견하였다. 둘째, 최초로 아무런 성장인자가 없는 상태에서도 그래핀 위에서 줄기세포가 cardiomyogenic 로의 분화로 촉진하는 과정을 규명하였다. 마지막으로, 배아줄기세포가 그래핀 위에서 중배엽 세포와 내배엽 세포로 단계적 분화과정을 거치고 결론적으로

cardiomyogeic으로의 분화를 촉진 시킬 수 있음을 증명하였다. 하지만 성공적인 생체조직공학의 임상적 적용을 위해서, 세포가 발달할 수 있도록 생체 내 조건과 유사한 3차원 구조를 가지면서 세포의 부착 및 기능 수행을 극대화한 플랫폼의 개발은 필수적인 요소이다. 최근에 그래핀의 바이오 의학 소재로의 혁신적인 플랫폼으로써 줄기세포 분화를 조절하는 메커니즘 및 세포 배양 플랫폼으로써 제안됐다. 이에 그래핀이 복합화된 삼차원 투명 플랫폼의 개발은 재생의학과 이를 이용한 치료 분야에 아주 시급하게 요구되고 있다. 이에 따라 두 번째 분야 연구에서는 탄소 나노 재료기반의 3차원 플랫폼의 개발과 이 플랫폼의 성공적인 조직재생으로의 적용에 관한 것이다. 특별히, 그래핀을 실제 질병 모델에 적용하여 조직 재생에 효과적인 나노 복합체로써 임상적 이용이 가능한지 확인하는 것은 중요하다. 본 학위 논문에서 이러한 것을 가능하게 실현해 보이고자 뼈 재생을 위한 카본 나노튜브가 복합된 바이오 플랫폼을 제작하는 놀라운 방법을 제시하였다. 마지막으로 그래핀이 복합화된 3차원의 층상구조를 가진 플랫폼을 개발하였고 그 플랫폼을 기본적인 신경연구에 활용하는 연구를 진행하였다. 결과적으로 본 학위논문에선 조직공학과 재생의학에 최적화된 플랫폼을 개발하였으며 그에 대한 체계적인 연구 결과를 제시 하였다.

주요어: 그래핀, 카본나노튜브, 줄기세포, 생체모방, 생체 재료, 조직공학

학 번: 2011-30906

이학박사학위논문

Engineering Carbon Nanomaterials for Stem cell and Tissue regeneration
탄소 나노 재료를 이용한 줄기세포 조절 및 조직 재생에 관한 연구

2015 년 2 월

서울대학교 대학원

화학부 물리화학 전공

박 수 범

Engineering Carbon Nanomaterials for Stem cell and Tissue regeneration

탄소 나노 재료를 이용한 줄기세포 조절 및 조직 재생에 관한 연구

지도교수: 홍병희

이 논문을 이학박사 학위논문으로 제출함

2015년 10월

서울대학교 대학원

화학부 물리화학전공

박수범

박수범의 이학박사 학위논문을 인준함

2015년 1월

위원장 장두전 ㊞

부위원장 홍병희 ㊞

위원 이연 ㊞

위원 조성표 ㊞

위원 윤명한 ㊞

Ph. D. Thesis

Engineering Carbon Nanomaterials for Stem cell and Tissue regeneration

Supervisor: Professor Byung Hee Hong

Major: Physical Chemistry

By Subeom Park

Department of Chemistry

Graduate School of Seoul National University

2015

Abstract

With the recent advances in stem cell engineering and tissue regeneration, stem cell-based regenerative medicine provides a promising strategy for the treatment of heart failure, neuronal disorders or neurodegenerative diseases, which are still one of the leading causes of human death and disability in the world. Nevertheless, the current clinical treatments for heart failure, neuronal disorders or neurodegenerative disease are quite limited, and the number of people affected by these diseases consistently increases every year. As a direct result, there is a great need to discover alternative therapies for these disorders or diseases. Recently, graphene has been recognized as a biomimetic nanomaterial and has been proposed for a number of biomedical applications because of their fascinating properties different from those of the carbon-based graphitic materials. This dissertation is the result of an effort to develop 2D and 3D platforms for controlling cell microenvironment for various cell and tissue engineering applications. The specific objectives of my thesis are as follow: (1) the development of an efficient 2D platform for the growth and differentiation of stem cells, which is crucial for autologous cell therapy and tissue engineering to treat various disorders and diseases, and the investigation of the effects of graphene on the enhanced differentiation process through analyzing the expressions of extracellular matrix (ECM) proteins and cell signaling molecules, (2) the improvement of nanoengineering approaches for controlling 3D cell microenvironment and the use of these facile techniques to regulate cell fate decisions. The main results of my dissertation research can be summarized as follows.

First, we found that the 3D spheroid structure could be formed from aggregated hMSCs grown on monolayer of graphene without the use of any external factors. Second, we have provided the first demonstration that graphene can be used as a stem cell culture substrate to promote the cardiomyogenic differentiation process of MSCs without the use of any exogenous chemical inducers. Finally, the culture of hESCs on graphene promotes the stepwise differentiation of these cells into mesodermal cells and endodermal cells and their subsequent cardiomyogenic differentiation compared with their culture on glass. However, for the success of clinical regenerative application, a three-dimensional (3D) scaffold is a demanding field in terms of development of microenvironments and appropriate synergistic cell guidance cues. Thus, the following part II of the thesis presents the development and applications of carbon nanomaterial-based 3D scaffolds. Recently, graphene has been proposed as a tool for pioneering approach in the progress of designing nano-engineered cell culture platforms or scaffolds. Development of transplantable 3D hybrid graphene scaffold *in vivo* that can be applied in practical use for regenerative therapy is urgently needed. Especially, it is important to verify the superiority of graphenes as regenerative nanocomposites by applying to real disease animal model. Here, we developed a novel method for fabricating a hybrid bioscaffold composed of CNTs and BC for bone regeneration. Lastly, we developed a strategy to hybridize graphene with the 3D layer by layer scaffold and investigate its impact on the fundamental neuron study. This dissertation provides the details of my work on all projects related to designing scaffolds for tissue engineering and regenerative

Keywords: Graphene, Carbon nanotubes, Stem cells, Biomimetic, Biomaterials, Tissue engineering

Student Number: 2011-30906

Contents

1. General introduction

Part I 2D Graphene based stem cell engineering

2. Graphene-directed spheroid formation of mesenchymal stem cells for enhanced neuronal differentiation

3. Graphene enhances the cardiomyogenic differentiation of human embryonic stem cells

4. Graphene-regulated cardiomyogenic differentiation process of mesenchymal stem cells by enhancing the expression of extracellular matrix proteins and cell signaling molecules

Part II Engineering nature-driven three-dimensional bioscaffolds with carbon nanomaterials

5. Binding behavior of hybrid system for the APCLP coated-carbon nanotube and graphene with bacterial cellulose

6. *In Situ* hybridization of carbon nanotubes with bacterial cellulose for three-dimensional bioscaffolds

7. *In vivo*-like three-dimensional neuronal networks engineered by Graphene bioscaffolds

Abstract (Korean)

Acknowledgement

List of Figures

Chapter 1

Figure 1. Graphene materials and their biological interactions. a, A parameter space for the most widely used graphene materials can be described by the dimensions and surface functionalization of the material, the latter defined as the percentage of the carbon atoms in sp3 hybridization. Green squares represent epitaxially grown graphene; yellow, mechanically exfoliated graphene; red, chemically exfoliated graphene; blue, graphene oxide. Note that a number of other graphene-related materials (such as graphene quantum dots and graphene nanoribbons) are also being used in experiments. b, Possible interactions between graphene-related materials with cells (the graphene flakes are not to scale). (a) Adhesion onto the outer surface of the cell membrane. (b) Incorporation in between the monolayers of the plasma membrane lipid bilayer. c, Translocation of membrane. d, Cytoplasmic internalization. e, Clathrin-mediated endocytosis. f, Endosomal or phagosomal internalization. g, Lysosomal or other perinuclear compartment localization. h, Exosomal localization. The biological outcomes from such interactions can be considered to be either adverse or beneficial, depending on the context of the particular biomedical application. Different graphene-related materials will have different preferential mechanisms of interaction with cells and tissues that largely await discovery.

Figure 2. Schematic diagram depicting the possible interaction between carbon nanomaterials with stem cells fates.

Figure 3. Schematic diagram depicting the possible ability of carbon nanomaterials to induce stem cells differentiation into specific cell lineages.

Chapter 2

Figure 1. Fabrication and characterization of highly uniform graphene for the growth and neuronal differentiation of stem cells. a, Schematic of the spheroid formation and neuronal differentiation of hMSCs using high-quality graphene. b, Raman spectroscopy of the transferred graphene. c, TEM image of a graphene sheet on a TEM grid. d, The SAED pattern. e, Intensity profile of the diffraction spots along a line connecting points p and q in the single-layer graphene diffraction pattern. The uniform intensity profile between the inner and outer spots proves that the graphene sheet consists of a single layer. f, High-resolution STEM image of at low-magnification. g, High-resolution STEM image of at high-magnification.

Figure 2. Growth of hMSCs on highly uniform graphene. a, Representative immunofluorescent images of hMSCs cultured on a graphene-uncoated glass substrate and high-quality graphene. b, Quantification of the cell body and the nucleus, indexed by the axial ratio of the cell body and the width and length of the nucleus. c, Quantification of the amount of focal adhesion. One-hundred cells were used in the quantification process. d, Western blot analysis and quantification of the levels of Cx43 expression in the hMSCs cultured. e, Proliferation of cells on the substrates for 7 days. Three independent experiments were conducted. f, Representative immunofluorescent images of STRO-1 and a western blot analysis of

the hMSCs cultured on the substrates for 10 days. The error bars represent the standard deviation.

Figure 3. Neuronal differentiation of hMSCs on highly uniform graphene. a, Representative phase-contrast images of the hMSCs cultured on the substrates in the growth medium or the neuronal differentiation medium. b, Representative immunostaining images of TUJ1, NeuN, GFAP, and DAPI of the hMSCs cultured in the neuronal differentiation medium for 5 days. c, Representative Nissl staining images of hMSCs cultured in the neuronal differentiation medium for 5 days. d, the neuritie lengths e. One-hundred cells were used in the quantification process. f, qRT–PCR analysis of hMSCs cultured in the neuronal differentiation medium for 5 days. Three independent experiments were conducted, and the error bars represent the standard deviation.

Figure 4. Response of neuronal differentiated cells from hMSCs grown on highly uniform graphene to high K^+ stimulation on high-quality graphene. The cells were pre-incubated with Fluo-4 AM dye and imaged before and after the stimulations. Representative fluorescence images on the fluorescence intensity change on the cells were obtained before and after high K^+ stimulations. Representative plot of the relative fluorescence intensity change $\Delta F/F$ of the cell indicated by the red arrow.

Figure 5. A case study for autologous stem cell based therapy. a, An *in vitro* protocol to highlight the potential of the differentiated neurons from hMSCs grown on graphene as a source for cell therapy to treat neuronal diseases. It was hypothesized that the differentiated neurons from hMSCs grown on graphene could be transferred into the body to treat neuronal diseases. b, Representative Nissl staining images of

the cells cultured on the glass substrates in the growth media for 2 days (total 10 day culture) after re-seeding the detached differentiated hMSCs onto graphene or a glass substrate using the trypsin treatment.

Figure S1. Schematic of fabrication of the high quality graphene on glass substrate for growth and neuronal differentiation of stem cells.

Figure S2. a, AFM image of graphene growth on copper foil. b, Atmosphere STM image of graphene grown on Cu foil. c, Typical optical microscope image of graphene transferred onto 300 nm SiO2/Si substrate. d, UV–vis spectra of transferred graphene on the glass substrate. e, Contact angle of graphene and coverslip f, Sheet resistance mapping of the graphene.

Figure S3. AFM topography images of the graphene and glass substrate. The values indicate the roughness of the surfaces.

Figure S4. a, Low magnification images of hMSCs cultured on the graphene and glass substrate for 1 day. The cells were stained by crystal violet to show the formation of 3D spheroids on the graphene. b, Representative phase-contrast images of hMSCs cultured on the graphene for 1 day and 7 days, respectively. The white arrows indicate the spheroids of hMSCs.

Figure S5. Representative immunostaining images of actin, nucleus, and fibronectin on the graphene and glass substrate after culturing hMSCs for 7 days.

Chapter 3

Figure 1. Preparation and characterization of large-area graphene substrates. a, Schematic of the preparation process used to produce the graphene coating on a glass

coverslip. b, A typical optical microscopic image of graphene transferred onto 300-nm-thick SiO_2/Si substrate. c, Photograph d, contact angle of a glass coverslip and graphene on a glass coverslip. e, Raman spectroscopy of the transferred graphene. f, UV-visible spectra of transferred graphene on a glass coverslip and a glass coverslip substratum, showing the transparency of the graphene on the coverslip. g, TEM image of graphene on a TEM grid. h, SAED pattern. i, Sheet resistance of monolayer graphene on a glass coverslip.

Figure 2. The coating of graphene with VN is required to achieve a high viability of hESCs cultured on the graphene. hESCs were cultured on graphene for two days. a, Light microscopic images of hESCs cultured on the graphene. b, Fluorescence microscopic images of hESCs stained with FDA and EB. The green and orange-red colors indicate viable and dead cells, respectively. c, SEM image of hESCs cultured on graphene. The scale bars indicate (a) 200 μm, (b) 100 μm, and (c) 20 μm.

Figure 3. Culture on graphene enhances the mesodermal and endodermal lineage differentiation of hESCs. a, A schematic diagram for the cardiomyogenic differentiation of hESCs in a two-dimensional, stepwise differentiation system. b, The mesodermal c, cardiac mesodermal d, endodermal, and e, ectodermal gene expression profiles of hESCs cultured for 21 days on Matrigel-coated glass (Matrigel), VN-coated glass (glass), or VN-coated graphene (graphene), as determined by qRT-PCR assay. The values were normalized to the levels obtained for the Matrigel group (n=4 per group, $^*p<0.05$ versus Matrigel, $\#p<0.05$ versus glass).

Figure 4. Culture on graphene enhances the cardiomyogenic differentiation of hESCs. a, A schematic diagram of the gene expression profile during the cardiomyogenic differentiation process of hESCs. b, Cardiomyogenic gene expression profiles of hESCs cultured for 21 days on Matrigel-coated glass (Matrigel), VN-coated glass (glass), or VN-coated graphene (graphene), as determined by qRT-PCR assay. The values were normalized to the levels obtained for the Matrigel group (n=4 per group, *p<0.05 versus Matrigel, #p<0.05 versus glass).

Figure 5. Culture on graphene enhances cardiac-specific ECM expression in hESCs. Gene expression profiles of extracellular matrix proteins in hESCs cultured for 21 days on Matrigel-coated glass (Matrigel), VN-coated glass (glass), or VN-coated graphene (graphene), as determined by qRT-PCR assay. The values were normalized to the levels obtained for the Matrigel group (n=4 per group, *p<0.05 versus Matrigel, #p<0.05 versus glass).

Figure 6. Mechanisms underlying the graphene-enhanced cardiomyogenic differentiation Nanoroughness of graphene, FAK, and ERK signaling. a, AFM images and surface nanoroughness of VN-coated glass (glass group) and VN-coated graphene (graphene group). b, a schematic diagram of the signal transduction pathways associated with the cardiomyogenic differentiation of hESCs cultured on graphene. The enhanced hESC adhesion and the subsequent upregulation of ERK signaling of hESCs cultured on graphene were likely attributed to the nanoroughness of the graphene. ECM: extracellular matrix, α, β: integrin α and β subunits, PAX: paxillin, VIN: vinculin. c, Western blot analyses of hESCs cultured on Matrigel-

coated glass (Matrigel), VN-coated glass (glass), or VN-coated graphene (graphene) to analyze the molecules involved in the signal transduction pathways, and quantification of the relative protein expression levels of the cell signaling molecules. The values were normalized to the levels obtained for the Matrigel group (n=3 per group, *p<0.05 versus Matrigel, #p<0.05 versus glass).

Chapter 4

Figure 1. Characterization of graphene substrates. a, AFM topography images, b, photographs, and c, contact angle images of (i) coverslip and (ii) graphene on coverslip. d, Raman spectroscopy of graphene. e, Transparency of graphene films transferred on coverslip. TEM image of graphene sheet on a TEM grid at f, low and g, high magnifications. h, The SAED pattern. i, Intensity profile of the diffraction spots along a line connecting points E and F in the single-layer graphene diffraction pattern. The uniform intensity profile between the inner and outer spots proves that the graphene sheet consists of a single layer.

Figure 2. *In vitro* biocompatibility of graphene. a, Live/dead assay of MSCs cultured on graphene and coverslips for 3 days and 1 week. The live cells were stained with calcein-AM (green), and the dead cells were stained with ethidium homodimer (red). The scale bar represents 200 μm. b, The number of live cells is expressed relative to the number of live cells on a coverslip on day 1. The number of live cells was counted using CCK-8. c, Upregulation of Bcl-2, an anti-apoptotic marker, and downregulation of caspase-3, a pro-apoptotic marker, in MSCs cultured on graphene for 3 weeks relative to MSCs cultured on coverslips, as evaluated by qRT-PCR. *p

< 0.05 compared to MSCs cultured on coverslips. d, Proliferation of MSCs cultured on coverslips and graphene. The proliferation was evaluated by PCNA staining. The proliferating cells were stained with PCNA (red), and the nuclei were stained with DAPI (blue). The scale bar represents 200 μm. e, Growth of MSCs cultured on graphene and coverslips. The growth was evaluated by counting the number of cells at various time points using hemocytometer.

Figure 3. Enhanced expression of cardiomyogenic genes in MSCs cultured on graphene without using chemical induction materials. Two and three weeks after cell seeding, the MSCs cultured on graphene exhibited an upregulation of the mRNA expression of an early cardiomyogenic transcriptional factor (GATA4), cardiomyogenic contractile proteins (cardiac actin, β-MHC, cTnT, MLC2a, and MLC2), and gap junction protein (Cx43) compared with MSCs cultured on coverslips. The mRNA expression levels were evaluated by qRT-PCR. *$p < 0.05$ compared to MSCs cultured on coverslips.

Figure 4. Enhanced gene expression of ECM proteins in MSCs cultured on graphene. The MSCs cultured on graphene for 2 weeks exhibited an upregulation of the mRNA expression of Col I, Col III, Col IV, fibronectin, and laminin, which are known to promote the cardiomyogenic differentiation of stem cells compared with those on coverslips. The mRNA expression levels were evaluated by qRT-PCR. *$p < 0.05$ compared to MSCs cultured on coverslips.

Figure 5. Activation of molecules involved in cardiomyogenic differentiation and survival-related signal transduction pathways in MSCs cultured on graphene. a, Western blot analyses of MSCs cultured on graphene or coverslips for 3 weeks to

analyze the molecules involved in the signal transduction pathways. Quantification of the relative protein expressions of the cell signaling molecules (n = 3). *$p < 0.05$ compared to MSCs cultured on coverslips. b, A schematic diagram of the signal transduction pathways associated with cardiomyogenic differentiation and survival. Arrows indicate expression upregulations.

Figure S1. Schematic of fabrication of the high quality graphene on glass substrate for growth and neuronal differentiation of stem cells.

Chapter 5

Figure 1. Dispersion behavior of CNT

Figure 2. Optimized geometries

Figure 3. Front and side views of a, the geometry optimized by DFT calculations and b, that obtained from molecular dynamics simulations for the cellulose-polymer (HPOEM)/CNT system

Figure 4. Front and side views of geometries obtained from the molecular dynamics simulations for a, cellulose-cellulose, b, polymer(HPOEM)-CNT hybrid, and c, cellulose-CNT systems

Figure 5. Front and side views of geometries obtained from the molecular dynamics simulations for a, cellulose-CNT, b, polymer(HPOEM)-CNT, and **c,** cellulose-polymer(HPOEM)/CNT systems for the time scale (0.0 ps - 4.0 ps - 12.5 ps)

Figure 6. Molecular dynamic simulations for a, rGO-BC and b, GO-BC

Figure 7. Molecular dynamic simulations for a, rGO-APCLP and b, GO-APCLP

Figure 8. Molecular dynamic simulations for APCLP-coated a, rGO-BC and b, GO-

BC

Chapter 6

Figure 1. APCLP-mediated dispersion of CNTs. a, MD simulation of APCLP-coated CNT. b, SEM and TEM images of CNTs before and after APCLP coating. c, Fourier transform infrared spectroscopy spectrum of CNT, APCLP and APCLP-coated CNT. d, Colloidal stability of CNT and APCLP-coated CNT after centrifugation and after 3 months. e, Colloidal stability of APCLP-coated CNT in various pH conditions of culture medium.

Figure 2. APCLP-induced hybridization of CNTs and BC. a, Schematic representation of APCLP-coated CNT-BC hybridization. b, Binding energies measured by ab initio calculations. c, MD simulations for CNT-BC and APCLP-coated CNT-BC. d, Schematic illustration for the fabrication processes of BC, CNT-BC-Imm and CNT-BC-Syn.

Figure 3. TEM analyses of CNT-BC hybrid. a, TEM images of BC, CNT-BC-Imm and CNT-BC-Syn. b, Thickness distribution of BC on CNTs, showing the partial exposure of bare CNTs. c, EELS spectra of BC and CNT-BC-Syn showing the core-shell hybridization structure of CNT-BC-Syn.

Figure 4. Analyses showing the homogenous distribution of CNTs in CNT-BC-Syn. a, Cross-sectional optical images of BC, CNT-BC-Imm and CNT-BC-Syn. Scale bars, 20 µm. b, SEM images of BC, CNT-BC-Imm and CNT-BC-Syn with top and cross-sectional views. Scale bar, 5 µm. c, Raman mapping of CNT-BC-Imm and CNT-BC-

Syn. d, Force mapping of BC, CNT-BC-Imm and CNT-BC-Syn on the surface measured by contact-mode AFM. Scale bars, 2 μm.

Figure 5. Bone regeneration efficacy of the scaffolds. a, Bone regeneration evaluated by micro-CT analyses. Quantification of the bone formation area of defects. b, Goldner's trichrome staining of mouse calvarial defect areas. Quantification of bone formation area and bone density of defects. **c,** Immunohistochemistry of mouse calvarial defect areas. DAPI staining indicates osteoconductivity of the scaffolds. Osteocalcin staining indicates osteoinductivity of the scaffolds. Scale bars, 2 mm. *p < 0.05 compared to any other group. #p < 0.05 compared to no treatment, BC and CNT-BC.

Figure S1. BC preparation and optimization processes and parameters. a, Images of *G. xylinus* and BC. b, Effect of pH, temperature, culture time, APCLP concentration and ethanol concentration on BC yield. Cells were cultivated for 7 days in a mannitol medium.

Chapter 7

Figure 1. Fabrication and characterization of bare/graphene composited BC. a, Schematic explanation of Acetobacter Xylinum producing cellulose nanofiber and in situ composition of graphene. b, Top view and lateral view of bacterial cellulose exhibit nanofibrillar cellulose and stacked layered structure, respectively. c, Top view of GO (left) and rGO (right) composited BC. d, High resolution TEM image of bare bacterial cellulose and their crystallinity. e, Raman spectroscopic measurement confirms the presence of GO and rGO with corresponding vibration peaks. f. Liquid

AFM measurement of elastic modulus along normal direction.

Figure 2. Detailed neuronal morphology and controlled z-directional neuronal outgrowth. a, scanning electron microscope images represent interfacial region between 3-div neuron and BC. b z-directional neuronal outgrowth of bare and graphene composited BC. MAP2 and Tau labels neuronal dendrites and axons, respectively. c, statistical representation of z-directional neuronal outgrowth depending presence of graphene composition d, BET measurements exhibit modulation of bacterial cellulose porosity by means of graphene composition. e, schematic figure of outgrowing neuron toward to counter BC surfaces. f, Fluorescence y-stacked image of widely culture (3.5 mm × 3.5 mm × 1 mm) 20-div neuron. g, Fluorescence light intensity decay of fluorescence beads depending on depth of BC.

Figure 3. Neuronal kinetics in BC a, comparison of neuronal development on glass and BC substrate b, statistical analysis of neuronal polarity. c, time evolutional trajectory of 3-div outgrowing axon on BC and glass substrate. (n = 20 for BC and glass, 5 sec for time interval) d, extracted quantitative information of outgrowing axon reveal total traveling length and final length of axon which composed or substrate by forward and backward motion. e, traced 20-div neuronal morphology on BC exhibits delicate and distinct neuronal sub-cell type. f, synchronization of axon branching at the certain depth (700 μm) of BC.

Figure 4. Comparison of calcium signalling of cultured neuron on BC and glass substrates. a,b, calcium signalling of 14-div cultured neurons show difference calcium spike frequency and duration. Cell density is 20-30/mm^2. c, collection of

calcium spike peakes with respect to time for 14-div neuron on glass and BC substrate.

List of Tables and Schemes

Scope and Format of Dissertation

The dissertation is divided into two parts comprised of six research chapters. Chapter 1 describe the current advances made with carbon nanomaterials based platforms in the stem cell engineering field and the challenges facing these exciting new tools both in terms of biological activity and toxicological profiling *in vitro* and *in vivo*. The next three chapter provide the contents for Part I. Part I developed a series of graphene as an efficient platform for stem cell based therapy. In Chapter 2 shows that monolayer graphene-directed growth and neuronal differentiation of mesenchymal stem cells. In Chapter 3 describes that graphene-regulated cardiomyogenic differentiation process of mesenchymal stem cells by enhancing the expression of extracellular matrix proteins and cell signaling molecules. In Chapter 4 shows that graphene promotes the stepwise differentiation of embryonic stem cells into mesodermal cells and endodermal cells and their subsequent cardiomyogenic differentiation. The hybridization of functional nanomaterials with three-dimensional (3D) scaffolds for biomedical applications has been extensively studied, but further advancements have been hampered by unstable integration and inhomogeneous distribution of the nanomaterials. Part II is comprised of the next three chapters and develop a series of nature driven architecture for tissue engineering with controlled properties. In Chapter 5 provides a simple and nontoxic method for dispersal of carbon nanomaterials was investigated using amphiphilic comb-like polymer (APCLP) and its mechanism was elucidated by simulation. In Chapter 6 demonstrates that a new method for *in situ* hybridization of CNTs with bacterial cellulose (BC) by utilizing APCLP. In Chapter 7 demonstrates that *in vivo*-like three-dimensional neuronal networks engineered by graphene bioscaffolds.

Chapter 1

General introduction

Introduction

1.1 Summary

Stem cells represent a promising tool for tissue engineering and regenerative medicine. Nevertheless, they require a particular niche to grow and regenerate. Carbon nanomaterials have attracted much attention as promising materials for biomedical applications due to their extraordinary physicochemical properties, such as their extracellular matrix-like structure, nanotopographic surface, elasticity, high mechanical strength, high electrical conductivity, and good molecule absorption. Recently, the physicochemical properties of graphene and its biocompatibility have inspired scientists to utilize this material for regulating the growth and differentiation of stem cells engineering. Even though studies on carbon-based nanomaterials are still very much at the ‘nascent’ stage, graphene has been attracting great interest in stem cell engineering and tissue regeneration. In this chapter, we introduce some of the interesting properties of graphene that could impose profound effects on stem cell behavior. After introduction of the properties of graphene, we summarize the advances in graphene-based stem cell engineering applications; how it affects cell behavior and differentiation.

1.2 Histological background

The existence of graphene was predicted over 40 years ago but it was not until 2004 when Geim and Novoselov of Manchester University successfully isolated single layer of graphite for the first time using scotch tapes. In 2005, Geim group discovered particles that follow Fermi Dirac statistics and Philip Kim group of Columbia University found the Half-Integer Quantum Hall Effect in graphene, bringing light to some of the toughest conundrums in physics. Previously the general belief was that graphene cannot maintain its 2D structure in the natural environment and it is thermodynamically unstable with low melting point. However the discovered graphene was very stable and had high crystallinity.

Graphene can be seen as carbon atoms with different electronic characteristics coming together to form two triangular sub-lattice and then form hexagonal lattices as they overlap. The electrons of carbon atoms move around by jumping between atoms of same characteristics. The speed of the electron mobility is 20,000-50,000cm^2/Vs, which is hundred times faster than that of Si semiconductors. Graphene also has low electrical resistivity and therefore have low heat generation. Recently, graphene has been recognized as a biomimetic nanomaterial and has been proposed for a number of biomedical applications because of their fascinating properties different from those of the carbon-based graphitic materials. (e.g., high elasticity, extremely high charge carrier mobility, large surface area, thermal/electrical conductivity, mechanical strength and chemical/mechanical stability). The carbon atoms forming graphene provide the basis for its enhancement with both positive and negative functional groups. In biomedical and nanoengineering, graphene and its derivatives have been used for a variety of applications such as nano carriers for drug/gene delivery, photodynamic therapy of cancer, biosensors, conductive scaffolds, cell imaging and to name a few. It also has the potential to be used as a reinforcement material in hydrogels, biodegradable films, electrospun fibers and other tissue engineering scaffolds. (Fig. 1.)

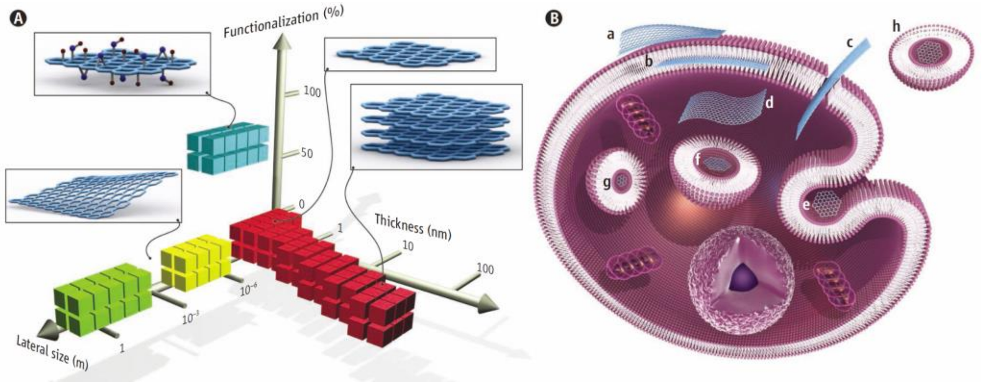

Figure 1 | Graphene materials and their biological interactions. (A) A parameter space for the most widely used graphene materials can be described by the dimensions and surface functionalization of the material, the latter defined as the percentage of the carbon atoms in sp3 hybridization. Green squares represent epitaxially grown graphene; yellow, mechanically exfoliated graphene; red, chemically exfoliated graphene; blue, graphene oxide. Note that a number of other graphene-related materials (such as graphene quantum dots and graphene nanoribbons) are also being used in experiments. (B) Possible interactions between graphene-related materials with cells (the graphene flakes are not to scale). (a) Adhesion onto the outer surface of the cell membrane. (b) Incorporation in between the monolayers of the plasma membrane lipid bilayer. (c) Translocation of membrane. (d) Cytoplasmic internalization. (e) Clathrin-mediated endocytosis. (f) Endosomal or phagosomal internalization. (g) Lysosomal or other perinuclear compartment localization. (h) Exosomal localization. The biological outcomes from such interactions can be considered to be either adverse or beneficial, depending on the context of the particular biomedical application. Different graphene-related materials will have different preferential mechanisms of interaction with cells and tissues that largely await discovery.[1]

1.3 Plausible mechanism of carbon nanomateirals's positive effects on the stem cell and tissue regeneration

It has been well known that surface morphology, physical properties, and chemistry of carbon nanomateirals are critical parameters for regulating cell fates. With recent years, the several possible mechanisms have been reported to explain the interactive effects and further develop carbon nanomateirals as a scaffold for tissue engineering applications. (Fig. 2).

The ability of graphene sheets and carbon nanotubes to enhance the adhesion and differentiation of cells, including neurons[2], osteoblasts[3], cardiomyocytes[4,5], and stem cells has been demonstrated (Fig. 3).

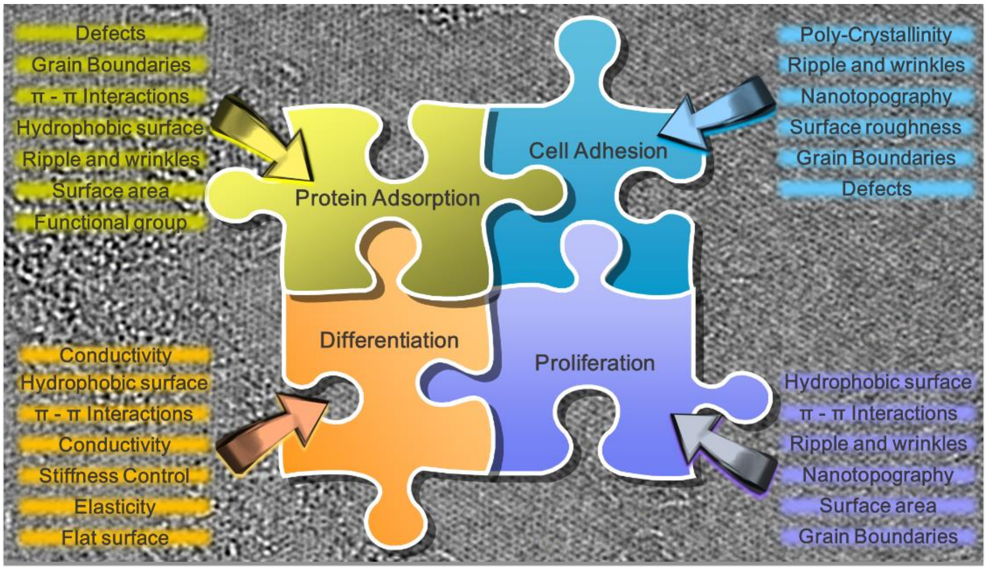

Figure **2 |** Schematic diagram depicting the possible interaction between carbon nanomaterials with stem cells fates

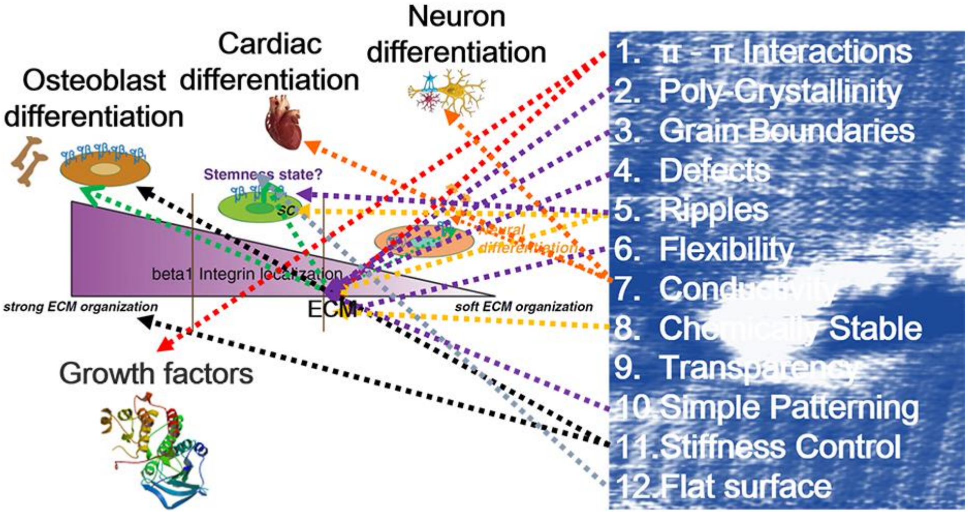

Figure 3 | Schematic diagram depicting the possible ability of carbon nanomaterials to induce stem cells differentiation into specific cell lineages.

Protein adhesion mechanism

Another important aspect of the protein and small molecular chemicals adsorption capacity is the effect on the stem cell niche. In order to or communicate with neighboring cells many of the stem cells secrete signaling molecules that affect both their differentiation status and the influence of their local microenvironments. Graphene show quite high adsorption performance. Solution based reduced graphene oxide (rGO) and Graphene oxide (GO), the oxidized counterpart of graphene, contains functional groups such as oxygen, hydrogen, epoxide, carboxyl and hydroxyl groups in variable ratios which can undergo electrostatic, covalent or hydrogen bonding with protein. CVD graphene, the two dimensional sheet of sp^2-conjugated atomic carbon basal plane, contains defects, nano topographical repetitious structure, numerous nano-sized grain boundary, and recurrent ripples which provide delocalized surface π electrons with protein and small molecular chemicals. Presence of delocalized surface π electrons and functional groups of graphene allows for high density protein adhesion via both covalent and non-covalent bonding. Such substances such as TGF-β, insulin, albumin, fibrinogen, interferons and etc, are adsorbed onto graphene surface via hydrophobic or π–π stacking interactions which affect cell proliferation and differentiation. Moreover, large theoretical specific surface area ($2630\ m^2g^{-1}$) of graphene allows for high density protein loading capacity. For instance, protein loading capacity was ~2-fold, ~9-fold, and ~10-fold higher than that of BSA of single-walled carbon nanotubes

(SWNTs), multiwalled carbon nanotubes (MWNTs), and graphene, respectively, which are well known carbon materials with high protein adsorption ability.

Furthermore, the attractive π-π stacking forces are created by the sp^2-conjugated atomic carbon basal plane allow some amino acids contain benzene rings to absorb on graphene via hydrophobic-hydrophobic interactions. For example, bone morphogenetic proteins (BMPs), a well are a group of multi-functional growth factors, was found that graphene tends to bind well with proteins. It appears that graphene tends to bind or interaction well with a range of proteins such as trypsin, heparin, lysozyme, and peptides. The π electron cloud carried on graphene is speculated to interact with hydrophobic part of protein, resulting in the initial stage of addition involving the physicochemical linkages between cells and graphene through strong covalent bonding or indirectly bonding through an alteration in the adsorption of conditioning molecules. Findings on the effect of benzene rings of graphene surface is affected not only by surface chemistry but also by topographical parameters such as roughness and texture. Graphene on osteogenic and adipogenic differentiation inferred to be caused by the adsorption of small molecule dexamethasone and beta-glycerolphosphate protein on graphene. Moreover, insulin, which is known to enhance adipogenic differentiation gets denatured on graphene surface which in turn results in inhibition of adipogenic differentiation. Hence as protein and low molecular weight chemical gets adsorbed and deformed by graphene. Graphene can impose a great influence on cells depending on their hydrophobicity.

The protein and small molecular chemicals adsorption capacity is affected not only by surface functionality but by nano topographical parameters such as roughness and texture. The protein and small molecular chemicals adsorption capacity would make the graphene to serve as a promising platform for stem cell engineering

Conductivity

Owing to their conductivity properties, Carbon nanotube and graphene have been intensively studied for electro-active tissue. In particular, graphene has emerged as a powerful platform for enhancing the differentiation of stem cells into neurons due to its excellent properties, including nanotopographic surface and electrical conductivity. On this account, the graphene based materials would be an ideal breakthrough for biomedical applications of nervous system model. Firstly, excellent electrical conductivity of graphene make them suitable for nervous system model. In the presence of an electrical stimulation, excellent electrical conductivity graphene can modulate cell adhesion, migration, propagation, differentiation, protein secretion and DNA synthesis of electrically active cells, such as muscle, bone, cardiac and nerve cells. For example, Park et al. reported that graphene as a substrate improved cell adhesion and differentiation of human neural stem cell into neurons.[2] This study demonstrated that graphene-coated glass can enhance the promotion of neuronal differentiation of neural stem cells, especially favoring neurons versus glia cells, compared to the use of a substrate not coated with graphene (pure glass). In another study, Li et al. indicated graphene substrates enhanced expression of growth-associate protein-43(GAP43), resulting in the boost of neurite sprouting and outgrowth to the maximal extent. There are mainly two causes for such phenomena. First, the surrounding matrix of neurons may have mimicked the topography of wrinkled and rippled chemical vapor deposition (CVD)-grown graphene substrate, which may assist neuron growth. Second, the high electrical conductivity of graphene could also account for better neurite outgrowth, as in previous study it has been shown that the electrical conductivity of carbon nanotube (CNT) does promote neuron growth. In another study, Heo et al. used graphene/ polyethylene terephthalate substrate for modulating neural cell-to-cell interactions.[6] The results show that graphene-coated glass can increase cell-to-cell interaction and further strengthened. Not only that the graphene/PET film substrata was improved cell adhesion and differentiation compared to the conventional polystyrene tissue culture substrata which indicated that the graphene substrata was biocompatible and suitable for neuronal biomedical applications. In addition, not only can the electronic properties of graphene can be tailored to match the charge transport required for electrical cellular interfacing, but also the chemically stable properties of graphene can facilitate integration with neural tissues. These unique properties offer great advantages for neuronal or other purposes.

Surface morphology

Surface wrinkling in 2D materials is a well-known and common phenomenon.[7] It has been evident from TEM images and Monte Carlo simulations that graphene is not perfectly flat but contoured with intrinsic ripples with deformations up to 1 nm normal to the plane. Specially, CVD graphene consists of high densities of wrinkles on the nanometer- scale. The main driving force for wrinkling in 2D materials is difference between the thermal expansion coefficient mismatch of graphene and copper generated during growth and cooling process. Surface wrinkling is an important factor to be considered to account for the stem cell adhesion, growth and differentiation.

The Cell and molecular biology have shown that cell interaction with adhesive substrates. Furthermore, it is clear that interaction exists between cells and nano- and micro-scale topological features. However, there are not good enough to prove that the mechanism of these effects.

Nayak et al. shows that graphene provides a promising biocompatible scaffold that does not hamper the proliferation of human mesenchymal stem cells (hMSCs) and accelerates their specific differentiation into bone cells.[8] Nayak et al. also found that Wrippled and wrinkled topography of CVD graphene mimics the disordered nanopit array.[9] Such large-scale disorder in CVD graphene could play a role in protein adsorption, cell adhesion, proliferation, and differentiation. Nayak et al. believe that the surface wrinkling and ripples provide local curvature and, hence, could further enhance the reactivity of such graphene sheets. Ripples in graphene suggest that the resultant local curvatures affect reactivity such as protein anchoring, cell adhesion, and cell align which can change many aspects of the cell function. The study by Tang a et al. studies show that increasing roughness of the cross-linked GO film facilitates the adhesion of stem cells, which in turns increases the rate of proliferation.[10] Furthermore, the rougher surface topology of cross-linked GO film provides more anchoring points for the stem cell adhesion, growth and differentiation of hMSCs. In another study, Kim et al. hypothesized that the unique characteristics of the asymmetrical nanotopology cue of graphene and its secondary effects such as stiffness and roughness within substrata might play a crucial role in the enhancement of hMSC differentiation.[11] This study demonstrated that that RGO–chitosan substrata with asymmetrical nanotopology provided a suitable environment for the adhesion and proliferation of hMSCs as well as enhanced cell–substrate interaction and cell–cell contacts.

1.4 2D graphene based stem cell engineering

Stem cells represent a promising tool for tissue engineering and regenerative medicine. However, they require appropriate environments to grow and regenerate. Recently, 2D graphene based platforms have attracted much attention as promising materials for cell modulation applications due to the physicochemical properties of graphene and its biocompatibility have inspired scientists to utilize this material for regulating the growth and differentiation of stem cells engineering. Although 2D graphene based stem cell engineering, it is in a relatively nascent stage. Graphene has been attracting great interest in the field of biomedical engineering. Many systematic studies have been carried out on various topics of interest that range from cell regulation to tissue regeneration. Many results that are rigorously proved and accepted for future 2D graphene based platforms and will no doubt greatly benefit tissue engineering and regenerative medicine. In this context, we introduce some of the interesting advances in 2D graphene-based stem cell engineering applications; how it affects cell behavior and differentiation. Some of the most interesting examples that have reported use of 2D graphene based platforms for cell engineering purposes.

For bone tissue engineering, there are a large number of studies which report the promise of biomimetic 2-D graphene platform which promote the adhesion, proliferation, and osteogenic differentiation of MSCs or osteoblasts. Graphene provides a new kind of solutions to integrate several elements (active and passive) on the 2D graphene scaffolds. The variety of favourable properties for bone tissue engineering that graphene provides include also efficient modulation of stem cell, due to the intrinsic properties. The physiochemical and mechanical property implies that graphene has unique properties for the differentiation of stem cell. This was well described by Lee et al.[3] This study represents an interesting example where MSC osteogenic differentiation can be achieved even in the absence of chemical inducer in the culture medium. The protein adsorption ability of graphene is of particular importance because the chemical interactions between the substrates and soluble factors is able to stimulate cell growth and differentiation.

For neural tissue engineering, there are several studies have been reported about the interactions of nervous systems with 2D graphene platform. Recent studies strongly appealed that the potential of graphene to stimulate neurite sprouting. For example, Solanki et al. found that the engineered microenvironment consisting of nanotopographical features modified with GO provides instructive physical cues that lead to enhanced and then. They also demonstrated that the engineered microenvironment consisting of nanotopographical features modified with GO provides instructive physical cues that lead to enhanced neuronal differentiation of hNSCs along with significant axonal alignment.[12] The same positive results have been observed by Li et al. that utilized graphene as a substrate for the promotion of neurite sprouting and the outgrowth of mouse hippocampal cells. Furthermore, graphene was recently applied as an electrode in the electrical stimulation of NSCs, because stimulation can control the physiological activities of stem cells, such as cell viability, division, differentiation and migration, applicable in spinal cord and tumor therapies.[13] In this regard, Park et al. reported that CVD graphene as a substrate improved cell adhesion and differentiation of human neural stem cell into neurons. This study demonstrated that graphene-coated glass can enhance the promotion of neuronal differentiation of neural stem cells rather than glia, which differentiate further in the absence of biochemical motifs or co-culturing.[2] In fact, the increased differentiation of hNSCs towards neurons than glia is essential in neural regeneration and brain repair.

For cardiac tissue engineering, as well reported above, it is reported that MSC differentiation could be modulated through cellular interactions with culture substrates *in vitro*. However, only a few studies have studied the effect of cell culture substrates on cardiomyogenic differentiation of MSCs. Recently, Park et al. demonstrated that graphene can be used as a stem cell culture substrate to promote the cardiomyogenic differentiation process of MSCs without the use of any exogenous chemical inducers.[5] Graphene exhibited no sign of cytotoxicity for stem cell culture, and provided a suitable environment for MSC proliferation. The MSC commitment towards cardiomyogenic lineage was stimulated by simply culturing the MSCs on graphene, even in the absence of exogenous inducers for cardiomyogenic differentiation. They suggest that graphene may promote the cardiomyogenic differentiation and diverse behaviors of MSCs through specific cell–ECM interactions and regulation of cell signaling pathway. Lee et al. demonstrated that graphene enhances the cardiomyogenic differentiation of human ESCs (hESCs).[4] The coating of the graphene with vitronectin (VN) was required to ensure high viability of the hESCs cultured on the graphene. hESCs were cultured on either VN-coated glass (glass group) or VN-coated graphene (graphene group) for 21 days. The spontaneous cardiomyogenic differentiation of hESCs was investigated by culturing hESCs on either glass (control) or graphene without the addition of exogenous chemicals for differentiation induction and by evaluating the expression of cardiac-specific genes. The differentiation of these cells was also compared with that of cells cultured on Matrigelcoated glass, which is a substrate used in the conventional, directed two-dimensional culture differentiation systems for the cardiomyogenic differentiation of hESCs without forming embryoid bodies. This culture system showed an efficient differentiation into cardiomyocyte phenotype. The mesodermal and endodermal differentiations were compared among the experimental groups because these differentiations are known to be intermediate stages of the cardiomyogenic differentiation of hESCs. The mechanisms underlying the enhanced cardiomyogenic differentiation were also investigated. Moreover, the analysis of the cardiomyogenic differentiation of hESCs cultured on graphene or Matrigel revealed that graphene was superior to Matrigel, which is a substrate used in conventional cardiomyogenic differentiation systems. The enhanced cardiomyogenic differentiation may be, at least in part, due to nanoroughness of graphene, which enhanced hESC adhesion and the upregulation of extracellular signal-regulated kinase signaling. We further highlight how 2D graphene based platforms are being exploited for cell modulation in tissue engineering, comprehensively surveying recent experimental works are summarized in Table 1.

Table 1. 2D graphene based cell modulation

2D graphene based platform	Cell type	Main results	References
CVD graphene on SiO_2	SAOS-2, MSCs	The graphene probably has a potential to induce MSC differentiation into the osteoblast lineage	Kalbacova et al, *Carbon*, 48, 4323 (2010)
Graphene/chitosan composite film	L929	The graphene/chitosan composites were biocompatible to L929 cells	Fan et al, *Biomacromolecules*, 11, 2345 (2010)
CVD graphene on glass	hNSCs	Graphene substrate enhanced the differentiation of hNSCs to neurons compared with glass substrates	Park et al, *Adv Mater*, 23, 263 (2011)
Graphene and GO	iPSCs	The different surface properties of G and GO governed the iPSCs behavior	Chen et al. *Biomaterials*, 33, 418 (2012)
Graphene and fluorinated graphene	hMSCs	Fluorinated graphene can be used to enhance cell adhesion and proliferation of MSCs	Wang et al, *Adv Mater*, 24, 4285 (2012)
CVD graphene on glass	hMSCs	MSC commitment towards cardiomyogenic lineage was stimulated by simply culturing the MSCs on graphene, even in the absence of chemical inducers	Park et al, *Adv. Healthcare Mater*. 3, 176 (2013)
Graphene-incorporated chitosan composite film	hMSCs	Graphene enhance cell–cell and cell–material interactions for promoting functions of hMSCs	Kim et al, *J. Mater. Chem*. B, 1, 933 (2013)
CVD graphene on glass	hESCs	Graphene enhanced the gene expression of cardiac-specific extracellular matrices	Lee et al, *Biochem Biophys Res Commun*, 12, 174 (2014)
CVD graphene on glass	hMSCs	Graphene is advantageous for the differentiation of hMSCs into neurons	Kim et al, *J. Biomed. Nanotech*, (2014)

1.5 3D graphene based stem cell engineering

Two-dimensional (2D) surface represent a simple model system for isolating the control factors for stem cell in fundamental research. Much of our understanding of the biological mechanisms that underlie cellular functions, such as migration, differentiation and force sensing has been garnered from studying cells cultured on two-dimensional (2D) glass or plastic surfaces. However, the natural niche for cell is not two-dimensional (2D) surface. Cells are not static and can “feel” the presence of cellular microenvironments in which cells relies on *in vivo* comprise soluble chemical factors, biomechanic factors, structural environment, neighbor cells, and ECM, and cell–biomaterial interactions which can eventually be converted into biological signals to regulate the function of cells. A 3D porous structure is an indispensable component of tissue engineering scaffolds for the provision of sufficient surface and space for cell adhesion, migration, growth and tissue formation. Therefore, this has spurred substantial efforts towards the development of in vitro 3D biomimetic environments and has encouraged much cross-disciplinary work among biologists, material scientists and tissue engineers. In this context, we introduce some of the interesting advances in 3D graphene-based stem cell engineering applications; how it affects cell behavior and differentiation. Recently, multi-dimensional carbon-nanomaterial (zero-dimensional, one-dimensional, two-dimensional, and three dimensional) has been shown to promote cell adhesion, proliferation, and differentiation *in vitro* and repair tissue *in vivo*. Among these materials, graphene could be combined with commonly used bio-scaffolds for stem cell engineering to modulate their biological functionality. 3D graphene based platforms have attracted much attention as promising new platform for cell modulation applications due to the physicochemical properties of graphene and its biocompatibility have inspired scientists to utilize this material for engineering a range of biomaterial and tissue-engineering applications. To date, several fabrication technologies, such as chemical vapor deposition method using template, a polymeric sponge impregnation process, foaming, sol–gel methods, extrusion forming, gel-casting, thermally induced phase separation, carbonization with thermal decomposition, and etc have been developed for the fabrication of 3D graphene based platforms. Some of the most interesting examples that have reported use of 3D graphene based platforms for cell engineering purposes are summarized in Table 2.

Table 2. 3D graphene based cell modulation

3D graphene based platform	Cell type	Main results	References
Graphene LbL Deposition on 3D Scaffolds.	E14 Primary Cortical Neurons.	Electroactive scaffold modification assist in neuronal regeneration,	Zhou et al, *ACS Appl. Mater. Interfaces*, 4, 4524 (2012)
rGO/ZnO/Anti-EpCAM Foam	MCF7 cell	It can successfully capture cancer cells from blood spiked with MCF-7 cells due to the enhanced local topographic interactions.	Yin et al, *Adv. Mater. Interfaces*, 1, 13 (2014)
Three-dimensional graphene foams (3D-GFs)	Human mesenchymal stem cells (hMSCs)	3D GFs support the attachment and viability of hMSCs, and induce spontaneous osteogenic differentiation.	W. Crowder et al, *Nanoscale*, 5, 4171 (2013)
Three-dimensional graphene foams (3D-GFs)	Neural stem cell (NSC)	3D-GFs keep cells at a more active proliferation state with upregulation of Ki67 expression than that of 2D graphene films.	Li et al, *Scientific Reports*, 3, 1604 (2013)
Porous and flexible 3D GOx-based scaffolds	Embryonic neural progenitor cells	Highly viable and interconnected neural networks were formed on these 3D scaffolds	Serrano et al, *J. Mater. Chem. B*, 2, 5698 (2014)

1.7 References

[1]. Kostarelos, Kostas, and Kostya S. Novoselov. Exploring the Interface of Graphene and Biology. *Science*. **2014**, 344. 261-263.

[2]. Park, S. Y., Park, J., Sim, S. H., Sung, M. G., Kim, K. S., Hong, B. H., & Hong, S. Enhanced differentiation of human neural stem cells into neurons on graphene. *Adv Mater.* **2011**, 23(36), H263-H267.

[3]. Lee, W. C., Lim, C. H. Y., Shi, H., Tang, L. A., Wang, Y., Lim, C. T., & Loh, K. P. Origin of enhanced stem cell growth and differentiation on graphene and graphene oxide. *ACS nano*, **2011**, 5(9), 7334-7341.

[4]. Lee, T. J., Park, S., Bhang, S. H., Yoon, J. K., Jo, I., Jeong, G. J., & Kim, B. S. Graphene enhances the cardiomyogenic differentiation of human embryonic stem cells. *Biochem. Biophys. Res. Commun.* **2014**, 452.1, 174-180.

[5]. Park, J., Park, S., Ryu, S., Bhang, S. H., Kim, J., Yoon, J. K & Kim, B. S. Graphene–Regulated Cardiomyogenic Differentiation Process of Mesenchymal Stem Cells by Enhancing the Expression of Extracellular Matrix Proteins and Cell Signaling Molecules. *Adv Healthcare Mater*. **2014**, 3(2), 176-181.

[6]. Heo, Chaejeong, et al. The control of neural cell-to-cell interactions through non-contact electrical field stimulation using graphene electrodes. *Biomaterials*, **2011**, 32.1, 19-27.

[7]. Sutter, Peter, Jerzy T. Sadowski, and Eli Sutter. Graphene on Pt (111): Growth and substrate interaction. *Phys Rev B,* **2009**, 80.24, 245411.

[8]. Nayak, Tapas R., et al. Graphene for controlled and accelerated osteogenic differentiation of human mesenchymal stem cells. *ACS nano*, **2011**, 5.6, 4670-4678.

[9]. Dalby, Matthew J., et al. The control of human mesenchymal cell differentiation using nanoscale symmetry and disorder. *Nat Mater*, **2007**, 6.12, 997-1003.

[10]. Tang, Lena AL, et al. Highly Wrinkled Cross-Linked Graphene Oxide Membranes for Biological and Charge-Storage Applications. *Small*, **2012**, 8.3, 423-431.

[11]. Kim, Jangho, et al. "Graphene-incorporated chitosan substrata for adhesion and differentiation of human mesenchymal stem cells." *J Mater Chem B*, **2013**, 1, 933-938.

[12]. Solanki, Aniruddh, et al. Axonal Alignment and Enhanced Neuronal Differentiation of Neural Stem Cells on Graphene-Nanoparticle Hybrid Structures. *Adv Mater.* **2013**, 25, 5477-5482

[13]. Li, Ning, et al. The promotion of neurite sprouting and outgrowth of mouse hippocampal cells in culture by graphene substrates. *Biomaterials*. **2011**, 32.35, 9374-9382

Part I

2D Graphene based stem cell engineering

Chapter 2

Graphene-directed spheroid formation of mesenchymal stem cells for enhanced neuronal differentiation

Introduction

Neuronal disorders or neurodegenerative diseases are still one of the leading causes of human death and disability in the world. For example, stroke causes approximately 150,000 American die every year, and Parkinson's disease affects over 1 million people in the European Union.[1-4] Nevertheless, the current clinical treatments for neuronal disorders or neurodegenerative disease are quite limited, and the number of people affected by these diseases consistently increases every year.[1] As a direct result, there is a great need to discover alternative therapies for these disorders or diseases. Autologous stem cell based therapy and tissue engineering are currently considered as promising strategies that could allow the functional replacement of missing or damaged neurons by transplanting undifferentiated or/and differentiated stem cells alone or in combination with appropriate scaffolds for the treatment of neuronal disorders or diseases.[1-5] In this regard, it is crucial to develop a highly efficient platform for the growth and neuronal differentiation of stem cells.

Carbon-based nanomaterials have exhibited great potential for regulating the growth and differentiation of stem cells due to their biocompatibility and their unique physicochemical properties, which are comparable to a natural extracellular matrix (ECM) and can promote essential cellular processes for enhancing the growth and function of stem cells.[6-14] Guided by these considerations, here, we propose the use of highly uniform graphene as an efficient platform for stem cell based therapy for the treatment of neuronal disorders or diseases. It is hypothesized that the use of high quality graphene would provide a unique environment for the growth and neuronal differentiation of stem cells (Fig. 1A). To address this challenge, we fabricated highly uniform monolayers of graphene and investigated how this platform could influence the adhesion, proliferation, and differentiation of human mesenchymal stem cells (hMSCs) into functional neurons, which may have considerable potential for use in autologous stem cell-based therapy to treat neuronal disorders or diseases.

Experimental

Fabrication and characteristics of highly uniform graphene

Highly uniform graphene was synthesized by the CVD process (Supplementary Fig. S1).[14,15] The graphene film grown on the copper foil was covered by poly(methyl methacrylate) (PMMA) and floated on the surface of an aqueous solution of 0.1 M ammonium persulphate [$(NH_2)_4S_2O_8$]. After all of the copper layers were etched away, the floating PMMA/graphene film was collected using a clean PET film and transferred to deionized water. The cleaning process was repeated five times. The graphene film with the PMMA support was transferred to coverslips. The samples were dried with nitrogen gas immediately after the transfer and baked for 8 h on a hot plate at 60℃. The samples were then cleaned using acetone at room temperature for 30 min to remove the PMMA support layer. The samples were then dried and baked for 8 h on a hot plate at 60℃.

The graphene fabricated in this study were characterized by atomic force microscopy (AFM), Raman spectroscopy, ultraviolet–visible spectrometer, TEM, and SAED. The surface morphology examination of the samples was conducted through non-contact mode AFM (XE-100 system, Park Systems, Korea). The structural properties of the graphene on the coverslip were further investigated through Raman spectroscopy (RM 1000-Invia, Renishaw, UK). The Raman spectra were recorded by using an argon ion laser (514 nm) as the excitation source with a notch filter of 50 cm^{-1}. The typical scan range was from 1000 to 3000 cm^{-1} and the instrumental resolution was 10 cm^{-1}. The optical transmittance of the graphene on the coverslip was measured using an ultraviolet–visible spectrometer (UV-3600, Shimadzu, Japan). The TEM and SAED analyses were conducted on a transmission electron microscopy (TEM) (JEOL 2100, JEOL, Japan) operated at 200 kV. The rotation between the TEM images and the corresponding SAED patterns was calibrated using molybdenum trioxide crystals. The sheet resistances of the graphene on the glass were measured through the van der Pauw four-probe method using a Hall measurement system.

hMSC culture on highly uniform graphene

Adipose tissues were isolated from the patients undergoing ear surgeries under sufficient informed consent at the Ajou University School of Medicine (Suwon, Korea).[12,21,28] The experimental protocol was approved by the Institutional Review Board at the same university. Tissues were washed with PBS and digested with 100 Unit/mL collagenase type I (Sigma-Aldrich, St. Louis, MO, USA) with low glucose Dulbecco's modified Eagle's medium (DMEM; Gibco-BRL, Grand Island, NY, USA) and incubated for 8 h to lyse the adipose tissues. The stromal fraction was collected by centrifugation and then passed through a cell strainer (100 μm size) to remove any large cell clumps and particles. For cell culture and expansion of adipose-derived hMSCs, cells were grown in low glucose DMEM with 10% fetal bovine serum (FBS) and 1% penicillin-streptomycin (Gibco, Milan, Italy) at 37℃ in a 5% CO2 atmosphere. All cells used in this study were at passage 3 or 4.

For the adhesion and proliferation of hMSCs, cells (4×10^4 cells/sample) were seeded onto samples and cultured in DMEM (Sigma-Aldrich, Milwaukee, WI, USA) with 10% FBS (Sigma-Aldrich, Milwaukee, WI, USA) and 1% antibiotics (Sigma-Aldrich, Milwaukee, WI, USA) at 37℃ in a humidified atmosphere containing 5% CO_2. The quantitative analysis of the cell proliferation on the nanogrooved matrices was performed using WST-1 assay (EZ-Cytox Cell Viability Assay Kit, Daeillab Service Co., LTD). For the neuronal differentiation of hMSCs, early-passage hMSCs and commercially available neuronal differentiation media (Promocell, Heidelerg, Germany) were used.

Immunofluorescence staining

Adhered cells on samples were fixed with a 4% paraformaldehyde solution (Sigma-Aldrich, Milwaukee, WI, USA) for 20 min, permeabilized with 0.2% Triton X-100 (Sigma-Aldrich, WI, Milwaukee, USA) for 15 min, and stained with TRITC-conjugated phalloidin (Millipore, Billerica, MA, USA) and 4, 6-diamidino-2-phenylindole (DAPI; Millipore, Billerica, MA, USA) for 1 h. FAs were also stained with a monoclonal anti-vinculin antibody (1:100; Millipore, Billerica, MA, USA) and a FITC-conjugated goat anti-mouse secondary antibody (1:500; Millipore, Billerica, MA, USA). To check neurogenesis of hMSCs, analysis of the immunostaining of TUJ1 (Cell Signaling Technology, Beverly, MA, USA), NeuN (Millipore, Billerica, MA, USA), and GFAP (Millipore, Billerica, MA, USA) were used. Images of the stained cells were taken using a fluorescence microscope (Zeiss, Germany). Mouse anti-STRO-1 (R&D systems, USA) and secondary anti-rabbit IgG (FITC) (Jackson ImmunoResearch Laboratories) were used for the investigation of hMSCs phenotype. For the quantitative analysis of the images, the custom written

MATLAB script was used.

Western blot

Cells were lysed in RIPA buffer, supplemented with Xpert Protease Inhibitor Cocktail Solution (100X) GenDepot, Barker, TX, USA). An equal amount of protein was loaded in each lane of a sodium dodecyl sulfate polyacrylamide gel electrophoresis (SDS-PAGE). Proteins were separated by electrophoresis and transferred to a (Polyvinylidene difluoride) PVDF membrane. Following transfer, membranes were blocked for 1 h with 5% skim milk in PBS + 0.05% Tween 20. Primary antibodies against Connexin 43 (Cell Signaling Technology, Danvers, MA, USA), STRO-1 (R&D systems, USA) and β-actin (Cell Signaling Technology, Danvers, MA, USA) were used. The immunoblots were washed and incubated with secondary antibodies conjugated with horseradish peroxidase (Santa Cruz Biotechnology, CA). Immunoblot bands were visualized by enhanced chemiluminescence (ECL; GenDEPOT, TX, USA).

Nissle staining

The Nissle staining was performed to evaluate the differentiated cells from hMSCs in the neuronal differentiation. The cells were fixed with a 4% paraformaldehyde solution (Sigma-Aldrich, Milwaukee, WI, USA) for 20 min after PBS washing three times. The cells were washed by PBS three times and then stained by 1% Cresyl violet solution.

Quantitative real-time polymerase chain reaction (qRT-PCR)

To evaluate Nestin, TUJ1, and MAP2 mRNA expression levels, quantitative real time PCR (qRT-PCR) was performed. Total RNA was extracted from cells according to the manufacturer's instructions using an Easy-BLUE RNA extraction kit (iNtRON Biotech, Sungnam, Korea). First-strand cDNA synthesis was carried out in a 20 μl reverse transcription (RT) reaction with oligo dT, dNTPs and reverse transcriptase (GenDEPOT, Barker, TX, USA). Fuorescence based real-time PCR was carried out using SYBR Green Premix Ex Taq (TaKaRa, Dalian, China) and an applied Biosystems 7500 Real-Time PCR system (Applied Biosystems; Foster City, CA, USA). The following primers were used for qRT-PCR: human Nestin (Fw) 5'- GAA ACA GCC ATA GAG GGC AAA-3'; (Rv) 5'- TGG TTT TCC AGA GTC TTC AGT GA-3', beta III tubulin (Fw) 5'- CGA AGC CAG CAG TGT CTA AA-3'; (Rv) 5'- GGA GGA CGA GGC CAT AAA TA -3', beta III tubulin (Fw) 5'- CCA ATG GAT TCC CAT ACA GG -3'; (Rv) 5'- TCC TTG CAG ACA CCT CCT CT--3', GAPDH (Fw) 5'- GCA AAT TCC ATG GCA CCG TC -3'; (Rv) 5'- TCG CCC CAC TTG ATT TTG G--3'. For quantification, GAPDH was used as the reference for normalization of each sample.

Calcium imaging

For high K^+ stimulation experiment, culture media were exchanged to Normal Tyrode's (NT) solution (pH 7.3, 148 mmol NaCl, 5 mmol KCl, 2 mmol $CaCl_2$, 2 mmol $MgCl_2$, 10 mmol HEPES, 10 mmol Glucose). After washing the cells by NT solution, the cells were loaded with Fluo-4 AM dye (2 μmol, Invitrogen, CA, USA) for 30 min at 37℃ followed by washing for 30 min at room temperature. The fluorescence was monitored using Nikon TE-2000U (Nikon, Japan) equipped with CV-S3200 CCD camera (JAI, Japan). All fluorescent images were analyzed by NIS-Elements software version 2.4 (Nikon, Japan) and ImageJ.

Statistical analysis

Student’s t-test or one-way ANOVA followed by Duncan's multiple range test was used for statistical analysis. All quantitative results were presented as mean ± standard deviation (SD).

Results and Discussion

We synthesized highly uniform graphene by using the chemical vapor deposition (CVD) method.[14,15] The detailed procedure to prepare a high quality graphene-coated glass substrate is described in Supplementary Fig. S1. As shown in Fig. 1 and Supplementary Figs. S2-S5, we qualified the presence of the high-quality monolayer graphene used in this study. In particular, a selected-area electron diffraction (SAED) pattern (Figs. 1D and E) and high-resolution scanning transmission electron microscopy (STEM) images (Figs. 1F and G) clearly demonstrated that high-quality graphene was successfully synthesized. We also determined that the sheet resistance and surface roughness (root-mean-square deviation, Rq) of graphene-coated glass were 552 ± 22 Ω/□ (Supplementary Fig. S4) and 2.90 nm (Supplementary Fig. S5) with a high uniformity, respectively. Note that the surface roughness of graphene-uncoated glass was 5.03 nm (Supplementary Fig. S5). We first explored the effects of stem cell growth on highly uniform graphene (Fig. 2). To investigate the adhesion of stem cells, we cultured hMSCs on the graphene-coated substrates and the uncoated substrates using normal growth medium. After culturing the cells onto the substrates for 14 h, we carefully removed the unattached cells from the substrates by washing with phosphate buffered saline. As shown in Fig. 2A, the typically spread shapes and focal adhesions (FAs) of hMSCs were observed on the glass substrate in the immunofluorescence staining analysis. In contrast, we found that the hMSCs on graphene exhibited distinctly different properties of adhesion compared to those on the glass substrate. Interestingly, three dimensional (3D) spheroids of hMSCs were

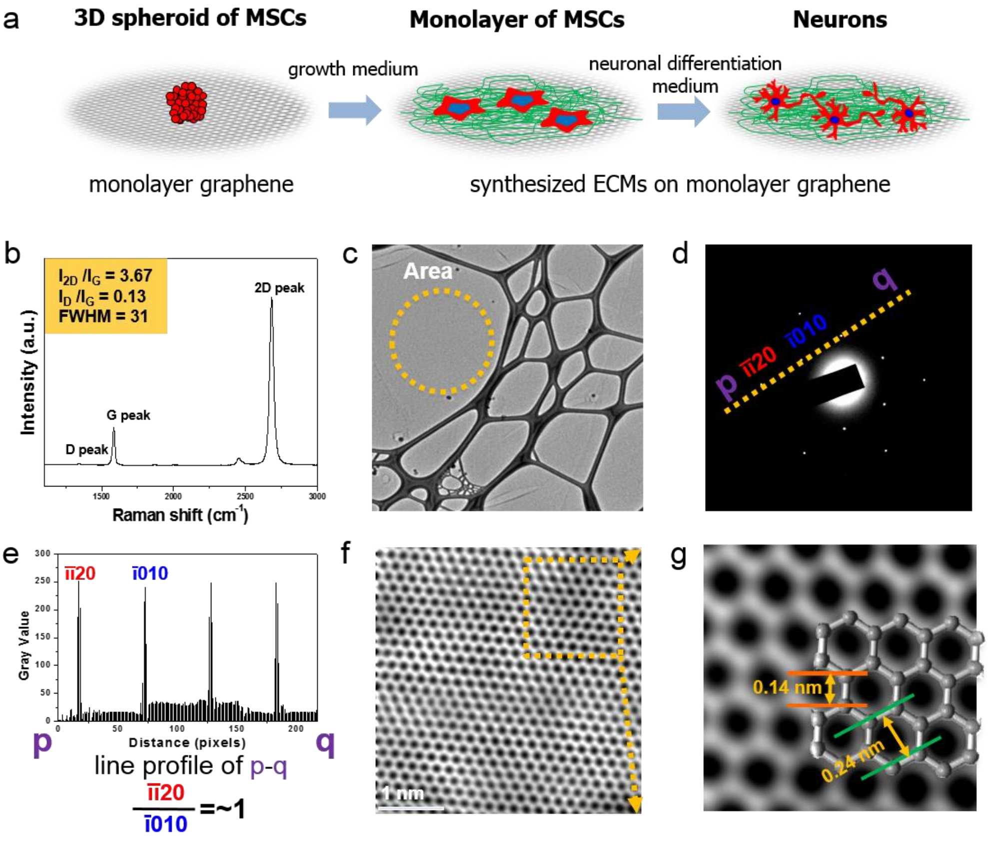

Figure 1 | Fabrication and characterization of highly uniform graphene for the growth and neuronal differentiation of stem cells. a, Schematic of the spheroid formation and neuronal differentiation of hMSCs using high-quality graphene. b, Raman spectroscopy of the transferred graphene. c, TEM image of a graphene sheet on a TEM grid. d, The SAED pattern. e, Intensity profile of the diffraction spots along a line connecting points p and q in the single-layer graphene diffraction pattern. The uniform intensity profile between the inner and outer spots proves that the graphene sheet consists of a single layer. f, High-resolution STEM image of at (F) low-magnification. g, High-resolution STEM image of at high-magnification.

formed on the graphene (Fig. 1A and Supplementary Fig. S6A). The size of cell spheroids for hMSCs ranged from 50 µm to 150 µm.

To our knowledge, this is the first report demonstrating that graphene can induce spheroid formation of aggregated cells in the absence of any external factors.[16-21] A possible explanation for the spheroid formation is the surface properties of the highly uniform graphene, which might not provide sufficient cell adhesion motifs for the cells at the initial stage of the cell culture. Namely, the limited cell adhesion motifs on the surface of high-quality graphene might restrict the full adhesion of cells to the substrates, which could eventually promote high cell-cell adhesion instead of cell-substrate adhesion. It is widely accepted that the initially stable cell-cell interactions, such as those in 3D tissues or organs, play an important role in regulating cellular behavior.[22] In particular, the phenomenon of spheroid formation of stem cells is highly related to the direct functions of the stem cells, such as stemness and differentiation,[13,24] suggesting that that the use of high quality graphene alone to generate 3D spheroid of stem cells would an interesting method for use in stem cell biology or engineering.

We observed the spheroids formed of aggregated hMSCs on the graphene up to ~ 7 days during the cell culture period, after which the spheroids usually disappeared (Supplementary Fig. S6B). The produced extracellular matrix (ECM) from the aggregated cells and the adsorbed adhesive-related molecules from the growth medium on the graphene during the process time of the cell culture could promote the full adhesion of the cells onto the substrates (Fig. 2A, Supplementary Figs. S4 and S5). The single cells that migrated from the spheroids on the graphene exhibited

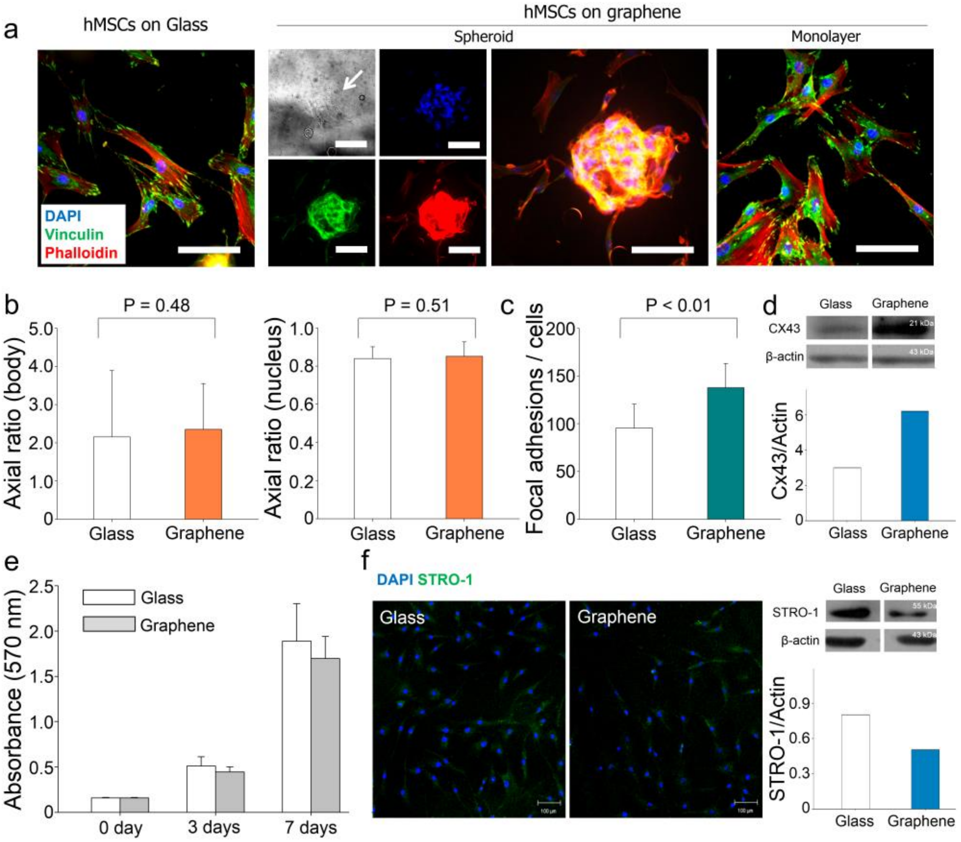

Figure 2 | Growth of hMSCs on highly uniform graphene. a, Representative immunofluorescent images of hMSCs cultured on a graphene-uncoated glass substrate and high-quality graphene. b, Quantification of the cell body and the nucleus, indexed by the axial ratio of the cell body and the width and length of the nucleus. c, Quantification of the amount of focal adhesion. One-hundred cells were used in the quantification process. d, Western blot analysis and quantification of the levels of Cx43 expression in the hMSCs cultured. e, Proliferation of cells on the substrates for 7 days. Three independent experiments were conducted. f, Representative immunofluorescent images of STRO-1 and a western blot analysis of the hMSCs cultured on the substrates for 10 days. The error bars represent the standard deviation.

the typical hMSC morphology (Fig. 1A).

To determine whether the high quality graphene is capable of altering the interactions at the cell-substrate and the cell-cell interfaces, we cultured hMSCs on the substrates for 7 days before the complete confluence of hMSCs. We analyzed the body and nucleus elongation of cells at the single cell level because it is known that the architecture and organization of the body and the nucleus may influence the cell function.[25-28]

To determine whether the high quality graphene is capable of altering the interactions at the cell-substrate and the cell-cell interfaces, we cultured hMSCs on the substrates for 7 days before the complete confluence of hMSCs. We analyzed the body and nucleus elongation of cells at the single cell level because it is known that the architecture and organization of the body and the nucleus may influence the cell function.[25-28] Our results indicated that there was no significant difference between using the graphene-coated and the glass (graphene uncoated) substrates, suggesting that the presence of a uniform monolayer of graphene does not strongly influence the structural changes of hMSC (Fig. 2B). However, we found that the use of graphene enhanced the formation of FAs, as determined by vinculin immunostaining, compared to the use of glass substrates (Fig. 2C). In addition, a western blot analysis clearly indicated the greatly enhanced expression of the connexin 43 (Cx43), a major cell junction protein, in cultured hMSCs on the graphene compared to that on the glass substrates (Fig. 2C). Taken together, these findings indicate that the high quality graphene provides specific environmental cues to hMSCs, resulting in the enhanced cell-substrate and cell-cell interactions.

The proliferation of hMSCs cells on the high quality graphene was continually monitored during the experiment. We cultured hMSCs on the graphene-coated and the uncoated substrates using a normal growth medium for 7 days. Our quantified data at 1, 3, and 7 days indicate that the proliferation of cells on the graphene was slightly lower than on the glass substrates although the graphene exhibited time-dependent proliferation of the hMSCs (Fig. 2E). We hypothesized that a uniform monolayer of graphene alone might induce the differentiation of hMSCs into other lineages. Note that the initial formation of spheroids from aggregated MSCs, even in a short time, could affect their differentiation.[22] To verify this hypothesis, we cultured for 10 days hMSCs on the graphene-coated and the uncoated substrates using a normal growth medium that did not induce the differentiation of hMSCs. To identify the phenotypes of the stem cells, the expression of STRO-1 protein from cells cultured on the substrates was determined. Interestingly, our immunostaining analysis and western blot analysis clearly indicated the down-regulation of STRO-1 protein expression on the graphene compared to that on the glass substrate, suggesting that the high-quality graphene might promotes the differentiation of hMSCs.

In this study, we aimed to promote the neuronal differentiation of hMSCs as a step towards the neurogenesis of stem cells by using a highly uniform monolayer graphene with unique nanosurface properties and electrical conductivity (Fig. 1 and Supplementary Figs. S2-S5) as well as enhanced cellular interactions on the graphene (i.e., the initial 3D spheroid formation, the enhanced formation of FAs, and the gap junction expression of hMSCs) (Fig. 2). After culturing the hMSCs on the

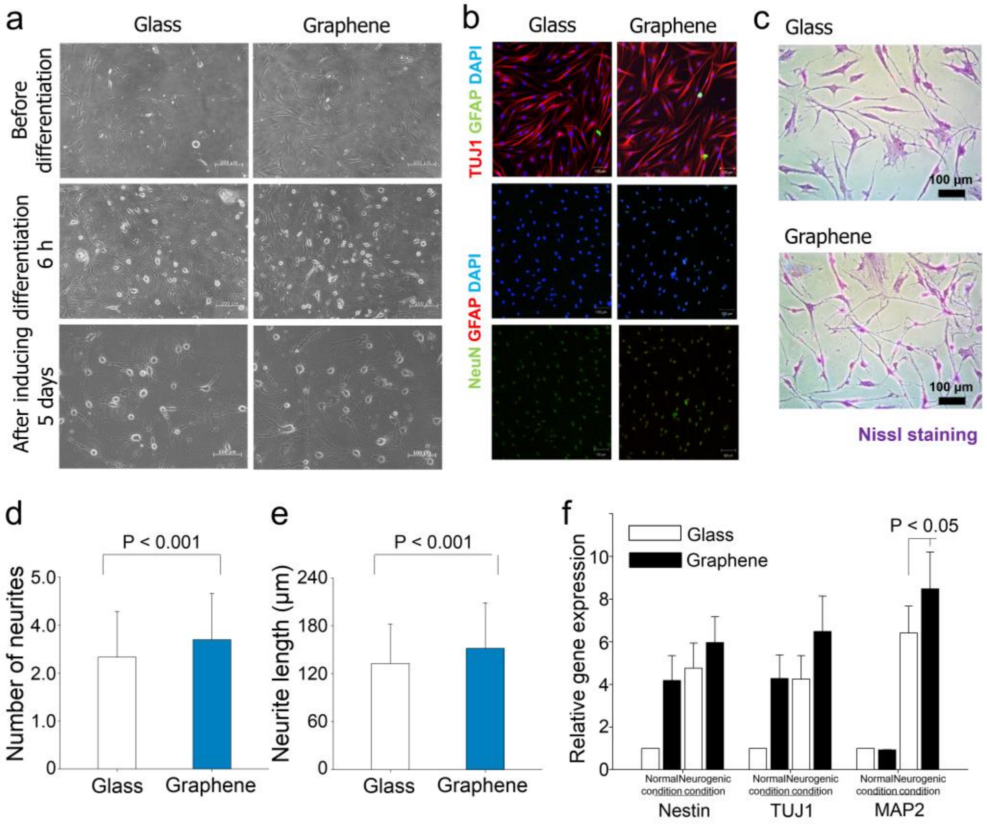

Figure 3 | Neuronal differentiation of hMSCs on highly uniform graphene a, Representative phase-contrast images of the hMSCs cultured on the substrates in the growth medium or the neuronal differentiation medium. b, Representative immunostaining images of TUJ1, NeuN, GFAP, and DAPI of the hMSCs cultured in the neuronal differentiation medium for 5 days. c, Representative Nissl staining images of hMSCs cultured in the neuronal differentiation medium for 5 days. d, Quantification of the number of neurities and the neuritie lengths. One-hundred cells were used in the quantification process. f, qRT–PCR analysis of hMSCs cultured in the neuronal differentiation medium for 5 days.

substrates for 3 days in the normal growth media, we then replaced the media withthe neurogenic media to induce neuronal differentiation of the hMSCs. After inducing neuronal differentiation of the hMSCs on the substrates for 6 h, we observed that the hMSCs exhibited higher activation for neuronal differentiation on graphene.

Three independent experiments were conducted, and the error bars represent the standard deviation.the graphene compared to the differentiation exhibited on the glass substrate (Fig. 3A). After 5 days of neuronal differentiation, the cells on both of the substrates exhibited neuron-like cell morphology and neurite outgrowths. Compared to the cells differentiated on the glass substrates, the cells on the graphene exhibited a more elongated neuritis, which lead to network formations (Fig. 3A).

To confirm the differentiated cells, we first analyzed the immunostaining of TUJ1 (early neuron marker), Neun (later neuron marker), and GFAP (glia cell marker). We observed that the cells expressed TUJ1 and Neun, whereas they did not express GFAP on both of the substrate types, indicating that we successfully induced the differentiation of hMSCs into only neurons and not into glia cells (Fig. 3B). Interestingly, the higher expression of TUJ1 and Neun as well as the enhanced neurite outgrowths were observed on the monolayer graphene than on the glass substrate. We also verified the presence of the differentiated cells using Nissl staining, which indicated that most of the cells were stained on the graphene, whereas the cells were only slightly stained on the glass substrata; which again confirmed that the graphene could enhance the neurite outgrowths (Figs. 3D and E).

To quantify the degree of enhanced neuronal differentiation of hMSCs by high-quality graphene in further detail, we performed the quantitative real-time reverse transcription-polymerase chain reaction (qRT-PCR) analysis. We cultured hMSCs on the graphene-coated substrates and the uncoated substrates with normal or neurogenic medium for 5 days after cell seeding. Strikingly, the expressions of neurogenesis-related genes (i.e., Nestin (early marker), TUJ1 (early marker), and MAP2 (later marker)) were promoted on the high-quality graphene relative to the expressions on the glass substrate (Fig. 3D). An interesting finding was derived from this experiment: the expressions of the early neurogenic transcriptional factors (Nestin and TUJ1) were upregulated in the hMSCs cultured on graphene, even in the normal growth medium, compared to those on the uncoated substrates. Surprisingly, the upregulation degree of the early neurogenesis-related genes in the hMSCs cultured on graphene with the normal growth medium was similar to that in the hMSCs cultured on the glass substrate with the neurogenic medium. Taken together, our findings demonstrated that highly uniform graphene could promote the neurogenesis of hMSCs as well as the neurite outgrowths, which can be used as a platform for autologous stem cell-based therapy to treat neuronal disorders or diseases.

We evaluated the response of differentiated neurons from hMSCs on the highly uniform graphene by external cues. It is known that the $Ca2^+$ uptake plays a major role in controlling the excitability for regulating a range of processes in neurons.[29] To investigate whether the differentiated neurons respond to external signals, high K^+ stimulation was applied to the cells using Fluo-4 AM dye to analyze the intracellular $Ca2^+$ uptake after hMSC differentiation for 5 days.[29] As shown in Fig. 4, the fluorescence level of the cells on graphene was greatly increased during the

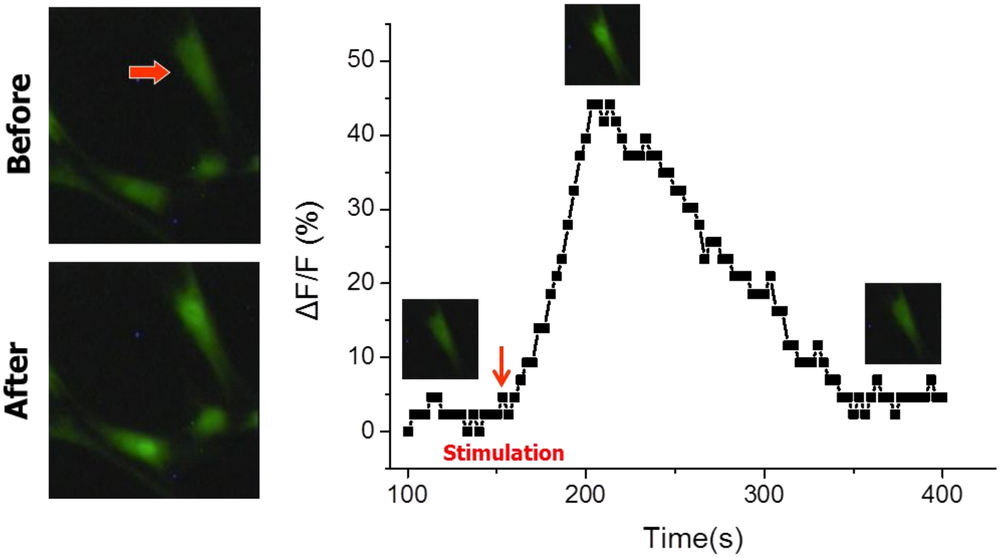

Figure 4 | Response of neuronal differentiated cells from hMSCs grown on highly uniform graphene to high K^+ stimulation on high-quality graphene. The cells were pre-incubated with Fluo-4 AM dye and imaged before and after the stimulations. Representative fluorescence images on the fluorescence intensity change on the cells were obtained before and after high K^+ stimulations. Representative plot of the relative fluorescence intensity change ΔF/F of the cell indicated by the red arrow.

stimulation. Approximately 40-100% fluorescence intensity, defined by the fluorescence intensity ΔF/F, was increased by K^+ treatment, indicating that the activated voltage-operated calcium channels of cells allowed the extracellular $Ca2^+$ influx. Our data demonstrated that the differentiated neurons from hMSCs on the graphene could be sensitive to external stimulation, thereby exhibiting potential as activated functional neurons in the neural networks.

One possible autologous stem cell based therapy for the treatment of neuronal diseases is to transplant differentiated functional neurons from stem cells in the in vitro culture into the target locations for the replacement of missing or damaged neurons. Here, we explore a possible therapeutic application for autologous stem cell based therapy by using the differentiated neurons of hMSCs on graphene. To this end, we prepared an *in vitro* protocol to indicate the potential of the differentiated neurons from hMSCs on highly uniform graphene for use as a source of cells for stem cell therapy to treat neuronal diseases (Fig. 5A): (i) culturing hMSCs on graphene in a growth medium → (ii) inducing neuronal differentiation of hMSCs using differentiation medium → (iii) detaching the differentiated hMSCs (neurons) on the graphene and re-seeding them onto a glass substrate → (iv) growing the differentiated cell culture on the glass substrate in the growth medium. We hypothesized that the differentiated cells detached from the graphene could maintain the functional neuronal property, in contrast to those from the graphene-uncoated glass substrate; this experiment simulated the transplanting of neurons into the body as a cell therapy to treat neuronal diseases.

We cultured the cells under study (i.e., the detached differentiated hMSCs from highly uniform graphene or the glass substrate with the trypsin treatment) on glass substrates. After the cells grew for 2 days in the growth media, we evaluated whether the cells could maintain their differentiated properties. Interestingly, using the Nissl staining, we found that the differentiated cells detached from the graphene were still expressed and had more elongated neuritis and network formations compared to the differentiated cells from the glass (Figs. 5 B and C). Our case study suggests that the differentiated neurons from hMSCs on the graphene could maintain their functional property even after re-seeding the cells detached from the graphene into the normal cell culture substrate in the growth medium, which can be an efficient source for autologous stem cell based therapy to treat neuronal disorders or diseases, although a more in-depth study, including molecular signaling and an *in vivo* study, must be performed to further verify the clinical applicability.

Nanoengineering systems have attracted considerable attention from scientific communities for stem cell engineering platforms, which can create biomimetic cellular environments to control or improve the function of stem cells.[30-34] Recently, the use of carbon-based nanomaterials, such as carbon nanotubes and graphene, has been proposed as a pioneering approach in the progress of designing nanoengineered stem cell culture platforms or scaffolds. [6-13,20,21] Two distinct strategies in using carbon-based nanomaterials have been typically used for stem cell engineering, with specific emphasis on differentiating the cells into various tissue lineages, including neuronal differentiation[12]: (i) stem cell culture with nanomaterials as the suspended conditions and (ii) stem cell culture on nanomaterials-coated or -incorporated substrates. Among them, the second approach has been widely proposed to

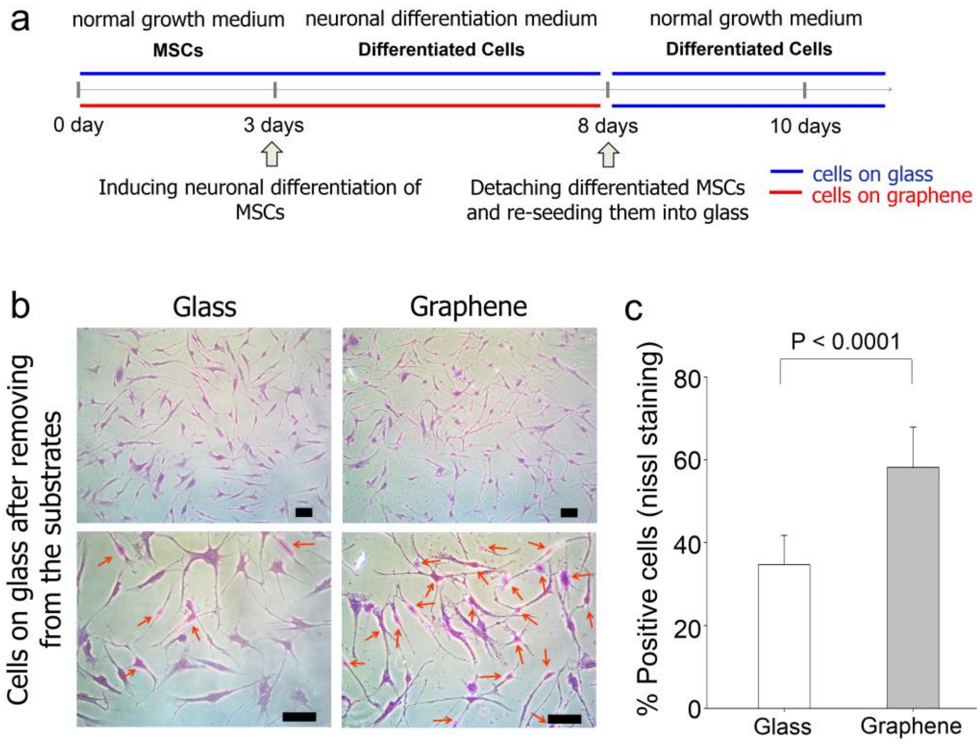

Figure 5 | A case study for autologous stem cell based therapy. a, An *in vitro* protocol to highlight the potential of the differentiated neurons from hMSCs grown on graphene as a source for cell therapy to treat neuronal diseases. It was hypothesized that the differentiated neurons from hMSCs grown on graphene could be transferred into the body to treat neuronal diseases. b, Representative Nissl staining images of the cells cultured on the glass substrates in the growth media for 2 days (total 10 day culture) after re-seeding the detached differentiated hMSCs onto graphene or a glass substrate using the trypsin treatment. c, Quantification of the number of cells stained by Nissl staining. Two-hundred cells were used in the quantification process regulate the growth and differentiation of stem cells because nanomaterials-coated substrates could provide ECM-like topographical cues as well as chemical cues. In conjunction with the context, our current study proposes that the highly uniform graphene may provide a unique cellular environment in promoting the growth and neuronal differentiation of stem cells, which can be used as efficient stem cell culture platforms or scaffolds.

Based on our experimental observations in this study, we found two notable findings: the highly uniform graphene (Fig. 1) can (1) create the unique cellular environments for 3D spheroid formation from aggregated hMSCs (Fig. 2) and (2) promote the neurogenesis of hMSCs, even in absence of any external neurogenic factors (Figs. 3-5).

(1) hMSCs have emerged as a primary candidate for cell therapy and tissue engineering, especially in clinical trials for a wide range of diseases.[4,35] Recently, it has been reported that self-assembly of hMSCs into tightly packed clusters to form 3D cellular aggregates can create an "*in vivo*-like" microenvironment that can enhance the regenerative capacity of hMSCs by promoting the secretion of cytokines and chemotaxic factors, even during short-term post expansion[35-37]; along these lines, we demonstrated that the short 3D spheroid formation of hMSCs (~ 7 days) could enhance the neuronal differentiation of hMSCs (Figs. 2 and 3). Thus, we believe that our finding that the highly uniform graphene alone can result in 3D spheroid formation of stem cells would be a valuable and easy protocol for various stem-cell applications, including cell therapy and tissue engineering. For example, our protocol can be used for the assembly of neural stem cells into 3D neurospheres,

which has been found to cause progenitor cells to revert to an early phenotype, thereby promoting the growth and differentiation of neural stem cells.[35]

(2) Neural differentiation of adult stem cells has been a promising strategy for the treatment of neuronal disorders or neurodegenerative diseases1. In particular, hMSCs hold great potential in clinical trials for autologous cell therapy because they can be easily obtained from patients and can potentially provide neuronal protection and repair.[4,35] Interestingly, we found that the high-quality graphene alone enhances the neural differentiation process of hMSCs without the use of any neurogenic chemical factors (Fig. 3). Leong's group reported that anisotropically nanopatterned substrates could induce the differentiation of hMSCs into the neuronal lineage without use of the neuronal induction medium.[38] They speculated that the significantly aligned and elongated cytoskeleton as well as the nuclei of the hMSCs by the nanotopographical cues might upregulate the neuronal markers.[38] In contrast, we found that the body and nuclei shapes of hMSCs on the graphene was not significantly different compared to those on the graphene-uncoated glass substrate (Fig. 2B), suggesting that other graphene-induced factors, such as the small 3D spheroid structure formation (Figs. 2A and Supplementary Fig. S4), enhanced FA formation (Fig. 2C) and cell-cell communication (Fig. 2D) of hMSCs as well as the natural properties of graphene (Supplementary Figs. S2 and S3), such as nanoscale structure, strong stiffness, roughness, electrical conductivity, and absorption of biomolecules, can collectively influence the enhanced neural differentiation of hMSCs.

In this study, although we have focused on the enhancement of differentiation of hMSCs into the functional neurons, we believe that the use of high-quality graphene is equally applicable to other systems, such as osteogenesis, adipogenesis, epithelial genesis, cardiomyogenic differentiation, or differentiation into the glia cells by various types of stem cells and appropriate chemical agents. We also expect to find further enhanced stem cell functions, including differentiation into specific lineages, by using high-quality graphene-based platforms (e.g., graphene-incorporated scaffolds and graphene-coated biomimetic tissue-like structure) for stem-based regenerative medicine.

Conclusions

In summary, our study supports the notion that highly uniform graphene can be used as an efficient platform for the growth and neural differentiation of hMSCs. We found that the 3D spheroid structure could be formed from aggregated hMSCs grown on highly uniform monolayer of graphene without the use of any external factors. We also found that the produced ECM molecules from hMSCs on graphene might guide the full adhesion of the cells onto the substrates, thereby enhancing the formation of FAs and the expression of the connexin 43 of the hMSCs. These graphene-induced interactions at the cell-substrate and cell-cell interfaces might collectively promote the neurogenesis of hMSCs as well as the neurite outgrowths. In particular, we found that the early neurogenesis-related genes in the hMSCs were highly upregulated on grapheme, even in the absence of any external neurogenic factors. The responses of differenced neurons from hMSCs on graphene were quite sensitive to external stimulation. The cells could maintain their neuronal properties, even after re-seeding the detached differenced neurons removed from graphene onto the normal cell culture substrate in the growth medium. Although in-depth studies must be performed to accurately understand the underlying molecular mechanisms, our current work has revealed that the highly uniform graphene may be able to regulate the growth and the neural differentiation of hMSCs, which would enable an efficient strategy for autologous stem cell based therapy to treat neuronal disorders or diseases, as well as for designing scaffolds for tissue engineering and regenerative medicine.

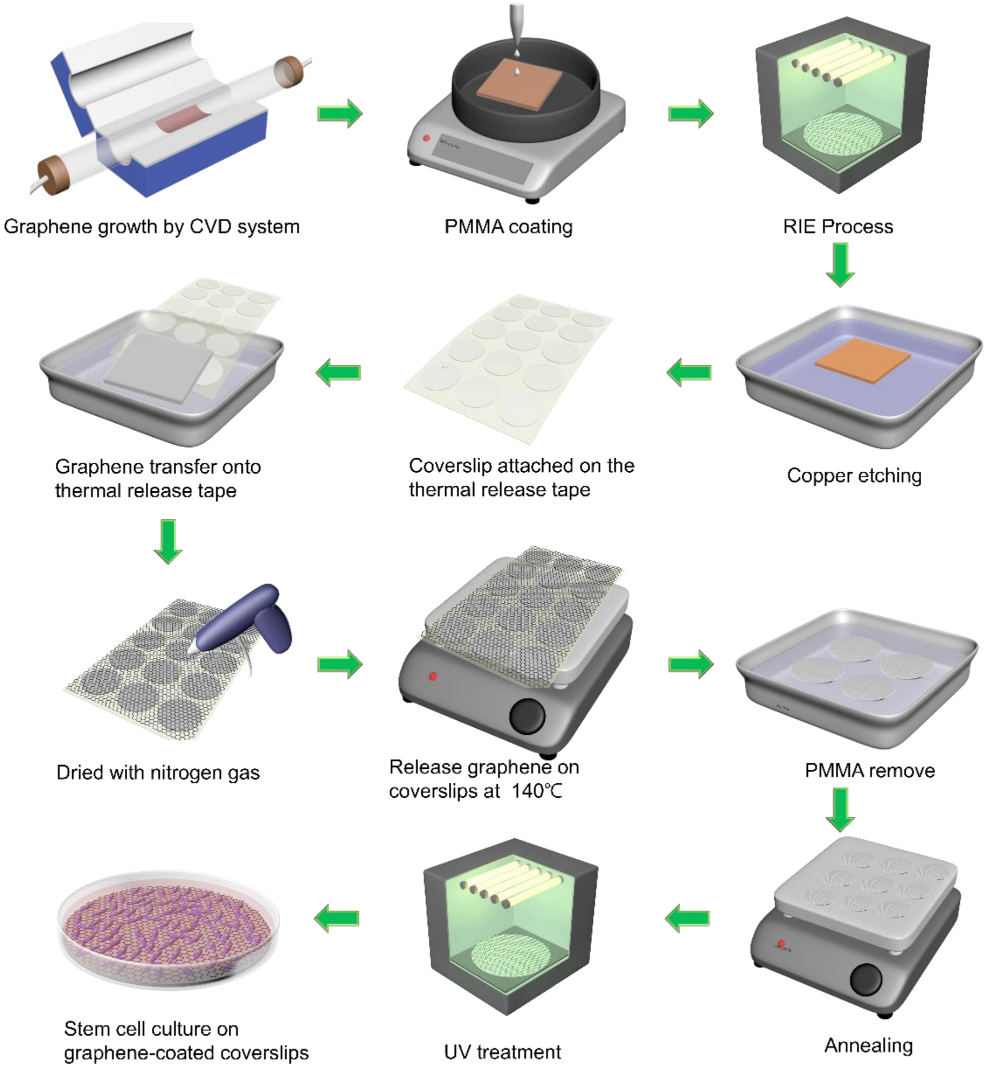

Figure S1 | Schematic of fabrication of the high quality graphene on glass substrate for growth and neuronal differentiation of stem cells

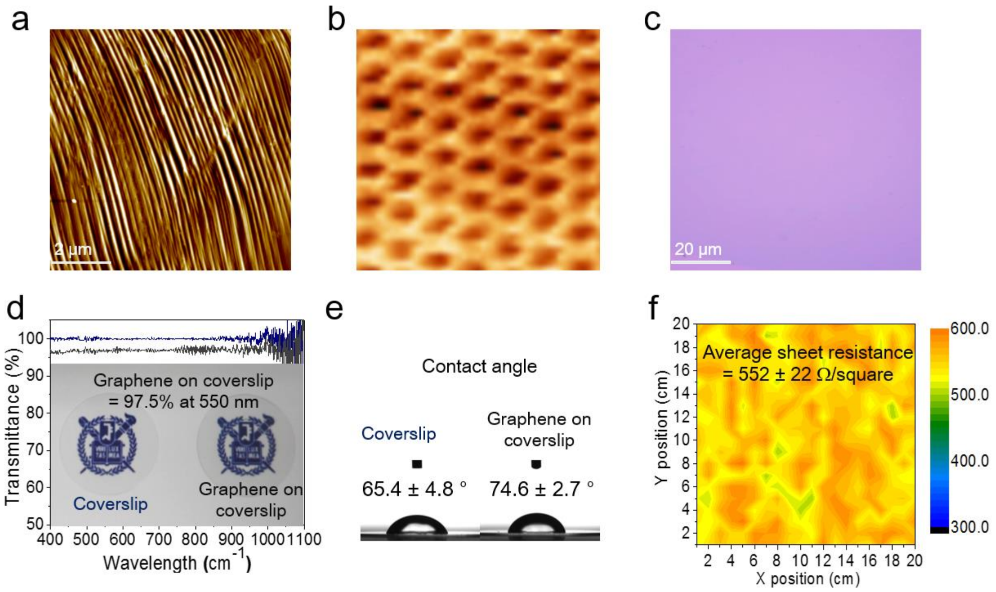

Figure S2 | a, AFM image of graphene growth on copper foil. b, Atmosphere STM image of graphene grown on Cu foil. c, Typical optical microscope image of graphene transferred onto 300 nm SiO_2/Si substrate. d, UV–vis spectra of transferred graphene on the glass substrate. e, Contact angle of graphene and coverslip f, Sheet resistance mapping of the graphene.

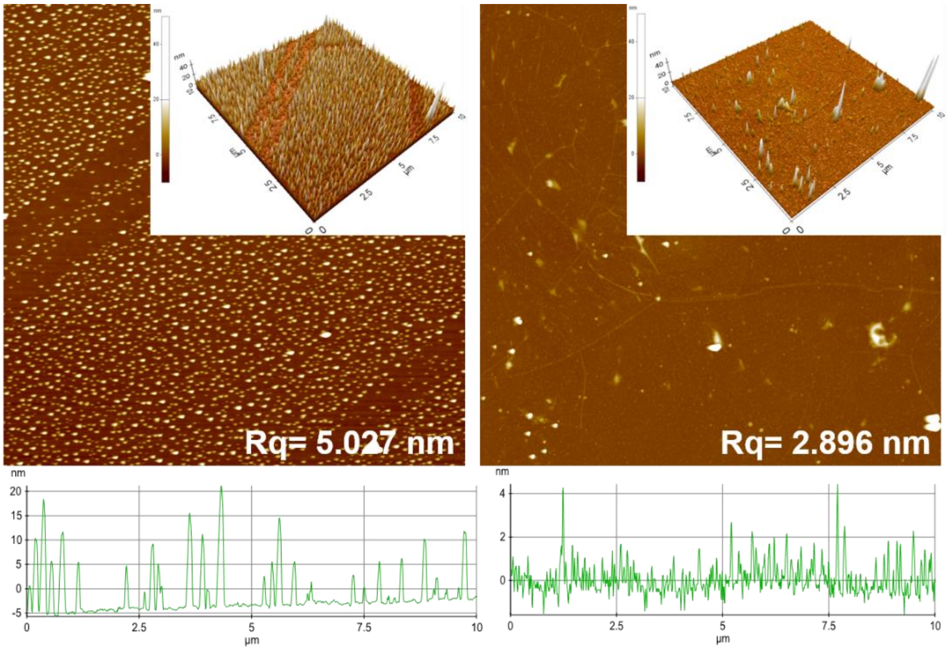

Figure S3 | AFM topography images of the graphene and glass substrate. The values indicate the roughness of the surfaces.

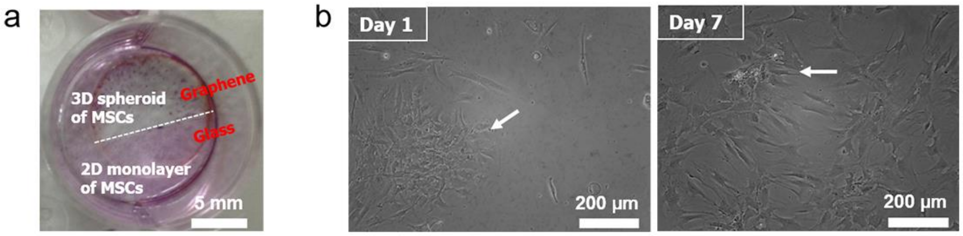

Figure S4 | a, Low magnification images of hMSCs cultured on the graphene and glass substrate for 1 day. The cells were stained by crystal violet to show the formation of 3D spheroids on the graphene. b, Representative phase-contrast images of hMSCs cultured on the graphene for 1 day and 7 days, respectively. The white arrows indicate the spheroids of hMSCs.

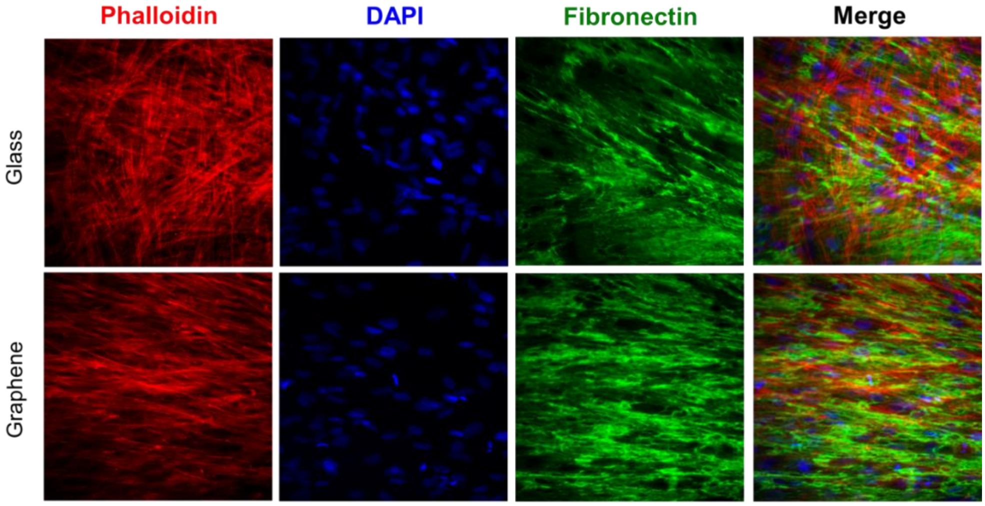

Figure S5 | Representative immunostaining images of actin, nucleus, and fibronectin on the graphene and glass substrate after culturing hMSCs for 7 days.

References

[1]. Delcroix, G. J., Schiller, P. C., Benoit, J. P. & Montero-Menei, C. N. Adult cell therapy for brain neuronal damages and the role of tissue engineering. *Biomaterials.* **2010**, 31, 2105-2120.

[2]. Prabhakaran, M. P., Venugopal, J. R. & Ramakrishna, S. Mesenchymal stem cell differentiation to neuronal cells on electrospun nanofibrous substrates for nerve tissue engineering. *Biomaterials*, **2009**, 30, 4996-5003.

[3]. David J., T. et al. Traumatic brain injury-related hospital discharges. results from a 14-state surveillance system, 1997. MMWR: Surveillance Summaries, **2003**, 52, 1-20.

[4]. Kim, S. U. & de Vellis, J. Stem cell-based cell therapy in neurological diseases: a review. *Journal of neuroscience research*, **2009**, 87, 2183-2200.

[5]. Deng, J., Petersen, B. E., Steindler, D. A., Jorgensen, M. L. & Laywell, E. D. Mesenchymal stem cells spontaneously express neural proteins in culture and are neurogenic after transplantation. *Stem cells*, **2006**, 24, 1054-1064.

[6]. Park, S. Y. et al. Enhanced differentiation of human neural stem cells into neurons on graphene. *Adv Mater.* **2011**, 23, 263-267.

[7]. Li, N. et al. Three-dimensional graphene foam as a biocompatible and conductive scaffold for neural stem cells. *Scientific reports*, **2013**, 3, 1604.

[8]. Wang, Y. et al. Fluorinated graphene for promoting neuro-induction of stem cells. *Adv Mater.* **2012**, 24, 4285-4290.

[9]. Solanki, A. et al. Axonal alignment and enhanced neuronal differentiation of neural stem cells on graphene-nanoparticle hybrid structures. *Adv Mater.* **2013**, 25, 5477-5482.

[10]. Nayak, T. R. et al. Graphene for Controlled and Accelerated Osteogenic Differentiation of Human Mesenchymal Stem Cells. *ACS Nano.* **2012**, 5, 4670-4678.

[11]. Lee, W. C. et al. Origin of Enhanced Stem Cell Growth and Differentiation on Graphene and Graphene Oxide. *ACS Nano.* **2012**, 5, 7334-7341.

[12]. Kim, J. et al. Bioactive effects of graphene oxide cell culture substratum on structure and function of human adipose-derived stem cells. *Journal of biomedical materials research. Part A.* **2013**, 101, 3520-3530.

[13]. Kalbacova, M., Broz, A., Kong, J. & Kalbac, M. Graphene substrates promote adherence of human osteoblasts and mesenchymal stromal cells. *Carbon,* **2010**, 48, 4323-4329.

[14]. Bae, S. et al. Roll-to-roll production of 30-inch graphene films for transparent electrodes. *Nat. Nanotechnol.***2010**, 574-578.

[15].Kim, K. S. et al. Large-scale pattern growth of graphene films for stretchable transparent electrodes. *Nature*. **2009**, 457, 706-710.

[16]. Li, N. et al. The promotion of neurite sprouting and outgrowth of mouse hippocampal cells in culture by graphene substrates. *Biomaterials.* **2011**, 32, 9374-9382.

[17]. Shi, X. et al. Regulating Cellular Behavior on Few-Layer Reduced Graphene Oxide Films with Well-Controlled Reduction States. *Adv Funct Mater*. **2012**, 22, 751-759.

[18]. Bendali, A. et al. Purified neurons can survive on peptide-free graphene layers. *Adv Healthcare Mater*. **2013**, 2, 929-933.

[19]. Ku, S. H. & Park, C. B. Myoblast differentiation on graphene oxide. *Biomaterials*. **2013**, 34, 2017-2023.

[20]. Park, J. et al. Graphene-Regulated Cardiomyogenic Differentiation Process of Mesenchymal Stem Cells by Enhancing the Expression of Extracellular Matrix Proteins and Cell Signaling Molecules. *Adv Healthcare Mater*. **2013**, 1-6.

[21]. Kim, J. et al. Graphene-incorporated chitosan substrata for adhesion and differentiation of human mesenchymal stem cells. *J. Mater. Chem. B*. 2013, 1, 933.

[22]. Kim, J. A. et al. High-throughput generation of spheroids using magnetic nanoparticles for three-dimensional cell culture. *Biomaterials*. **2013**, 34, 8555-8563.

[23]. Huang, G. S., Dai, L. G., Yen, B. L. & Hsu, S. H. Spheroid formation of mesenchymal stem cells on chitosan and chitosan-hyaluronan membranes. *Biomaterials*. **2011**, 32, 6929-6945.

[24]. Hsu, S. H. et al. Enhanced chondrogenic differentiation potential of human gingival fibroblasts by spheroid formation on chitosan membranes. *Tissue Eng Part A*. **2012**, 18, 67-79.

[25]. Chalut, K. J., Kulangara, K., Giacomelli, M. G., Wax, A. & Leong, K. W. Deformation of stem cell nuclei by nanotopographical cues. *Soft matter*. **2010**, 6, 1675-1681.

[26]. Cha, C., Liechty, W. B., Khademhosseini, A. & Peppas, N. A. Designing Biomaterials To Direct Stem Cell Fate. *ACS Nano*. **2012**, 6, 9353-9358.

[27]. Kim, J. et al. Charged nanomatrices as efficient platforms for modulating cell adhesion and shape. *Tissue Eng Part C Methods*, **2012**, 18, 913-923.

[28]. Kim, J. et al. Synergistic effects of nanotopography and co-culture with endothelial cells on osteogenesis of mesenchymal stem cells. *Biomaterials*. **2013**, 34, 7257-7268.

[29]. Tang, M. et al. Enhancement of electrical signaling in neural networks on graphene films. *Biomaterials*. **2013**, 34, 6402-6411.

[30]. Ferreira, L., Karp, J. M., Nobre, L. & Langer, R. New Opportunities: The Use of Nanotechnologies to Manipulate and Track Stem Cells. *Cell Stem Cell*. **2008**, 3, 136-146.

[31]. Kim, H. N. et al. Nanotopography-guided tissue engineering and regenerative medicine. *Adv. Drug Deliv. Rev*. **2013**, 65, 536-558.

[32]. Kim, J. et al. Designing nanotopographical density of extracellular matrix for controlled morphology and function of human mesenchymal stem cells. *Sci Rep*. **2013**, 3, 3552.

[33]. Guilak, F. et al. Control of Stem Cell Fate by Physical Interactions with the Extracellular Matrix. *Cell Stem Cell*. **2009**, 5, 17-26.

[34]. Kim, D. H., Provenzano, P. P., Smith, C. L. & Levchenko, A. Matrix nanotopography as a regulator of cell function. *J. Cell Biol*. **2012**,197, 351-360.

[35]. Sart S Fau - Tsai, A.-C., Tsai Ac Fau - Li, Y., Li Y Fau - Ma, T. & Ma, T. Three-dimensional Aggregates of Mesenchymal Stem Cells: Cellular Mechanisms, Biological Properties, and Applications.

[36]. Bartosh, T. J. et al. Aggregation of human mesenchymal stromal cells (MSCs) into 3D spheroids enhances their antiinflammatory properties. *Proc. Natl. Acad. Sci. U.S.A.* **2010**, 107, 13724-13729.

[37]. Cheng, N.-C., Chen, S.-Y., Li, J.-R. & Young, T.-H. Short-Term Spheroid Formation Enhances the Regenerative Capacity of Adipose-Derived Stem Cells by Promoting Stemness, Angiogenesis, and Chemotaxis. *Stem Cells Transl Med*. 2013, 2, 584-594.

[38]. Yim, E. K. F., Pang, S. W. & Leong, K. W. Synthetic nanostructures inducing differentiation of human mesenchymal stem cells into neuronal lineage. *Exp Cell Res*. **2007**, 313, 1820-1829.

Chapter 3

Graphene enhances the cardiomyogenic differentiation of human embryonic stem cells

Introduction

Due to the unique physical and chemical properties of graphene, this material has been reported to act as a culture substrate that promotes the lineage specification of adult mesenchymal stem cells (MSCs) and neural stem cells, both of which are multipotent stem cells. The culture of human neural stem cells (hNSCs) on graphene promotes their differentiation toward neurons through electrical stimulation facilitated by graphene. [1,2] Graphene can also promote the adhesion of MSCs,[3] and the culture of MSCs on graphene enhances their osteogenic differentiation through strong cell adhesion to graphene.[4] Graphene has also been used for the culture of pluripotent stem cells. Graphene maintains the pluripotency of mouse induced pluripotent stem cells.[5] Human embryonic stem cells (hESCs) adhered to Geltrex® - coated graphene remained viable and pluripotent and proliferated.[6] However, the effect of graphene on the differentiation of pluripotent ESCs has not yet been reported.

Cardiomyocytes generated from stem cells would be a useful cell source for cell-based therapies for ischemic heart diseases. A variety of adult stem cells, such as bone marrow-derived stem cells,[7] adipose-derived stem cells,[8] resident cardiac stem cells,[9] and umbilical cord blood stem cells,[10] have been used to treat ischemic heart diseases. However, these adult stem cells are known to have limited ability to differentiate into cardiomyocytes.[11] In contrast, ESCs are known to differentiate spontaneously into cardiomyocytes.[12] When these cells are transplanted into a damaged heart, ESCs integrate into the recipient heart and improve the heart functions.[13] Therefore, hESCs would be a useful cell-source for stem cell-based therapy for ischemic heart diseases.

Although graphene exerts stimulatory effects on the lineage specification of multipotent adult stem cells, its effects on the differentiation of pluripotent ESCs have not yet been reported. In the present study, we investigated whether culture on graphene enhances the cardiomyogenic differentiation of hESCs. Large-area graphene on glass coverslips was prepared through the chemical vapor deposition method. The spontaneous cardiomyogenic differentiation of hESCs was investigated by culturing hESCs on either glass (control) or graphene without the addition of exogenous chemicals for differentiation induction and by evaluating the expression of cardiac-specific genes. The differentiation of these cells was also compared with that of cells cultured on Matrigel-coated glass, which is a substrate used in the conventional, directed two-dimensional culture differentiation systems for the cardiomyogenic differentiation of hESCs without forming embryoid bodies.[14] The direct two-dimensional culture differentiation system is an efficient method for cardiomyogenic differentiation of hESCs, since it was reported that 70% of hESC clusters were contracting and 90% of cells had a cardiomyocyte phenotype after culture through.[14] The mesodermal and endodermal differentiations were compared among the experimental groups because these differentiations are known to be intermediate stages of the cardiomyogenic differentiation of hESCs.[14] The mechanisms underlying the enhanced cardiomyogenic differentiation were also investigated.

Experimental

Graphene Preparation and Characterization

Monolayer graphene was synthesized through the CVD process. The graphene film grown on the copper foil was covered by poly(methyl methacrylate) (PMMA) and floated on the surface of an aqueous solution of 0.1 M ammonium persulphate [$(NH_2)_4S_2O_8$]. After all of the copper layers were etched away, the floating PMMA/graphene film was collected using a clean PET film and transferred to deionized water. The cleaning process was repeated five times. The graphene film with the PMMA support was transferred to glass coverslips. The samples were dried with nitrogen gas immediately after the transfer and baked for 8 h on a hot plate at 60 ℃. The samples were then cleaned using acetone at room temperature for 30 min to remove the PMMA support layer. The samples were then dried and baked for 8 h on a hot plate at 60 ℃. The graphene was sterilized by UV treatment for 30 min prior to cell culture. The samples were characterized by Raman spectroscopy, ultraviolet-visible spectrometry, transmission electron microscopy (TEM), and selected area electron diffraction (SAED). The structural properties of the graphene on the glass coverslip were further investigated through Raman spectroscopy (RM 1000-Invia, Renishaw, UK). The Raman spectra were recorded using an argon ion laser (514 nm) as the excitation source with a notch filter of 50 cm^{-1}. The typical scan range was from 1000 to 3000 cm^{-1}, and the instrumental resolution was 10 cm^{-1}. The optical transmittance of the graphene on the coverslip was measured using an ultraviolet-visible spectrometer (UV-3600, Shimadzu, Japan). The TEM and SAED analyses were conducted on a TEM (JEOL 2100, JEOL, Japan) operated at 200 kV. The rotation between the TEM images and the corresponding SAED patterns was calibrated using molybdenum trioxide crystals. The sheet resistances of the graphene on the coverslip were measured through the van der Pauw four-probe method using a Hall measurement system. The surface morphology of graphene and glass was examined with non-contact mode AFM (XE-100 system, Park Systems, Suwon, Korea).

hESC culture

SNUhES31 (Institute of Reproductive Medicine and Population, Medical Research Center, Seoul National University, Seoul, Korea), which is a hESC line, was maintained in their undifferentiated state by feeder-free culturing on human recombinant VN (Life Technologies, Carlsbad, CA, USA)-coated (0.5 μg/cm^2) culture dishes with Essential 8^{TM} medium (Life Technologies) as previously described.[40] The culture medium was changed daily, and the hESCs were passaged every week.

Differentiation of hESCs into cardiomyocytes using a two-dimensional system

For the cardiomyogenic differentiation of cultured hESCs using a two-dimensional system, cultured hESC colonies were fragmented into small clumps with uniform sizes using the STEMPRO® EZPassage tool (Life Technologies). Prior to cell plating, glass coverslips were coated with Matrigel (BD Bioscience, San Jose, CA, USA)[41] or VN[42] as previously described for hESCs culture. Graphene on glass coverslips was also coated with VN. The Matrigel- or VN-coated glass and VN-coated graphene were placed onto six-well plates. Small clumps of hESCs were plated on each of the Matrigel- or VN-coated glass and VN-coated graphene in the six-well plates (150 clumps per well). The cardiomyogenic differentiation of the culture was performed as previously described.[14] Briefly, the attached hESCs were expanded in hESC media composed of Dulbecco's Modified Eagle's Medium (DMEM)/F12 (Gibco BRL, Gaithersburg, MD, USA) supplemented with 20% (v/v) knockout serum replacement (Life Technologies), 4 ng/ml FGF2 (R&D Systems, Minneapolis, MN, USA), 1% nonessential amino acid (Life Technologies), 0.1 mM β-mercaptoethanol (Sigma), and 0.2% primocin (InvivoGen, San Diego, CA, USA) for four days and then cultured in hESC media without FGF2 for three days. The cells were cultured in DMEM (Gibco BRL) containing 10% (v/v) fetal bovine serum (FBS, Gibco BRL) for seven days. Finally, the cells were cultured in DMEM containing 20% (v/v) FBS for seven days. The culture media were changed every 24 h.

Viability of hESCs cultured on graphene

The viability of hESCs cultured on graphene was examined by live and dead assay at day 2. The live and dead cells on non-coated graphene or VN-coated graphene were detected with fluorescein diacetate (FDA, Sigma-Aldrich, St. Louis, MO, USA) and ethidium bromide (EB, Sigma). The hESCs were incubated in FDA/EB (5 μg/ml or 10 μg/ml) solution for 5 min at 37 °C and then washed twice in PBS. The dead cells were stained orange due to the nuclear permeability of EB. The viable cells, which are capable of converting the non-fluorescent FDA into fluorescein, were stained green. After staining, the samples were examined using a fluorescence microscope (Model IX71 Olympus, Tokyo, Japan). Adhesion morphology of hESCs on graphene was examined by scanning electron microscopy (SEM; JSM-6701F, JEOL, Tokyo, Japan).

Quantitative real-time reverse transcription-polymerase chain reaction (qRT-PCR) of EBs

The mRNA expression levels of differentiated hESCs were analyzed through qRT-PCR. The total RNA was extracted from the differentiated hESCs on days 4, 7, 14, and 21 and reverse-transcribed into cDNA. The qRT-PCR was performed using the StepOnePlus real-time PCR system (Applied Biosystems, Foster City, CA, USA) with a FAST SYBR Green PCR master mix (Applied Biosystems). Each of the 45 cycles performed consisted of the following temperature program: 94 ℃ for 3 sec and 60 ℃ for 30 sec. The primer sequences are shown in Table 1.

Western blot assay

hESCs cultured for 21 days on Matrigel- or VN-coated glass and VN-coated graphene were lysed with sodium dodecyl-sulfate (SDS) sample buffer [62.5 mM Tris–HCl (pH 6.8), 2% (w/v) SDS, 10% (v/v) glycerol, 50 mM dithiothreitol, and 0.1% (w/v) bromophenol blue]. The total protein concentration was determined through a bicinchoninic acid protein assay (Pierce Biotechnology, USA). Western blot analysis was performed through 10% (w/v) SDS-polyacrylamide gel electrophoresis. The proteins were first transferred to an Immobilon-P membrane

(Millipore Corp., USA) and then probed with antibodies against human vinculin (Abcam, Cambridge, UK), paxillin (Abcam), FAK (Abcam), pFAK (Abcam), ERK 1/2 (Abcam), and pERK 1/2 (Abcam). The proteins were then incubated with a horseradish peroxidase-conjugated secondary antibody (Santa Cruz Biotechnology, USA) for 1 h at room temperature. The blots were developed using an enhanced chemiluminescence detection system (Amersham Bioscience, USA). The data were quantified through densitometric scanning (Image-Pro Plus software, Media Cybernetics, Marlow, UK).

Statistical analysis

The quantitative data are expressed as the means ± standard deviation. The statistical analysis was performed by analysis of variance (ANOVA) using a Bonferroni test. A p value < 0.05 was considered statistically significant.

Results and Discussion

The large-area, monolayer graphene used in this study was synthesized on copper foils through the chemical vapor deposition (CVD) method (Figure 1a). To confirm the presence of graphene, the graphene was transferred onto a SiO_2/Si substrate according to a previously reported method.[15] Figure 1b shows an optical micrograph of a graphene film transferred onto a SiO_2/Si substrate. The uniform color contrast of the optical micrograph indicates that the graphene film has excellent thickness uniformity. Although the graphene film was only one-atom thick on SiO_2/Si substrates with a well-defined oxide thickness (300 nm), it was easily observed with a simple conventional optical microscope. Optical images of the glass coverslip and the graphene-coated glass coverslip showed that both were transparent (Figure 1c). The contact angle measurements showed that the graphene-coated glass coverslip was slightly hydrophobic (74.4 ± 3.5°), whereas the contact angle of the coverslip was 64.2 ± 3.7° (Figure 1d). To determine the quality of the graphene, the transferred graphene film was characterized through Raman spectroscopy (Figure 1e). The Raman spectrum of graphene is characterized by three main characteristic peaks. The G peak is commonly found in carbon-based materials with a hexagonal pattern. The G peak near 1580 cm^{-1} arises from the emission of zone-center optical phonons, the D band near 1350 cm^{-1} arises from the doubly resonant disorder-induced mode, and the 2D peak is the second order of the D peak that moves from the K to the K' point and the symmetry-allowed 2D over-tune mode near 2700 cm^{-1}. The shift and

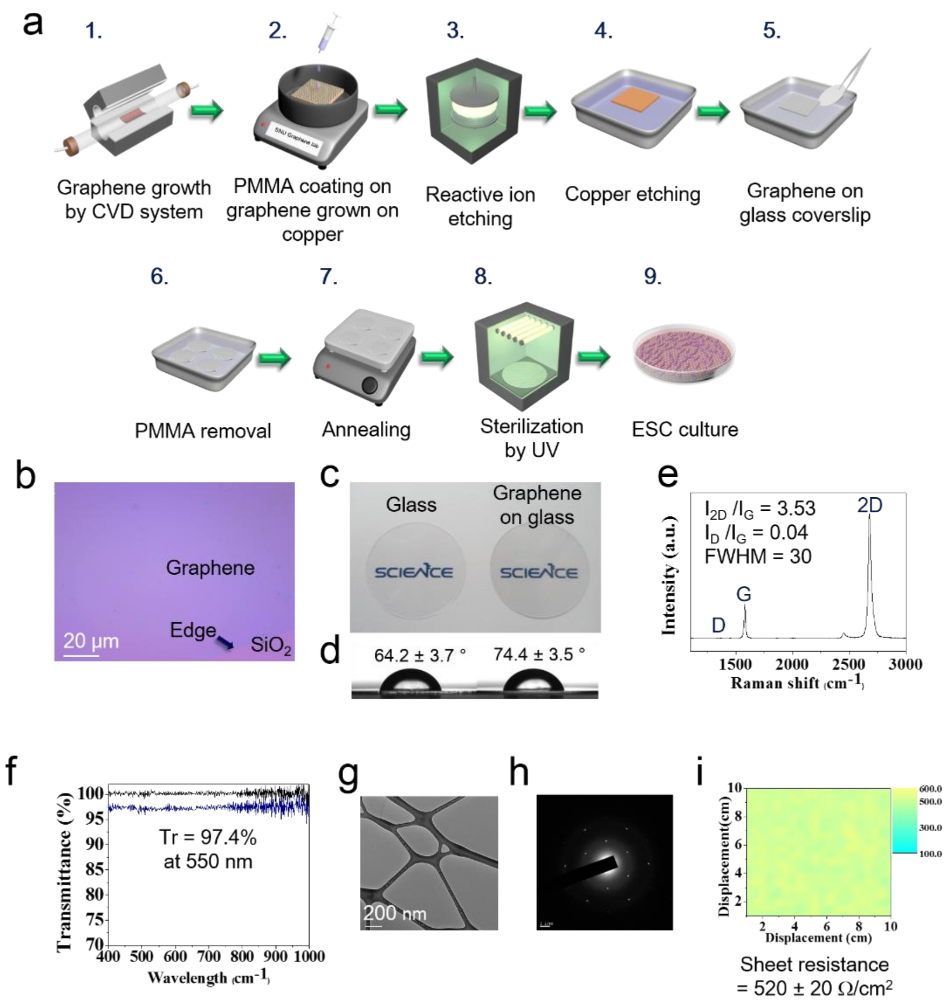

Figure 1 | Preparation and characterization of large-area graphene substrates. a, Schematic of the preparation process used to produce the graphene coating on a glass coverslip. b, A typical optical microscopic image of graphene transferred onto 300-nm-thick SiO_2/Si substrate. c, Photograph d, contact angle of a glass coverslip and graphene on a glass coverslip. e, Raman spectroscopy of the transferred graphene. f, UV-visible spectra of transferred graphene on a glass coverslip and a glass coverslip substratum, showing the transparency of the graphene on the coverslip. g, TEM image of graphene on a TEM grid. h, SAED pattern. i, Sheet resistance of monolayer graphene on a glass coverslip.

line shape associated with these modes have been used to determine the quality of graphene and the number of graphene layers. The peak located at ~2700 cm^{-1} (G′ band) exhibits a full width at half-maximum (fwhm) of 26~33 cm^{-1}. The intensity of the I_{2D}/I_G ratio is more than three-fold higher than that of the peak located at ~1600 cm^{-1} (the G band), and there is no measurable peak observed at ~1350 cm^{-1} (the D band), which indicates the synthesis of high-quality monolayer graphene. In addition, the graphene-coated glass coverslip exhibited high transparency with a transmittance that exceeded 97.4% at a wavelength of 550 nm (Figure 1f), which confirms the presence of uniform and monolayer graphene. Figure 1g shows a representative low-magnification TEM image of graphene sheet on a TEM grid. The typical SAED pattern for well-synthesized graphene was observed for the graphene used in this study (Figure 1h). The transferred graphene on the coverslip showed a sheet resistance of 520 ± 20 Ω/cm^2 with a high uniformity (Figure 1i).

Prior to culture for cardiomyogenic differentiation, we tested whether hESCs could adhere to graphene and survive. hESC clumps were plated on non-coated graphene and vitronectin (VN)-coated graphene. Two days later, the hESCs on VN-coated graphene showed good cell-attachment and colony formation (Figure 2a). In contrast, the hESCs did not adhere to non-coated graphene. The viability of hESCs cultured on non-coated graphene and VN-coated graphene was evaluated by live and dead assays with FDA/EB staining (Figure 2b). The hESCs on non-coated graphene were dead (orange-red color), whereas the hESCs cultured on VN-coated graphene were viable (green color, Figure 2b). A SEM image showed that hESCs are well-adherent to VN-coated graphene (Figure 2c), whereas all hESCs were detached from non-coated graphene. These results indicate that coating of graphene with VN is required for a high viability of hESCs cultured on the graphene. Thus, VN-coated graphene was used for the hESC culture in the present study.

hESCs first differentiate into mesodermal cells and endodermal cells, and the mesodermal cells further differentiate into cardiogenic lineages in two-dimensional, directed differentiation systems (Figure 3a).[14] Endodermal cells appear to interact with mesodermal cells to induce the differentiation of the mesodermal cells toward cardiogenic lineages.[14] hESCs were cultured on Matrigel-coated glass (Matrigel group), VN-coated glass (glass group), or VN-coated graphene (graphene group) for 21 days, and the mesodermal, cardiac mesodermal, endodermal, and ectodermal gene expression profiles were determined by qRT-PCR assay. On day 14, the graphene group showed a significantly enhanced expression of mesodermal genes (T and M-CAD) and a cardiac mesodermal gene (MESP1) compared with both the Matrigel and the glass groups (Figure 3b, c). On day 21, only a cardiac mesodermal gene (MESP1) was enhanced in the graphene group compared with both the Matrigel and the glass groups. T expression is known to induce the expression of MESP1,[16] which is a master regulator of cardiac progenitor specification and is needed to enter the cardiac mesodermal stage.[17-19] The graphene group showed higher expression of SOX17 on day 14 and FOXA2 on days 14 and 21, both of which are endodermal genes, compared with the Matrigel and the glass groups (Figure 3d). In contrast, the ectodermal gene (TUBB3) expression, which may not be involved in the cardiomyogenic differentiation process of hESCs, was not increased in the graphene

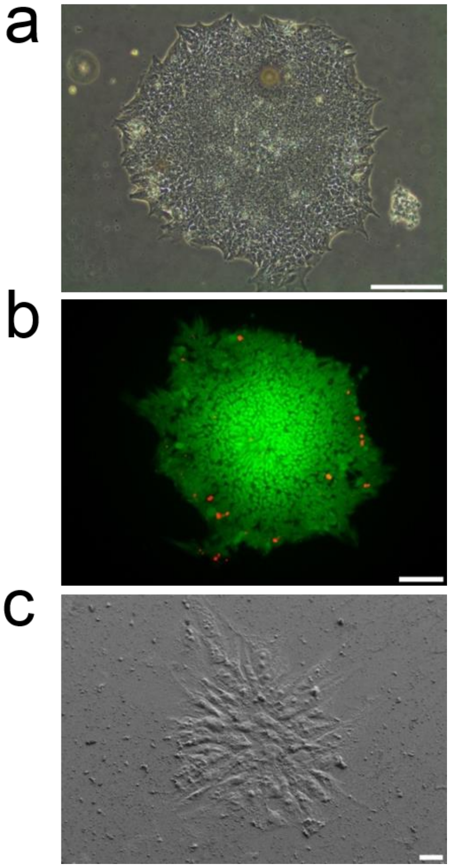

Figure 2 | The coating of graphene with VN is required to achieve a high viability of hESCs cultured on the graphene. hESCs were cultured on graphene for two days. a, Light microscopic images of hESCs cultured on the graphene. b, Fluorescence microscopic images of hESCs stained with FDA and EB. The green and orange-red colors indicate viable and dead cells, respectively. c, SEM image of hESCs cultured on graphene. The scale bars indicate (a) 200 μm, (b) 100 μm, and (c) 20 μm.

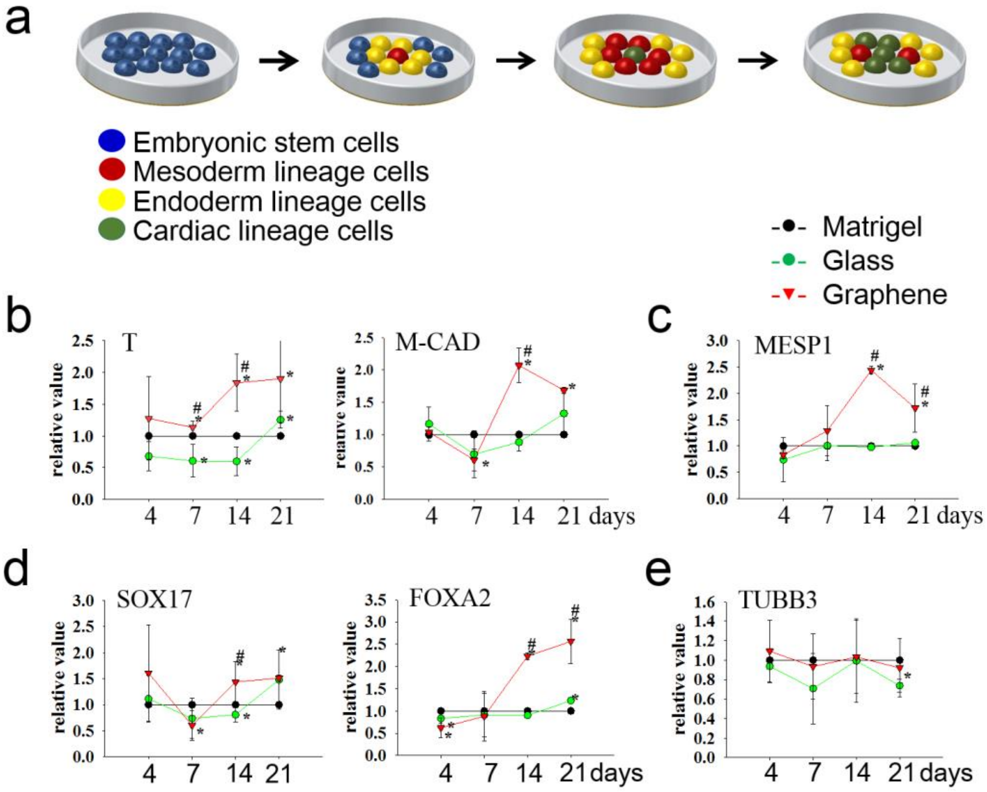

Figure 3 | Culture on graphene enhances the mesodermal and endodermal lineage differentiation of hESCs. a, A schematic diagram for the cardiomyogenic differentiation of hESCs in a two-dimensional, stepwise differentiation system. b, The mesodermal c, cardiac mesodermal d, endodermal, and e, ectodermal gene expression profiles of hESCs cultured for 21 days on Matrigel-coated glass (Matrigel), VN-coated glass (glass), or VN-coated graphene (graphene), as determined by qRT-PCR assay. The values were normalized to the levels obtained for the Matrigel group (n=4 per group, *p<0.05 versus Matrigel, #p<0.05 versus glass).

group compared with the Matrigel and the glass group throughout the culture period (Figure 3e). These results suggest that graphene promotes mesodermal lineage differentiation at the middle-stage time point and differentiation into the cardiac mesodermal lineage, which is a more cardiogenic lineage than the mesodermal lineage, at the end-stage time point.

The endodermal lineage induction by graphene may promote the cardiomyogenic differentiation of hESCs. Signals from the endoderm, such as bone morphogenetic protein (BMP) and fibroblast growth factor (FGF), are important for cardiac development.[20] It is known that factors secreted by endodermal lineage cells, such as BMP-2, FGF4, and transforming growth factor-β, are needed to induce the cardiac differentiation of murine ESCs and heart development.[21, 22] It has also been reported that co-culture with a endodermal cell line induces the cardiac differentiation of hESCs.[23] In two-dimensional culture systems, the presence of endodermal cells around the mesodermal cells appear to induce the cardiomyogenic differentiation of hESCs.[14] Therefore, the enhanced endodermal lineage differentiation by graphene (Figure 3d) may induce an enhancement in the cardiomyogenic differentiation of hESCs.

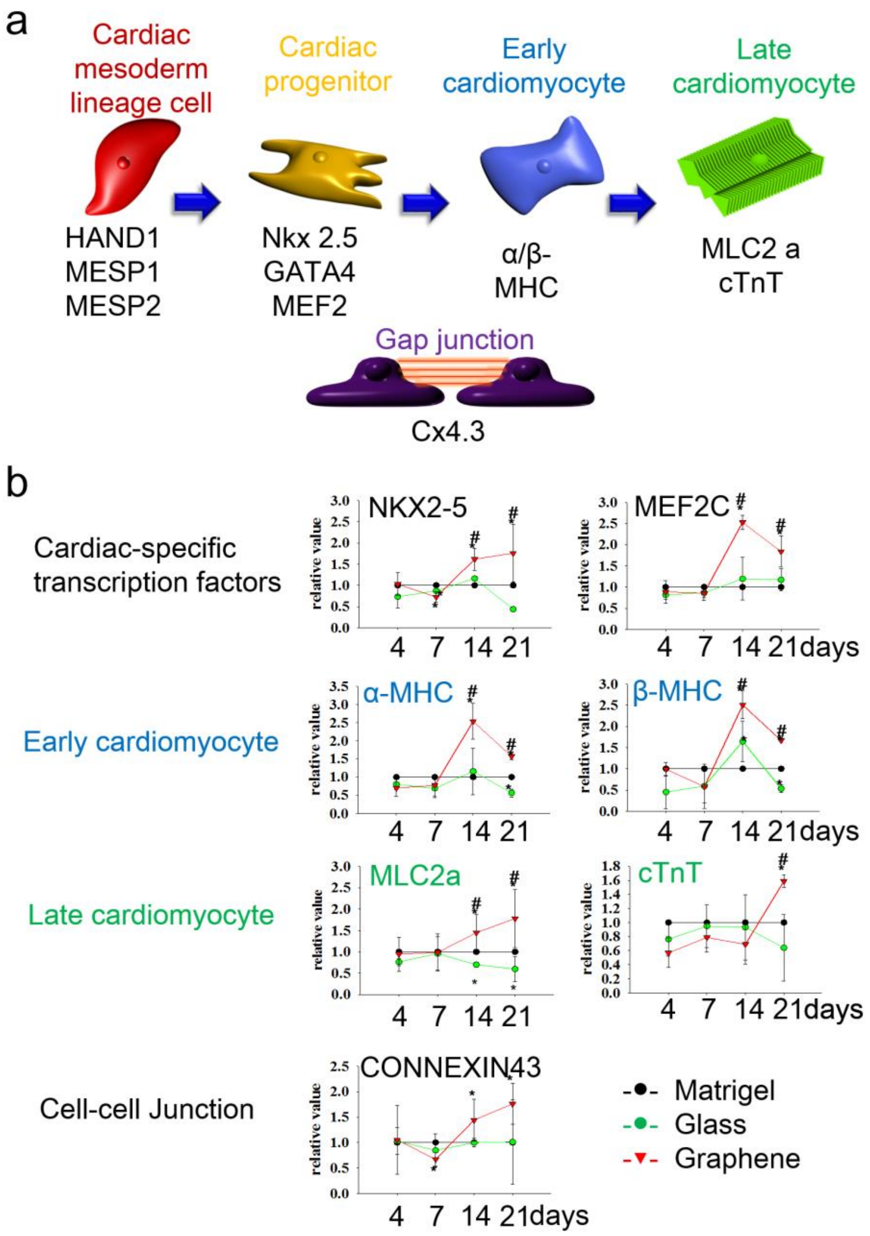

Figure 4 | Culture on graphene enhances the cardiomyogenic differentiation of hESCs. a, A schematic diagram of the gene expression profile during the cardiomyogenic differentiation process of hESCs. b, Cardiomyogenic gene expression profiles of hESCs cultured for 21 days on Matrigel-coated glass (Matrigel), VN-coated glass (glass), or VN-coated graphene (graphene), as determined by qRT-PCR assay. The values were normalized to the levels obtained for the Matrigel group (n=4 per group, *p<0.05 versus Matrigel, #p<0.05 versus glass).

We investigated whether the culture of hESCs on graphene promotes their cardiomyogenic differentiation by evaluating the cardiomyogenic gene expression through a qRT-PCR assay. Cardiac mesodermal lineage cells differentiate into cardiac progenitor cells, which further differentiate into cardiomyocytes (Figure 4a). Strikingly, the expression of many cardiomyogenic markers, as shown in Figure 4a, was enhanced in the graphene group compared with both the Matrigel and the glass groups, even in the absence of cardiomyogenic inducers in the culture medium (Figure 4b).

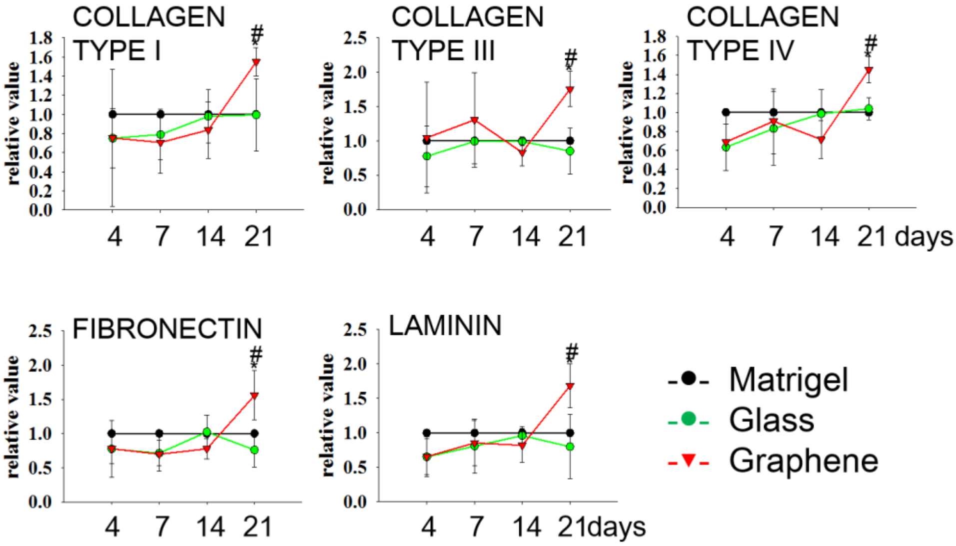

Figure 5 | Culture on graphene enhances cardiac-specific ECM expression in hESCs. Gene expression profiles of extracellular matrix proteins in hESCs cultured for 21 days on Matrigel-coated glass (Matrigel), VN-coated glass (glass), or VN-coated graphene (graphene), as determined by qRT-PCR assay. The values were normalized to the levels obtained for the Matrigel group (n=4 per group, *p<0.05 versus Matrigel, #p<0.05 versus glass).

The gene expression of cardiomyogenic transcriptional factors (NKX2-5, GATA4, and MEF2C), cardiomyogenic contractile proteins (α-MHC, β-MHC, MLC2a, and cTnT), and gap junction proteins (CONNEXIN43) was significantly higher in the graphene group compared with both the Matrigel and the glass groups on days 14 and/or 21. Early cardiomyocyte marker (α-MHC and β-MHC) expression was maximal on day 14 and decreased on day 21 in the graphene group, whereas late cardiomyocyte marker (MLC2a, and cTnT) expression increased with the culture time from day 14 to day 21. To further investigate the effects of graphene on the cardiomyogenic differentiation of hESCs, the gene expression of cardiac-specific ECMs was evaluated through a qRT-PCR assay. The gene expression of cardiac-specific ECMs, such as COLLAGEN TYPE I, COLLAGEN TYPE III, COLLAGEN TYPE IV, FIBRONECTIN, and LAMININ, was enhanced on day 21 in the graphene group compared with both the Matrigel and the glass groups (Figure 5).

The mechanisms underlying the graphene-enhanced cardiomyogenic differentiation were investigated. The enhanced cardiomyogenic differentiation may be, at least in part, due to nanotopography of graphene, which enhanced hESC adhesion and the upregulation of extracellular signal-regulated kinase (ERK) signaling. Graphene showed more nanotopographical features than glass (Figure 6a).

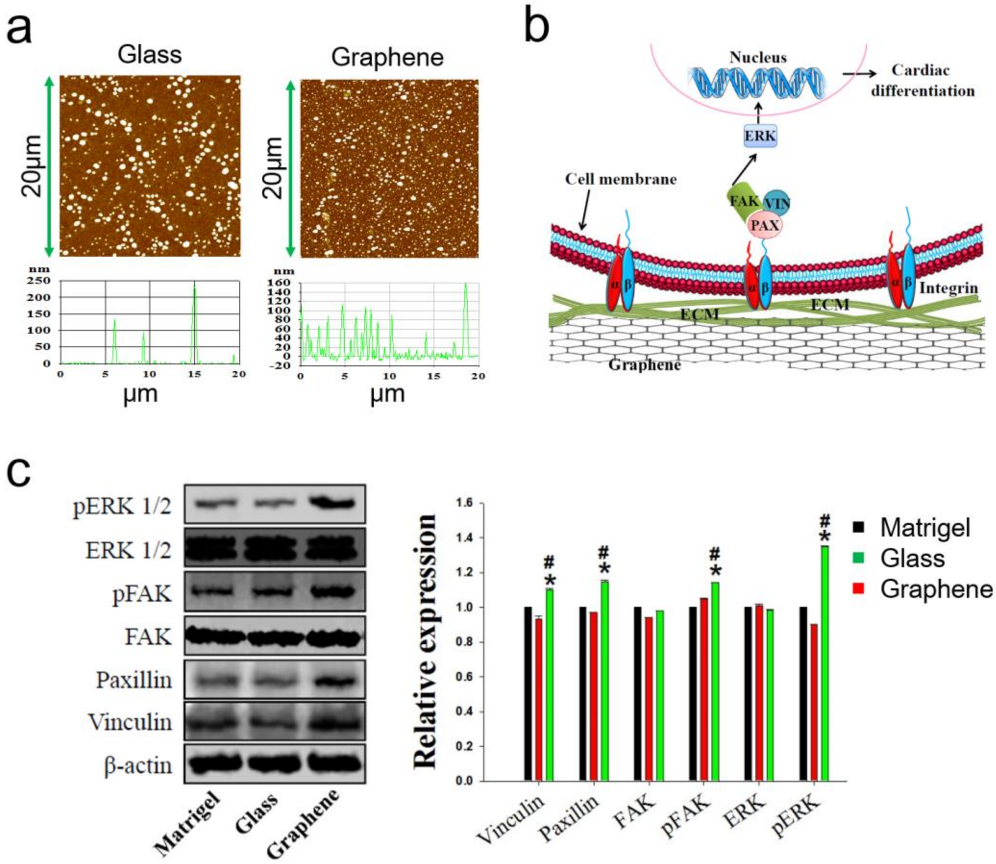

Figure 6 | Mechanisms underlying the graphene-enhanced cardiomyogenic differentiation Nanoroughness of graphene, FAK, and ERK signaling. a, AFM images and surface nanoroughness of VN-coated glass (glass group) and VN-coated graphene (graphene group). b, a schematic diagram of the signal transduction pathways associated with the cardiomyogenic differentiation of hESCs cultured on graphene. The enhanced hESC adhesion and the subsequent upregulation of ERK signaling of hESCs cultured on graphene were likely attributed to the nanoroughness of the graphene. ECM: extracellular matrix, α, β: integrin α and β subunits, PAX: paxillin, VIN: vinculin. c, Western blot analyses of hESCs cultured on Matrigel-coated glass (Matrigel), VN-coated glass (glass), or VN-coated graphene (graphene) to analyze the molecules involved in the signal transduction pathways, and quantification of the relative protein expression levels of the cell signaling molecules. The values were normalized to the levels obtained for the Matrigel group (n=3 per group, *p<0.05 versus Matrigel, #p<0.05 versus glass).

Graphene enhanced hESC adhesion, as the expression of phosphorylated focal adhesion kinase (pFAK), vinculin, and paxillin, which are related to the focal adhesion of cells (Figure 6b),[24,25] was enhanced in the graphene group compared with the other groups (Figure 6c). The enhanced hESC adhesion on graphene with nanotopographical features is consistent with the results of previous studies in which cell adhesion was enhanced on substrates with nanoscale protrusions (15-45 nm [26] and 250-300 nm [27]). First, strong hESC adhesion to graphene may be responsible for the enhanced cardiomyogenic differentiation. It has been shown that stem cell differentiation is enhanced on nanotopographical substrates through FAK.[28] Also, a previous study showed that the enhanced neuronal differentiation of hNSCs cultured on laminin-coated graphene compared to laminin-coated glass was likely due to the enhanced cell adhesion to laminin-coated graphene.[2] Second, the enhancement of hESC adhesion in the graphene group may promote the cardiomyogenic differentiation of hESCs through ERK signaling (Figure 6b). Graphene enhanced the expression of phosphorylated ERK (pERK) compared with both the Matrigel and the glass groups (Figure 6c). It has been reported that the activation of ERK enhances the cardiomyogenic differentiation of hESCs.[29]

Conclusions

The culture of hESCs on graphene promotes the stepwise differentiation of these cells into mesodermal cells and endodermal cells and their subsequent cardiomyogenic differentiation compared with their culture on glass. Moreover, the analysis of the cardiomyogenic differentiation of hESCs cultured on graphene or Matrigel revealed that graphene was superior to Matrigel, which is a substrate used in conventional cardiomyogenic differentiation systems. The graphene-enhanced cardiomyogenic differentiation may be, at least in part, due to nanotopography of graphene, which enhanced hESC adhesion and the upregulation of ERK signaling. The data suggest that graphene is a novel culture substrate for the enhancement of the differentiation of hESCs into cardiomyogenic lineage cells, which would be useful for the development of stem cell-based therapies for ischemic heart diseases.

Table 1. Human-specific primers for each gene analyzed through the qRT-PCR assay.

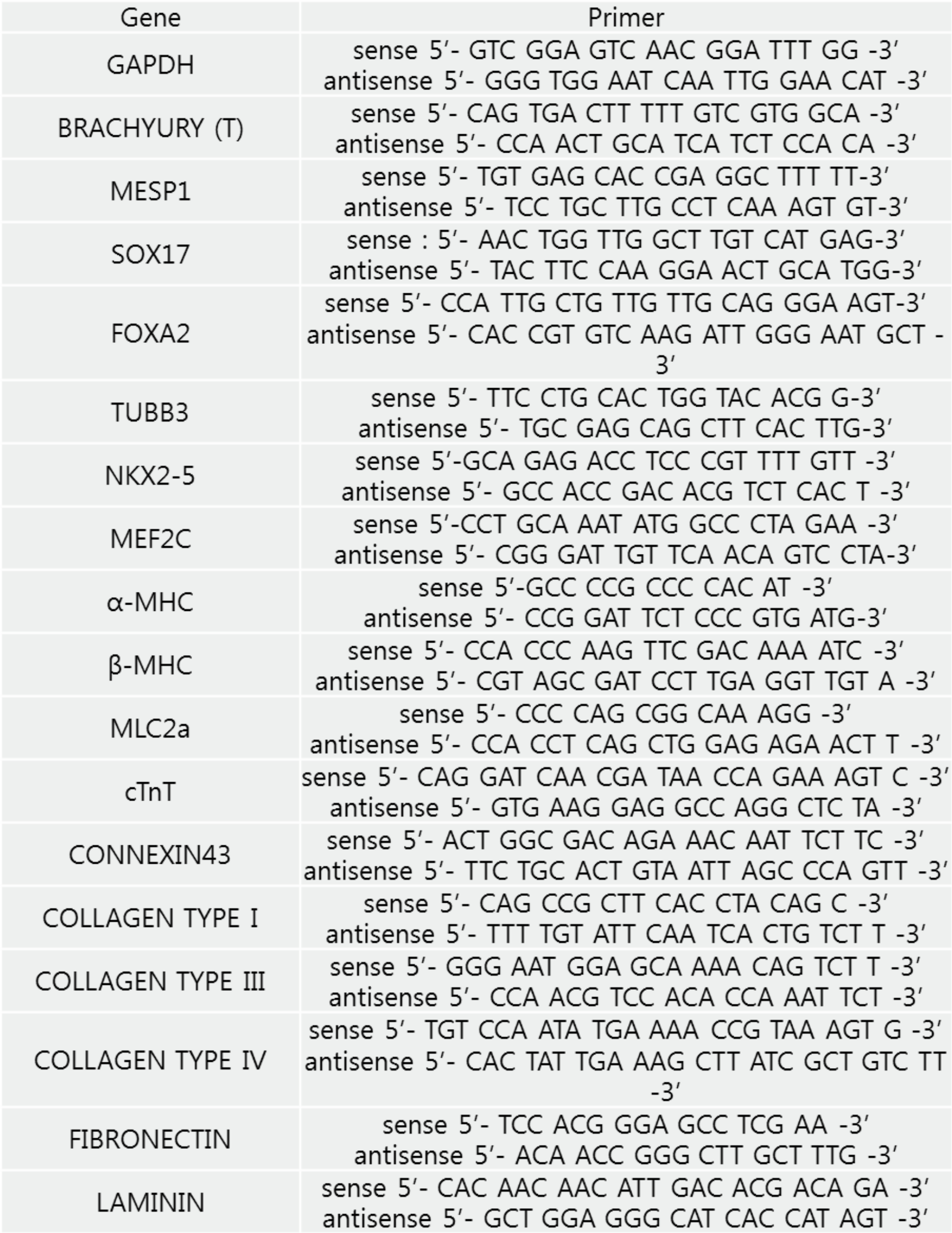

Gene	Primer
GAPDH	sense 5′- GTC GGA GTC AAC GGA TTT GG -3′ antisense 5′- GGG TGG AAT CAA TTG GAA CAT -3′
BRACHYURY (T)	sense 5′- CAG TGA CTT TTT GTC GTG GCA -3′ antisense 5′- CCA ACT GCA TCA TCT CCA CA -3′
MESP1	sense 5′- TGT GAG CAC CGA GGC TTT TT-3′ antisense 5′- TCC TGC TTG CCT CAA AGT GT-3′
SOX17	sense : 5′- AAC TGG TTG GCT TGT CAT GAG-3′ antisense 5′- TAC TTC CAA GGA ACT GCA TGG-3′
FOXA2	sense 5′- CCA TTG CTG TTG TTG CAG GGA AGT-3′ antisense 5′- CAC CGT GTC AAG ATT GGG AAT GCT -3′
TUBB3	sense 5′- TTC CTG CAC TGG TAC ACG G-3′ antisense 5′- TGC GAG CAG CTT CAC TTG-3′
NKX2-5	sense 5′-GCA GAG ACC TCC CGT TTT GTT -3′ antisense 5′- GCC ACC GAC ACG TCT CAC T -3′
MEF2C	sense 5′-CCT GCA AAT ATG GCC CTA GAA -3′ antisense 5′- CGG GAT TGT TCA ACA GTC CTA-3′
α-MHC	sense 5′-GCC CCG CCC CAC AT -3′ antisense 5′- CCG GAT TCT CCC GTG ATG-3′
β-MHC	sense 5′- CCA CCC AAG TTC GAC AAA ATC -3′ antisense 5′- CGT AGC GAT CCT TGA GGT TGT A -3′
MLC2a	sense 5′- CCC CAG CGG CAA AGG -3′ antisense 5′- CCA CCT CAG CTG GAG AGA ACT T -3′
cTnT	sense 5′- CAG GAT CAA CGA TAA CCA GAA AGT C -3′ antisense 5′- GTG AAG GAG GCC AGG CTC TA -3′
CONNEXIN43	sense 5′- ACT GGC GAC AGA AAC AAT TCT TC -3′ antisense 5′- TTC TGC ACT GTA ATT AGC CCA GTT -3′
COLLAGEN TYPE I	sense 5′- CAG CCG CTT CAC CTA CAG C -3′ antisense 5′- TTT TGT ATT CAA TCA CTG TCT T -3′
COLLAGEN TYPE III	sense 5′- GGG AAT GGA GCA AAA CAG TCT T -3′ antisense 5′- CCA ACG TCC ACA CCA AAT TCT -3′
COLLAGEN TYPE IV	sense 5′- TGT CCA ATA TGA AAA CCG TAA AGT G -3′ antisense 5′- CAC TAT TGA AAG CTT ATC GCT GTC TT -3′
FIBRONECTIN	sense 5′- TCC ACG GGA GCC TCG AA -3′ antisense 5′- ACA ACC GGG CTT GCT TTG -3′
LAMININ	sense 5′- CAC AAC AAC ATT GAC ACG ACA GA -3′ antisense 5′- GCT GGA GGG CAT CAC CAT AGT -3′

References

[1]. Heo, C.; Yoo, J.; Lee, S.; Jo, A.; Jung, S.; Yoo, H.; Lee, Y.H.; Suh, M. The control of neural cell-to-cell interactions through non-contact electrical field stimulation using graphene electrodes. *Biomaterials*. **2011**, 32, 19-27.

[2]. Park, S.Y.; Park, J.; Sim, S.H.; Sung, M.G.; Kim, K.S.; Hong, B.H.; Hong, S. Enhanced differentiation of human neural stem cells into neurons on graphene. *Adv. Mater.* **2011,** 23, H263-267.

[3]. Kalbacova, M.; Broz, A.; Kong, J.; Kalbac, M. Graphene substrates promote adherence of human osteoblasts and mesenchymal stromal cells. *Carbon*. **2010,** 48, 4323-4329.

[4]. Nayak, TR.; Andersen, H.; Makam, V.S.; Khaw, C.; Bae, S.; Xu, X.; Ee, P.L.; Ahn, J.H.; Hong, B.H.; Pastorin, G.; *et al*. Graphene for controlled and accelerated osteogenic differentiation of human mesenchymal stem cells. *ACS Nano*. **2011,** 5, 4670-4678.

[5]. Chen, G.Y.; Pang, D.W.; Hwang, S.M.; Tuan, H.Y.; Hu,Y.C. A graphene-based platform for induced pluripotent stem cells culture and differentiation. *Biomaterials*. **2012,** 33, 418-427.

[6]. Sebaa, M.; Nguyen, T. Y.; Paul, R. K.; Mulchandani, A.; Liu, H. Graphene and carbon nanotube–graphene hybrid nanomaterials for human embryonic stem cell culture. *Materials Letters*. **2013,** 92, 122–125.

[7]. Tang, X.L.; Rokosh, D.G.; Guo, Y.; Bolli, R. Cardiac progenitor cells and bone marrow-derived very small embryonic-like stem cells for cardiac repair after myocardial infarction. *Circ. J.* **2010,** 74, 390-404.

[8]. Planat-Bénard, V.; Menard, C.; André, M.; Puceat, M.; Perez, A.; Garcia-Verdugo, J.M.; Pénicaud, L.; Casteilla, L. Spontaneous cardiomyocyte differentiation from adipose tissue stroma cells. *Circ. Res.* **2004,** 94, 223-229.

[9]. Unno, K.; Jain, M.; Liao, R. Cardiac side population cells: moving toward the center stage in cardiac regeneration. *Circ. Res.* **2012,** 110, 1355-1363.

[10]. Schlechta, B.; Wiedemann, D.; Kittinger, C.; Jandrositz, A.; Bonaros, N.E.; Huber, J.C.; Preisegger, K.H.; Kocher, A.A. Ex-vivo expanded umbilical cord blood stem cells retain capacity for myocardial regeneration. *Circ. J.* **2010,** 74, 188-194.

[11]. Mignone, J.L.; Kreutziger, K.L.; Paige, S.L.; Murry, C.E. Cardiogenesis from human embryonic stem cells. *Circ. J.* **2010,** 74, 2517-2526.

[12]. Kehat, I.; Kenyagin-Karsenti, D.; Snir, M.; Segev, H.; Amit, M.; Gepstein, A.; Livne, E.; Binah, O.; Itskovitz-Eldor, J.; Gepstein, L. Human embryonic stem cells can differentiate into myocytes with structural and functional properties of cardiomyocytes. *J. Clin. Invest.* **2001,** 108, 407-414.

[13]. Shiba, Y.; Fernandes, S.; Zhu, W.Z.; Filice, D.; Muskheli, V.; Kim, J.; Palpant, N.J.; Gantz, J.; Moyes, K.W.; Reinecke, H.; *et al*. Human ES-cell-derived cardiomyocytes electrically couple and suppress arrhythmias in injured hearts. *Nature*. **2012,** 489, 322-325.

[14]. Moon, S.H.; Ban, K.; Kim, C.; Kim, S.S.; Byun, J.; Song, M.K.; Park, I.H.; Yu, S.P.; Yoon, Y.S. Development of a novel two-dimensional directed differentiation

system for generation of cardiomyocytes from human pluripotent stem cells. *Int. J. Cardiol.* **2013,** 168, 41-52.

[15]. Kim, K.S.; Zhao, Y.; Jang, H.; Lee, S.Y.; Kim, J.M.; Kim, K.S.; Ahn, J.H.; Kim, P.; Choi, J.Y.; Hong, B.H. Large-scale pattern growth of graphene films for stretchable transparent electrodes. *Nature.* **2009,** 457, 706-710.

[16]. David, R.; Jarsch, V.B.; Schwarz, F.; Nathan, P.; Gegg, M.; Lickert, H.; Franz, W.M. Induction of MesP1 by Brachyury(T) generates the common multipotent cardiovascular stem cell. *Cardiovasc. Res*. **2011,** 92, 115-122.

[17]. Bondue, A.; Lapouge, G.; Paulissen, C.; Semeraro, C.; Iacovino, M.; Kyba, M.; Blanpain, C. Mesp1 acts as a master regulator of multipotent cardiovascular progenitor specification. *Cell Stem Cell*. **2008,** 3, 69-84.

[18]. Wu, S.M. Mesp1 at the heart of mesoderm lineage specification. *Cell Stem Cell*. **2008,** 3, 1-2.

[19]. Bondue, A.; Tännler, S.; Chiapparo, G.; Chabab, S.; Ramialison, M.; Paulissen, C.; Beck, B.; Harvey, R.; Blanpain, C. Defining the earliest step of cardiovascular progenitor specification during embryonic stem cell differentiation. *J. Cell. Biol.* **2011,** 192, 751-765.

[20]. Olson, E.N. Development. The path to the heart and the road not taken. *Science.* **2001,** 291, 2327-2328.

[21]. Rudy-Reil, D.; Lough, J. Avian precardiac endoderm/mesoderm induces cardiac myocyte differentiation in murine embryonic stem cells. *Circ. Res*. **2004,** 94, e107-116.

[22]. Lough, J.; Sugi, Y. Endoderm and heart development. *Dev. Dyn.* **2000,** 217, 327-342.

[23]. Mummery, C.; Ward-van Oostwaard, D.; Doevendans, P.; Spijker, R.; van den Brink, S.; Hassink, R.; van der Heyden, M.; Opthof, T.; Pera, M.; de la Riviere, A.B.; Differentiation of human embryonic stem cells to cardiomyocytes: role of coculture with visceral endoderm-like cells. *Circulation*. **2003,** 107, 2733-2740.

[24]. Rodina, A.; Schramm, K.; Musatkina, E.; Kreuser, E.D.; Tavitian, A.; Tatosyan, A. Phosphorylation of p125FAK and paxillin focal adhesion proteins in src-transformed cells with different metastatic capacity. *FEBS Lett.* **1999,** 455, 145-148.

[25]. Raz, A.; Geiger, B. Altered organization of cell-substrate contacts and membrane-associated cytoskeleton in tumor cell variants exhibiting different metastatic capabilities. *Cancer Res.* **1982,** 42, 5183-5190.

[26]. Lim, J.Y.; Hansen, J.C.; Siedlecki, C.A.; Hengstebeck, R.W.; Cheng, J.; Winograd, N.; Donahue, H.J. Osteoblast adhesion on poly(L-lactic acid)/polystyrene demixed thin film blends: effect of nanotopography, surface chemistry, and wettability. *Biomacromolecules.* **2005,** 6, 3319-3327.

[27]. Milner, K.R.; Siedlecki, C.A. J. Submicron poly(L-lactic acid) pillars affect fibroblast adhesion and proliferation. *Biomed. Mater. Res. A.* **2007,** 82, 80-91.

[28]. Teo, B.K.; Wong, S.T.; Lim, C.K.; Kung, T.Y.; Yap, C.H.; Ramagopal, Y.; Romer, L.H.; Yim, E.K. Nanotopography modulates mechanotransduction of stem cells and induces differentiation through focal adhesion kinase. *ACS Nano*. **2013,** 7, 4785-4798.

[29]. Gao, M.; Yang, J.; Wei, R.; Liu, G.; Zhang, L.; Wang, H.; Wang, G.; Gao, H.; Chen, G.; Hong, T. Ghrelin induces cardiac lineage differentiation of human embryonic stem cells through ERK1/2 pathway. *Int. J. Cardiol.* **2013,** 167, 2724-2733.

[30]. Chen, G.; Gulbranson, D.R.; Hou, Z.; Bolin, J.M.; Ruotti, V.; Probasco, M.D.; Smuga-Otto, K.; Howden, S.E.; Diol, N.R.; Propson, N.E.; *et al*. Chemically defined conditions for human iPSC derivation and culture. *Nat. Methods*. **2011,** 8, 424-429.

[31]. Braam, S.R.; Denning, C.; Matsa, E.; Young, L.E.; Passier, R.; Mummery, C.L. Feeder-free culture of human embryonic stem cells in conditioned medium for efficient genetic modification. *Nat. Protoc.* **2008,** 3,1435-1443.

[32]. Braam, S.R.; Zeinstra, L.; Litjens, S.; Ward-van Oostwaard, D.; van den Brink, S.; van Laake, L.; Lebrin, F.; Kats, P.; Hochstenbach, R.; Passier, R. et al. Recombinant vitronectin is a functionally defined substrate that supports human embryonic stem cell self-renewal via alphavbeta5 integrin. *Stem Cells.* **2008,** 26, 2257-2265.

Chapter 4

Graphene-regulated cardiomyogenic differentiation process of mesenchymal stem cells by enhancing the expression of extracellular matrix proteins and cell signaling molecules

Introduction

Stem cell-based regenerative medicine provides a promising strategy for the treatment of heart failure, which is one of the common causes of mortality in the world.[1] Specifically, mesenchymal stem cells (MSCs) have been shown to have great potential to repair heart diseases. However, the therapeutic efficacy of the treatment is quite limited as MSCs hardly differentiate into cardiomyocytes *in vivo*.[2] For example, it has been known that the transplantation of cardiomyogenically differentiated MSCs greatly improved myocardial contractility.[3] Therefore, many researchers have attempted to develop methods for the promotion of *in vitro* cardiomyogenic differentiation of MSCs. Specifically, 5-azacytidine has been utilized to commit MSCs toward the cardiomyogenic lineage.[4] However, 5-azacytidine-treated MSCs are not clinically suitable because it has been anticipated to interfere with normal cell activity by inhibiting deoxyribonucleic acid methylation, [5] suggesting that other methods for MSC commitment toward the cardiomyogenic lineage without using exogenous chemical inducers that may interfere with normal cell activity should be developed for clinical stem cell therapies for myocardial infarction.

It is reported that MSC differentiation could be modulated through cellular interactions with culture substrates *in vitro*.[6] However, only a few studies have studied the effect of cell culture substrates on cardiomyogenic differentiation of MSCs. Recently, graphene has drawn attention as a platform for cell culture due to its unique physical, chemical, and mechanical properties and its effects on stem cell lineage specifications.[7-9] Guided by these considerations, here we propose for the first time that graphene can promote the expression of cardiomyogenic genes of MSCs. We also investigated a potential mechanism of the effects of graphene on the enhanced cardiomyogenic differentiation process through analyzing the expressions of extracellular matrix (ECM) proteins and cell signaling molecules that are known to promote the cardiomyogenic differentiation of stem cells.

Experimental

Graphene Preparation

The entire fabrication process to produce graphene on coverslips is shown in the schematic illustration. In the first step, high-quality, large-scale monolayer graphene was synthesized by chemical vapor deposition (CVD) process, which is described in the literature.[46] Secondly, 300nm thin poly(methyl methacrylate) (PMMA), which we call the ‘supporting layer’, was coated onto as graphene films and annealed at 140 ℃ for 1min to cure it. Thirdly, the back side growth graphene is then removed by reactive ion etching (RIE) with a power of 100 W and O_2 etching gas of 20 sccm. the PMMA coated graphene growth copper foil is subsequently etched away and floated on the surface of an aqueous solution of 0.1 M ammonium persulphate [$(NH_2)_4S_2O_8$]. After all of the copper layers were etched away, the floating PMMA/graphene film was collected using a clean PET film and transferred to deionized water. The cleaning process was repeated five times. After that, the graphene film with the PMMA support was transferred to the coverslips. The samples were dried with nitrogen gas immediately after the transfer and baked for 8 h on a hot plate at 60 ℃. The samples were then cleaned using acetone at room temperature for 30 min to remove the PMMA support layer. The samples were dried with nitrogen gas immediately after the transfer and baked for 8 h on a hot plate at 60 ℃. The samples were then dried and baked for 8 h on a hot plate at 60 ℃. Finally, the graphene on coverslips sample was obtained. (Figure S1).

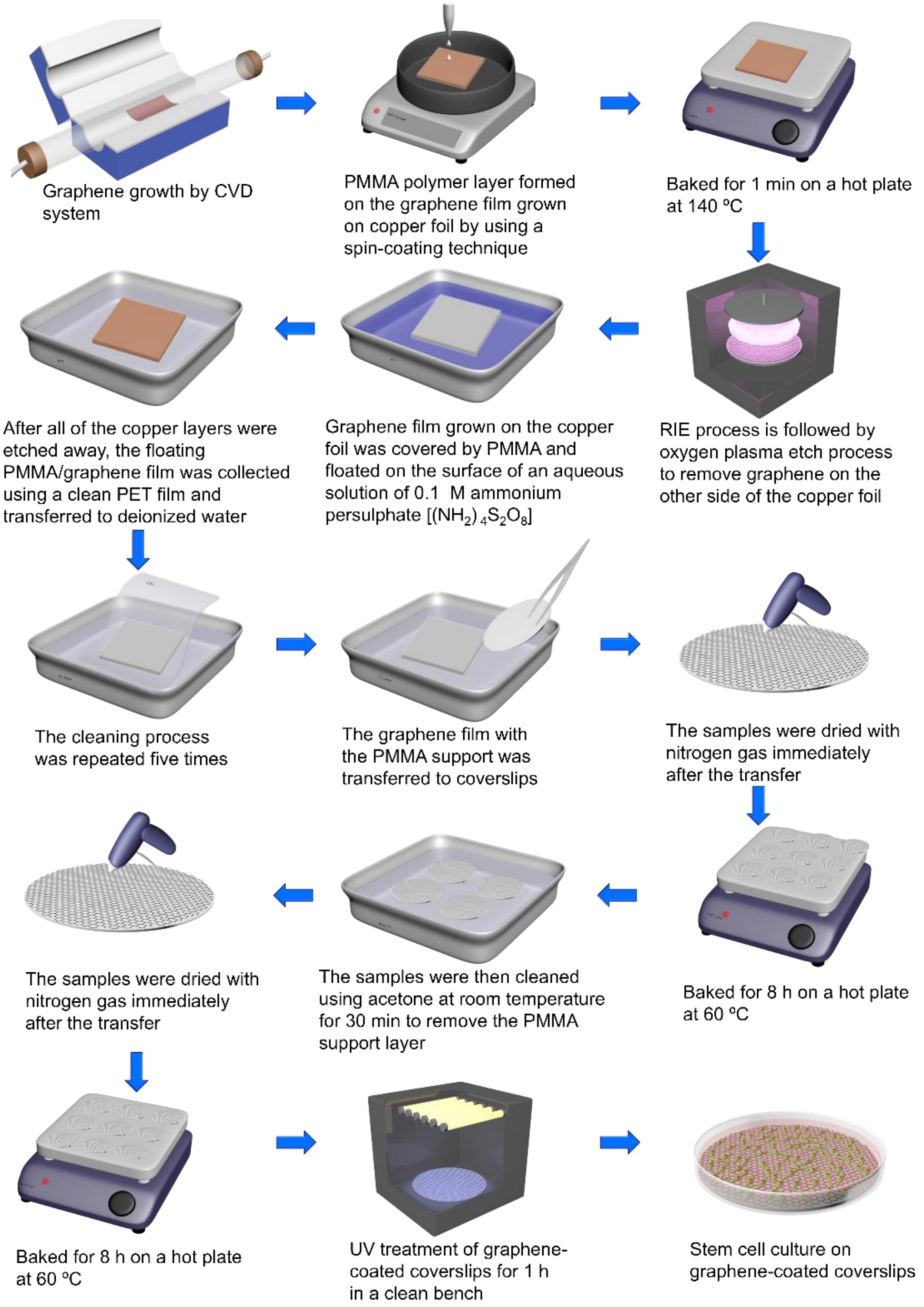

Figure S1 | Schematic flows of various key steps during the fabrication of showing preparation process to produce graphene on coverslips

Characterization

The samples were characterized by AFM, Raman spectroscopy, ultraviolet–visible spectrometer, TEM, and SAED. The surface morphology examination of the samples was conducted through non-contact mode AFM (XE-100 system, Park Systems, Korea). The structural properties of the graphene on the coverslip were further investigated through Raman spectroscopy (RM 1000-Invia, Renishaw, UK). The Raman spectra were recorded by using an argon ion laser (514 nm) as the excitation source with a notch filter of 50 cm^{-1}. The typical scan range was from 1000 to 3000 cm^{-1} and the instrumental resolution was 10 cm^{-1}. The optical transmittance of the graphene on the coverslip was measured using an ultraviolet–visible spectrometer (UV-3600, Shimadzu, Japan). The TEM and SAED analyses were conducted on a TEM (JEOL 2100, JEOL, Japan) operated at 200 kV. The rotation between the TEM images and the corresponding SAED patterns was calibrated using molybdenum trioxide crystals. The sheet resistances of the graphene on the coverslip were measured through the van der Pauw four-probe method using a Hall measurement system.

Cell Culture

Human bone marrow-derived MSCs were purchased from a commercial source (Lonza, USA) and cultured in Dulbecco's modified Eagle's medium (DMEM, Gibco BRL, USA) containing 10% (v/v) fetal bovine serum (FBS; Gibco-BRL) and 1% (v/v) penicillin–streptomycin (PS; Gibco-BRL). At passage 4, the MSCs were plated at a cell density of 1×10^3 cells/cm^2 for the experiments. The medium was changed every 2 days.

Cell Viability and Proliferation

The live and dead cells were assessed by calcein-AM and ethidium homodimer, relatively, using a two-color fluorescence live/dead assay kit (Molecular Probes, USA). The gene expression levels of Bcl-2 and caspase-3 were evaluated by qRT-PCR to assess the expression of anti-apoptotic and apoptotic genes, respectively, in MSCs. The proliferating cells were analyzed by immunofluorescence staining using antibodies against PCNA (Abcam, UK). The samples were mounted in 4,6-diamidino-2-phenylindole (DAPI, Vector Laboratories, USA) for nuclear staining. The cell proliferation was quantitatively measured by counting the number of cells using CCK-8 (Sigma, USA) and a hemocytometer (Paul Marienfeld GmbH and Co., Germany).

Cardiomyogenic Gene Expression

The hMSCs were cultured for 2 and 3 weeks on a coverslip or graphene in DMEM containing 10% FBS and 1% PS and analyzed through qRT-PCR.

Gene Expression of Extracellular Matrix Proteins: The hMSCs were cultured for 2 and 3 weeks on a coverslip or graphene in DMEM containing 10% FBS and 1% PS and analyzed through qRT-PCR.

qRT-PCR

Ribonucleic acid (RNA) samples were extracted using Qiagen RNeasy mini kit according to the manufacturer's instructions (Qiagen, Germany). The total RNA concentration was determined using a NanoDrop spectrometer (ND-2000, NanoDrop Technologies, USA). The RNA (500 ng) from each sample was reverse-transcribed to obtain cDNA using GoScript Reverse Transcriptase (Promega, USA). SYBR green-based qRT-PCR was performed using a StepOnePlus Real-Time PCR System (Applied Biosystems, USA) instrument with the TOPreal qPCR Premix (Enzynomics, Korea). After a 10-min pre-incubation, 40 amplification cycles were performed and each cycle consists of three steps; 30 s at 94℃, 45 s at 55℃, and 45 s at 72℃. The primer sequences for the qRT-PCR analyses are listed in Table 1. All of the data were analyzed using the $2^{-\Delta\Delta Ct}$ method.

Analysis of the Signal Transduction Molecules

The MSCs cultured for 3 weeks on a coverslip or graphene were lysed with sodium dodecyl-sulfate (SDS) sample buffer (62.5 mM Tris–HCl (pH 6.8), 2% (w/v) SDS, 10% (v/v) glycerol, 50 mM dithiothreitol, and 0.1% (w/v) bromophenol blue). The total protein concentration was determined through a bicinchoninic acid protein assay (Pierce Biotechnology, USA). Western blot analysis was performed through 10% (w/v) SDS-polyacrylamide gel electrophoresis. The proteins were first transferred to an Immobilon-P membrane (Millipore Corp., USA) and then probed with antibodies against human FAK (Abcam, USA), paxillin (Abcam), vinculin (Abcam), Src (Abcam), ERK (Abcam), JNK (Abcam), PI3K (Abcam), Cdc42 (Abcam), Rac1 (Abcam), Wnt7a (Abcam), and Akt (Abcam). The proteins were then incubated with a horseradish peroxidase-conjugated secondary antibody (Santa Cruz

Biotechnology, USA) for 1 h at room temperature. The blots were developed using an enhanced chemiluminescence detection system (Amersham Bioscience, USA). The data were quantified through densitometric scanning (Image-Pro Plus software, Media Cybernetics, Marlow, UK).

Results and Discussion

High quality and large-scale graphene used in this study was synthesized by the chemical vapor deposition (CVD) method on copper foils. After synthesis, copper foil was etched and the same batch of graphene was transferred to coverslip, following a previously reported method.[36] Atomic force microscopy (AFM) was used to analyze the surface roughness (the root-mean-square deviation (Rq)) of the coverslip with and without graphene. AFM images of graphene on coverslip and coverslip distinctly show difference in their morphological property (figure 2a). AFM image of graphene on coverslip revealed the typical flat but wrinkled graphene morphology compared to graphene on coverslip. The surface roughness (Rq) was 4.87 nm and 4.93 nm for coverslip and graphene-coated coverslip, respectively, and there was no significant difference. Optical image of coverslip and graphene transferred to coverslip, showing that both coverslip and graphene-coated coverslip are nearly transparent (Figure 1b). Contact angle measurement showed that graphene transferred coverslip is slightly hydrophobic (73.9 ± 1.2°), while the contact angle of coverslip is 64.7 ± 2.8° (Figure 1c).

To confirm monolayer graphene, the transferred graphene film was characterized by Raman spectroscopy. Raman spectra result of as-grown graphene transferred on SiO_2 (300 nm)/Si substrate (Figure 1d). The Raman spectrum of graphene is characterized by three main characteristic peaks. G peak is shown commonly in carbon-based materials that have hexagonal pattern. The G peak near 1580 cm^{-1} arising from emission of zone-center optical phonons, the D band near

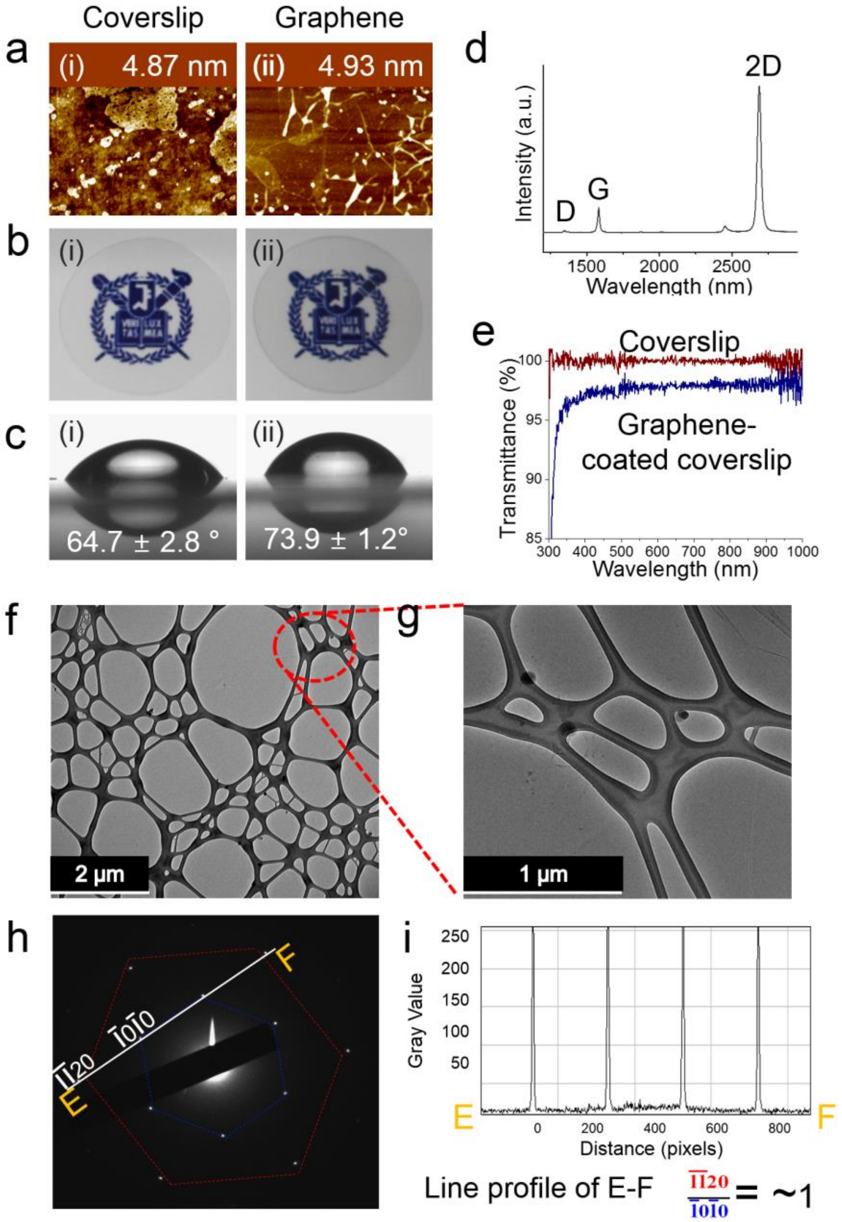

Figure 1| Characterization of graphene substrates. a, AFM topography images, b, photographs, and c, contact angle images of (i) coverslip and (ii) graphene on coverslip. d, Raman spectroscopy of graphene. e, Transparency of graphene films transferred on coverslip. TEM image of graphene sheet on a TEM grid at f, low and g, high magnifications. h, The SAED pattern. i, Intensity profile of the diffraction spots along a line connecting points E and F in the single-layer graphene diffraction pattern. The uniform intensity profile between the inner and outer spots proves that the graphene sheet consists of a single layer.

1350 cm^{-1} arising from the doubly resonant disorder-induced mode and 2D peak is the second order of D peak moves from K to K' point and the symmetry-allowed 2D over tune mode near 2700 cm^{-1}. The shift and line shape associated with these modes have been used to determine the quality of grapheme and the number of graphene layers. The peak located at ~2700 cm^{-1} (G′ band) with a full width at half-maximum (FWHM) is 26~33 cm^{-1}, the ration of I_{2D}/I_G ratio is more than three times as intense as the peak located at ~1600 cm^{-1} (the G band) and there is no measurable peak observed at ~1350 cm^{-1} (the D band), indicating the successful growth of high-quality monolayer graphene. In addition, graphene-coated coverslip exhibited high transparency with transmittance exceeding 97.4% at 550 nm wavelength (Figure 1e). This is evidence of uniform and monolayer graphene. Raman spectrum and the transmittance are consistent with previously reported paper[13] and we confirmed that graphene film used in this study was monolayer. Figure 1f shows the representative low-magnification transmission electron microscopy (TEM) image of graphene sheet on a TEM grid, and Figure 1g shows TEM image of the circled region in Figure 1f.

We have included a selected area electron diffraction (SAED) patterns image in order to show the good crystallinity of the graphene used in our experiments (see Figure 1h). A typical SAED pattern obtained from graphene sheet shows the six-fold symmetry that is expected for graphene. Intensity profile of equivalent Bragg reflections taken along the line denoted showed that the intensities of the $\bar{1}0\bar{1}0$(inner hexagon) and $\bar{1}\bar{1}20$(outer hexagon) spots were equivalent, indicating that the set of diffraction spots originated from a single-layer graphene sheet (Figure 1i).[14] We

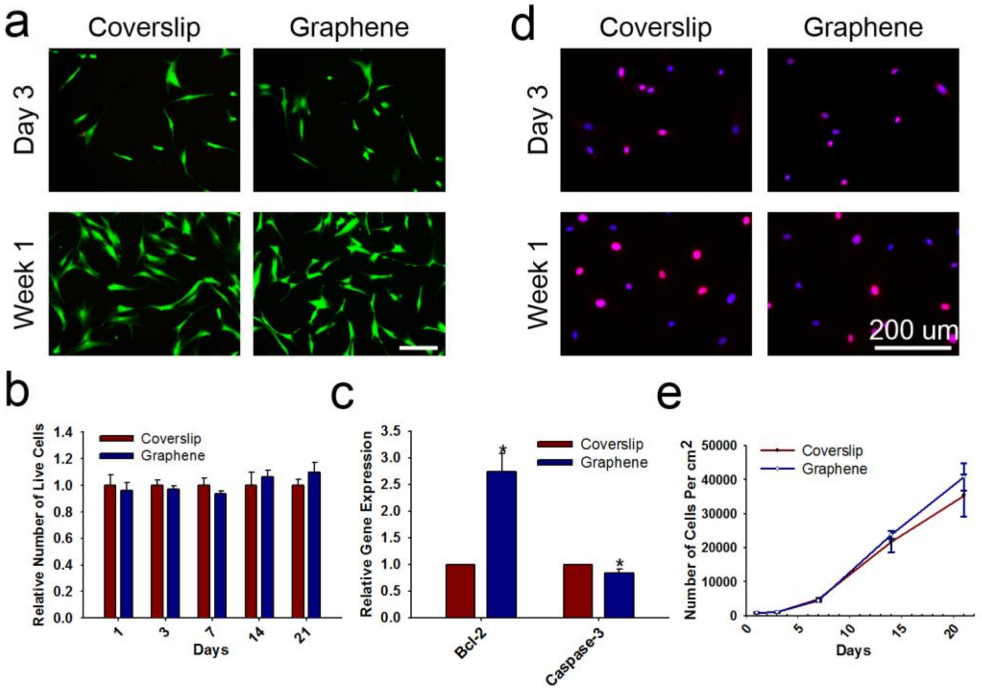

Figure 2 | *In vitro* biocompatibility of graphene. a, Live/dead assay of MSCs cultured on graphene and coverslips for 3 days and 1 week. The live cells were stained with calcein-AM (green), and the dead cells were stained with ethidium homodimer (red). The scale bar represents 200 µm. b, The number of live cells is expressed relative to the number of live cells on a coverslip on day 1. The number of live cells was counted using CCK-8. c, Upregulation of Bcl-2, an anti-apoptotic marker, and downregulation of caspase-3, a pro-apoptotic marker, in MSCs cultured on graphene for 3 weeks relative to MSCs cultured on coverslips, as evaluated by qRT-PCR. $*p < 0.05$ compared to MSCs cultured on coverslips. d, Proliferation of MSCs cultured on coverslips and graphene. The proliferation was evaluated by PCNA staining. The proliferating cells were stained with PCNA (red), and the nuclei were stained with DAPI (blue). The scale bar represents 200 µm. e, Growth of MSCs cultured on graphene and coverslips. The growth was evaluated by counting the number of cells at various time points using hemocytometer.

continually investigated the sheet resistance of the graphene on coverslip by a four-point probe method. The transferred graphene on coverslip show 500 Ω/□ sheet resistance with high uniformity.

We first evaluated the biocompatibility of graphene by comparing viability and proliferation of MSCs cultured on graphene and coverslips. MSCs were cultured in Dulbecco’s modified Eagle’s medium (DMEM) containing 10% (v/v) fetal bovine serum (FBS) and 1% (v/v) penicillin/streptomycin (PS). The viabilities of MSCs after culturing on graphene and coverslips were evaluated using live/dead staining with calcein-AM and ethidium homodimer. It stains live cells with green and dead cells with red, respectively. Fluorescence microscopy revealed that most of the cells were alive regardless of the substrate (Figure 2a). Figure 2b shows that there were no significant difference in the relative numbers of live cells at various time points when analyzed using cell counting kit-8 (CCK-8). CCK-8 was used instead of methylthiazolyldiphenyl-tetrazolium bromide (MTT) assay because MTT is spontaneously reduced by graphene, and therefore results in false positive signal.[15] However, it is very interesting to note that when we analyzed the gene expression at 3 weeks after cell seeding, Bcl-2, an anti-apoptotic gene, was upregulated on MSCs cultured on graphene compared MSCs cultured on coverslips, while caspase-3, a cysteine protease that is activated during programmed cell death, was decreased when cells were cultured on graphene as compared to cells cultured on coverslips (Figure 2c). Next, the proliferation of MSCs cultured on graphene was assessed by proliferating cell nuclear antigen (PCNA) staining and counting of the cells using hemocytometer. PCNA staining that stains proliferating cells demonstrated cell

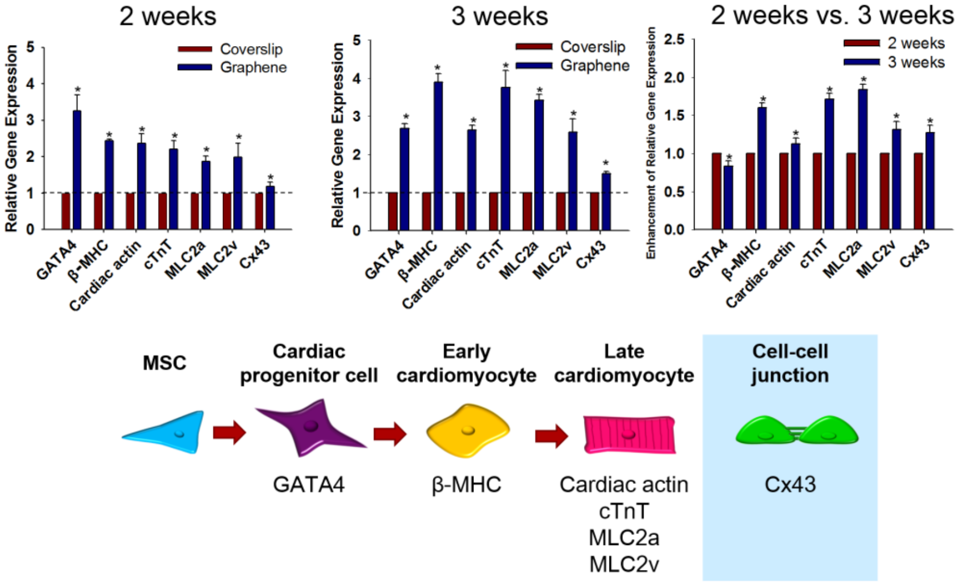

Figure 3 | Enhanced expression of cardiomyogenic genes in MSCs cultured on graphene without using chemical induction materials. Two and three weeks after cell seeding, the MSCs cultured on graphene exhibited an upregulation of the mRNA expression of an early cardiomyogenic transcriptional factor (GATA4), cardiomyogenic contractile proteins (cardiac actin, β-MHC, cTnT, MLC2a, and MLC2), and gap junction protein (Cx43) compared with MSCs cultured on coverslips. The mRNA expression levels were evaluated by qRT-PCR. *$p < 0.05$ compared to MSCs cultured on coverslips.

proliferation is similar regardless of the substrate (Figure 2d). Cell counting also showed that there was no significant difference in the number of cells cultured on graphene and coverslip at all time points (Figure 2e). The cell viability and proliferation assay indicated that graphene is biocompatible when single-layer is coated on coverslips for cell culture.

In a second set of experiments, we have examined cardiomyogenic specific markers at transcript level to determine the cardiomyogenic commitment of MSCs cultured on graphene in DMEM (10% FBS and 1% PS) at 2 and 3 week time points after cell seeding. Interestingly, all cardiomyogenesis-related markers have been enhanced in MSCs cultured on graphene compared to MSCs cultured on coverslip even in the absence of the induction media. Early cardiomyogenic transcriptional factor GATA4 was enhanced on MSCs cultured on graphene compared to the MSCs cultured on coverslip, indicating the enhanced early stage cardiomyogenesis by using graphene as cell culture substrate. Although the fold increase of GATA4 of MSCs cultured on graphene compared to the cells on coverslip has decreased slightly at week 3 compared to week 2, the presence of graphene was able to maintain more than 2-fold increase in GATA4 expression in MSCs compared to MSCs cultured on coverslips (Figure 3). In addition, the gene expressions of all cardiomyogenic contractile proteins, including cardiac actin, beta-type myosin heavy chain (β-MHC), cardiac troponin T (cTnT), ventricular myosin light chain-2 (MLC2v), and atrial myosin light chain 2 (MLC2a), were enhanced on graphene compared to coverslips at 2 weeks after cell seeding (Figure 3a). These genes have been further upregulated at week 3 in MSCs cultured on graphene compared to MSCs cultured on normal coverslips. Gene expression of gap junction protein, connexin 43 (Cx43), has also been enhanced by culturing MSCs on graphene, which may have been attributed to conductivity of graphene (Figure 3).[16] However, MSCs did not show functional and electrophysiological properties of mature cardiomyocytes regardless of the substrate.

Stem cell-ECM interactions may play key roles in cardiomyogenic differentiation of the stem cells. Thus, we next investigated whether MSC culture on graphene as compared to culture on coverslips affected on the expressions of cardiomyogenic differentiation-related ECM genes in the MSCs. Among various ECM proteins, we chose type I collagen (Col I), type III collagen (Col III), type IV collagen (Col IV), fibronectin, and laminin for analysis. Collagen, fibronectin, and laminin are the major components of cardiac ECM.[17] Embryonic stem cell-derived beating cardiomyocytes were reported to be surrounded in a network of fibronectin,

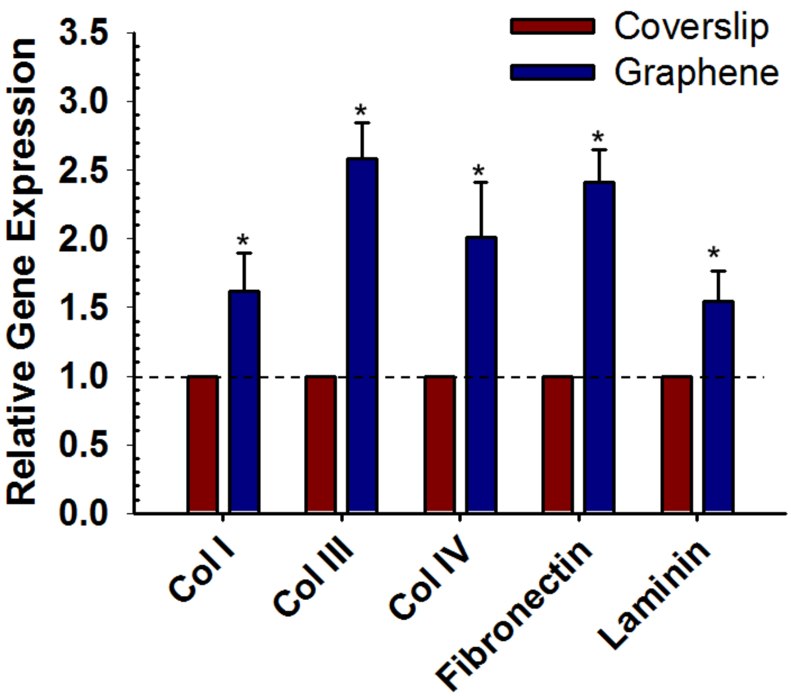

Figure 4 | Enhanced gene expression of ECM proteins in MSCs cultured on graphene. The MSCs cultured on graphene for 2 weeks exhibited an upregulation of the mRNA expression of Col I, Col III, Col IV, fibronectin, and laminin, which are known to promote the cardiomyogenic differentiation of stem cells compared with those on coverslips. The mRNA expression levels were evaluated by qRT-PCR. $*p < 0.05$ compared to MSCs cultured on coverslips.

laminin, Col I and Col IV.[18] Col I and Col III, both of which are produced by cardiac stem cells and cardiac fibroblasts,[19] represent approximately 80% and 11% of total collagen in myocardium, respectively.[20] Collagen was essential for cardiomyogenic differentiation of mouse embryonic stem cells, as the use of collagen synthesis inhibitors inhibited cardiac differentiation.[25] A recent study also demonstrated that culture of embryonic stem cell-derived embryonic bodies on Col IV-coated surfaces enhanced cardiomyogenic differentiation synergistically with hypoxia, while culture on fibronectin-coated surfaces enhanced cardiomyogenic differentiation under normoxia.[21] Laminin was essential for development to cardiomyocytes capable of propagating electrical signals between neighboring cardiomyocytes.[27] As compared to MSC culture on coverslips, that on graphene upregulated the gene expressions of cardiomyogenic differentiation-related ECMs (i.e., Col I, Col III, Col IV, fibronectin, and laminin), as evaluated by quantitative reverse transcriptase polymerase chain reaction (qRT-PCR, Figure 4). The upregulation of the ECM gene expression may, at least in part, be responsible for the enhanced cardiomyogenic differentiation of MSCs cultured on graphene (Figure 3).

Cardiomyogenic differentiation of stem cells could be regulated through modulation of signal transduction. Therefore, we investigated how signal transduction of MSCs cultured on graphene is affected as compared to MSCs cultured on coverslips (Figure 5a). Among various cell signaling molecules, we first examined the effect of graphene on Focal adhesion kinase (FAK) expression (Figure 5b). FAK was upregulated in MSCs cultured on graphene. Next, we examined the expression of focal adhesion components, such as vinculin and paxillin, which are

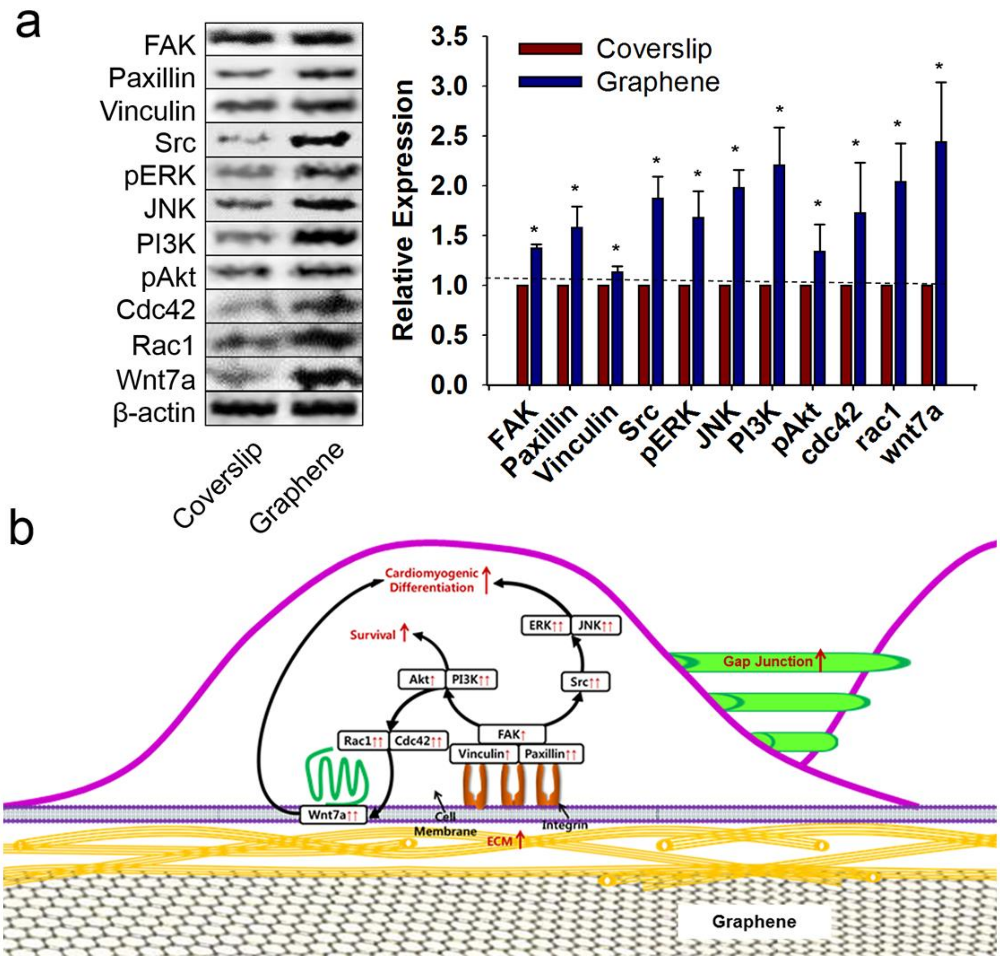

Figure 5 | Activation of molecules involved in cardiomyogenic differentiation and survival-related signal transduction pathways in MSCs cultured on graphene. a, Western blot analyses of MSCs cultured on graphene or coverslips for 3 weeks to analyze the molecules involved in the signal transduction pathways. Quantification of the relative protein expressions of the cell signaling molecules (n = 3). $^*p < 0.05$ compared to MSCs cultured on coverslips. b, A schematic diagram of the signal transduction pathways associated with cardiomyogenic differentiation and survival. Arrows indicate expression upregulations.

recruited for the clustering of activated integrins, and the remodeling of actin cytoskeletons. Graphene enhanced the expression of both paxillin and vinculin (Figure 5b), which may occur due to the cell-substrate adhesiveness of graphene.[22,23]

FAK is activated by binding of integrins to ECM ligands when cell adhesion to the substrate occurs, and in turn, mediate a series of signaling events in cells. Integrins are transmembrane receptors that are engaged in the attachment between cells and surrounding cells and ECM. Activation of FAK mediates variety of adhesion-dependent biological processes including cell proliferation, migration, differentiation, and apoptosis.[24] Autophosphorylation of tyrosine 397 of FAK and allows FAK to bind Src[25] and phosphatidylinositol 3-kinase (PI3K),[26] which in turn mediates multiple signaling events that regulate stem cell survival and differentiation (Figure 5a).

Extracellular signal-regulated kinases (ERK) and c-Jun N-terminal kinases (JNK) were analyzed to examine whether cardiomyogenic gene expressions of MSCs could be affected by using graphene as the culture substrate. JNK and ERK are activated during cardiomyogenic differentiation.[27] Graphene has upregulated both ERK and JNK (Figure 5b). Both PI3K and Akt were upregulated in MSCs cultured on graphene compared to MSCs cultured on coverslips (Figure 5b). Upregulation of PI3K/Akt promotes cell survival, at least in part by regulating the downstream effectors, such as Bcl-2 family proteins.[28] The enhanced Bcl-2 gene expression of MSCs cultured on graphene compared to group cultured on coverslip (Figure 2b) may be, at least in part, due to the upregulation of PI3K/Akt (Figure 5b). In addition, activation of PI3K/Akt may have attributed to enhanced cardiomyogenic gene expressions of MSCs cultured on graphene as compared to coverslips, as it has been demonstrated in previous studies that the inhibition of PI3K suppresses cardiomyocyte differentiation[29], while upregulation of PI3K/Akt signaling pathway enhances cardiomyogenesis.[30,31]

In this study, Wnt7a, which have been demonstrated to be required for the myogenic differentiation of stem cells,[32] the development of cardiac conduction system,[33] and the modulation of cardiomyogenic versus chondrogenic cell fate decision,[34] was also highly expressed in MSCs cultured on graphene (Figure 5b). Wnt 7a has been shown to be upregulated when Cdc42 and Rac1 expressions are enhanced.[34] Cdc42 and Rac1 are proteins that are upregulated by the activation of PI3K/Akt, and promote the formation of actin polymerization.[35] Cdc42 and Rac1 are both upregulated in MSCs cultured on graphene (Figure 5b). Therefore, graphene may have upregulated cardiomyogenic gene expressions of MSCs through regulation of cell-substrate adhesion, but soluble signals may be needed to promote MSC differentiations to mature cardiomyocytes.

Conclusions

To summarize, we have demonstrated that for the first time the cardiomyogenic gene expression of MSCs can be upregulated by culturing MSCs on graphene. The viability and proliferation analyses of MSCs cultured on graphene compared to MSCs cultured on coverslips show that graphene is highly biocompatible and supportive when single-layer graphene is coated on coverslips. In addition, we confirmed that the ECM gene expressions of MSCs have been enhanced on graphene, resulting in the activation of cell signaling molecules in signal transduction pathways. The activated cell signaling transduction pathways and the ECM gene expressions possibly enhances cardiomyogenic gene expressions by culturing MSCs on graphene. Therefore, graphene has significant effects on the cell viability, proliferation, and cardiomyogenic gene expressions as well as extracellular matrix gene expressions of MSCs. Our results suggest that graphene is a promising scaffold for MSC adhesion and differentiation to be utilized for various therapeutic applications including cardiomyogenic regeneration.

References

[1]. Pittenger, M. F.; Mackay, A. M.; Beck, S. C.; Jaiswal, R. K.; Douglas, R.; Mosca, J. D.; Moorman, M. A.; Simonetti, D. W.; Craig, S.; Marshak, D. R. Multilineage Potential of Adult Human Mesenchymal Stem Cells. *Science* **1999,** *284*, 143-147.

[2]. Minguell, J. J.; Erices, A.; Conget, P. Mesenchymal Stem Cells. *Exp. Biol. Med.* **2001,** *226*, 507-520.

[3]. Devine, S. M. Mesenchymal Stem Cells: Will They Have a Role in the Clinic? *J. Cell. Biochem.* **2002**, 73-79.

[4]. Engler, A. J.; Sen, S.; Sweeney, H. L.; Discher, D. E. Matrix Elasticity Directs Stem Cell Lineage Specification. *Cell* **2006,** *126*, 677-689.

[5]. Dalby, M. J.; Gadegaard, N.; Tare, R.; Andar, A.; Riehle, M. O.; Herzyk, P.; Wilkinson, C. D. W.; Oreffo, R. O. C. The Control of Human Mesenchymal Cell Differentiation Using Nanoscale Symmetry and Disorder. *Nat. Mater.* **2007,** *6*, 997-1003.

[6]. Orza, A.; Soritau, O.; Olenic, L.; Diudea, M.; Florea, A.; Ciuca, D. R.; Mihu, C.; Casciano, D.; Biris, A. S. Electrically Conductive Gold-Coated Collagen Nanofibers for Placental-Derived Mesenchymal Stem Cells Enhanced Differentiation and Proliferation. *ACS Nano* **2011,** *5*, 4490-4503.

[7]. Curran, J. M.; Chen, R.; Hunt, J. A. The Guidance of Human Mesenchymal Stem Cell Differentiation in Vitro by Controlled Modifications to the Cell Substrate. *Biomaterials* **2006,** *27*, 4783-4793.

[8]. Park, S. Y.; Park, J.; Sim, S. H.; Sung, M. G.; Kim, K. S.; Hong, B. H.; Hong, S.

Enhanced Differentiation of Human Neural Stem Cells into Neurons on Graphene. *Adv. Mater.* **2011,** *23*, H263-+.

[9]. Wang, Y.; Lee, W. C.; Manga, K. K.; Ang, P. K.; Lu, J.; Liu, Y. P.; Lim, C. T.; Loh, K. P. Fluorinated Graphene for Promoting Neuro-Induction of Stem Cells. *Adv. Mater.* **2012,** *24*, 4285-+.

[10]. Kalbacova, M.; Broz, A.; Kong, J.; Kalbac, M. Graphene Substrates Promote Adherence of Human Osteoblasts and Mesenchymal Stromal Cells. *Carbon* **2010,** *48*, 4323-4329.

[11]. Nayak, T. R.; Andersen, H.; Makam, V. S.; Khaw, C.; Bae, S.; Xu, X. F.; Ee, P. L. R.; Ahn, J. H.; Hong, B. H.; Pastorin, G., *et al.* Graphene for Controlled and Accelerated Osteogenic Differentiation of Human Mesenchymal Stem Cells. *ACS Nano* **2011,** *5,* 4670-4678.

[12]. Lee, W. C.; Lim, C. H.; Shi, H.; Tang, L. A.; Wang, Y.; Lim, C. T.; Loh, K. P. Origin of Enhanced Stem Cell Growth and Differentiation on Graphene and Graphene Oxide. *ACS Nano* **2011,** *5*, 7334-7341.

[13]. Kim, K. S.; Zhao, Y.; Jang, H.; Lee, S. Y.; Kim, J. M.; Ahn, J. H.; Kim, P.; Choi, J. Y.; Hong, B. H. Large-Scale Pattern Growth of Graphene Films for Stretchable Transparent Electrodes. *Nature* **2009,** *457*, 706-710.

[14]. Datta, S. S.; Strachan, D. R.; Khamis, S. M.; Johnson, A. T. C. Crystallographic Etching of Few-Layer Graphene. *Nano Lett.* **2008,** *8*, 1912-1915.

[15]. Liao, K. H.; Lin, Y. S.; Macosko, C. W.; Haynes, C. L. Cytotoxicity of Graphene Oxide and Graphene in Human Erythrocytes and Skin Fibroblasts. *ACS Appl. Mater. Interfaces* **2011,** *3*, 2607-2615.

[16]. You, J.-O.; Rafat, M.; Ye, G. J. C.; Auguste, D. T. Nanoengineering the Heart: Conductive Scaffolds Enhance Connexin 43 Expression. *Nano Lett.* **2011,** *11*, 3643-3648.

[17]. Moore, L.; Fan, D.; Basu, R.; Kandalam, V.; Kassiri, Z. Tissue Inhibitor of Metalloproteinases (Timps) in Heart Failure. *Heart Fail. Rev.* **2012,** *17*, 693-706.

[18]. van Laake, L. W.; van Donselaar, E. G.; Monshouwer-Kloots, J.; Schreurs, C.; Passier, R.; Humbel, B. M.; Doevendans, P. A.; Sonnenberg, A.; Verkleij, A. J.; Mummery, C. L. Extracellular Matrix Formation after Transplantation of Human Embryonic Stem Cell-Derived Cardiomyocytes. *Cellular and molecular life sciences : CMLS* **2010,** *67*, 277-90.

[19]. Kurazumi, H.; Kubo, M.; Ohshima, M.; Yamamoto, Y.; Takemoto, Y.; Suzuki, R.; Ikenaga, S.; Mikamo, A.; Udo, K.; Hamano, K., *et al.* The Effects of Mechanical Stress on the Growth, Differentiation, and Paracrine Factor Production of Cardiac Stem Cells. *PLoS One* **2011,** *6*, e28890.

[20]. Eghbali, M.; Weber, K. T. Collagen and the Myocardium: Fibrillar Structure, Biosynthesis and Degradation in Relation to Hypertrophy and Its Regression. *Mol. Cell. Biochem.* **1990,** *96*, 1-14.

[21]. Horton, R. E.; Auguste, D. T. Synergistic Effects of Hypoxia and Extracellular Matrix Cues in Cardiomyogenesis. *Biomaterials* **2012,** *33*, 6313-6319.

[22]. Bendori, R.; Salomon, D.; Geiger, B. Contact-Dependent Regulation of Vinculin Expression in Cultured Fibroblasts - a Study with Vinculin-Specific Cdna Probes. *EMBO J.* **1987,** *6*, 2897-2905.

[23]. Ungar, F.; Geiger, B.; Benzeev, A. Cell Contact-Dependent and Shape-

Dependent Regulation of Vinculin Synthesis in Cultured Fibroblasts. *Nature* **1986,** *319*, 787-791.

[24]. Hynes, R. O. Integrins - Versatility, Modulation, and Signaling in Cell-Adhesion. *Cell* **1992,** *69*, 11-25.

[25]. Schaller, M. D.; Hildebrand, J. D.; Shannon, J. D.; Fox, J. W.; Vines, R. R.; Parsons, J. T. Autophosphorylation of the Focal Adhesion Kinase, Pp125fak, Directs Sh2-Dependent Binding of Pp60src. *Mol. Cell. Biol.* **1994,** *14*, 1680-1688.

[26]. Chen, H. C.; Appeddu, P. A.; Isoda, H.; Guan, J. L. Phosphorylation of Tyrosine 397 in Focal Adhesion Kinase Is Required for Binding Phosphatidylinositol 3-Kinase. *J. Biol. Chem.* **1996,** *271*, 26329-26334.

[27]. Eriksson, M.; Leppa, S. Mitogen-Activated Protein Kinases and Activator Protein 1 Are Required for Proliferation and Cardiomyocyte Differentiation of P19 Embryonal Carcinoma Cells. *J. Biol. Chem.* **2002,** *277*, 15992-16001.

[28]. Cantley, L. C. The Phosphoinositide 3-Kinase Pathway. *Science* **2002,** *296*, 1655-1657.

[29]. Naito, A. T.; Tominaga, A.; Oyamada, M.; Oyamada, Y.; Shiraishi, I.; Monzen, K.; Komuro, I.; Takamatsu, T. Early Stage-Specific Inhibitions of Cardiomyocyte Differentiation and Expression of Csx/Nkx-2.5 and Gata-4 by Phosphatidylinositol 3-Kinase Inhibitor Ly294002. *Exp. Cell Res.* **2003,** *291*, 56-69.

[30]. Naito, A. T.; Akazawa, H.; Takano, H.; Minamino, T.; Nagai, T.; Aburatani, H.; Komuro, I. Phosphatidylinositol 3-Kinase–Akt Pathway Plays a Critical Role in Early Cardiomyogenesis by Regulating Canonical Wnt Signaling. *Circ. Res.* **2005,** *97*, 144-151.

[31]. Heo, J. S.; Lee, J. C. Beta-Catenin Mediates Cyclic Strain-Stimulated Cardiomyogenesis in Mouse Embryonic Stem Cells through Ros-Dependent and Integrin-Mediated Pi3k/Akt Pathways. *J. Cell. Biochem.* **2011,** *112*, 1880-1889.

[32]. Polesskaya, A.; Seale, P.; Rudnicki, M. A. Wnt Signaling Induces the Myogenic Specification of Resident Cd45+ Adult Stem Cells During Muscle Regeneration. *Cell* **2003,** *113*, 841-852.

[33]. Bond, J.; Sedmera, D.; Jourdan, J.; Zhang, Y. H.; Eisenberg, C. A.; Eisenberg, L. M.; Gourdie, R. G. Wnt11 and Wnt7a Are up-Regulated in Association with Differentiation of Cardiac Conduction Cells in Vitro and in Vivo. *Dev. Dyn.* **2003,** *227*, 536-543.

[34]. Kim, M.-H.; Kino-oka, M.; Maruyama, N.; Saito, A.; Sawa, Y.; Taya, M. Cardiomyogenic Induction of Human Mesenchymal Stem Cells by Altered Rho Family Gtpase Expression on Dendrimer-Immobilized Surface with D-Glucose Display. *Biomaterials* **2010,** *31*, 7666-7677.

[35]. Auer, M.; Hausott, B.; Klimaschewski, L. Rho Gtpases as Regulators of Morphological Neuroplasticity. *Ann. Anat.* **2011,** *193*, 259-266.

[36]. Bae, S.; Kim, H.; Lee, Y.; Xu, X. F.; Park, J. S.; Zheng, Y.; Balakrishnan, J.; Lei, T.; Kim, H. R.; Song, Y. I., *et al.* Roll-to-Roll Production of 30-Inch Graphene Films for Transparent Electrodes. *Nat. Nanotechnol.* **2010,** *5*, 574-578.

Part I I

Engineering nature-driven three-dimensional bioscaffolds with functional nanomaterials

Chapter 5

Binding behavior of hybrid system for the APCLP coated-carbon nanotube and graphene with bacterial cellulose

Introduction

Natural materials can be extremely complex, the key structural motifs that lead to their extraordinary properties typically span multiple length scales, and it is often not clear which of them are critical to achieve certain properties. Bacterial cellulose, for example, are remarkably robust because a specific combination of 2 dimensional network and 3 dimensional layer by layer structure results in the excellent properties, but at present it is challenging to fabricate new materials with such key structural advantages across so many length scales.

Today it is possible to routinely synthesize nanoscale building blocks with many excellent material properties, such as carbon nanotubes or graphene sheets which have unique electrical conductivity, chemical structure, and mechanical resilience. However, support structure is required to utilize carbon nanomaterials for various applications. It seems natural therefore; the two building blocks in the new nanocomposite are both exciting materials in their own properties.

In previous methods, carbon nanomaterials are simply mixed with polymer solution or coated on polymer matrices. However, disordered carbon nanomaterials arrays, and inhomogeneous structure were generated by these methods. In addition, high dispersity and strong attachment of carbon nanomaterials on polymer matrices are still unsolved problems that still need to be solved. For the first time, we propose a method to utilize a living organism for the production of uniform and stable integration carbon nanomaterials into three-dimensional highly porous matrices composed of nano-fibrils. In order for stable CNT colloidal suspension, we have modified CNTs with water soluble amphiphilic comb-like polymer. APCLP is composed of a long hydrophobic (methyl methacrylate, MMA) backbone, short hydrophilic (hydroxyl-poly (oxyethylene) methacrylate (HPOEM)), and (poly (ethylene glycol) methacrylate (POEM)) side chains. APCLP-modified carbon nanomaterials were able to maintain stable colloidal solution. We hypothesize that the hydrophobic backbone of APCLP would be adsorbed on hydrophobic carbon nanomaterials surface by hydrophobic interaction, whereas the hydrophilic side chains that face outwards would provide an environment where hydrophilic BC nano-fibrils can adhere and grow, thereby acting as a glue between carbon nanomaterials and BC nano-fibrils (Fig. 1b). This was also demonstrated by the simulation.

Experimental

Computational methods for CNT-BC-Syn

To explain binding mechanism among CNT, polymer and cellulose, we have performed the density functional theory (DFT) calculation within generalized gradient approximation (GGA) using the Vienna ab initio simulation package (VASP). [1-3] The projector augmented wave (PAW) potentials, as implemented in the VASP, were employed to describe the potentials from atom centers. The energy cutoff for the plane-wave basis was set to 400 eV in GGA. Geometries were optimized until the Hellman-Feynman forces acting on the atoms became smaller than 0.03 eV/Å. For investigation of binding mechanism, amphiphilic comb-like polymers (MMA and HPOEM) is considered between cellulose and CNT. To include weak van der Waals (vdW) interactions among them, we adopt the Grimme's DFT-D2 vdW correction based on a semi-empirical GGA-type theory.[4] For the Brillouin-zone interaction we used a 5×1×1 grid in Monkhorst-Pack special k-point scheme. In order to explain the behaviors of GO hybrids for large-scale dynamic system, we also have performed molecular dynamics (MD) simulation for GO hybrids structures at room temperature (300 K). We performed NVT-MD simulations using the Large-scale Atomic/Molecular Massively Parallel Simulator (LAMMPS) with a reactive force field (ReaxFF) potential[5] for 12.5 ps.

Computational methods for GO-Syn-BC-Syn

Our density functional theory (DFT) calculations use generalized gradient approximation (GGA) in the Vienna ab initio simulation package (VASP). [1-3] The kinetic energy cut-off is set to 400 eV. For the van der Waals (vdW) correction, we employ Grimme's DFT-D2 method, based on a semi-empirical GGA-type theory.[4] All atomic coordinates are fully relaxed until the Hellmann-Feynman forces are less than 0.025 eV/Å . For the Brillouin-zone integration, we use 3x3x1 and 3x1x1 for GO hybrids with BC and APCLP, respectively. In order to explain the binding behaviors of (r)GO hybrids for large-scale dynamic system, we also have performed molecular dynamics (MD) simulation for (r)GO hybrid structures at room temperature (300 K). For NVT-MD simulations, we use the Large-scale Atomic/Molecular Massively Parallel Simulator (LAMMPS) with a reactive force field (ReaxFF) potential[5]

Results and discussion

Before explaining about the binding mechanism for these hybrid systems, we have focused the dispersion of CNTs. The dispersion of CNTs have been given a considerable attention in producing CNT and polymer composites for CNT applications. However, it is difficult to disperse the CNTs in solution due to the entanglement of CNT bundles. Now, we have considered the CNT dispersion using APCLP. Figure 1 shows the dispersion behavior of CNT with APCLP. Three different configurations of CNTs are selected for the dispersion behavior in MD calculations. After doing ultra-sonication for the CNT in solutions, the CNTs are separated small size of bundles or each other as shown in figure 2. The inter-CNT distance is about (a) 3.3, (b) 10.0, and (c) 30.0 Å, respectively. The short distance between CNTs such as small size bundles do not have enough space to insert the APCLPs to them. Thus, the APCLPs are wrapping the small size CNT bundle as shown in figure 2 (a). On the other hand, the APCLPs infiltrate into the large separation of CNTs then the CNTs are well dispersed as shown in figure 2 (b) and (c). The dispersion ability of CNTs with APCLPs are good for the biomedical applications.

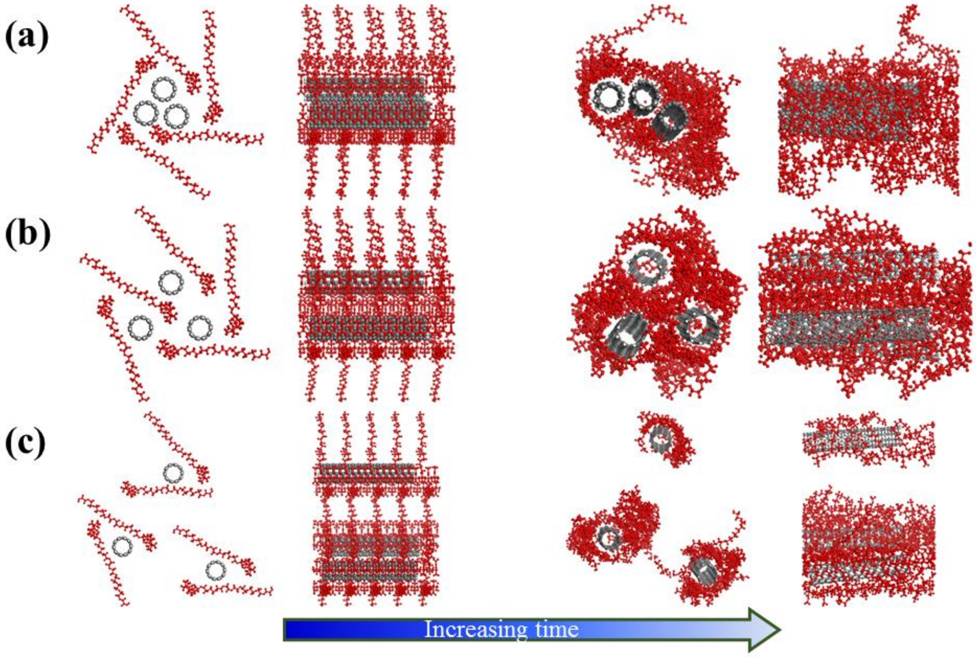

Figure 1 | Dispersion behavior of CNT

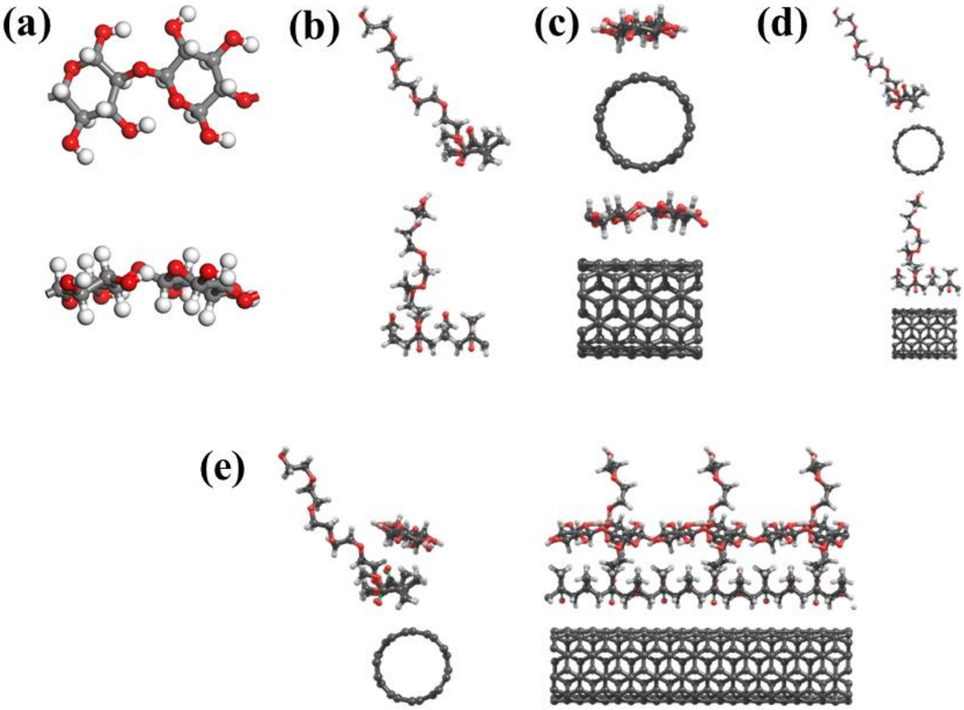

Figure 2 | Optimized geometries

First, we have performed the density functional theory calculations to find the geometries optimized for the bacterial cellulose and amphiphilic comb-like polymer. Figure 2 (a) and (b) show the optimized geometries of BC and APCLP, respectively. The component ratio of MMA (backbone), HPOEM (chain), and POEM (chain) is 6:2:2, respectively, in the hydrophobic backbone of APCLP. For our calculations, APCLP is approximated to only HPOEM connected to MMA because the structure of POEM is very similar to that of HPOEM except for the terminal part. We investigate the binding strength of hybridized cellulose-cellulose, cellulose-polymer, cellulose-CNT, polymer-CNT, and cellulose-polymer/CNT configurations. Here, the binding energies are defined as $E_b = -[E_{total}-E_{constituent1}-E_{constituent2}]$, where E_{total}, $E_{constituent1}$, and $E_{constituent2}$ are total energies of total combined system (e.g., cellulose-CNT), constituent 1 (cellulose), and constituent 2 (CNT), respectively. It is found that the binding energies are 0.68, 0.68, -0.05, and 0.03 eV (per given unit) for cellulose-cellulose, cellulose-polymer, cellulose-CNT, and polymer-CNT systems, respectively, which means that CNT does not interact with cellulose or polymer.

Figure 2(e) shows the optimized geometries of hybrid cellulose-polymer/CNT structure obtained by DFT calculations. The nearest interatomic distances between cellulose and HPOEM (or HPOEM and CNT) are 2.22 (or 2.78 Å) and the binding energy between cellulose and polymer/CNT is 0.71 eV. The polymer and cellulose are weakly combined with CNTs. From these results, the interfacial interaction between polymer (APCLP) and CNT and between cellulose and polymer/CNT is found to be a weak one. Overall, our ab initio calculations show that APCLP does not combine well with CNT contrary to our expectation.

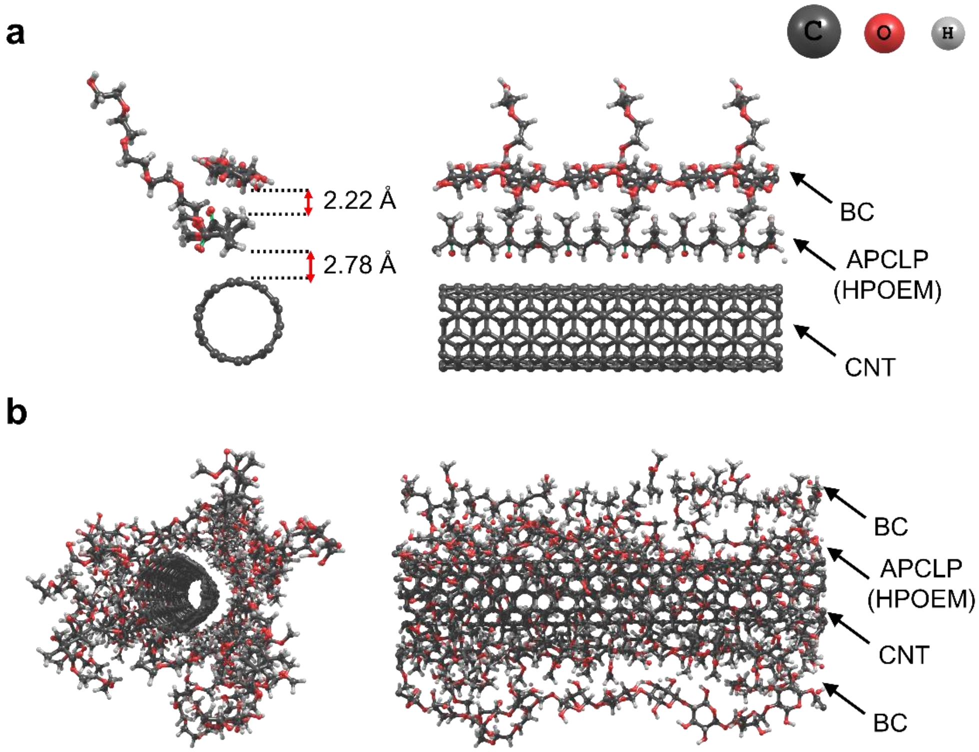

Figure 3 | Front and side views of (a) the geometry optimized by DFT calculations and (b) that obtained from molecular dynamics simulations for the cellulose-polymer (HPOEM)/CNT system

To clearly understand binding behaviors between BC and CNTs mediated by APCLPs, we have performed density functional theory (DFT) calculations and molecular dynamics (MD) simulations..

First, we investigate the binding strength of hybridized cellulose-cellulose, cellulose-polymer, cellulose-CNT, polymer-CNT, and cellulose-polymer/CNT configurations. Here, the binding energies are defined as $E_b = -[E_{total}-E_{constituent1}-E_{constituent2}]$, where E_{total}, $E_{constituent1}$, and $E_{constituent2}$ are total energies of total combined system (e.g., cellulose-CNT), constituent 1 (cellulose), and constituent 2 (CNT), respectively. It is found that the binding energies are 0.68, 0.68, -0.05, and 0.03 eV (per given unit) for cellulose-cellulose, cellulose-polymer, cellulose-CNT, and polymer-CNT systems, respectively, which means that CNT does not interact with cellulose or polymer. Figure 3(a) shows the optimized geometries of hybrid cellulose-polymer/CNT structure obtained by DFT calculations. The nearest interatomic distances between cellulose and HPOEM (or HPOEM and CNT) are 2.22 (or 2.78 Å) and the binding energy between cellulose and polymer/CNT is 0.71 eV. The polymer and cellulose are weakly combined with CNTs. From these results, the interfacial interaction between polymer (APCLP) and CNT and between cellulose and polymer/CNT is found to be a weak one. Overall, our ab initio calculations show that APCLP does not combine well with CNT contrary to our expectation.

In this regard, we have performed the molecular dynamics (MD) calculations to investigate binding mechanism of cellulose with cellulose itself, CNT, or polymer/CNT and further to understand their dynamical combining processes. Since

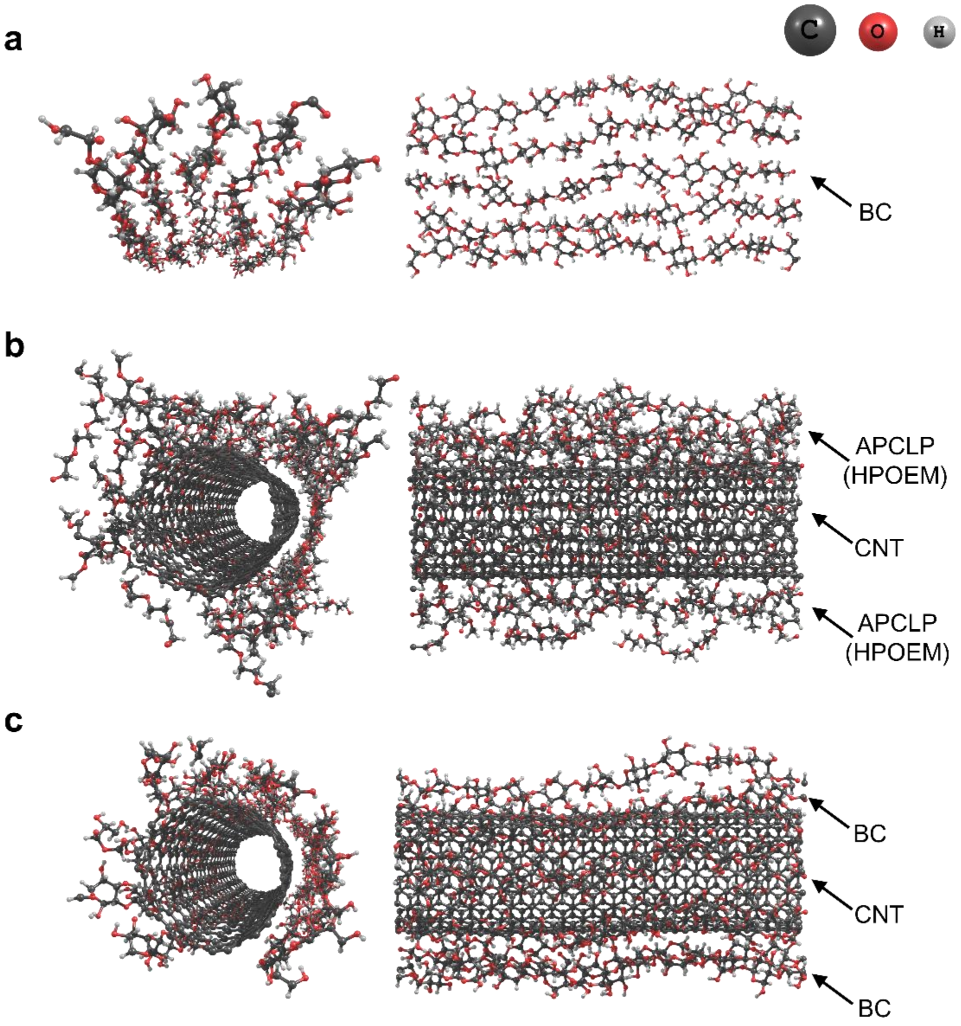

Figure 4 | Front and side views of geometries obtained from the molecular dynamics simulations for (a) cellulose-cellulose, (b) polymer(HPOEM)-CNT hybrid, and (c) cellulose-CNT systems cellulose is found to be formed into a comb-like structure when spurted out from G. xylinus bacteria, the binding behavior between cellulose is first considered. Cellulose looks like being self-assembled in our calculations, forming comb-like structures, as shown in Figure 4 (a). Note that the HPOEM or POEM is a chain-like structure as shown in Figure 3 (a). Thus, the CNTs are wrapped by the HPOEM of APCLP during the dispersion of CNTs, as shown in Figure 4(b) in calculations. It seems that the CNTs are structurally covered up with the HPOEM of APCLPs as a hook; that is, they are expected to mechanically bind each other. We simulate the CNTs surrounded by the HPOEM with cellulose. As a result, the celluloses are combined with the APCLP-covered CNT surface, as shown in Figure 3 (b). We finally consider the cellulose-CNT hybrids without APCLP to investigate the effect of APCLP on binding between cellulose and CNT. After the cellulose is assembled each other, the assembled cellulose is placed on the CNT as shown in Figure 3 (c), in comparison with the hybrid cellulose-polymer/CNT system. Figure 5 shows the obtained geometries for the time scale by 0.0 ps – 4.0 ps – 12.5 ps, for left, middle, and right panel, respectively. Our MD simulation results well explain the hybrid structures consisting of cellulose, APCLP and CNT, observed in experiment. Based on our results, we suggest that APCLP is a good medium to help binding between cellulose and CNT.

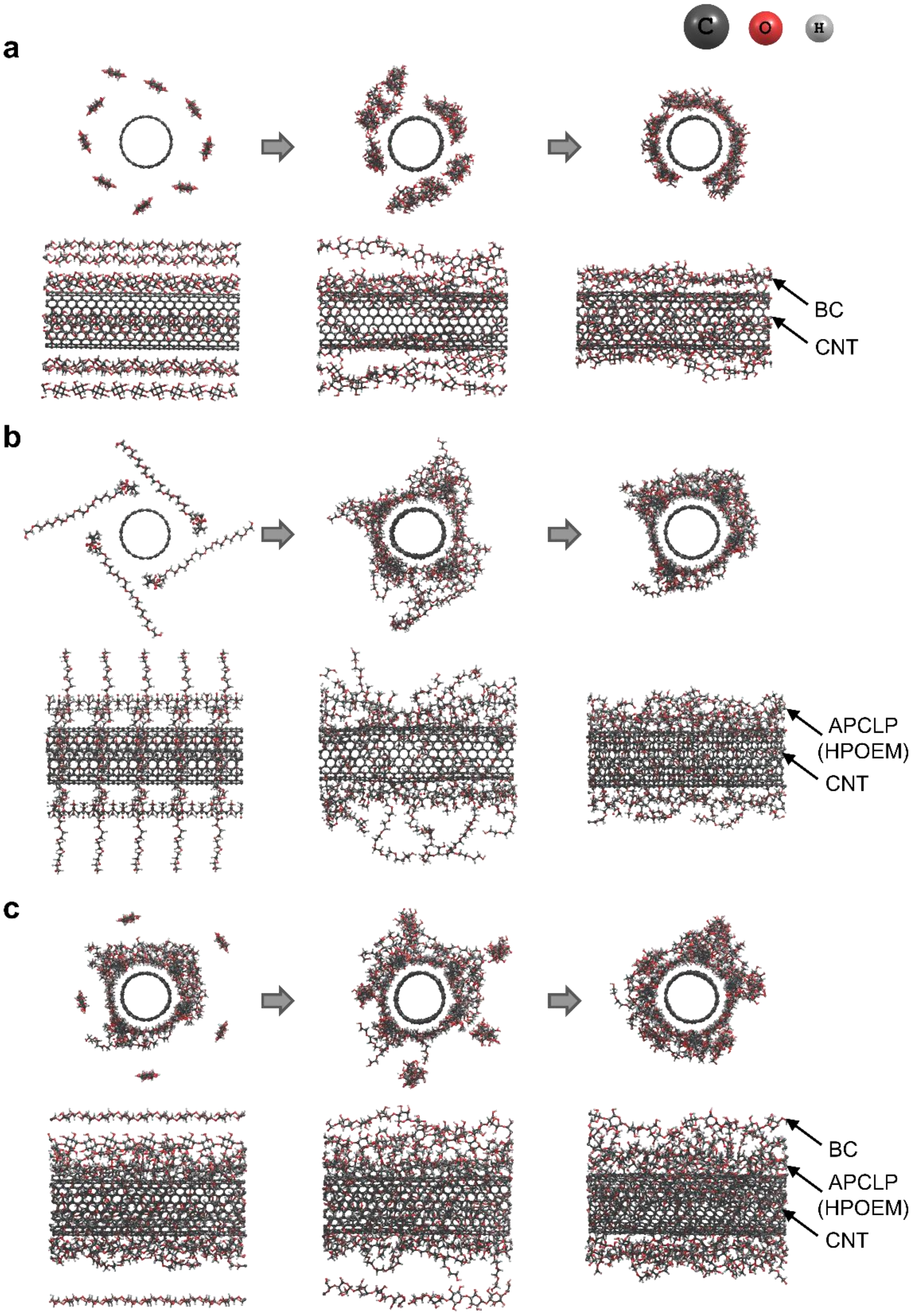

Figure 5 | Front and side views of geometries obtained from the molecular dynamics simulations for (a) cellulose-CNT, (b) polymer(HPOEM)-CNT, and (c) cellulose-polymer(HPOEM)/CNT systems for the time scale (0.0 ps - 4.0 ps - 12.5 ps)

We have performed DFT calculations for graphene oxide (GO) and reduced graphene oxide (rGO) hybrids with bacterial cellulose (BC) and amphiphilic comb-like polymer (APCLP). Table 1 shows the binding energies Eb and interatomic distance d between (r)GO and several adsorbates (APCLP, BC, or APCLP+BC). Binding energies are defined by following equation for each (r)GO hybrid.

$$E_b = -[\, E_{total} - E_{(r)GO} - E_{adsorbate} \,]$$

Here, E_{total}, $E_{(r)GO}$, and $E_{adsorbate}$ are total energies of the (r)GO hybrid system, (r)GO, adsorbate, respectively. Our calculation results represent weak interaction between (r)GO and adsorbates with small binding energies. However, GO interact more strongly with all adsorbates than rGO, representing the small interatomic distance as shown in Table 1.

We have performed DFT calculations for graphene oxide (GO) and reduced graphene oxide (rGO) hybrids with bacterial cellulose (BC) and amphiphilic comb-like polymer (APCLP). Table 1 shows the binding energies E_b and interatomic distance d between (r)GO and several adsorbates (APCLP, BC, or APCLP+BC). Binding energies are defined by following equation for each (r)GO hybrid.

$$E_b = -[\, E_{total} - E_{(r)GO} - E_{adsorbate} \,]$$

Here, E_{total}, $E_{(r)GO}$, and $E_{adsorbate}$ are total energies of the (r)GO hybrid system, (r)GO, adsorbate, respectively. Our calculation results represent weak interaction between (r)GO and adsorbates with small binding energies. However, GO interact more strongly with all adsorbates than rGO, representing the small interatomic distance as shown in Table 1.

Table 1. Binding energies E_b and interatomic distance d between GO(rGO) and adsorbates

	GO(rGO)-BC	GO(rGO)-APCLP	APCLP-coated GO(rGO)-BC
E_b (eV)	0.69 (0.83)	0.77 (0.93)	1.61 (1.64)
d (Å)	2.09 (2.42)	2.10 (2.60)	2.05 (2.60)

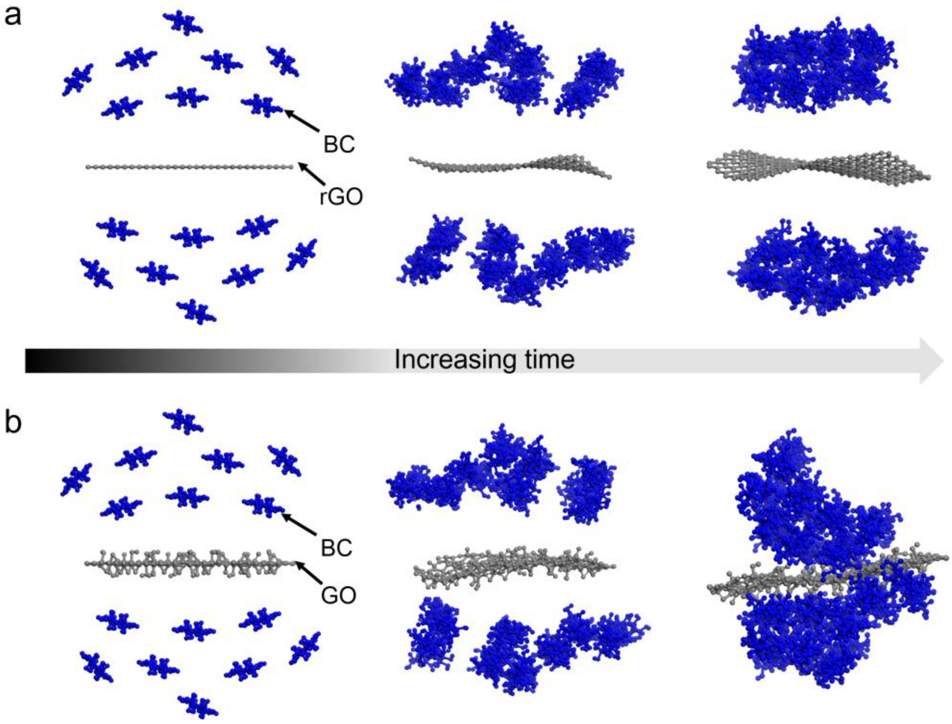

Figure 6 | Molecular dynamic simulations for (a) rGO-BC and (b) GO-BC

First, we have performed the MD simulations for the (r)GO hybrids with BC as shown in Figure 6(a) and (b). Our simulations show that BCs prefer to move toward the GO than rGO in the same time. These behaviors explain that functional groups of GO such as O or –OH play an essential role in interaction between GO and BC, implying a weaker interaction between BC and rGO than GO due to elimination of some functional groups in GO.

Second, MD simulation is done for the (r)GO hybrids with APCLP, as shown in Figure 8. Our results show that both GO and rGO are covered up with APCLP layers, representing the different behaviors to each other. APCLPs prefer to move towards another APCLP than rGO due to more strong interaction with APCLP than rGO. As a result, APCLP are evenly well adsorbed on rGO as shown in Figure 7(a). However, APCLP moves directly toward GO than another APCLP. This binding behavior implies that the functional groups of GO interacts more strongly with APCLP. Therefore, it seems that APCLP are randomly adsorbed on GO than rGO as shown in Figure 7(b).

Finally, we perform MD simulation for the (r)GO hybrid with APCLP+BC by considering adsorption of BC on the (r)GO hybrid structure shown in Figure 8(a) and (b). Our calculations show that BCs move towards APCLP and become seated on APCLP covering (r)GO as shown in Figure 8(a) and (b). (r)GO hybrid with APCLP interacts well with BC due to the presence of APCLP which mediates binding between (r)GO and BC. As shown in Figure 8(a), BC is evenly well adsorbed on APCLP-coated rGO, because APCLP is already evenly well dispersed on rGO in Figure 7(a). However, BCs seem that randomly adsorbed on APCLP-coated GO in

Figure 8(b), because they are adsorbed on APCLPs which are already randomly adsorbed on GO in Figure 7(b). These behaviors are well matched with experimental results, representing adsorption of BC on the (r)GO hybrid with APCLP.

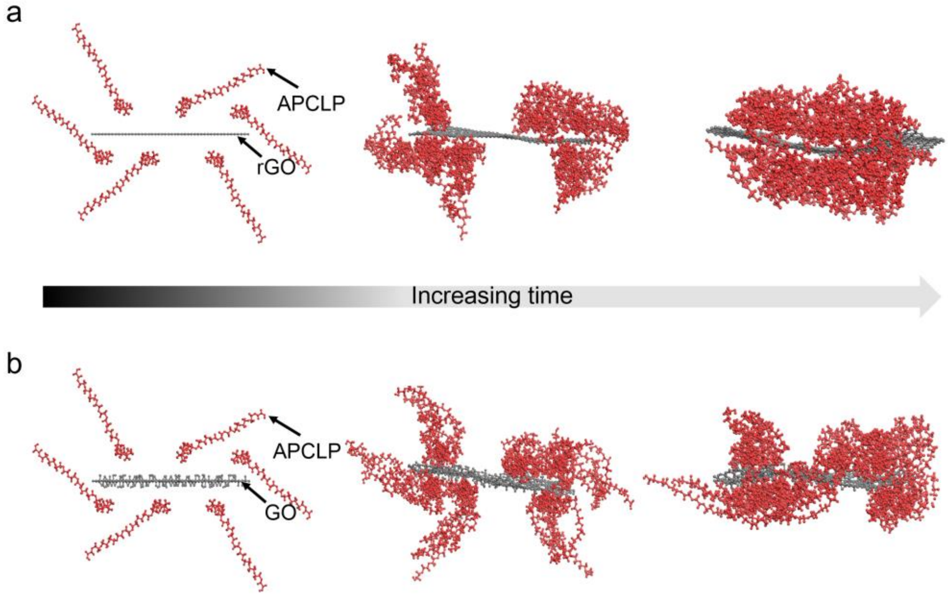

Figure 7 | Molecular dynamic simulations for a, rGO-APCLP and b, GO-APCLP

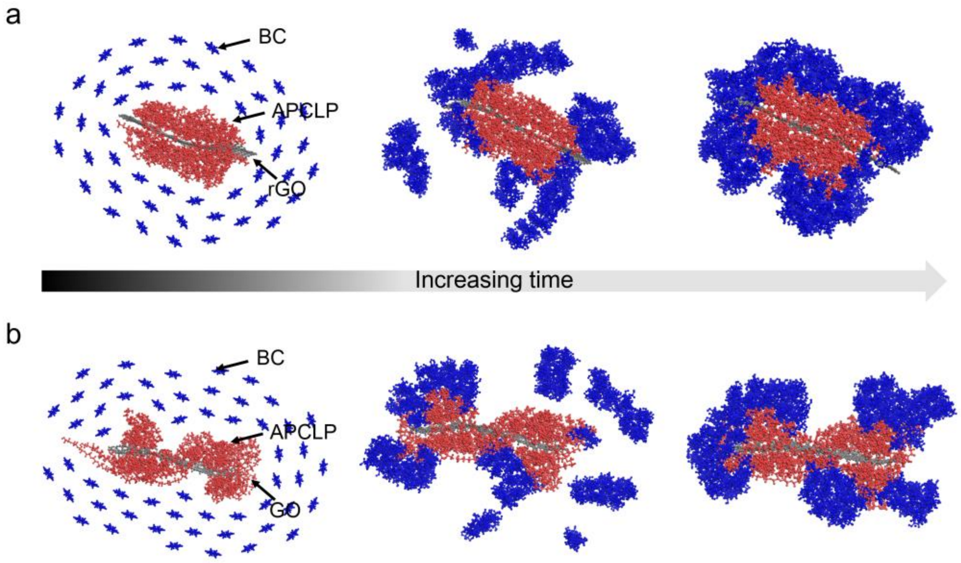

Figure 8 | Molecular dynamic simulations for APCLP-coated a, rGO-BC and b, GO-BC

Conclusions

In this study, an important method was introduced for the development 3D biofunctional scaffolds through hybridization with carbon nanomaterials for biomedical applications. BC was chosen as the 3D scaffold material for the hybridization of carbon nanomaterials due to its ideal structure for tissue engineering scaffolds. APCLP was utilized to promote colloidal stability of carbon nanomaterials and induce the hybridization between carbon nanomaterials and BC, which enabled homogeneous and effective.

References

[1]. Kresse, G.; Furthmuller, Efficient iterative schemes for ab initio total-energy calculations using a plane-wave basis set. *J. Phys. Rev. B* **1996**, 54 (16), 11169–11186.

[2]. Kresse, G.; Furthmuller, Efficient iterative schemes for ab initio total-energy calculations using a plane-wave basis set. *J. Comput. Mater. Sci*. **1996**, 6 (1), 15–50.

[3]. Perdew J P, Burke K and Ernzerhof M, Generalized Gradient Approximation Made Simple. Phys. Rev. Lett., **1996,** 77, 3865.

[4]. Grimme, S. Semiempirical GGA-type density functional constructed with a long-range dispersion correction. *J. Comput. Chem.* **2006**, *27*, 1787-1799.

[5] A. Strachan, A. C. T. van Duin, D. Chakraborty, S. Dasgupta, and W. A. Goddard III, Shock waves in high-energy materials: the initial chemical events in nitramine RDX, *Phys. Rev. Lett.* **2003**, 91, 098301.

Chapter 6

In situ hybridization of carbon nanotubes with bacterial cellulose for three-dimensional bioscaffods

Introduction

Microorganisms in nature are capable of forming remarkable structures with unique characteristics that are difficult to mimic artificially. *Gluconacetobacter xylinus* (*G. xylinus*), for example, can easily synthesize a large amount of bacterial cellulose (BC) composed of nanofiber networks stacked into layer-by-layer hierarchical structures. BC consists of many structural aspects favourable for bone grafting, including large pores, and nano-scale fibers in three-dimensional (3D) structure.[1-3] These requirements were difficult to achieve simultaneously using polymers or hydrogels because of the current technical limitations.[4]

Carbon nanotubes (CNTs) have gained great popularity for the use in bone regeneration. It is known that CNTs can promote osteogenesis of mesenchymal stem cells,[5] as well as osteoblast functioning,[6] and bone calcification.[7] However, despite the enormous efforts made in utilizing CNTs for *in vivo* bone regeneration, further advancements have been hampered by the technical limitations for the fabrication of 3D porous scaffolds using CNT framework. A 3D porous structure is an indispensable component of tissue engineering scaffolds for the provision of sufficient surface and space for cell adhesion, migration, growth, and tissue formation.[8,9] Although the method for fabricating 3D CNT-based scaffolds by soaking bioscaffolds in a CNT-containing solution has been reported, the resulting scaffolds showed an inhomogeneous distribution of CNTs.[10]

In this study, we developed a new method to fabricate CNT-based 3D scaffold that is composed of nanoscale fiber framework and large pores. Amphiphilic comb-like polymer (APCLP) was used to facilitate colloidal stability of CNTs in medium and to induce the hybridization of CNTs and BC. When *G. xylinus* was cultured in a culture medium containing APCLP-coated CNTs, the BC nanofibrils synthesized by *G. xylinus* wrap around APCLP-coated CNTs, resulting in a stable hybridization between CNTs and BC. As collodally stable CNTs are hybridized *in situ* into the newly forming BC nanofibers, which form the framework of the final scaffold, CNTs are homogeneously distributed throughout the scaffold.

The resulting scaffold showed a combination of the advantages of BC and CNTs for bone regeneration. The structure of the CNT-BC hybrid scaffold resembles the architecture of BC with larger pores. 3D architecture that is composed of nanofibers and large pores resulted in high osteoconductivity of the scaffold. In addition, the CNT-based framework caused high osteoinductivity, which is not achievable solely by BC. Therefore, with high osteoconductivity and osteoinductivity, the CNT-BC hybrid showed high bone regeneration efficacy *in vivo*

Experimental

Preparation of amphiphilic comb-like polymer (APCLP)

APCLP was synthesized by free radical polymerization of MMA (Aldrich), poly(ethylene glycol) methacrylate (Aldrich, Mn 360 g/mol, corresponding to n = 6) and poly(ethylene glycol) methyl ether methacrylate (Aldrich, Mn 475 g/mol, corresponding to n = 9), in tetrahydrofuran for 18 h. The CNTs (purity >95%, lljin Nanotech Co., Korea) produced by the chemical vapor deposition method were used without further purification or treatment. The CNTs were determined to have an outer diameter of about 10–20 nm and a length of 150–200 μm. A total of 1 mg of CNT was added to 10 mL of APCLP solution (30% ethanol, 0.001% APCLP), after which the samples were sonicated using a horn-type ultrasonic generator (Fisher Scientific Co., USA) with a frequency of 23 kHz and a power of 30 W for 20 min at room temperature**.**

G.xylinus culture

G. xylinus (KCCM 40216) was obtained from the Korean Culture Center of Microorganisms. The bacterium was cultured on medium composed of 2.5% (w/w) mannitol, 0.5% (w/w) yeast extract and 0.3% (w/w) bacto-peptone. The culture media were sterilized in an autoclave at 120 ◦C for 20 min and then poured into 500 mL flasks. The pre-inoculum for all experiments was prepared by transferring a single G. xylinus colony grown on agar culture medium into a 100 mL Erlenmeyer flask filled with mannitol culture medium. The optimal culture conditions were determined empirically (Figure S1).

Computational methods

To explain binding mechanism among CNT, polymer and cellulose, we have performed the density functional theory (DFT) calculation within generalized gradient approximation (GGA) using the Vienna ab initio simulation package (VASP).[1-3] The projector augmented wave (PAW) potentials, as implemented in the VASP, were employed to describe the potentials from atom centers. The energy cutoff for the plane-wave basis was set to 400 eV in GGA. Geometries were optimized until the Hellman-Feynman forces acting on the atoms became smaller than 0.03 eV/Å. For investigation of binding mechanism, amphiphilic comb-like polymers (MMA and HPOEM) is considered between cellulose and CNT. To include weak van der Waals (vdW) interactions among them, we adopt the Grimme's DFT-D2 vdW correction based on a semi-empirical GGA-type theory.[4] For the Brillouin-zone interaction we used a 3×1×1 grid in Monkhorst-Pack special k-point scheme. In order to explain the behaviors of CNT-BC hybrids for large-scale dynamic system, we also have performed molecular dynamics (MD) simulation for CNT hybrids structures at room temperature (300 K). We performed NVT-MD simulations using the Large-scale Atomic/Molecular Massively Parallel Simulator (LAMMPS) with a reactive force field (ReaxFF) potential for 12.5 ps.[5]

Preparation of CNT-BC

The pre-cultured culture cell suspension was introduced into 1 × 10^{-3} % (w/v) multi-walled CNT-dispersed culture medium (pH 6.0) at a ratio of 1:10 and incubated at 28 ◦C for 2 weeks. The CNT-incorporated BC (CNT–BC) membrane biosynthesized in the medium was simply harvested and purified by boiling in 1 wt% sodium hydroxide for 2 h at 90 ◦C. Subsequently, the membrane was thoroughly washed with running distilled water, after which it was soaked in 1 wt% aqueous sodium hydroxide solution for 24 h at room temperature to eliminate the cell debris and components of the culture liquid. The pH was then reduced to 7.0 by repetitive washing with distilled water. Next, the membrane was bleached by immersion in 1 wt% aqueous sodium hypochlorite for 2 h, after which it was washed with running distilled water until pH 7 was attained. Finally, the membrane was vacuum-dried at 60 ◦C for 12 h. The normal BC membrane was prepared by harvesting a single *G. xylinus* colony in mannitol culture medium without CNTs, purifying and bleaching as described above. The membrane stored in distilled water was immersed in 1×10^{-3}% (w/v) CNT-dispersed culture medium (pH 6.0) at 28 ◦C for 2 weeks. The BC membranes were washed with running distilled water and vacuum-dried at 60 ◦C for 12 h.

In vivo implatation

Six-week-old, female ICR mice (Koatech, Pyeongtaek, Korea) were anesthetized with xylazine (10 mg kg-1) and ketamine (100 mg kg-1) intraperitoneally. After shaving the scalp hair, a longitudinal incision was made in the midline of the cranium from the nasal bone to the posterior nuchal line and the periosteum was elevated to expose the surface of the parietal bones. Using a surgical trephine bur (Ace Surgical Supply Co., Brockton, MA, USA) and a low speed micromotor, two transosseous defects (4 mm diameter, circular) were produced in the skull. The defect size corresponded to the critical defect size for the mouse calvarial defect model. The drilling site was irrigated with saline, and bleeding points were electrocauterized. The periosteum was removed and never restored. The defect was filled with nothing, BC, CNT-BC-imm, CNT-BC-syn, or Col-BMP-2 (n = 6 implants per group). The periosteum and skin were then closed in layers with resorbable 6-0 Vicryl® sutures (Ethicon, Edinburgh, UK). The mice were housed singly after surgery. The study was approved by the Institutional Animal Care and Use Committee of Seoul National University (SNU-110121-3). The implants were retrieved for analysis at 8 weeks after the surgery.

Statistical analysis

Quantitative data were expressed as mean ± standard deviation. Statistical analyses were performed using analysis of variance (ANOVA). A p value of less than 0.05 was considered statistically significant.

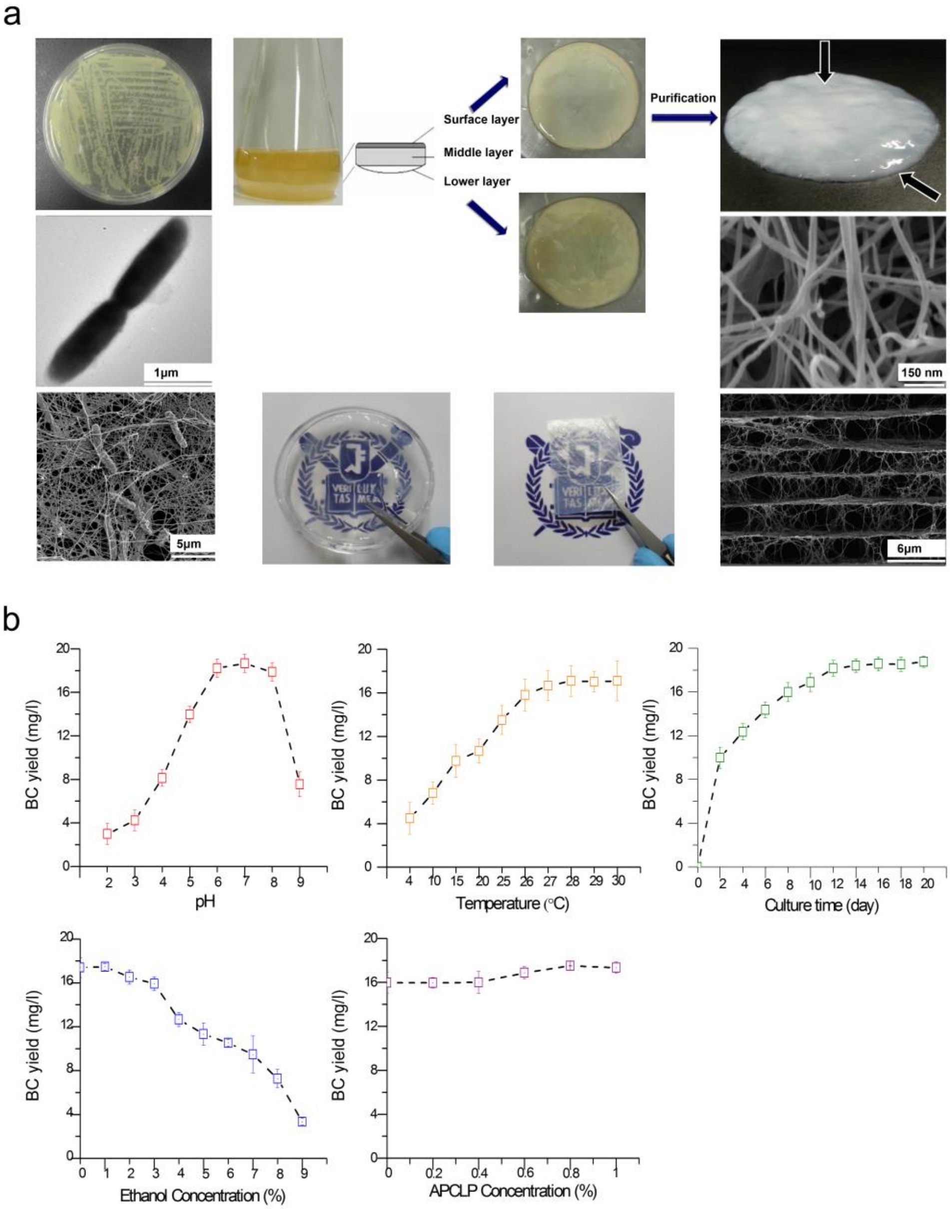

Figure S1 | BC preparation and optimization processes and parameters. a, Images of *G. xylinus* and BC. b, Effect of pH, temperature, culture time, APCLP concentration and ethanol concentration on BC yield. Cells were cultivated for 7 days in a mannitol medium.

Results and Discussion

APCLP plays a critical role in the fabrication of CNT-BC-Syn as it facilitates the dispersion of CNTs and meanwhile induces the hybridization of CNTs with BC. APCLP is composed of long a hydrophobic methyl methacrylate (MMA) backbone and short hydrophilic side chains that consist of hydroxyl polyoxyethylene methacrylate (HPOEM) and polyethylene glycol methacrylate (POEM) (Figure 1a). Molecular dynamics (MD) simulation suggested that APCLP modified the CNT surface through its unique comb-like molecular structure. The simulation showed that the hydrophobic backbone was attached to CNTs via hydrophobic-hydrophobic interactions, and the hydrophilic side chains wrapped around CNTs to form an amphiphilic surface (Figure 1a).

The amphiphilic surface facilitates the dispersion of APCLP-coated CNTs in the culture medium (Figure 1). Images obtained by scanning electron microscopy (SEM) and transmission electron microscopy (TEM) indicated that CNTs were uniformly dispersed after being treated with APCLP (Figure 1b). We further confirmed the APCLP coating on CNTs by means of fourier transform infrared spectroscopy (Figure 1c), and the results showed that APCLP-coated CNTs were well dispersed in culture medium for more than 3 months after APCLP coating (Figure 1d). In addition, the colloidal stability of APCLP-coated CNTs was not influenced by pH change (Figure 1e).

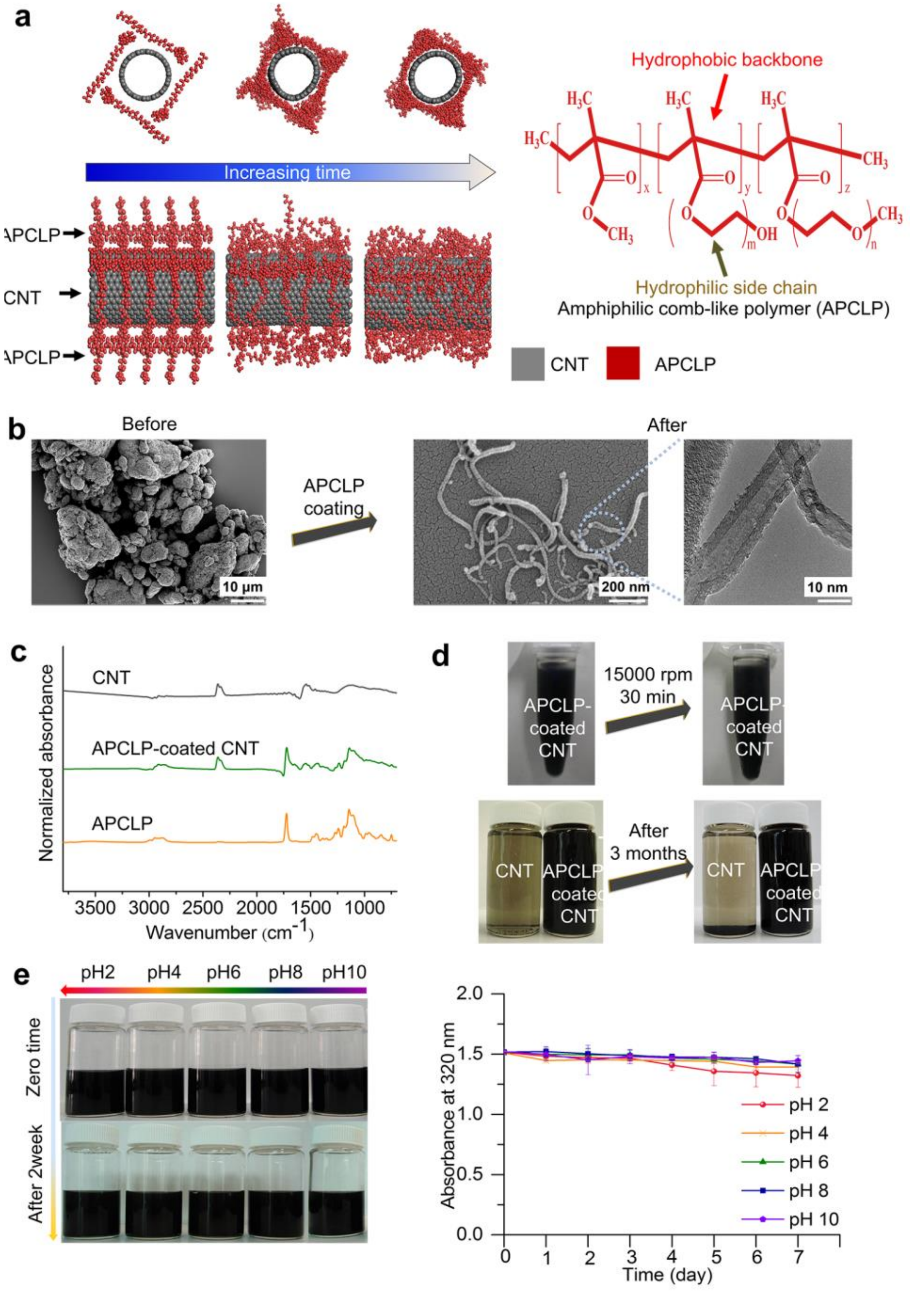

Figure 1 | APCLP-mediated dispersion of CNTs. a, MD simulation of APCLP-coated CNT. b, SEM and TEM images of CNTs before and after APCLP coating. c, Fourier transform infrared spectroscopy spectrum of CNT, APCLP and APCLP-coated CNT. d, Colloidal stability of CNT and APCLP-coated CNT after centrifugation and after 3 months. e, Colloidal stability of APCLP-coated CNT in various pH conditions of culture medium.

We prepared a CNT-based scaffold by utilizing *G. xylinus* for synthesizing BC nanofibrils that wrapped around CNTs. To achieve this, *G. xylinus* was simply cultured in a culture medium containing APCLP-coated multi-walled CNTs. The hybrid scaffold was purified after fabrication to eliminate *G. xylinus* and other contaminations.

As stated earlier, APCLP can induce the hybridization of CNTs with BC (Figure 2a). To clearly understand the APCLP-mediated binding of CNTs to BC, we performed *ab initio* calculations and MD simulations. First, the binding energies of CNT-BC and APCLP-coated CNT-BC were compared (Figure 2b). The binding energy, E_b, is defined as $E_b = -[E_{total} - E_{constituent1} - E_{constituent2}]$, where E_{total}, $E_{constituent1}$ and $E_{constituent2}$ are the energies of the total system (i.e., CNT-BC), constituent 1 (BC), and constituent 2 (CNT), respectively. The binding energy of CNTs and BC nanofibrils was -0.05 eV (per given unit), while the binding energy between BC nanofibrils was 0.68 eV (Figure 2b). Therefore, BC nanofibrils entangle around each other without having interactions with CNTs. On the other hand, the binding energy of APCLP-coated CNTs and BC nanofibrils was 0.71 eV (Figure 2b), causing BC nanofibrils to bind to and wrap around APCLP-coated CNTs. In this regard, MD simulation was performed to investigate the mechanism of CNT-BC and APCLP-coated CNT-BC formation (Figure 2c). In the case of CNT-BC, BC assembled with each other without being hybridized with CNTs. On the contrary, in the case of APCLP-coated CNT-BC, BC nanofibrils wrapped around APCLP-coated CNTs to form a hybrid, indicating the essential role of APCLP in the hybridization of CNTs

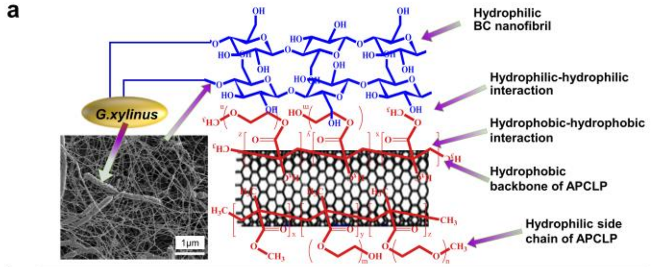

b

	BC nanofibril-BC nanofibril	CNT-BC	APCLP-coated CNT-BC
E_b	+0.68 eV	-0.05 eV	+0.71 eV

$E_b = -1/n \times [E_{tot} - n \times E_{BC}]$, n being the number of BC nanofibrils, for BC nanofibril-BC nanofibril
where $E_b = [E_{tot} - E_{CNT} - E_{BC}]$ for CNT-BC, and
$E_b = [E_{tot} - E_{APCLP/CNT} - E_{BC}]$ for APCLP-coated CNT-BC

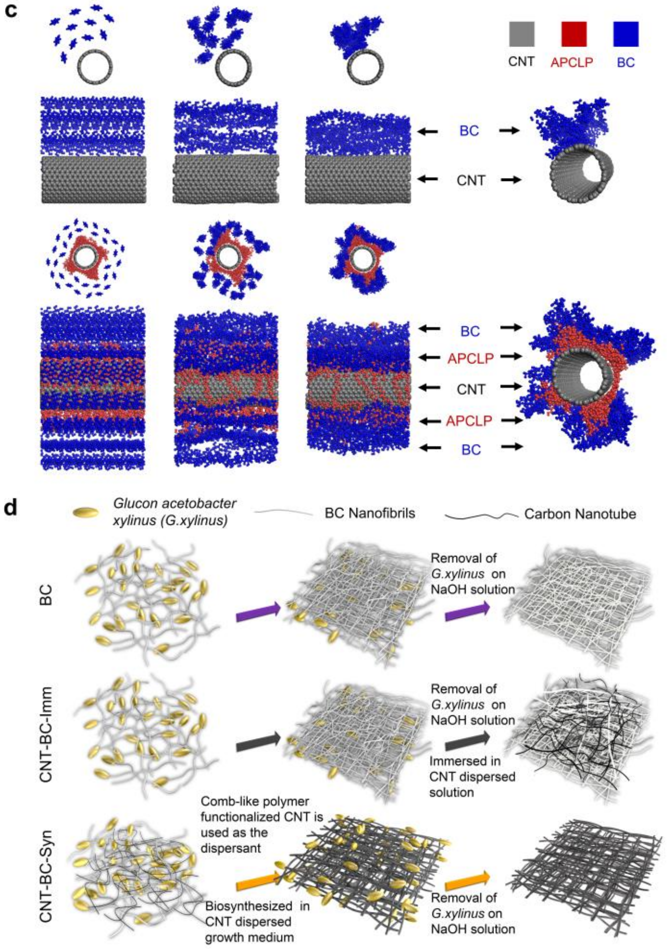

Figure 2 | APCLP-induced hybridization of CNTs and BC. a, Schematic representation of APCLP-coated CNT-BC hybridization. b, Binding energies measured by ab initio calculations. c, MD simulations for CNT-BC and APCLP-coated CNT-BC. d, Schematic illustration for the fabrication processes of BC, CNT-BC-Imm and CNT-BC-Syn.

with BC. All CNTs used in the following experiments were present in the form of APCLP-coated CNTs, as pure CNTs agglomerate and would be unsuitable for use in this study. Therefore, the word “CNTs” in all instances in the following paper indicate APCLP-coated CNTs. Due to the impracticality of using CNTs (without APCLP-coating) for the experiments, we compared the characteristics of the CNT-BC hybrid (i.e., CNT-BC-Syn) with those of CNT-coated BC formed by immersion (i.e., CNT-BC-Imm). The fabrication processes of both are shown in Figure 2d.

TEM was performed to characterize the hybridization between CNTs and BC. TEM analysis showed that CNT-BC-Syn exhibited a core-shell structure, where CNTs were packed by BC nanofibril entanglements (Figure 3a). In contrast, CNTs and BC nanofibrils in CNT-BC-Imm were separate from each other (Figure 3a). It is noteworthy that the BC nanofibrils in CNT-BC-Syn did not cover the entire surface of CNTs, resulting in a partial exposure of the CNTs to the surrounding environment (Figure 3b). The average thickness of the BC nanofibril entanglements was 4.3 nm, and about 3.9% of the CNT surface was uncovered (Figure 3b). The exposure of CNTs and thin BC coating would enable the interaction of cells with CNTs. The electron energy loss spectroscopy (EELS) spectrum collected from BC showed a broad peaks at 291 eV assigned to the 1s to 2σ* transition of carbon (Figure 3c). On the other hand, EELS spectrum of CNT-BC-Syn showed a sharp peak at 291 eV due to the 1s to p-orbital anti-bonding 2σ* band transition (Figure 3c), which was a characteristic of CNTs. This difference in EELS spectrum indicated that CNTs were embedded in the thin layer of BC in CNT-BC-Syn.

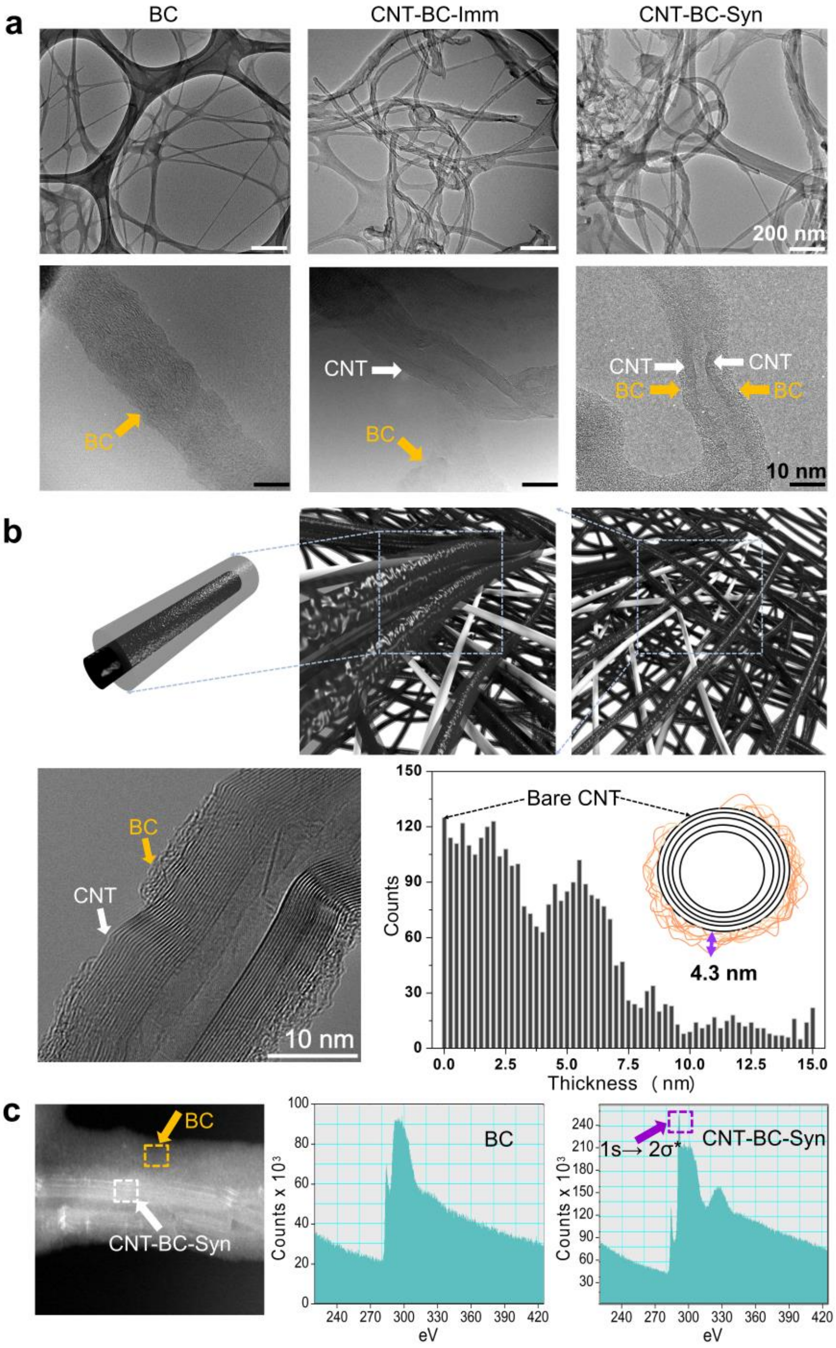

Figure 3 | TEM analyses of CNT-BC hybrid. a, TEM images of BC, CNT-BC-Imm and CNT-BC-Syn. b, Thickness distribution of BC on CNTs, showing the partial exposure of bare CNTs. c, EELS spectra of BC and CNT-BC-Syn showing the core-shell hybridization structure of CNT-BC-Syn.

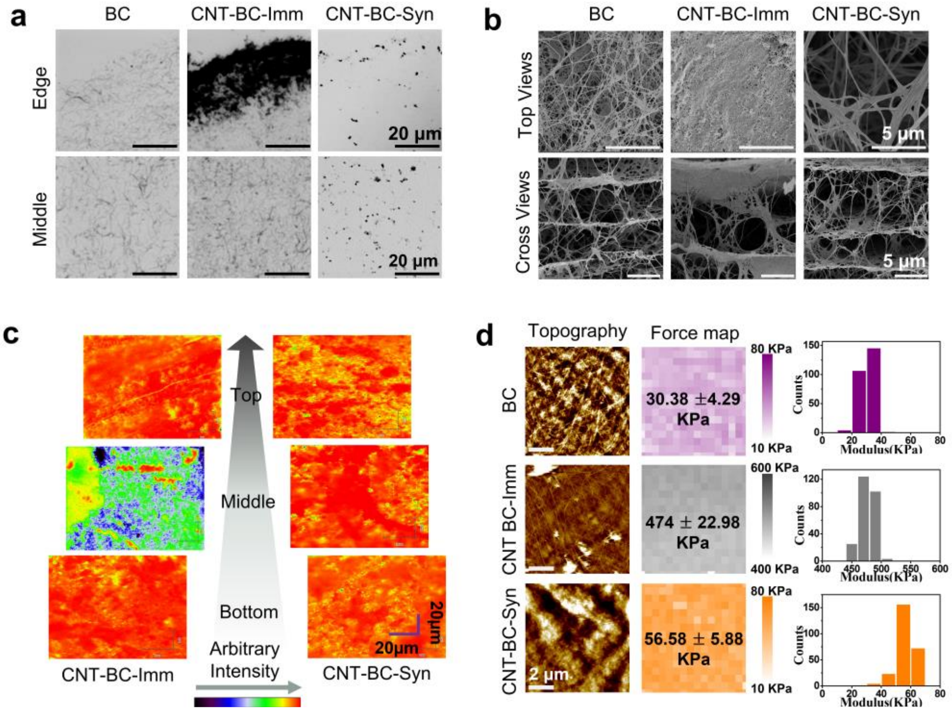

Figure 4 | Analyses showing the homogenous distribution of CNTs in CNT-BC-Syn. a, Cross-sectional optical images of BC, CNT-BC-Imm and CNT-BC-Syn. Scale bars, 20 µm. b, SEM images of BC, CNT-BC-Imm and CNT-BC-Syn with top and cross-sectional views. Scale bar, 5 µm. c, Raman mapping of CNT-BC-Imm and CNT-BC-Syn. d, Force mapping of BC, CNT-BC-Imm and CNT-BC-Syn on the surface measured by contact-mode AFM. Scale bars, 2 µm.

Intensive accumulations of black dots (i.e., CNTs) were observed on the edge of CNT-BC-Imm (Figure 4a). In contrast, CNTs in CNT-BC-Syn were homogeneously distributed throughout the scaffold. The SEM images showed that the accumulation of CNTs caused pore clogging at the CNT-BC-Imm surface (Figure 4b); on the other hand, no CNT accumulation, thus no clogged pores were observed in CNT-BC-Syn (Figure 4a and b). It is interesting to note that the porosity and pore size of CNT-BC-Syn were larger than that of pure BC (Figure 4b and Table 1). This might be because *G. xylinus* regarded CNTs as foreign substances, and therefore, formed a less compact BC.[11] In addition, all scaffolds maintained the original layer-by-layer structure of BC (Figure 4b). G-peak intensity mapping by means of Raman spectroscopy was performed to clearly depict the distribution of CNTs (Figure 4c). Although the top and bottom surfaces of CNT-BC-Imm were fully covered with CNTs, CNTs were rarely observed inside the scaffolds. This result indicated that CNTs were predominantly present on the surface and absent from the interior of the scaffold in CNT-BC-Imm (Figure 4c). On the other hand, CNTs were homogeneously distributed over the entire scaffold in CNT-BC-Syn (Figure 4c). The high Young’s modulus of the CNT-BC-Imm surface measured by atomic force microscopy (AFM) indicated that the surface of the scaffold was fully covered by CNT agglomerates (Figure 4d). In addition, the homogenous distribution of CNTs in CNT-BC-Syn resulted in a reduced specific resistance and enhanced electrical conductivity, as compared with that of BC and CNT-BC-Imm (Table 1).

Overall, these results suggest that CNT-BC-Syn can be used as an ideal bone graft material due to its unique architecture. We were able to fabricate CNT-BC-Syn composed of large pores and nano-scale fibers by utilizing *G. xylinus*. The pore size of CNT-BC-Syn was suitable for cell migration and osteogenesis.[12] The nano-scale fibers constituting CNT-BC-Syn are favourable for cell attachment, proliferation, alkaline phosphatase synthesis and extracellular calcium deposition, which are all essential aspects of bone regeneration.[13,14] The resulting CNT-BC-Syn showed mechanical strength appropriate for osteogenic differentiation.[15] In addition, the hydrogel-like BC layers surrounding CNTs may act as a reservoir for accommodating various growth factors,[16,17] which in turn can enhance the cell differentiation to facilitate bone regeneration.

Previous studies have demonstrated that although CNTs and BC are not biodegradable, both have shown a high level of biocompatibility.[18,19] CNTs showed minimized local inflammatory reactions and were well integrated into the newly formed bone after *in vivo* implantation for bone regeneration.[18] Similarly, BC was well integrated into the host tissue without inducing any inflammation when implanted *in vivo*.[19] BC is composed of only cellulose without any unwanted biogenic compounds, and it is less immune-stimulatory as compared with collagen, a commonly used scaffold material.[20] To evaluate the *in vivo* performance of CNT-BC-Syn, it was applied as a bone graft for bone regeneration application, and the results were compared with those obtained by using BC, CNT-BC-Imm, and collagen sponge loaded with bone morphogenetic protein-2 (Col-BMP-2), a clinically used bone graft.[21]

The microscopic computed tomographic (micro-CT) analyses performed 8 weeks after the implantation of the scaffolds into the critical-sized defect in mouse

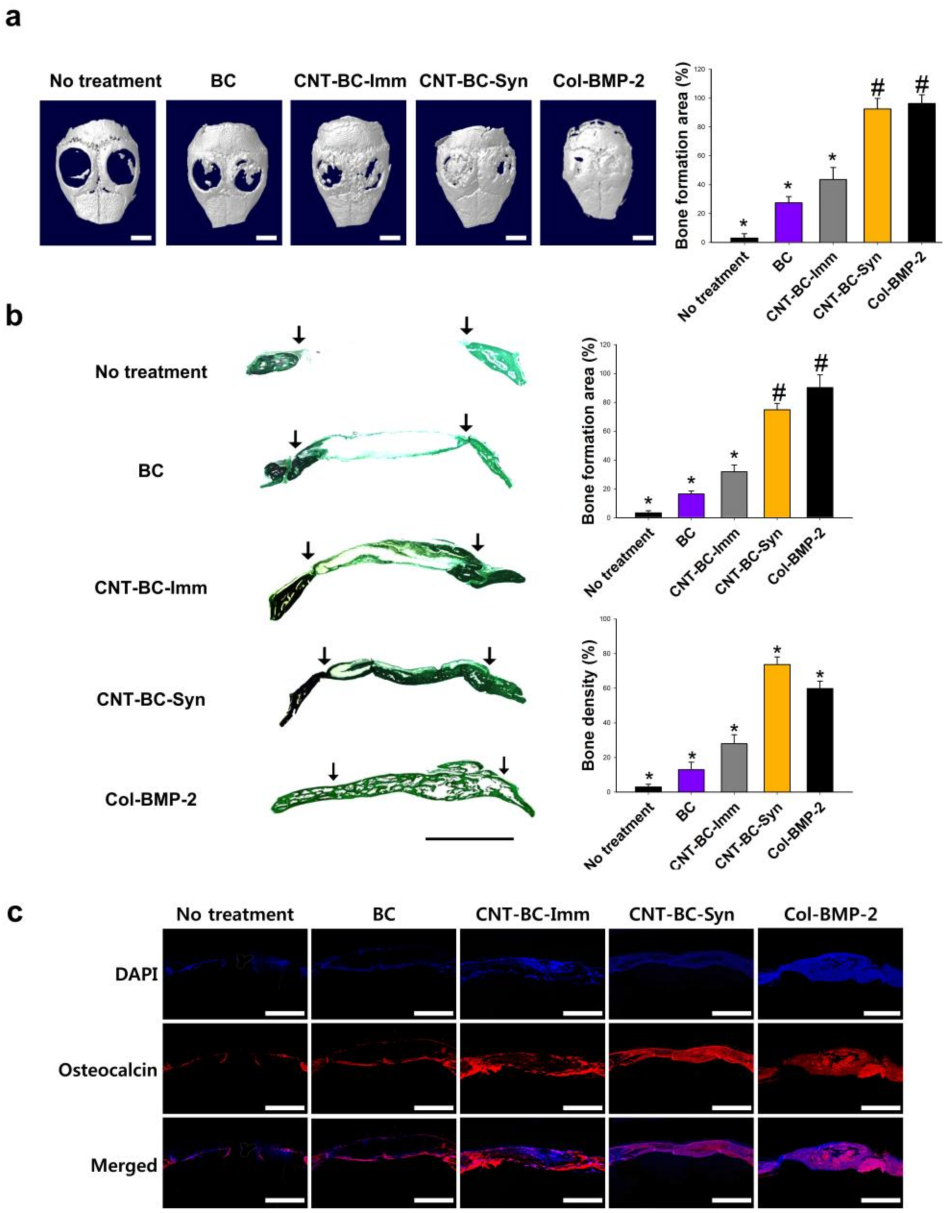

Figure 5 | Bone regeneration efficacy of the scaffolds. a, Bone regeneration evaluated by micro-CT analyses. Quantification of the bone formation area of defects. b, Goldner's trichrome staining of mouse calvarial defect areas. Quantification of bone formation area and bone density of defects. c, Immunohistochemistry of mouse calvarial defect areas. DAPI staining indicates osteoconductivity of the scaffolds. Osteocalcin staining indicates osteoinductivity of the scaffolds. Scale bars, 2 mm. *$p < 0.05$ compared to any other group. #$p < 0.05$ compared to no treatment, BC and CNT-BC.

calvaria showed a similar bone regeneration efficacy of CNT-BC-Syn, and Col-BMP-2, which was much higher than that of BC or CNT-BC-Imm (Figure 5a). The analytical results of Goldner's trichrome staining of the histological sections revealed insufficient bone regeneration by BC and CNT-BC-Imm; in contrast, the use of CNT-BC-Syn resulted in extensive bone regeneration similar to that caused by Col-BMP-2 (Figure 5b). It is noteworthy that although Col-BMP-2 is capable of forming new bone with the area similar to that formed by CNT-BC-Syn, the density of the regenerated bone was lower than that formed by CNT-BC-Syn (Figure 5b). This indicates that CNT-BC-Syn is suitable for use as a bone graft material due to its capability in forming new bone with high density.

A good bone graft should facilitate migration of the cells from the surrounding environment to the defect area (i.e., high osteoconductivity) and promote their osteogenic differentiation (i.e., high osteoinductvity). In this study, we demonstrated that the fabricated CNT-BC-Syn exhibited excellent osteoconductivity and osteoinductivity, both of which are desirable properties for bone regeneration (Figure 5c). The 4',6-diamidino-2-phenylindole (DAPI, blue) staining of cell nuclei confirmed the cell migration into the scaffolds. The fluorescence of DAPI was visible throughout the defect area, demonstrating that CNT-BC-Syn exhibited excellent osteoconductivity for promoting cell migration (Figure 5c). In addition, the osteocalcin staining (red) revealed that the cells underwent pronounced osteogenic differentiation in CNT-BC-Syn. Most of the cells in CNT-BC-Syn were successfully labelled with red fluorescence (Figure 5c), suggesting that CNT-BC-Syn showed a high osteoinductivity. As regards to CNT-BC-Imm, the cells were found to only differentiate on the periphery of the defect area (Figure 5c).

The possible explanation for the enhanced osteoconductivity and osteoinductivity of CNT-BC-Syn, as compared with BC and CNT-BC-Imm, may be the structure of the scaffold and the distribution of CNTs. CNT-BC-Syn showed a larger average pore size than that of BC and CNT-BC-Imm (Table 1). This, at least partially, contributed to the enhanced cell migration into CNT-BC-Syn.[12] The migrated cells would interact with CNTs that were homogeneously distributed throughout CNT-BC-Syn. This, in turn, would enable the promotion of osteogenic differentiation of the migrated cells.[22] In contrast, the absence of CNTs from the core of CNT-BC-Imm resulted in the osteoinduction occurring only on the surface of the scaffold (Figure 5c)

Table 1| Properties of BC, CNT-BC-Imm and CNT-BC-Syn

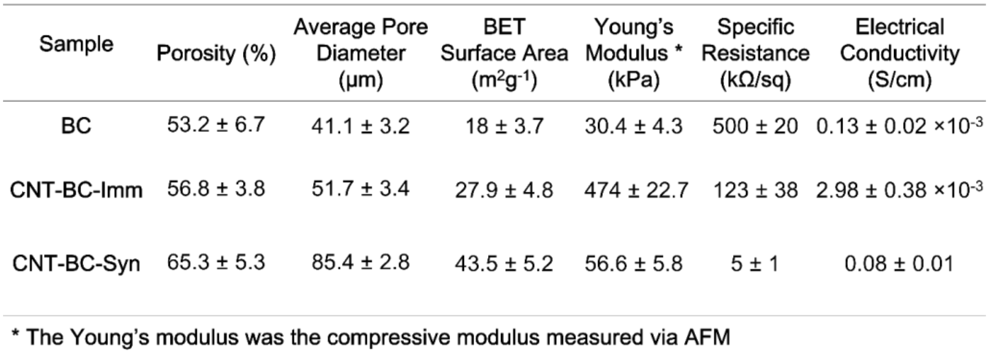

Sample	Porosity (%)	Average Pore Diameter (μm)	BET Surface Area (m^2g^{-1})	Young's Modulus * (kPa)	Specific Resistance (kΩ/sq)	Electrical Conductivity (S/cm)
BC	53.2 ± 6.7	41.1 ± 3.2	18 ± 3.7	30.4 ± 4.3	500 ± 20	0.13 ± 0.02 $\times 10^{-3}$
CNT-BC-Imm	56.8 ± 3.8	51.7 ± 3.4	27.9 ± 4.8	474 ± 22.7	123 ± 38	2.98 ± 0.38 $\times 10^{-3}$
CNT-BC-Syn	65.3 ± 5.3	85.4 ± 2.8	43.5 ± 5.2	56.6 ± 5.8	5 ± 1	0.08 ± 0.01

* The Young's modulus was the compressive modulus measured via AFM

Conclusions

In this study, an important method was introduced for the development 3D biofunctional scaffolds through hybridization with biofunctional nanomaterials for biomedical applications. BC was chosen as the 3D scaffold material for the hybridization of CNTs due to its ideal structure for tissue engineering scaffolds. APCLP was utilized to promote colloidal stability of CNTs and induce the hybridization between CNTs and BC, which enabled homogeneous and effective hybridization of CNTs with BC. Unlike conventional CNT-composite scaffolds fabricated through immersion of 3D BC scaffolds in CNT solution, CNT-BC-Syn scaffolds showed homogeneously distributed CNTs throughout the 3D microporous structure of BC. This resulted in excellent osteoinductivity and osteoconductivity of CNT-BC-Syn hybrid scaffolds, and in turn, high bone regeneration efficacy when implanted in vivo. This strategy for hybridizing 3D scaffolds with functional nanomaterials may present a new perspective for regenerative medicine.

References

[1]. Vandamme, E. J.; De Baets, S.; Vanbaelen, A.; Joris, K.; De Wulf, P. Improved Production of Bacterial Cellulose and Its Application Potential. *Polym. Degrad. Stab.* **1998,** *59*, 93-99.

[2]. Yeo, M.; Lee, H.; Kim, G. Three-Dimensional Hierarchical Composite Scaffolds Consisting of Polycaprolactone, Beta-Tricalcium Phosphate, and Collagen Nanofibers: Fabrication, Physical Properties, and in Vitro Cell Activity for Bone Tissue Regeneration. *Biomacromolecules* **2011,** *12*, 502-510.

[3]. Venugopal, J.; Low, S.; Choon, A. T.; Ramakrishna, S. Interaction of Cells and Nanofiber Scaffolds in Tissue Engineering. *J Biomed Mater Res B Appl Biomater* **2008,** *84*, 34-48.

[4]. Tuzlakoglu, K.; Bolgen, N.; Salgado, A. J.; Gomes, M. E.; Piskin, E.; Reis, R. L. Nano- and Micro-Fiber Combined Scaffolds: A New Architecture for Bone Tissue Engineering. *J Mater Sci Mater Med* **2005,** *16*, 1099-1104.

[5]. Li, X. M.; Liu, H. F.; Niu, X. F.; Yu, B.; Fan, Y. B.; Feng, Q. L.; Cui, F. Z.; Watari, F. The Use of Carbon Nanotubes to Induce Osteogenic Differentiation of Human Adipose-Derived Mscs in Vitro and Ectopic Bone Formation in Vivo. *Biomaterials* **2012,** *33*, 4818-4827.

[6]. Shao, S.; Zhou, S.; Li, L.; Li, J.; Luo, C.; Wang, J.; Li, X.; Weng, J. Osteoblast Function on Electrically Conductive Electrospun Pla/Mwcnts Nanofibers. *Biomaterials* **2011,** *32*, 2821-2833.

[7]. Shimizu, M.; Kobayashi, Y.; Mizoguchi, T.; Nakamura, H.; Kawahara, I.; Narita,

N.; Usui, Y.; Aoki, K.; Hara, K.; Haniu, H., *et al.* Carbon Nanotubes Induce Bone Calcification by Bidirectional Interaction with Osteoblasts. *Adv. Mater.* **2012,** *24*, 2176-2185.

[8]. Correa-Duarte, M. A.; Wagner, N.; Rojas-Chapana, J.; Morsczeck, C.; Thie, M.; Giersig, M. Fabrication and Biocompatibility of Carbon Nanotube-Based 3d Networks as Scaffolds for Cell Seeding and Growth. *Nano Lett.* **2004,** *4*, 2233-2236.

[9]. Murphy, C. M.; Haugh, M. G.; O'Brien, F. J. The Effect of Mean Pore Size on Cell Attachment, Proliferation and Migration in Collagen-Glycosaminoglycan Scaffolds for Bone Tissue Engineering. *Biomaterials* **2010,** *31*, 461-466.

[10]. Hirata, E.; Uo, M.; Takita, H.; Akasaka, T.; Watari, F.; Yokoyama, A. Multiwalled Carbon Nanotube-Coating of 3d Collagen Scaffolds for Bone Tissue Engineering. *Carbon* **2011,** *49*, 3284-3291.

[11]. Heßler, N.; Klemm, D. Alteration of Bacterial Nanocellulose Structure by in Situ Modification Using Polyethylene Glycol and Carbohydrate Additives. *Cellulose* **2009,** *16*, 899-910.

[12]. Karageorgiou, V.; Kaplan, D. Porosity of 3d Biomaterial Scaffolds and Osteogenesis. *Biomaterials* **2005,** *26*, 5474-5491.

[13]. Ma, P. X. Biomimetic Materials for Tissue Engineering. *Adv. Drug Delivery Rev.* **2008,** *60*, 184-198.

[14]. Elias, K. L.; Price, R. L.; Webster, T. J. Enhanced Functions of Osteoblasts on Nanometer Diameter Carbon Fibers. *Biomaterials* **2002,** *23*, 3279-3287.

[15]. Engler, A. J.; Sen, S.; Sweeney, H. L.; Discher, D. E. Matrix Elasticity Directs Stem Cell Lineage Specification. *Cell* **2006,** *126*, 677-689.

[16]. Silva, A. K.; Richard, C.; Bessodes, M.; Scherman, D.; Merten, O. W. Growth Factor Delivery Approaches in Hydrogels. *Biomacromolecules* **2009,** *10*, 9-18.

[17]. Shi, Q.; Li, Y.; Sun, J.; Zhang, H.; Chen, L.; Chen, B.; Yang, H.; Wang, Z. The Osteogenesis of Bacterial Cellulose Scaffold Loaded with Bone Morphogenetic Protein-2. *Biomaterials* **2012,** *33*, 6644-6649.

[18]. Usui, Y.; Aoki, K.; Narita, N.; Murakami, N.; Nakamura, I.; Nakamura, K.; Ishigaki, N.; Yamazaki, H.; Horiuchi, H.; Kato, H., *et al.* Carbon Nanotubes with High Bone-Tissue Compatibility and Bone-Formation Acceleration Effects. *Small* **2008,** *4*, 240-246.

[19]. Helenius, G.; Backdahl, H.; Bodin, A.; Nannmark, U.; Gatenholm, P.; Risberg, B. In Vivo Biocompatibility of Bacterial Cellulose. *J. Biomed. Mater. Res. A* **2006,** *76*, 431-438.

[20]. Petersen, N.; Gatenholm, P. Bacterial Cellulose-Based Materials and Medical Devices: Current State and Perspectives. *Appl. Microbiol. Biotechnol.* **2011,** *91*, 1277-1286.

[21]. Yang, H. S.; La, W. G.; Cho, Y. M.; Shin, W.; Yeo, G. D.; Kim, B. S. Comparison between Heparin-Conjugated Fibrin and Collagen Sponge as Bone Morphogenetic Protein-2 Carriers for Bone Regeneration. *Exp. Mol. Med.* **2012,** *44*, 350-355.

[22]. Baik, K. Y.; Park, S. Y.; Heo, K.; Lee, K. B.; Hong, S. Carbon Nanotube Monolayer Cues for Osteogenesis of Mesenchymal Stem Cells. *Small* **2011,** *7*, 741-745.

[23]. Kresse, G.; Furthmuller, J. Efficient Iterative Schemes for Ab Initio Total-

Energy Calculations Using a Plane-Wave Basis Set. *Phys Rev B* **1996,** *54*, 11169-11186.

[24]. Kresse, G.; Furthmuller, J. Efficiency of Ab-Initio Total Energy Calculations for Metals and Semiconductors Using a Plane-Wave Basis Set. *Comp Mater Sci* **1996,** *6*, 15-50.

[25]. Perdew, J. P.; Burke, K.; Ernzerhof, M. Generalized Gradient Approximation Made Simple. *Phys. Rev. Lett.* **1996,** *77*, 3865-3868.

[26]. Grimme, S. Semiempirical Gga-Type Density Functional Constructed with a Long-Range Dispersion Correction. *J. Comput. Chem.* **2006,** *27*, 1787-1799.

[27]. Strachan, A.; van Duin, A. C. T.; Chakraborty, D.; Dasgupta, S.; Goddard, W. A. Shock Waves in High-Energy Materials: The Initial Chemical Events in Nitramine Rdx. *Phys. Rev. Lett.* **2003,** *91*.

Chapter 7

Nature-induced bioengineered nano-scaffolds for constructing three-dimensional mini-brain

Introduction

Over the last decade there has been remarkable progress in neurobiology and neural engineering mainly encouraged by development of innovative scientific methodologies[1]. One of the most dominant efforts is controlling neuronal functions at *in vivo* condition with targeted genetic engineering such as optogenetics[2]. An *in vitro* model system which is intended to emulate the physiological conditions at the well-defined state, shows a great advantage in terms of simplicity and thereby controllability compared to the *in vivo* model systems.

Constructing three-dimensional neuronal networks has been a challenging issue due to its difficulty in inducing physiologically-critical neuronal characteristics such as long term culture viability, appropriate protein expression, layered network formation, and synaptic connectivity evolution over time. Hydrogel is typically an attractive platform for hosting a general three-dimensional (3D) *in vitro* culture, however, several practical issues, i.e., neuronal toxicity caused by unreacted scaffold-forming monomers and complexity in anchoring cell adhesive ligands[3–5] need to be resolved. In parallel, the entangled electrospun microfiber networks or closely-packed microbead arrays were attempted as a synthetic scaffold for the 3D neuronal culture[6–13]. Such a micro-engineered material platform chemically modified with polylysine exhibit the structural modularity for scaffold fabrication and the improved viability in neuronal culture compared to the hydrogel platform, however, the microscale topographic environment allows only for the confined surface to neuronal cells, therefore, the 3D network formation is severely limited.

Moreover, the incident light is either scattered by the microscale objects or distorted at the interfacial region between water and scaffold material due to the refractive index mismatch. Such an optical hindrance prevents the microscopic interrogation of the resultant 3D neuronal network using optical tomography tools. Above all, the neuronal cells cultivated in a given neuronal scaffold have requirements to behave as if they reside at the physiological condition so that this artificial culture platform is viable as an *in vitro* model system for neuronal network study.

Bacterio-cellulose (BC) is historically known as Nata-de-coco, a tropical dietary jelly-like substance commonly used for adding flavor of appetizer in fruit salad and, recently, have found many interesting applications in biotechnonology, microbiology, and materials science due to its interesting material properties. This cellulose-based nanostructured natural material which is formed by straight sugar chain repetition and strong hydrogen bonding interactions among neighboring monosaccharides exhibit intriguing properties such as decent wettability via enriched hydroxyl functionality, nanoscopically well-organized architecture with high crystallinity, mechanical modulus as high as steel, and optical transparency above 80% in the visible light range[14–17]. The most striking aspect of this material is that this nanostructured cellulose is synthesized by bacteria even though its function is still under investigation[18–20] and this natural machinery driven by bacteria can be utilized for preparing artificial composite materials, too. Herein, the natural synthetic machinery of a bacterial strain (*Acetobacter Xylinum*) is successfully demonstrated for synthesizing the nanoengineered bacteriocellulose homogeneously hybridized with nanocarbon materials with an aim to combine the benefits from the natural nanostructured cellulose and artificial GO or rGO sheets. The resultant GO and rGO-incorporated BC carries many interesting characteristics for a novel neuronal culture platform for 3D artificial neuronal network study. Particularly, the optical transparency was remained allowing for the phase-contrast and fluorescence imaging with depth up to several mm without two-photon microscope and the nanofibillar structure of bacterial cellulose was greatly mimics the mechanical property of the brain. The growing kinetics, neuronal phenotypes, and long-range interneuronal connectivity were closely emulated with this novel material platform.

Experimental

Preparation of amphiphilic comb-like Polymer (APCLP)

APCLP was synthesized by free radical polymerization of MMA (Aldrich), poly(ethylene glycol) methacrylate (Aldrich, Mn 360 g/mol, corresponding to n = 6) and poly(ethylene glycol) methyl ether methacrylate (Aldrich, Mn 475 g/mol, corresponding to n = 9), in tetrahydrofuran for 18 h as previously described.47 The CNTs (purity >95%, lljin Nanotech Co., Korea) produced by the chemical vapor deposition method were used without further purification or treatment. The CNTs were determined to have an outer diameter of about 10–20 nm and a length of 150–200 μm. A total of 1 mg of CNT was added to 10 mL of APCLP solution (30% ethanol, 0.001% APCLP), after which the samples were sonicated using a horn-type ultrasonic generator (Fisher Scientific Co., USA) with a frequency of 23 kHz and a power of 30 W for 20 min at room temperature.

G. xylinus culture

G. xylinus (KCCM 40216) was obtained from the Korean Culture Center of Microorganisms. The bacterium was cultured on mannitol medium composed of 2.5% (w/w) mannitol, 0.5% (w/w) yeast extract and 0.3% (w/w) bacto-peptone. The culture media were sterilized in an autoclave at 120 ◦C for 20 min and then poured into 500 mL flasks. The pre-inoculum for all experiments was prepared by transferring a single *G. xylinus* colony grown on agar culture medium into a 100 mL Erlenmeyer flask filled with mannitol culture medium.

Preparation of GO and rGO-BC

The pre-cultured culture cell suspension was introduced into 1 × 10^{-3} % (w/v) GO and rGO-dispersed culture medium (pH 6.0) at a ratio of 1:10 and incubated at 28 °C for 2 weeks. The GO and rGO -incorporated BC (GO BC and rGO–BC) membrane biosynthesized in the medium was simply harvested and purified by boiling in 1 wt% sodium hydroxide for 2 h at 90 °C. Subsequently, the membrane was thoroughly washed with running distilled water, after which it was soaked in 1 wt% aqueous sodium hydroxide solution for 24 h at room temperature to eliminate the cell debris and components of the culture liquid. The pH was then reduced to 7.0 by repetitive washing with distilled water. Next, the membrane was bleached by immersion in 1 wt% aqueous sodium hypochlorite for 2 h, after which it was washed with running distilled water until pH 7 was attained. Finally, the membrane was vacuum-dried at 60 °C for 12 h. The normal BC membrane was prepared by harvesting a single *G. xylinus* colony in mannitol culture medium, purifying and bleaching as described above.

Analyses of GO and rGO distribution in scaffolds

To analyse the distribution of GO and rGO in BC scaffolds, BC, GO-BC-Syn, and rGO-BC-Syn were embedded in an optimal cutting temperature compound (TISSUE-TEK® 4583, Sakura Finetek USA Inc., Torrance, CA, USA), followed by freezing and slicing into 10 µm thick sections at -22 ℃. Cross-sections of the samples were analysed using an image analysis system (Axio Observer Z1, Zeiss, Göttingen, Germany) coupled to a light microscope at a magnification of ×400 and ×1000. For scanning electron microscopy (SEM) analysis, BC, GO-BC-Syn, and rGO-BC-Syn were frozen at -70 ℃, followed by freeze-drying for 1 day. The surface morphology of the samples was observed at an acceleration voltage of 5 kV using SEM (JSM-6330F, JEOL). Raman spectra were taken from top, middle and bottom layer. Raman maps are of the G peak (1560 to 1620 $cm^{-1)}$ bands. Raman spectra were recorded using a Renishaw inVia micro-Raman spectrometer (λ laser = 514 nm, ~500 nm spot size, 100× objector). The AFM observations and measurements were carried out by means of a Park systems XE-100 scanning probe microscope at ambient conditions. Silicon cantilever NSC-36 C (Mikromasch Inc) having pyramidal tips with 10 nm nominal radii of curvature(R_c). Cantilever spring constant of 0.60 N m-1 were used. Topological data was employed a compressive load of 10 nN during scanning. After getting topography images, z-scanner displacement versus force curves were recorded. Forward and backward rate was 0.3 µm/sec and a maximum compressive load of 40 nN was applied to the surface during data acquisition. The Young’s modulus (E) of the samples were calculated using the Hertzian model, equation. Poisson’s ratio(ν) is set to 0.5 and parabolic geometry of the indenter is set.

Analyses of scaffold properties

The porosity and the pore sizes of fabricated scaffolds were measured using mercury intrusion porosimetry (AutoporeIV9500, Micromeritics Instrument Corporation, Norcross, GA). Nitrogen physisorption measurements at 77 K were performed by a Quantachrome NOVA 4000 (U.S.A.), and Brunauer-Emmett-Teller (BET) and Barrett-Joyner-Halenda (BJH) analyses were done by Autosorb software (Quantachrome). The BET analysis was done for relative vapor pressure of 0.05 to 0.3. The BJH analysis was done from the desorption branch of the isotherm. The sheet resistance and electrical conductivity of GO-BC-Syn, and rGO-BC-Syn were measured by the van der Pauw four-probe technique with using a Hall measurement system (2400 Source Meter, Keithley).

Analyses of GO-BC-Syn, and rGO-BC-Syn integration

Transmission electron microscopy (TEM, JEOL 2100, JEOL, Japan) analyses were operated at 200 kV.

Results and Discussion

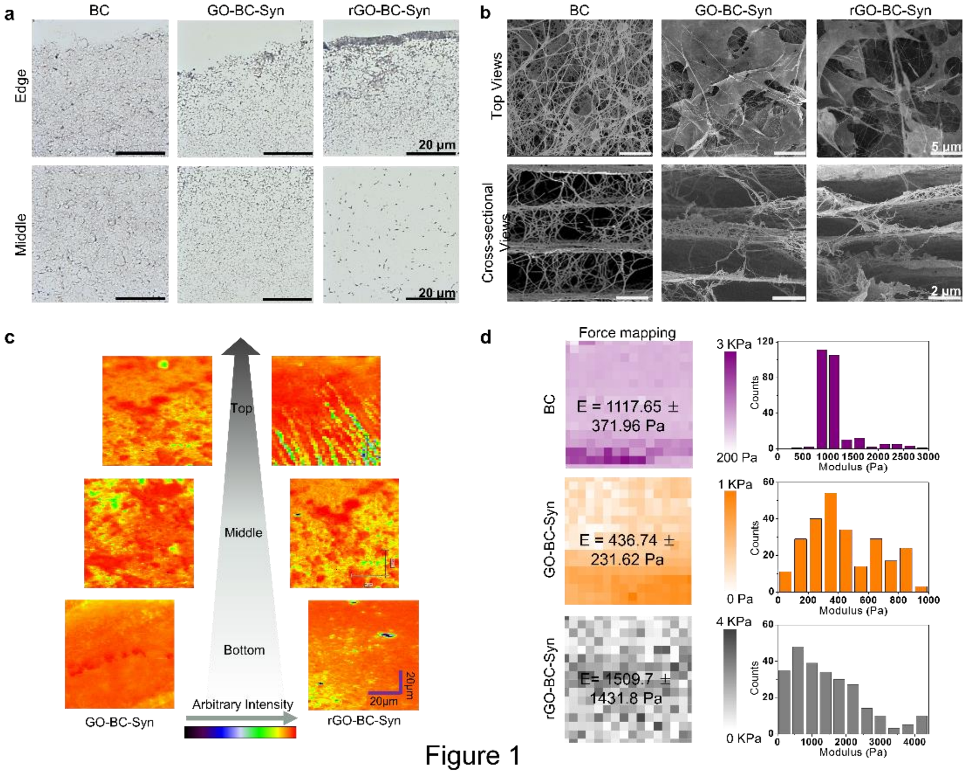

Figure 1

Figure 1 | Fabrication and characterization of bare/graphene composited BC. a, Schematic explanation of Acetobacter Xylinum producing cellulose nanofiber and in situ composition of graphene. b, Top view and lateral view of bacterial cellulose exhibit nanofibrillar cellulose and stacked layered structure, respectively. c, Top view of GO (left) and rGO (right) composited BC. d, High resolution TEM image of bare bacterial cellulose and their crystallinity. e, Raman spectroscopic measurement confirms the presence of GO and rGO with corresponding vibration peaks. f. Liquid AFM measurement of elastic modulus along normal direction.

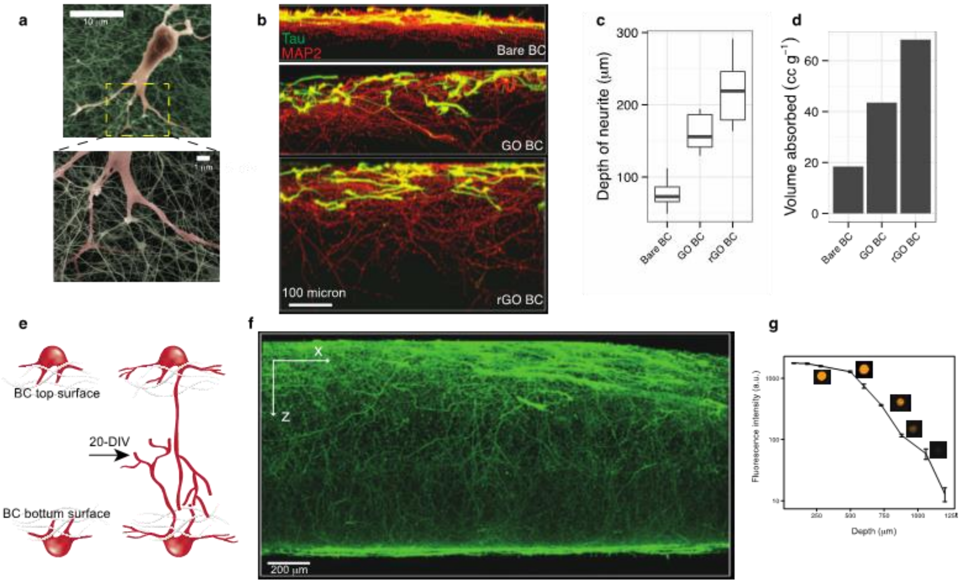

Figure 2 | Detailed neuronal morphology and controlled z-directional neuronal outgrowth. a, scanning electron microscope images represent interfacial region between 3-div neuron and BC. b z-directional neuronal outgrowth of bare and graphene composited BC. MAP2 and Tau labels neuronal dendrites and axons, respectively. c, statistical representation of z-directional neuronal outgrowth depending presence of graphene composition d, BET measurements exhibit modulation of bacterial cellulose porosity by means of graphene composition. e, schematic figure of outgrowing neuron toward to counter BC surfaces. f, Fluorescence y-stacked image of widely culture (3.5 mm × 3.5 mm × 1 mm) 20-div neuron. g, Fluorescence light intensity decay of fluorescence beads depending on depth of BC.

Since the pristine BC is a complex fibrillar network with large internal porosity and hydrophilic surface, each cellulose nanofiber is surrounded by a large number of water molecules leading to hydrogel in an aqueous condition. The hydrophilic nature of BC networks allows for an approximate swelling ratio of 25[21] . Such a high content of water in the water-absorbed BC matrix in combination with very fine morphology of nanofibrillar structures (~30 nm in diameter) and minimal visible light absorption in cellulose moiety enables marginal light scattering and autofluorescence resulting in an ideal culture platform for optical microscopy[22]. Indeed, the actin filmaments and microtubules in outgrowing neurites and growth cones of cultured neurons are clearly visible inside a milimeter-thick BC scaffold by optical fluorescence microscopy while the nanofibrillar structure of bacterial cellulose is dimly imaged by the reflection mode. The resultant 3D-organized cellular architecture could be easily reconstituted by 3D stacking method using confocal microscopy. As confirmed by the depth profile of fluorescence intensity (Figure 2b), the entangled structure of nanofibrous network does not severely interrupt light passage up to one milimeter thickness.

Figure 2c shows the false-colored SEM images of the fixed neuronal cell which is deposited on top of the pristine BC, GO-BC, and rGO-BC. Unlike the cell cultured on the flat rigid substrate, the neuronal cell on nanotextured scaffold exhibits a spherical shape of cell body reminiscent of the shape of the cell culture on very soft substrate. The neurites initially follow the BC nanofiber morphologies on the top surface and eventually penetrate into the scaffolds growing downward. The vertical movement of neurties after penetration is more prominent in the neuronal culture on the GO-BC than on the pristine BC and most prominent on rGO-BC (Figure 2d). To correlate the extent of z-directional neurite outgrowth and the porosity of culture scaffold, the surface area of each nanoengineered BC was experimentally extracted by the BET theory as the ratio between matrix surface area and its own mass so that higher surface area per volume represents higher porosity. As displayed in Figure 2f, the GO- or rGO-hybridized BCs exhibit much higher porosity than the unmodified bare BC. With the addition of nanostructured carbon materials, the cellulose chains are expected to be easily adsorbed and homogeneously hybridized on the surface of nanoscale carbon platelet during bacterial synthesis as shown in the high resolution TEM images (Figure 1). In fact, the suspended nano-membrane-like structures are more easily found in GO or rGO-incorporated BC resulting in the increased surface area (Supporting information). Furthermore, the smaller particle size of rGO may explain the larger porosity of rGO-hybridized BC than GO-BC. Therefore, the vertical outgrowth of neurites is deliberately manipulated and, possibly, inter-neuronal connectivity along the vertical direction is effectively fine-tuned by incorporation of nanostructured carbon materials.

The cellular phenotype is not only affected by genetically-encoded information but also by the external cellular environment[23–25]. It is very important to maintain the appropriate physiological condition particularly at the embryonic neuronal development stage since the minute change in the cellular environment may lead to the defect in cellular function and subsequent dysfunction of the resultant neuronal network. In this regard, the emulation of physiological condition is assumed to be

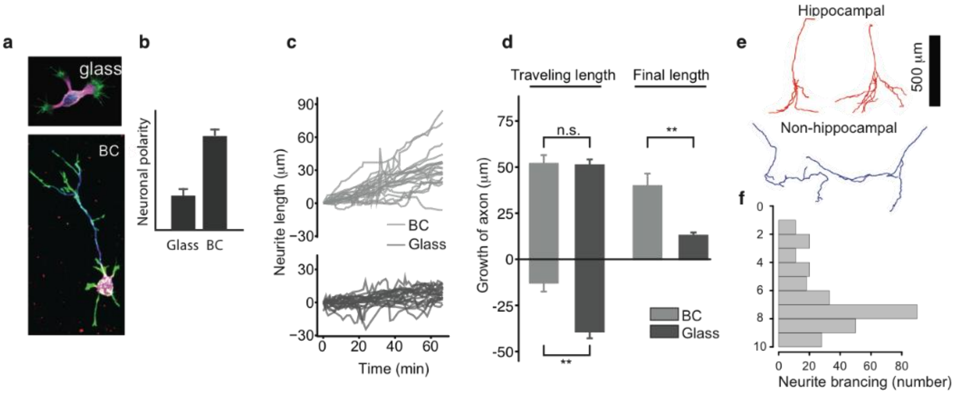

Figure 3 | Neuronal kinetics in BC a, comparison of neuronal development on glass and BC substrate b, statistical analysis of neuronal polarity. c, time evolutional trajectory of 3-div outgrowing axon on BC and glass substrate. (n = 20 for BC and glass, 5 sec for time interval) d, extracted quantitative information of outgrowing axon reveal total traveling length and final length of axon which composed or substrate by forward and backward motion. e, traced 20-div neuronal morphology on BC exhibits delicate and distinct neuronal sub-cell type. f, synchronization of axon branching at the certain depth (700 μm) of BC.

critical to generate a reliable neuronal culture condition for establishing an *in vitro* neuronal network model. From the mechanical point of view, it is well known that a brain tissue typically exhibits very low elastic modulus (<1 kPa) and the phenotypes of the constituent cells (e.g., neurons and glia) are very sensitive to the mechanical properties of culture scaffold. In the case of the 2-D neuronal culture on the flat rigid glass having high elastic modulus, the cultured cells show the typical cone-like morphology of actin filaments at the tip of growth cone and the decent expression level of focal adhesion complex proteins (i.e., paxillin, vinculin) which are matured through the extensive tug war between the stiffened integrin-ECM junction point and the retrograding myosin motor protein [28–31]. In contrast, the cells deposited on the BC-based 3-D scaffold exhibit the distinct morphology of highly-branched growth cone with fine tips and overall large surface area. Furthermore, the promoted neurite outgrowth and its accelerated polarization to axon and dendrite are clearly observed. More strikingly, the expression level of the focal adhesion protein complex is remarkably low on the 3D scaffold.[26,27] These results imply that the neurons on the BC-based scaffolds are under significantly lower tension than those in the control 2-D glass culture[32,33], which are also reasonably supported by the experimentally-measured elastic moduli of the present 3D culture scaffolds as already shown in Figure 1f (< 1kPa). Note also that the growth cone on BC not only navigate through the 3D nanostructured fibers but also move in the forward direction only while that on the control 2D culture ruffles and rambles in the random direction (Figure 1c and d and supporting movie clip). The apparent directionality of neurite outgrowth and viability of neuronal culture even without chemical modification might be related to

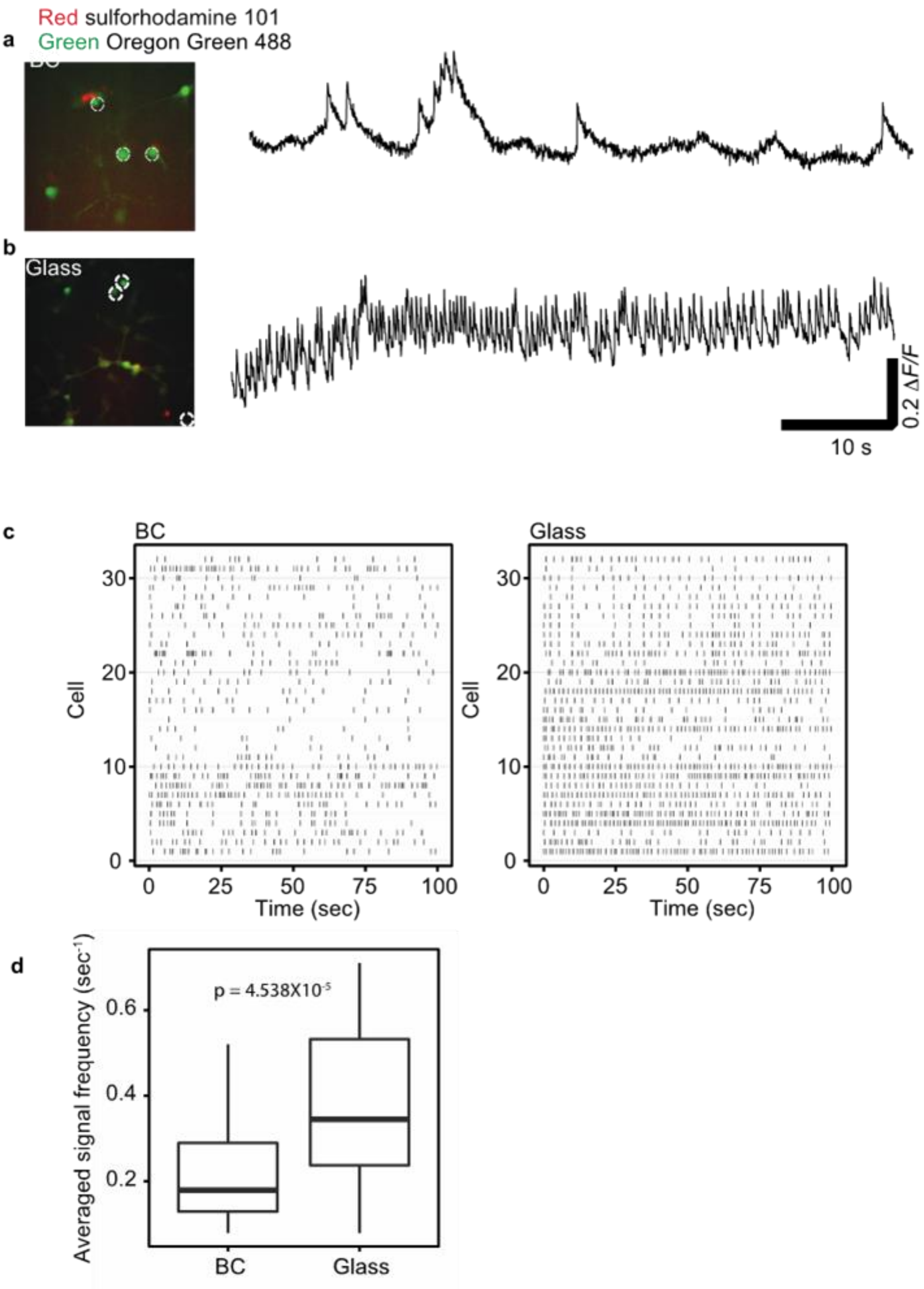

Figure 4 | Comparison of calcium signalling of cultured neuron on BC and glass substrates. a,b, calcium signalling of 14-div cultured neurons show difference calcium spike frequency and duration. Cell density is 20-30/mm^2. c, d, collection of calcium spike peakes with respect to time for 14-div neuron on glass and BC

the topographic stimulation of growth cone via nanoscale fiber morphology, however, there need to be more experimental evidences to prove this hypothesis.

One of the obvious advantages of 3D neuronal culture for a model neuronal network study is the addition of spatial degree of freedom to the network structure. Especially, the extant central nervous system has a highly-organized layered structure where the neuronal circuit in each layer is capable of information processing in a parallel manner[34,35]. This type of structural integrity is intrinsically hard to be realized in a conventional 2D network system. To mimic the stacked layers of 2D neuronal circuits, the dissociated neuron cells were seeded on to both sides of GO and rGO-composited BC scaffolds successively and cultured in 20 days *in vitro* (Figure 4a). The resultant 3D network was fixed and stained with dendrite (MAP2) and axonal (Tau) markers for interrogating neurite outgrowth behaviour and topographic connectivity between layers. In contrast to axons moving vertically, the majority of dendrites on both top and bottom BC surfaces are confined on the same surface. The interlayer connectivity and synapse formation were confirmed by tracing single dendrites and axons and staining the synaptic proteins, respectively (Figure 4c). Approximately 15% of the neurons plated on the top layer have reached the opposite layer and their 90% exhibit pyramidal neuron-type morphologies with branching at a certain depth. Interestingly, there exists a strong correlation between the frequency and the depth of axonal branching. The most of branching points are concentrated at the depth of ~800 um which is very close the metric reported in the in vivo system revealing that the neuronal cells on the present culture platform mimic well those in the physiological condition. Furthermore, the calcium imaging of the 3D cultured neurons on BC show much more random pattern of neuronal activity which is characteristic of stochastic activity of the in vivo neuronal network than that of the 2D model system on glass.

Conclusions

Considering all the above mentioned results including the soma and axonal morphologies, neurite outgrowth pattern, focal adhesion protein expression, and intracellular calcium activity of the neuronal cells cultured on top as well as their optical transparency and appropriate mechanical property, the present nanoengineered BC-based composite materials are well suited for the 3D neuronal culture platform and will serve as a valuable tool for accessing the mini-brain-like 3D neuronal network to interrogate many critical questions in neurobiology and neural engineering fields.

References

[1]. Focus on neurotechniques. *Nat. Neurosci.* **16,** 771–771 (2013).

[2]. Boguski, M. S. & Jones, A. R. Neurogenomics: at the intersection of neurobiology and genome sciences. *Nat. Neurosci.* **7,** 429–433 (2004).

[3]. Xie, J. *et al.* Nanofiber Membranes with Controllable Microwells and Structural Cues and Their Use in Forming Cell Microarrays and Neuronal Networks. *Small* **7,** 293–297 (2011).

[4]. Pautot, S., Wyart, C. & Isacoff, E. Y. Colloid-guided assembly of oriented 3D neuronal networks. *Nat. Methods* **5,** 735–740 (2008).

[5]. Yu, M. *et al.* Semiconductor Nanomembrane Tubes: Three-Dimensional Confinement for Controlled Neurite Outgrowth. *ACS Nano* **5,** 2447–2457 (2011).

[6]. Dubois-Dauphin, M. L. *et al.* The long-term survival of in vitro engineered nervous tissue derived from the specific neural differentiation of mouse embryonic stem cells. *Biomaterials* **31,** 7032–7042 (2010).

[7]. Lampe, K. J., Antaris, A. L. & Heilshorn, S. C. Design of three-dimensional engineered protein hydrogels for tailored control of neurite growth. *Acta Biomater.* **9,** 5590–5599 (2013).

[8]. Mahoney, M. J. & Anseth, K. S. Three-dimensional growth and function of neural tissue in degradable polyethylene glycol hydrogels. *Biomaterials* **27,** 2265–2274 (2006).

[9]. Luo, Y. & Shoichet, M. S. A photolabile hydrogel for guided three-dimensional cell growth and migration. *Nat. Mater.* **3,** 249–253 (2004).

[10]. Melissinaki, V. *et al.* Direct laser writing of 3D scaffolds for neural tissue engineering applications. *Biofabrication* **3,** 045005 (2011).

[11]. Annabi, N. *et al.* 25th Anniversary Article: Rational Design and Applications of Hydrogels in Regenerative Medicine. *Adv. Mater.* **26,** 85–124 (2014).

[12]. Thiele, J., Ma, Y., Bruekers, S. M. C., Ma, S. & Huck, W. T. S. 25th Anniversary Article: Designer Hydrogels for Cell Cultures: A Materials Selection Guide. *Adv. Mater.* **26,** 125–148 (2014).

[13]. Burdick, J. A. & Murphy, W. L. Moving from static to dynamic complexity in hydrogel design. *Nat. Commun.* **3,** 1269 (2012).

[14]. Iwamoto, S., Kai, W., Isogai, A. & Iwata, T. Elastic Modulus of Single Cellulose Microfibrils from Tunicate Measured by Atomic Force Microscopy. *Biomacromolecules* **10,** 2571–2576 (2009).

[15]. Iguchi, M., Yamanaka, S. & Budhiono, A. Bacterial cellulose—a masterpiece of nature’s arts. *J. Mater. Sci.* **35,** 261–270 (2000).

[16]. Nogi, M., Handa, K., Nakagaito, A. N. & Yano, H. Optically transparent bionanofiber composites with low sensitivity to refractive index of the polymer matrix. *Appl. Phys. Lett.* **87,** 243110 (2005).

[17]. Nogi, M. & Yano, H. Transparent Nanocomposites Based on Cellulose Produced by Bacteria Offer Potential Innovation in the Electronics Device Industry. *Adv. Mater.* **20,** 1849–1852 (2008).

[18]. Williams, W. S. & Cannon, R. E. Alternative Environmental Roles for Cellulose Produced by Acetobacter xylinum. *Appl. Environ. Microbiol.* **55,** 2448–2452 (1989).

[19]. Valla, S. & Kjosbakken, J. Cellulose-negative Mutants of Acetobacter xylinum. *J. Gen. Microbiol.* **128,** 1401–1408 (1982).

[20]. Schramm, M. & Hestrin, S. Factors affecting Production of Cellulose at the Air/ Liquid Interface of a Culture of Acetobacter xylinum. *J. Gen. Microbiol.* **11,** 123–129 (1954).

[21]. Wei, B., Yang, G. & Hong, F. Preparation and evaluation of a kind of bacterial cellulose dry films with antibacterial properties. *Carbohydr. Polym.* **84,** 533–538 (2011).

[22]. Heller, W. Remarks on Refractive Index Mixture Rules. *J. Phys. Chem.* **69,** 1123–1129 (1965).

[23]. Trappmann, B. *et al.* Extracellular-matrix tethering regulates stem-cell fate. *Nat. Mater.* **11,** 642–649 (2012).

[24]. Discher, D. E., Mooney, D. J. & Zandstra, P. W. Growth Factors, Matrices, and Forces Combine and Control Stem Cells. *Science* **324,** 1673–1677 (2009).

[25]. Vogel, V. & Sheetz, M. Local force and geometry sensing regulate cell functions. *Nat. Rev. Mol. Cell Biol.* **7,** 265–275 (2006).

[26]. Fraley, S. I. *et al.* A distinctive role for focal adhesion proteins in three-dimensional cell motility. *Nat. Cell Biol.* **12,** 598–604 (2010).

[27]. Petroll, W. M., Ma, L. & Jester, J. V. Direct correlation of collagen matrix deformation with focal adhesion dynamics in living corneal fibroblasts. *J. Cell Sci.* **116,** 1481–1491 (2003).

[28]. Geiger, B., Spatz, J. P. & Bershadsky, A. D. Environmental sensing through focal adhesions. *Nat. Rev. Mol. Cell Biol.* **10,** 21–33 (2009).

[29]. Discher, D. E., Janmey, P. & Wang, Y. Tissue Cells Feel and Respond to the Stiffness of Their Substrate. *Science* **310,** 1139–1143 (2005).

[30]. Stricker, J., Beckham, Y., Davidson, M. W. & Gardel, M. L. Myosin II-Mediated Focal Adhesion Maturation Is Tension Insensitive. *PLoS ONE* **8,** e70652 (2013).

[31]. Kuo, J.-C., Han, X., Hsiao, C.-T., Yates Iii, J. R. & Waterman, C. M. Analysis of the myosin-II-responsive focal adhesion proteome reveals a role for β-Pix in negative regulation of focal adhesion maturation. *Nat. Cell Biol.* **13,** 383–393 (2011).

[32]. Kim, D.-H. *et al.* Actin cap associated focal adhesions and their distinct role in cellular mechanosensing. *Sci. Rep.* **2,** (2012).

[33]. Prager-Khoutorsky, M. *et al.* Fibroblast polarization is a matrix-rigidity-dependent process controlled by focal adhesion mechanosensing. *Nat. Cell Biol.* **13,** 1457–1465 (2011).

[34]. Kandel, E., Schwartz, J., Jessell, T., Siegelbaum, S. & Hudspeth, A. J. *Principles of Neural Science, Fifth Edition*. (McGraw Hill Professional, 2013).

[35]. Andersen, P. *The Hippocampus Book*. (Oxford University Press, 2007).

국문초록

최근 줄기세포와 조직공학의 발전과 더불어 줄기세포 기반의 재생의학은 심장 질환과 뇌 질환과 같은 다양한 난치병 치료에 희망적인 전략을 제공하고 있다. 그럼에도 불구하고 이러한 난치병의 치료에는 한계가 많을 뿐만 아니라 해가 지나면서 이병으로 사망하는 환자는 매년 증가 추세에 놓여있다. 이에 이러한 난치병을 효과적으로 치료할 대체치료방법의 개발은 중요하다. 최근 들어 그래핀의 표면적, 뛰어난 전자전달 능력, 높은 전기전도성과 같은 우수한 성질은 그래핀 기반의 새로운 바이오 의학 시대를 여는데 크게 이바질 할 것으로 인식되고 있다.

본 학위논문은 세포조절 및 조직공학 응용에 최적화된 이차원 혹은 삼차원 형태의 플랫폼 개발에 대한 것이다. 이에 따른 본 논문의 구체적인 목표는 다음과 같다. (1) 줄기세포의 성장 및 분화를 위한 2차원 그래핀 플랫폼 개발과 이의 세포 분화 효과를 조사하기 위하여 세포 신호 분자와 세포 외기 질 단백질의 분화도 등의 분석을 통한 메커니즘을 규명하는 것이다. (2) 나노 공학적 접근을 통한 세포 미세환경과 유사한 3차원 플랫폼을 개발하여 세포의 거동 및 분화 조절을 위한 새로운 방안제시이다.

본 논문의 주요 결과는 다음과 같다. 첫째, 처음으로 그래핀 위에서 줄기세포가 3차원 구 형태로 줄기세포가 뭉쳐지는 현상을 발견하였다. 둘째, 최초로 아무런 성장인자가 없는 상태에서도 그래핀 위에서 줄기세포가 cardiomyogenic로의 분화로 촉진하는 과정을 규명하였다. 마지막으로, 배아줄기세포가 그래핀 위에서 중배엽 세포와 내배엽 세포로 단계적 분화과정을 거치고 결론적으로

cardiomyogeic으로의 분화를 촉진 시킬 수 있음을 증명하였다. 하지만 성공적인 생체조직공학의 임상적 적용을 위해서, 세포가 발달할 수 있도록 생체 내 조건과 유사한 3차원 구조를 가지면서 세포의 부착 및 기능 수행을 극대화한 플랫폼의 개발은 필수적인 요소이다. 최근에 그래핀의 바이오 의학 소재로의 혁신적인 플랫폼으로써 줄기세포 분화를 조절하는 메커니즘 및 세포 배양 플랫폼으로써 제안됐다. 이에 그래핀이 복합화된 삼차원 투명 플랫폼의 개발은 재생의학과 이를 이용한 치료 분야에 아주 시급하게 요구되고 있다. 이에 따라 두 번째 분야 연구에서는 탄소 나노 재료기반의 3차원 플랫폼의 개발과 이 플랫폼의 성공적인 조직재생으로의 적용에 관한 것이다. 특별히, 그래핀을 실제 질병 모델에 적용하여 조직 재생에 효과적인 나노 복합체로써 임상적 이용이 가능한지 확인하는 것은 중요하다. 본 학위 논문에서 이러한 것을 가능하게 실현해 보이고자 뼈 재생을 위한 카본 나노튜브가 복합된 바이오 플랫폼을 제작하는 놀라운 방법을 제시하였다. 마지막으로 그래핀이 복합화된 3차원의 층상구조를 가진 플랫폼을 개발하였고 그 플랫폼을 기본적인 신경연구에 활용하는 연구를 진행하였다. 결과적으로 본 학위논문에선 조직공학과 재생의학에 최적화된 플랫폼을 개발하였으며 그에 대한 체계적인 연구 결과를 제시 하였다.

주요어: 그래핀, 카본나노튜브, 줄기세포, 생체모방, 생체 재료, 조직공학

학 번: 2011-30906